

University of Nottingham
UK | CHINA | MALAYSIA

Faculty of Engineering

Department of Mechanical, Materials and Manufacturing Engineering

Experimental and Numerical Investigation of Formability and Ductile Fracture in Incremental Sheet Forming

Shakir Madhloom Gatea

M.Sc. (Production Engineering)

Thesis submitted to the University of Nottingham for the degree of Doctor of Philosophy

September 2017

ABSTRACT

Incremental sheet forming (ISF), also referred to as single point incremental forming (SPIF), is a relatively new, flexible forming process. The ISF process has excellent adaptability to CNC milling machines due to the fact that it does not require the use of high capacity presses or specific dies and is easy to automate for both symmetric and non-symmetric shapes. In SPIF, a blank sheet is fixed by a holder onto a CNC milling machine. A workpiece is formed by the action of a small hemispheric tool in contact with the blank moving along a user-specified tool path and incrementally deforming the blank into the desired shape. According to the technical characteristics of ISF, it can be used to manufacture small batch and customised products. SPIF is a promising technique, which could be further developed as an alternative manufacturing approach for customised medical parts, e.g. cranial plates, with considerable benefits in lead time and cost reduction.

This thesis reports the findings of finite element (FE) analyses and experimental investigations into the formability and fracture in the ISF process, and their application with regard to manufacturing cranial plates, as well as the applicability of using the ISF process to form aluminium matrix composite (AMC).

A modified Gurson–Tvergaard-Needleman (GTN) damage constitutive model was developed with the consideration of shear. The developed GTN model was implemented in Abaqus/Explicit via a VUMAT user subroutine to predict ductile fracture in the ISF process due to void nucleation, growth and coalescence. In comparison with experimental testing, there is a good agreement in the occurrence of fracture. The results also show that shear plays a role under meridional tensile stress in accelerating fracture propagation in ISF processes.

The Nakajima test was used to construct the forming limit curve at necking (FLCN) and fracture (FLCF) for pure titanium sheet. The results of the FLCF are compared with those of the ISF to evaluate the ability of the Nakajima test to describe the fracture in ISF. Due to the fact that the GTN model can be used to capture fracture occurrence at high stress triaxiality, and the shear modified GTN model was developed to predict the fracture at zero stress or even negative stress triaxiality, the original GTN model and shear modified GTN model may not be suitable to predict the fracture in all

samples of the Nakajima test, as some samples are deformed under moderate stress triaxiality. Therefore, another GTN based model with the consideration of stress triaxiality was developed to predict fracture in the Nakajima specimens under different stress triaxiality. The experimental and FE results showed that the shear modified GTN model predicted the fracture accurately with samples under uniaxial tension conditions due to low stress triaxiality and the original GTN model was suitable for an equi-biaxial strain state (high stress triaxiality). On the other hand, the stress triaxiality modified GTN model should be used for samples which have moderate stress triaxiality. The Nakajima test can be applied to establish the FLCF, which in turn can be utilized to describe the formability of the SPIF test for conical and pyramidal truncated specimens.

Experiments and FE analyses were conducted to evaluate the influence of major forming parameters, including the step size, feed rate and tool size, on the formability and fracture of pure titanium. Two types of pure Ti (grades 1 and 2) were used to evaluate the sensitivity of the material type to forming parameters. It was found that the ISF parameters have different degrees of effect on the formability and fracture occurrence of pure titanium, and that grade 2 pure Ti is more sensitive to forming parameters. The optimal parameters from the parametric study were used to investigate the feasibility of using ISF to form a cranial plate; the results show that ISF can satisfactorily form a cranial plate.

By evaluating the deformation and fracture mechanisms of a 6092Al alloy metal matrix composite reinforced with 17.5p vol. % SiC particles (6092Al/SiCp), the applicability of the ISF process to form the 6092Al/SiCp aluminium matrix composite (AMC) was investigated. Tensile tests were carried out at different strain rates to study the microstructure and topography of the 6092Al/SiCp sheet by scanning electron microscopy (SEM), coupled with energy dispersive X-ray spectroscopy (EDS), transmission electron microscopy (TEM) and X-ray diffraction (XRD). The results show that this AMC material at T6 condition is brittle due to the formation of precipitations as a result of either the interaction between the Al and SiCp or from hardening precipitation treatment e.g. Al_2Cu, $Al_4Cu2Mg_8Si_7$ and $MgAl_2$. O-condition annealing was therefore used to reduce the detrimental effect of the intermetallic compounds in the interface region and can improve the fracture toughness and ductility

of the material. However, the Al/SiC sheet treated with O-condition annealing is more sensitive to the strain rate than that treated with T6.

By investigating the feasibility of using SPIF to form AMC sheets for the first time, the results show that the 6092Al/SiCp sheets can be satisfactorily formed after O-condition annealing.

LIST OF PUBLICATIONS

1. Gatea, S., H. Ou, and G. McCartney. *Numerical simulation and experimental investigation of ductile fracture in SPIF using modified GTN model*. In MATEC Web of Conferences. 2015. EDP Sciences.
2. Gatea, S., H. Ou, and G. McCartney, *Review on the influence of process parameters in incremental sheet forming*. International Journal of Advanced Manufacturing Technology, 2016. 87(1): p. 479-499.
3. Gatea, S., F. Chen., H. Long, and H. Ou, *Deformation and fracture of AMC under different heat treatment conditions and its suitability for incremental sheet forming*. International Conference on the Technology of Plasticity, ICTP 2017, 17-22 September 2017, Cambridge, United Kingdom (Accepted).
4. Gatea, S., Ou, H., Lu, B., McCartney, G., Modelling of ductile fracture in single point incremental forming using a modified GTN model, Engineering Fracture Mechanics, 2017. 186: p. 59–79
5. Gatea S., D. Xu, H. Ou, and G. McCartney, *Evaluation of formability and fracture of pure titanium in incremental sheet forming*. International Journal of Advanced Manufacturing Technology (Accepted).
6. Gatea S., B. Lu, J. Chen, H. Ou, and G. McCartney, *Effect of forming parameters on the formability and fracture in incremental sheet forming of pure titanium sheet.* International Journal of Mechanical Sciences (revision under review).
7. Gatea, S., H. Ou, and G. McCartney, *Deformation and fracture characteristics of Al6092/SiC/17.5p metal matrix composite sheets due to heat treatments.* (To be submitted)

ACKNOWLEDGEMENTS

I would like to acknowledge my supervisors, Dr. Hengan Ou and Prof. David Graham McCartney for their encouragement, expert advice and invaluable guidance at every stage of my PhD research and thesis writing.

I gratefully acknowledge the scholarship support provided by the Iraqi Ministry of Higher Education and Scientific Research (IMHESR), Kufa University. Also the support provided by the Engineering and Physical Sciences Research Council (EPSRC) of the UK (EP/L02084X/1), and the International Research Staff Exchange Scheme (IRSES, MatProFuture project, 318,968) within the 7th European Community Framework Programme (FP7).

Special thanks are given to Prof. Jun Chen and Dr. Bin Lu of the Department of Plasticity Technology, Shanghai Jiao Tong University, China; Dr. Dongkai Xu of the State Key Laboratory of Development and Application Technology of Automotive Steels (Baosteel), Shanghai, China and Dr. Hui Long and Mr. Jamie Booth of the Department of Mechanical Engineering, the University of Sheffield, UK for helping me perform the ISF testing and Nakajima test.

I would like to thank the technicians in our laboratories, particularly Dr. Nigel Neate, Dr. Martin Roe, Mr. Tom Buss, Mr. Jason Young, Mr. Mark Daine, Mr. Ben Shaw, Mr. John Hinchliffe and Mr. Andy Plummer for their guidance throughout my experimental work.

Many sincere thanks also go to my colleagues of Integrity and Dynamic Research Group, who provided a comfortable research environment.

Finally, I need to express my highest gratitude to my family; Maryam and Lujain for their continued support and encouragement. They have continually given me the strength to choose the hardest option when life required it.

LIST OFABBREVIATIONS AND SYMBOLS

A	function of the matrix of total equivalent plastic strain
AMC	Aluminium Matrix Composite
BSE	Back Scattered Electron
BS	British Standard
BUT	Bending Under Tension
c	orientation dependent parameter for ductile criterion
CAD	Computer Aided Design
CAM	Computer Aided Manufacturing
CCD	Coupled Charge Device
C3D8R	Continuum, 3D, 8-node, Reduced integration element
C_d	The dilatational wave speed
CDV	Critical Damage Value
CMM	Coordinate Measuring Machine
CNC	Computer Numerical Control
Cp Ti	Commercially pure titanium
CPU	Central Processing Unit
CT scan	Computerized Tomography scan
D	Distance between each two points in tool path
d_1-d_5	J-C damage parameters measured at room temperature
DIC	Digital Image Correlation
D_{ik}	Elastic Constant Matrix
$d\overline{\varepsilon}$	Increment in equivalent plastic strain
$d\varepsilon_{ii}^{p}$	trace of the plastic strain tensor
2D	Two Dimension
3D	Three Dimension
E	Modulus of Elasticity
EDM	Electrical Discharge Machining
EDS	Energy Dispersive X-ray Spectroscopy
f	orientation dependent parameter for shear criterion
F, G, H, L, M and N	Material constants in Hill yield function
FE	Finite Element
FEM	Finite Element Method
FLCN	Forming Limit Curve at the Necking
FLCF	Forming Limit Curve at Fracture
FLD	Forming Limit Diagram
FLSD	Forming Limit Stress Diagram
f_c	Critical Void Volume Fraction
f_f	Final Void Volume Fraction
f_N	Volume Fraction for Void Nucleation
f_o	Initial void volume fraction
g_o	parameter responsible for the inclusion of the Lode angle dependence on the shear mechanism
G01	Linear interpolation
G02	Clockwise circular interpolation
G03	Counter-clockwise circular interpolation
GTN model	Gurson–Tvergaard-Needleman model
H	Tangent of the flow stress
ISF	Incremental Sheet Forming

J-C model	Johnson-Cook model
J_3	Third invariant of the deviatoric stress
K	Stiffness matrix
k_w	parameter producing the damage rate in shear loading
LMIS	Liquid Metal Ion Source
L_{min}	Characteristic element length
M	Mass matrix / Material type
M-K	Marciniak-Kuczynski criteria
MMC	Metal Matrix Composite
MMFC	Modified Maximum Force Criterion
MSFLD	Müschenborn-Sonne Forming Limit Diagram
n	Strain Hardening Coefficient
NC	Numerical Control
ORB tool	Oblique Roller Ball tool
p	Hydrostatic stress
P	Normal contact pressure
PIPS	Precise Ion Polishing System
PM	Powder Metallurgy
q_1,q_2 and q_3	constitutive parameters proposed by Tvergaard
q_4, q_5	Constants of Xue's shear mechanism
R_a	Average roughness
R_1, R_2, R_3, R_{12}, R_{13}, and R_{23}	Factors in Hill's potential function
r_o, r_{45},and r_{90}	Anisotropy factors in direction of 0, 45, 90 degree
RMS	Response surface method
R_z	Maximum roughness
S1, S2 and S3	Deviatoric stress tensors in the principal plane
SADP	Selected Area Diffraction Pattern
SEM	Scanning Electron Microscopy
SFFL	Shear Fracture Forming Line
S_{ij}	Deviatoric Stress Tensor
S_N	Standard Deviation for Void Nucleation
SPIF	Single Point Incremental Forming
SQP	Sequential Quadratic Programming
Step Size (ΔZ)	The distance the tool moves down into the material after completing revolution around the part
STL	Stereolithography
T	Nondimensional temperature (J-C model)
TEM	Transmission Electron Microscopy
t_i, t_f	Initial and final thicknesses of the part
t_o, t	Initial time, time
Tool size (T)	Forming tool diameter
TPIF	Two Points Incremental Forming
u	Vector of displacement
$\dot{u}$	Vector of velocity
$\ddot{u}$	Vector of acceleration
UTS	Ultimate Tensile Strength
V	Feed rate
VUMAT	Vectorised User defined material subroutine in Abaqus/Explicit

VVF	Void Volume Fraction
ν	Poisson's ratio
XRD	X-Ray Diffraction
η	Stress triaxiality ratio
η^+, η^-	Stress triaxiality in equi-biaxial tensile deformation state and in equi-biaxial compressive deformation state
θ_S	Shear stress ratio
θ_S^+, θ_S^-	Values of θ_S at η^+ and η^-
$\varepsilon_d^+, \varepsilon_S^+$	Equivalent plastic strain for biaxial tensile of ductile and shear criterion
$\varepsilon_d^-, \varepsilon_S^-$	Equivalent plastic strain for biaxial compression of ductile and shear criterion
$\dot{\varepsilon}_0$	Reference strain rate
ξ	Time ratio
Δt	Time increment
α	Semi-cone angle
ϕ	Wall angle (sine law)
$\overline{\varepsilon}^p$	Equivalent plastic strain
$\overline{\varepsilon}_f$	Equivalent plastic strain to fracture (J-C model)
$\overline{\varepsilon}_{df}$	Fracture equivalent plastic strain for ductile criterion
$\overline{\varepsilon}_{sf}$	Fracture equivalent plastic strain for shear criterion
λ , $\overline{\mu}$	Lamé's constant
ρ	Mass density of material
τ_c	Critical frictional shear stress
$\varepsilon_1, \varepsilon_2$	Major principal strain, Minor principal strain
μ	Coefficient of friction
σ_1, σ_2, and σ_3	Principal stresses
σ_y	Yield stress
σ_q	Equivalent stress
θ_L	Lode angle
ε_N	mean value of the normal distribution of the nucleation strain
$\Delta\lambda$	change in plastic consistency parameter

CONTENTS

1 INTRODUCTION 1

1.1 Overview of ISF and its potential for medical applications 1
1.2 ISF research challenges 5
1.3 Research aim and objectives 6
1.4 Research methodology 7
1.5 Thesis contributions 8
1.6 Thesis structure 9

2 LITERATURE REVIEW 11

2.1 Introduction 11
2.2 Formability in SPIF 11
2.2.1 Effect of process parameters on formability 14
2.2.1.1 Forming temperature 14
2.2.1.2 Forming angle 16
2.2.1.3 Incremental depth (step size) 17
2.2.1.4 Forming speed (rotation and feed rate) 18
2.2.1.5 Tool size and shape 18
2.2.1.6 Tool path 20
2.3 Deformation and failure mechanics in SPIF 22
2.3.1 Application of a forming limit diagram 26
2.3.2 Effect of forming tool on deformation and failure 30
2.4 Springback and accuracy in SPIF 32
2.4.1 Effect of process parameters on springback and accuracy 32
2.4.1.1 Tool path 32
2.4.1.2 Forming parameters 33
2.4.1.3 Tensile force 34
2.5 Surface roughness in SPIF 35
2.5.1 Effect of process parameters on surface roughness 35
2.5.1.1 Tool rotation and advancement 35
2.5.1.2 Tool size and material 37
2.5.1.3 Tool path 39
2.5.1.4 Step size 39

2.5.1.5 Forming angle 40
2.6 Summary 41
2.6.1 Formability 41
2.6.2 Deformation and failure mechanics 42
2.6.3 Springback and accuracy 42
2.6.4 Surface roughness 42
2.7 Recommendations for future work 43
3 FINITE ELEMENT SIMULATION OF THE INCREMENTAL SHEET FORMING 45
3.1 Introduction 45
3.2 Material constitutive model 46
3.3 Strain hardening of materials 47
3.4 Failure criteria 50
3.5 Non-linear solution method 53
3.6 Mass scaling 55
3.7 Contact and boundary conditions 55
3.7.1 Contact algorithms 56
3.7.2 Friction model 56
3.7.3 Tool paths in ISF 57
3.8 Element type 59
3.9 SPIF benchmark 59
3.10 Numerical results 61
3.10.1 Influence of meshing density 61
3.10.2 Influence of mass scale 64
3.10.3 Influence of friction coefficient 66
3.10.4 Validation of SPIF simulation 68
3.11 Conclusions 69
4 MODELLING OF DUCTILE FRACTURE IN ISF 70
4.1 Introduction 70
4.2 Fracture mechanisms in SPIF 71
4.3 GTN based micromechanics damage model 72
4.4 Classification of GTN model parameters 77

4.5 Shear mechanism 78
4.5.1 Xue's shear mechanism 79
4.5.2 Nahshon-Hutchinson's shear mechanism 79
4.5.3 Lode angle dependency 80
4.6 Implementation of the modified GTN model 81
4.7 Experimental works 84
4.7.1 Tensile test 84
4.7.2 Determination of GTN model parameters of Ti grade 1 86
4.7.3 Single point incremental forming test 89
4.8 Validation of the modified GTN model 91
4.8.1 Benchmark tests on single element 91
4.8.1.1 Hydrostatic tension 91
4.8.1.2 Pure shear stress 92
4.8.2 Influence of meshing density 93
4.8.3 Validation of the modified GTN model under tensile and shear conditions 95
4.9 SPIF of hyperbolic cone and pyramidal shapes 99
4.10 Conclusions 107

5 FORMABILITY IN IN CREMENTAL SHEET FORMING 108

5.1 Introduction 108
5.2 Stress triaxiality modified GTN model 111
5.3 Experimental works 111
5.3.1 Nakajima test 111
5.3.2 Single point incremental forming 114
5.3.3 Thickness and strain measurement 115
5.4 Finite element simulation 116
5.5 Results and discussion 117
5.5.1 Nakajima test 117
5.5.2 Single point incremental forming 123
5.5.3 Forming limit diagram 126
5.6 Conclusions 128

6 ISF PARAMETRIC STUDY 129

6.1 Introduction 129
6.2 Experimental testing 131
6.2.1 Materials characterizations 131
6.2.2 Design of Experiments 136
6.3 FEA model 138
6.4 Results and discussion 139
6.4.1 Effect of step size 139
6.4.2 Effect of feed rate 144
6.4.3 Effect of tool diameter 149
6.5 Cranial plate reconstruction 153
6.6 Conclusions 162

7 DEFORMATION AND FRACTURE OF ALUMINIUM MATRIX COMPOSITE AND ITS APPLICABILITY FOR ISF 163

7.1 Introduction 163
7.2 Experimental procedures 166
7.2.1 Material 166
7.2.2 Heat treatment 166
7.2.3 Tensile test 167
7.2.4 Focused Ion Beam (FIB) 167
7.3 Results and discussion 169
7.3.1 Microstructural analysis 169
7.3.2 Hardness 174
7.3.3 Tensile test 175
7.3.4 Fracture mechanism in tensile test 177
7.3.5 Fracture mechanism in the SPIF 181
7.4 Conclusions 184

8 CONCLUSIONS AND FUTURE WORK 186

8.1 Introduction 186
8.2 Conclusions 186
8.2.1 Finite element simulation 186
8.2.2 Modelling of ductile fracture in ISF 187
8.2.3 Formability in ISF 188

8.2.4 Parametric study and cranial plate concluding remarks 188
8.2.5 Deformation and fracture of AMC and its applicability for ISF 190
8.3 Future work 192

REFERENCES 194

APPENDIX A: Mechanical drawings used for manufacture of SPIF fixture .. 206

APPENDIX B: Mechanical drawings used for manufacture of Nakajima die 213

TABLE OF FIGURES

Figure …… Page number

Figure 1.1Basic principle of incremental sheet forming [3]. 1
Figure 1.2 Two point incremental sheet forming :(a) TPIF with partial die and (b) TPIF with full die [15]. 3
Figure 1.3 Titanium cranial plate [17]. 4
Figure 2.1 Schematic representation of a cross-sectional view of the rotationally symmetric SPIF process [36]. 12
Figure 2.2 Forming limits diagram resulting from SPIF and traditional sheet forming [38]. 12
Figure 2.3 The principle of electric incremental forming [47]. 15
Figure 2.4 Experimental setup laser spot, forming tool and the procedure for the forming process [49]. 16
Figure 2.5 Minimum thickness and its location under condition of varying tool diameters [41]..... 19
Figure 2.6 Comparison of the thickness distributions [60]. 21
Figure 2.7 Sheet thickness distribution as a function of depth [13]..... 22
Figure 2.8 Instantaneous deformation zone and contact area between forming tool and workpiece during SPIF [63]. 23
Figure 2.9 Experimental evidence that SPIF is limited by fracture without necking [63]. 24
Figure 2.10 Crack propagation in SPIF: (a) schematic illustration of the typical crack propagation path in SPIF; (b) circumferential zigzag crack propagation path; (c) circumferential straight crack propagation path; and (d) circumferential straight crack propagation path in a rotational symmetric part obtained by conventional deep-drawing [20]. 24
Figure 2.11 Comparison of FEM and experimental work: (a) FEM based on MMFC to establish FLD, (b) FEM with regard to tool dimension to establish FLD, and (c) experimental work [75]. 28
Figure 2.12 Forming limit diagrams: (a) Conventional FLD. (b) Fracture strains in SPIF and Stretch-bending for a tool diameter of 10mm [76]..... 29
Figure 2.13 Determination of the fracture loci (FLCF and SFFL) from the experimental strains at fracture that were obtained from the SPIF and shear tests [23]..... 30

Figure 2.14 Incremental tool ratio (r_{part}/r_{tool}) as a function of tool radius for the SPIF of truncated conical shapes [81]. 31
Figure 2.15 Sectional profiles for (a) different forming processes and (b) different angle intervals [43]. 34
Figure 2.16 Form deviation and stretching force relationship [90]. 35
Figure 2.17 Typical roughness profiles measured in: (a) advancing tool direction (mean value around 0.3μm) and (b) perpendicular direction (mean value around 0.6 μm) [92]. 36
Figure 2.18 Roughness for different levels of tool rotation [93]. 37
Figure 2.19 Sensitivity of roughness to the shape factor [94]. 37
Figure 2.20 Variation of surface finish with tool diameter at different incremental depths [29]. 39
Figure 2.21 Bottom profiles measured on the best and the worst performing samples [15]. 40
Figure 3.1 Isotropic hardening: (a) yield surface and (b) the corresponding uniaxial stress–strain curve [104]. 47
Figure 3.2 Reversed loading with kinematic hardening: (a) the translation of the yield surface and (b) the resulting stress–strain curve which shows the Bauschinger effect [104]. 48
Figure 3.3 Combined kinematic and isotropic hardening: (a) yield surface with resulting stress–strain curve and (b) strain imposed resulting in cyclic plasticity [104]. 49
Figure 3.4 Forming limit diagram [64] 52
Figure 3.5 Steps for creating a tool path by using a CREO parametric 3.0 57
Figure 3.6 SPIF tool path: (a) profile tool-path and (b) helical tool-path 58
Figure 3.7 Configuration of FE model for SPIF process. 60
Figure 3.8 Flow stress of pure Ti grade 1. 60
Figure 3.9 Geometric shape of the truncated cone. 61
Figure 3.10 Equivalent strain distribution: (a) element length = 2mm and (B) element length = 0.5mm. 62
Figure 3.11 Comparison of equivalent strain for different meshing densities. 63
Figure 3.12 Comparison between numerical and experimental thickness distribution. 63

Figure 3.13 Distortion of final product with different stable time increments: (a) Δt 2E-4 s, (b) Δt 2E-5 s and (c) Δt 2E-6 s..... 65
Figure 3.14 The ratio of kinetic and internal energy for the ISF process. 65
Figure 3.15 Product geometry comparison. 66
Figure 3.16 The effect of friction on the ISF load. 67
Figure 3.17 Thickness distribution with different friction coefficients. 67
Figure 3.18 Comparison between experimental and numerical thickness distribution: (a) α=60^o and (b) α=70^o. 68
Figure 4.1 Schematic of the nucleation, growth and coalescence of voids. Adapted from [135]. 74
Figure 4.2 Comparing uniaxial behaviours of porous metals with Mises materials. Adapted from [64]. 75
Figure 4.3 The dependence of yield surface on the hydrostatic stress for various values of void volume fraction. Adapted from [137]. 75
Figure 4.4 Influence of constitutive parameters q1 and q2 on nonlinear response of GTN constitutive law at $\varepsilon 22 \varepsilon 11 = 1.0$ (a)$1.0 \leq q1 \leq 2.0$; (b) $0.75 \leq q2 \leq 1.25$. Adapted from [141]. 78
Figure 4.5 Normal fracture incipient delamination and shear fracture in the tensile specimen [144]. 81
Figure 4.6 VUMAT subroutine flowchart of shear modified GTN model. 84
Figure 4.7 Typical example of random pattern on specimen surface. 85
Figure 4.8 Experiment setup of digital image correlation. 86
Figure 4.9 Load-displacement curve in tensile test. 87
Figure 4.10 Microstructure of pure titanium at different stages throughout the tensile test: (a) before deformation (initial state), (b) at void nucleation state, (c) at critical stage and (d) fracture surface. 88
Figure 4.11 Tensile specimen under different displacements to determine the VVF at nucleation. 88
Figure 4.12 Geometries obtained by using SPIF: (a) cone; (b) pyramid. 89
Figure 4.13 SPIF experiments and formed titanium parts: (a) CNC milling machine, (b) the fixture used to fix the sheet and (c) parts produced by SPIF process. 90
Figure 4.14 Measuring fracture depth by digital height gage. 90
Figure 4.15 Boundary conditions for: (a) hydrostatic tension, (b) shear stress. 91

Figure 4.16 Results of the simulation of a hydrostatic tensile test as a function of axial strain: (a) void volume fraction (b) axial stress. 92
Figure 4.17 Results for shear stress simulations as a function of the equivalent strain: (a) the void volume fraction and (b) the effective stress. 93
Figure 4.18 Comparison of equivalent plastic strain for different mesh sizes. 94
Figure 4.19 Load-displacement curves for different mesh sizes and comparison with experimental data. 95
Figure 4.20 Comparison of force-displacement curves of experimental tensile test with the GTN models, with and without shear. 96
Figure 4.21 Specimen geometry for the modified ASTM shear test. 97
Figure 4.22 Fracture shape in pure shear test (equivalents strain distribution). 97
Figure 4.23 Evolution of stress triaxiality for the shear and tensile test. 98
Figure 4.24 Comparison of force-displacement curves of experimental shear test with GTN models, with and without shear. 99
Figure 4.25 Geometric shape of hyperbolic profile. 100
Figure 4.26 Distribution of the void volume fraction (SDV8) obtained by numerical simulation of a SPIF process with different depths. 101
Figure 4.27 Location of selected elements on the FE model. 102
Figure 4.28 Evolution of void volume fraction during the SPIF process. 102
Figure 4.29 Evolution of major strain during the SPIF process. 103
Figure 4.30 VVF reuslts for forming a hyperbolic shape using GTN models with and without shear. 104
Figure 4.31 Simulated results obtained from the original and shear modified GTN model in comparison with the actual forming experiment of the hyperbolic shape. 104
Figure 4.32 VVF results for forming a truncated pyramid using GTN models with and without shear. 106
Figure 4.33 Simulated results obtained from the original and shear modified GTN model in comparison with the actual forming experiment of the truncated pyramid. 106
Figure 5.1 Schematic diagram showing the FLCN and FLCF [73]. 109
Figure 5.2 Illustration of the cross section of the tool used for Nakajima testing [89]. 112
Figure 5.3 Nakajima test equipment and deformed specimen. 113
Figure 5.4 Dimensions of different FLD samples prepared for experiments. 113

Figure 5.5 Circular grid patterns, (a) before deformation and (b) after deformation. 114
Figure 5.6 The distorted grid on the deformed SPIF parts: (a) hyperbolic truncated cone shape and (b) hyperbolic truncated pyramid shape. 115
Figure 5.7 The sample of divided hyperbolic truncated cone. 116
Figure 5.8 Finite element model of Nakajima test. 117
Figure 5.9 Major strain distributions during the Nakajima test simulation in different strain states. 118
Figure 5.10 Distribution of major and minor strain in Nakajima test specimens. ... 119
Figure 5.11 Evaluation of stress triaxiality in Nakajima test specimens. 120
Figure 5.12 Evaluation of major strain in the fracture region of Nakajima specimens. 121
Figure 5.13 Fracture depth of simulated Nakajima test specimens with different widths obtained for the stress triaxiality modified GTN model. 122
Figure 5.14 Fracture depth of Nakajima test specimens with different widths. 123
Figure 5.15 Comparison of major strain concentration in (a) hyperbolic truncated cone and (b) hyperbolic truncated pyramid shape. 124
Figure 5.16 History of major and minor strain in the hyperbolic truncated cone and hyperbolic truncated pyramid shape. 125
Figure 5.17 The distorted grid on the deformed SPIF parts: (a) hyperbolic truncated cone shape and (b) hyperbolic truncated pyramid shape. 125
Figure 5.18 History of major strain in the fracture region of SPIF in both the hyperbolic truncated cone and hyperbolic truncated pyramid shapes..... 126
Figure 5.19 Forming limit diagram for 0.7 mm thick grade 1 titanium sheet..... 127
Figure 6.1 Fractured tensile specimens. 132
Figure 6.2 True stress true strain curves for grade 1 and 2 pure titanium deformed at different strain rates..... 132
Figure 6.3 Load-displacement curves for pure Ti grade 1 and 2 showing the stages of determination of the GTN model parameters..... 134
Figure 6.4 Microstructure of pure Ti grade 2 before deformation. 134
Figure 6.5 Determination of void volume fraction at nucleation: (a) microstructure of pure Ti grade 2 showing the voids nucleation and (b) strain distribution from digital image correlation at nucleation. 135

Figure 6.6 Determination of critical void volume: (a) microstructure of pure Ti grade 2 showing the voids at critical stage and (b) strain distribution from digital image correlation at necking. 135
Figure 6.7 Determination of void volume fraction at fracture: (a) microstructure of pure Ti grade 2 showing the voids at fracture and (b) strain distribution from digital image correlation at fracture. 136
Figure 6.8 Geometric shape of a hyperbolic cone: (a) CAD model and (b) cross-section profile. 137
Figure 6.9 Flow stress of pure Ti grade 2. 139
Figure 6.10 Simulated results obtained from the modified GTN model with stress triaxiality in comparison to the actual forming experiment of the pure Ti grade 1 hyperbolic cone shape with different step sizes. 140
Figure 6.11 Simulated results obtained from the modified GTN model with stress triaxiality in comparison to the actual forming experiment of the pure Ti grade 2 hyperbolic cone shape with different step sizes. 141
Figure 6.12 Comparison of vertical forming load for different step sizes (DZ): (a) pure Ti grade 1 and (b) pure Ti grade 2. 141
Figure 6.13 History of Mises Stress distribution for different step sizes (DZ): (a) pure Ti grade 1 and (b) pure Ti grade 2. 142
Figure 6.14 FLCFs for different step sizes (DZ): (a) pure Ti grade 1 and (b) pure Ti grade 2. 142
Figure 6.15 History of the void volume fraction obtained by numerical simulation of the ISF process with different step sizes (DZ): (a) pure Ti grade 1 and (b) pure Ti grade 2. 143
Figure 6.16 Thickness distribution for different step sizes (DZ): (a) pure Ti grade 1 and (b) pure Ti grade 2. 143
Figure 6.17 Simulated results obtained from the modified GTN model with stress triaxiality in comparison to the actual forming experiment of the pure Ti grade 1 hyperbolic cone shape with different feed rates. 145
Figure 6.18 Simulated results obtained from the modified GTN model with stress triaxiality in comparison to the actual forming experiment of the pure Ti grade 2 hyperbolic cone shape with different feed rates. 146
Figure 6.19 Comparison of vertical forming load for different feed rates (V): (a) pure Ti grade 1 and (b) pure Ti grade 2. 146

Figure 6.20 Strain rate history for different feed rates (V): (a) pure Ti grade 1 and (b) pure Ti grade 2. 147
Figure 6.21 FLCFs for different feed rates (V): (a) grade 1 pure Ti and (b) grade 2 pure Ti. 147
Figure 6.22 history of the void volume fraction obtained by numerical simulation of the ISF process with different feed rates (V): (a) pure Ti grade 1 and (b) pure Ti grade 2. 148
Figure 6.23 Thickness distribution for different feed rates (V): (a) pure Ti grade 1 and (b) pure Ti grade 2. 149
Figure 6.24 Simulated results obtained from the modified GTN model with stress triaxiality in comparison with the actual forming experiment of the pure Ti grade 1 hyperbolic cone shape with different tool sizes. 150
Figure 6.25 Simulated results obtained from the modified GTN model with stress triaxiality in comparison with the actual forming experiment of the pure Ti grade 2 hyperbolic cone shape with different tool sizes. 151
Figure 6.26 Comparison of vertical forming load for different tool sizes (T): (a) pure Ti grade 1 and (b) pure Ti grade 2. 152
Figure 6.27 FLCFs for different tool sizes (T): (a) pure Ti grade 1 and (b) pure Ti grade 2. 152
Figure 6.28 History of the void volume fraction obtained by numerical simulation of the ISF process with different tool sizes (DZ): (a) pure Ti grade 1 and (b) pure Ti grade 2. 152
Figure 6.29 Thickness distribution for different tool sizes (T): (a) pure Ti grade 1 and (b) pure Ti grade 2. 153
Figure 6.30 Geometric construction of a cranial plate: (a) skull model, (b) top view of the skull and (c) the CAD model of the cranial plate. 153
Figure 6.31 SPIF tool path generated for cranial plate forming. 154
Figure 6.32 Cranial plate geometry: (a) X-Y plane and (b) X-Z plane. 154
Figure 6.33 Finite element model of cranial plate forming. 155
Figure 6.34 A customized backing plate to support the cranial plate during deformation. 156
Figure 6.35 SPIF experiments of cranial plate forming: (a) SPIF experiment and (b) deformed cranial plate. 156

Figure 6.36 Distribution of the equivalent strain (SDV1) obtained by numerical simulation of cranial plate forming at different depths. 157
Figure 6.37 The final depth of the cranial plate with the location of cross-sections for thickness measurements. 158
Figure 6.38 Thickness distribution along sections X-X and Y-Y. 159
Figure 6.39 Void volume fraction distribution along sections X-X and Y-Y..... 159
Figure 6.40 Distribution of major and minor strain in forming limit diagram. 160
Figure 6.41 History of major and minor strain in cranial plate. 161
Figure 7.1 O-condition annealing for 6092Al composite based on ASM recommendations [179]. 167
Figure 7.2 SEM micrographs showing the stages of preparing samples of Al/SiC_p using a FIB machine: (a) platinum coating, (b) milling, (c) transparent foil of MMC and (d) EDS of MMC. 168
Figure 7.3 Microstructure of MMC-T6 Al6092/17.5% SiCp showing the distribution of reinforcement as well as phases and porosity. 169
Figure 7.4 : (a) BSE image showing the spectrum distribution in 6092Al matrix. (b) EDX spectrum from the matrix. 170
Figure 7.5 TEM micrographs and corresponding SADP of the interface of the 6092Al/SiC composites after T6 treatment: (a) TEM image of Al/SiC interface showing the intermetallic compound (Al_2Cu) formed around the SiC particle, (b) SAD pattern of Al_2Cu and (c) EDS analysis of Al_2Cu. 172
Figure 7.6 TEM micrographs and corresponding SADP of the interface of 6092Al/SiC composites after O-condition annealing: (a) TEM image of the Al/SiC interface showing the phase of $Al_4Cu_2Mg_8Si_7$ formed around the SiC particle, (b) SAD pattern of $Al_4Cu_2Mg_8Si_7$ and (c) EDS analysis of $Al_4Cu_2Mg_8Si_7$ 173
Figure 7.7 XRD pattern of 6092Al/SiCp: (a) T6 treatment composite and (b) O-condition annealing composite. 174
Figure 7.8 X-ray diffraction patterns measured on the specimen of 6092Al/SiCp under different heating conditions. 174
Figure 7.9 Hardness of 6092Al/SiC_p after different heat treatments. 175
Figure 7.10 True stress-true strain curves of Al6092/SiC/17.5p. 176
Figure 7.11 Effect of strain rate on fracture elongation and ultimate tensile strength: (a) relation between fracture elongation and strain rate and (b) relation between tensile strength and strain rate. 177

Figure 7.12 Effect of heat treatment on fracture surface at strain rate 8x10-5 s^{-1}: (a) T6- treatment and (b) O-condition annealing. 178
Figure 7.13 Debonding phenomenon with T6-treatment. 178
Figure 7.14 Effect of strain rate on fractograph of 6092Al/SiCp with T6-treament: (a) strain rate 0.16 s^{-1} (b) strain rate $8x10^{-5}$ s^{-1}. 179
Figure 7.15 Effect of strain rate on fractograph of 6092Al/SiCp with O-condition annealing: (a) strain rate 0.16 s^{-1}, (b) strain rate $8x10^{-2}$ s^{-1}, (c) strain rate $8x10^{-3}$ s^{-1}, (d) strain rate $8x10^{-4}$ s^{-1} and (e) strain rate $8x10^{-5}$ $s^{-1.}$ 180
Figure 7.16 Effect of heat treatment on the fracture of hyperbolic truncated shape: (a) after T6 treatment; (b) after O-condition annealing. 182
Figure 7.17 Effect of feed rate on fracture angle. 183
Figure 7.18 Comparison of forming load at different feed rates. 183
Figure 7.19 Effect of heat treatment on fracture surface of SPIF part: (a) T6- treatment and (b) O-condition annealing. 184

LIST OF TABLES

Table …….. Page number

Table 2-1 Roughness results [100]..... 41
Table 3-1 Mechanical properties of grade 1 pure titanium. 61
Table 3-2 Mechanical properties of AA1050-O. 68
Table 4-1 Mechanical properties of pure titanium. 85
Table 4-2 Damage parameters of pure titanium. 88
Table 5-1 The dimensions of Nakajima test specimens. 113
Table 6-1 Mechanical properties of pure titanium 2. 131
Table 6-2 GTN damage model parameters of 2 pure titanium. 133
Table 6-3 ISF parameters. 137
Table 6-4 Design of Experiments. 137
Table 6-5 Effect of ISF step size on the formability and fracture of grade 1 and 2 pure Ti. 139
Table 6-6 Effect of ISF feed rate on the formability and fracture of grade 1 and 2 pure Ti. 144
Table 6-7 Effect of ISF tool size on the formability and fracture of grade 1 and 2 pure Ti. 149
Table 7-1 Chemical composition of 6092 Al alloy. 166
Table 7-2 Elemental distribution of Al- matrix, SiC particle and interface region with T6 and O-condition annealing. 170
Table 7-3 Effect of strain rate on the fracture elongation and UTS of 6092Al/SiCp. 181

CHAPTER 1

INTRODUCTION

1.1 Overview of ISF and its potential for medical applications

Incremental sheet forming (ISF) generally refers to a group of forming processes that may be characterised by localized deformation, and this deformation is proceeded progressively on a certain path to cover the whole surface of the part. Based on this definition, there are several types of ISF, such us spinning, shear forming, flow forming and single- or two-point ISF. In spinning, a roller is used to push a rotating blank gradually onto a mandrel to produce axisymmetric shape with respect to the profile of the mandrel. A similar approach is used in shear forming, but it is designed to use a large force to produce a hollow or tubular part.

The main difference between spinning, shear forming and flow forming is in the thickness of the formed parts. Parts formed by spinning process show less change in thickness as compared with those formed by shear forming and flow forming processes. Several ISF techniques have been developed to make use of computer numerical controlled (CNC) equipment. One of these methods, single-point incremental forming (SPIF), may be characterised by the action of a CNC milling machine tool that has a single-point contact with the sheet metal blank. The blank is fixed by a holder that remains at the same height, as shown in Figure 1.1 [1]. In this process, a small-sized hemispheric tool moves along a user-defined path and incrementally creates the desired shape [2].

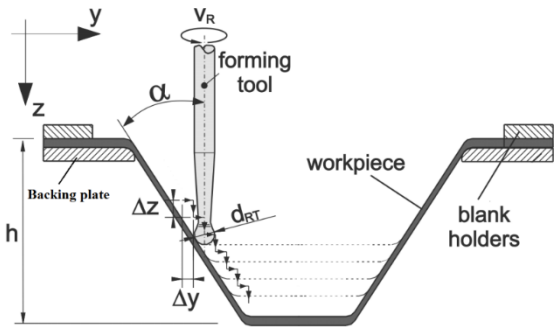


Figure 1.1Basic principle of incremental sheet forming [3].

One of the earliest report on ISF was by Leszak in 1967 in a patent [4] at the time when a CNC machine was not yet technically feasible. In the late 1970s and early 1980s, the principle of asymmetrical incremental sheet metal forming was first described by Mason and Appleton [5, 6]. They proved that the flexible forming of a sheet metal workpiece was possible by using a hemispherical tool that can be moved along a three-axis CNC mill. In 1990s Iseki and Kumon [7] constructed the forming limit for the ISF and they proved the forming limit curve is larger than that one based on the plastic instability theories. Another research was published by Iseki [8] in 2001 to simulate the ISF using FEM based on the shell theory. Filice et al. [9] proved in 2002 the forming limit curve of ISF is straight line with negative slope and it is different from that of stamping processes. The experimental results of Ceretti et al. [10] in 2004 showed the feasibility of ISF to produce prototypes for industrial application. Since then, many research papers have been published in this field. However, ISF is still under development in a number of areas requiring further research before this technology is used in industry, although the potential areas for applications have already been highlighted and clear advantages have been established as against conventional sheet metal forming techniques.

According to the forming method, the ISF technology can be classified as single point (SPIF) and two point (TPIF) incremental forming, in which the tool moves around a partial or fully fixed die on a programmed path to pull down the sheet. Figure 1.2 illustrates the TPIF process. Further classification can be made by the types of processes that are applied, such as negative or positive. In negative ISF, the force is applied inside the cavity to be formed and the application of positive force is the outside of the part. The positive process always happens in TPIF, where it is necessary to have a die that is located inside the part. This is because the tool force is applied on the convex side of the shape, to follow the contour lines. Negative increment sheet forming might be applied to SPIF [11].

The advantages that allow ISF to be developed as a viable solution for sheet metal products can be listed as follows:

- The setup costs can be largely neglected [12]
- ISF is a highly flexible process, and it is possible to simply modify the machine part program so that the product shape is changed [13].

- Due to the stress state induced during tool movement, the formability is greater than that of traditional stamping [12].
- ISF is suitable to make parts for replacement, such as for automotive parts where there is a lack of dies and tooling for a one-off part, and it can also be used for rapid prototyping of new products [12].
- The contact surface is small, and the forces during the forming process are low so the amount of lubricant required is reduced as compared to conventional sheet metal forming [13].

On the other hand, there are some significant drawbacks of the process, which may be given in the following:

- ISF requires a significant amount of time to form the part as deformation is processed gradually by the defined tool path [12].
- The accuracy of the final part is normally inferior to that by a conventional stamping process with a significant amount of springback to occur during tool movement and trimming of the blank.
- It is difficult to produce a part with a wall angle close to 90^{o}, hence many stages of ISF forming are needed to prevent failure [14].
- There are other limitations including material thinning and poor surface finish.

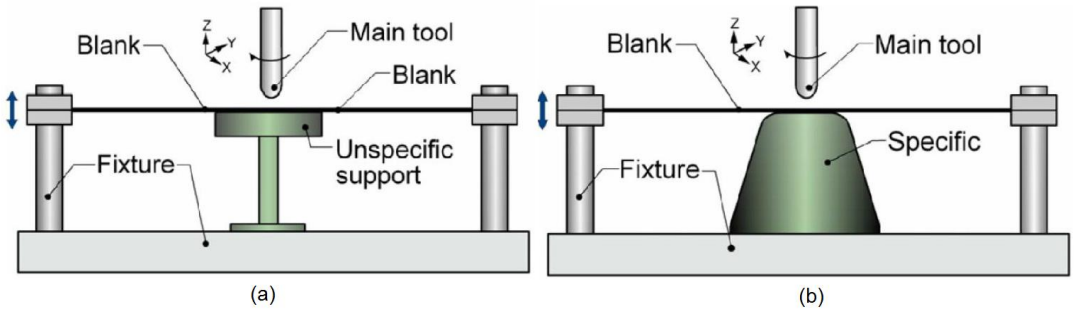


Figure 1.2 Two point incremental sheet forming :(a) TPIF with partial die and (b) TPIF with full die [15].

According to the technical characteristics presented, SPIF can be used for small batch, prototypes and customised products. For example, in the rapid prototyping, Jeswiet et al. [16] used SPIF to produce prototypes for the automotive industry and in the field of medical applications, Verbert et al. [17] produced a titanium skull implant by using multi-stage SPIF.

A cranial plate is a metal plate that is used for cranioplasty, as shown in Figure 1.3. It is used when part of the skull bone is damaged due to traffic accidents or tumour. Other application of a cranial plate is maxillo-facial corrections, if there is any deformation of the patient's head [18]. Medical grade titanium is a typical material used to produce cranial plates. Titanium is the preferred material, due to the fact that it has a high strength to weight ratio, inertness, and bio-compatibility [19].

To manufacture a cranial plate the CAD model for the real cranial plate is required. To generate a CAD model, a series of cross-sectional images of the patient's head are produced by using a computerized tomography scan (CT scan); these images can be processed by a computer programme to obtain a three dimensional CAD model. [18, 19].

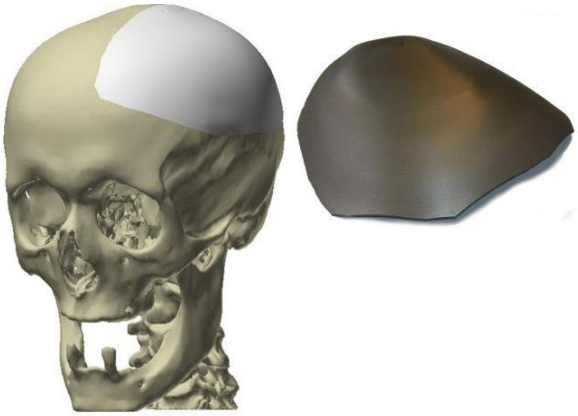


Figure 1.3 Titanium cranial plate [17].

Several traditional methods are used to manufacture cranial plates. One of the most common manufacturing processes for cranial plates is hydroforming; in this process, a clay model is used to obtain a negative die, typically made in silicone. Then this die is utilized to create a positive die made of composite material. The positive die is used to manufacture the actual cranial plate using hydroforming. The hydroforming technique is economically unfeasible, because every cranial plate is custom made [19]. Milling operations can also be used to manufacture cranial plates, but this process is very expensive due to tooling cost and waste of titanium. In addition, the casting process can be used to manufacture cranial plates, but the drawback of this technique is that only thicker plates of >0.6 mm can be produced [18]. Since every patient has a unique cranial plate, the traditional forming process would require to design and

manufacture a custom positive and negative die for each particular patient and that requires a significant amount of time and cost.

The aforementioned considerations justify the reasons that a new approach to the manufacture of cranial plates should be found. Thus, the SPIF is a promising technique that could be developed as an alternative manufacturing approach for cranial plates with considerable lead time and cost benefits due to the fact that it does not require any high capacity press or dies of a specific shape. Instead the part can be formed by moving the tool along a programmed path by using SPIF.

1.2 ISF research challenges

Incremental sheet forming is a relatively new process for the manufacture of small batches and customised non-axisymmetric sheet parts used in the aerospace and automotive industries. There is also potential for using this method to manufacture cranial plates from titanium metal sheets for medical applications.

Although ISF with a rigid tool is a viable process, several challenges remain. One of these is the effect of shear on the fracture. It is clear from the literature that there are different opinions about the deformation modes in ISF based on both experimental work and finite element simulation. Some researchers think that deformation occurs due to stretching [20], whilst others believe it is largely due to a combined through-thickness shear and stretching or through-thickness shear and local bending around the tool [21, 22]. Therefore, more work needs to be done to understand the deformation and fracture mechanisms in the ISF process of complex shapes.

The ability of the Nakajima test to describe the fracture in ISF is still debatable; some researchers claim that the test is identical to ISF tests on pyramidal and conical truncate parts [23], while others proved that the major strain at fracture in ISF is located above the Nakajima's forming limit curve at fracture (FLCF) when a small tool dimeter is used [24]. Thus, more work is needed to evaluate the ability of the Nakajima test to describe the fracture in ISF.

The original Gurson–Tvergaard-Needleman (GTN) model has been used to simulate the Nakajima test in order to construct the forming limit curve at necking (FLCN). The results showed that there was a good correlation between the FE prediction and experiments, especially in the biaxial strain state [25, 26] due to the high stress

triaxiality ratio created by this state, so further investigation to improve the prediction of the original GTN model with low and moderate stress triaxiality is recommended.

It appears from the literature that there is a lack of detailed understanding and even opposing views on the effect of ISF process parameters, such as the step size and feed rate on fracture occurrence in ISF. Some researchers claim that the effect of step size and feed rate are considered insignificant [27-30], while others believe that an increased step size and feed rate has a negative effect on formability [28, 29, 31-35]. Therefore, future work is needed to provide a better understanding of the effect of ISF parameters.

Until today, there has been no work carried out to investigate the applicability of ISF to form discontinuous reinforced materials e.g. aluminium matrix composite. AMC materials are attractive for many industrial applications, such as in the aerospace and automotive industries. ISF is a suitable process for manufacturing small batches or customised AMC sheet components. However, it can be technically challenging to form a complex shape of AMC sheets due to reduced ductility as an inherited trade-off between the enhanced strength and reduced ductility of AMC materials. Thus, there is clear need to examine the applicability of ISF to form new materials.

1.3 Research aim and objectives

Considering the above challenges, the aim of this thesis is to investigate the deformation and fracture mechanics of the ISF process and its application with regard to manufacturing customised medical parts (human cranial plates) from pure titanium metal sheets. The thesis will also examine the applicability of ISF to form new materials e.g. Al/SiCp composite materials, using rigid tools through extensive experimentation and finite element-based simulation. These aims are supported by achieving the following objectives:

1. Develop a GTN damage model with consideration of shear to evaluate the effect of shear on the formability and fracture of ISF.
2. Develop a GTN model with consideration of stress triaxiality to construct the FLCF in the Nakajima test and in ISF under deformation conditions of moderate stress triaxiality.
3. Compare the FLCF of the Nakajima test to that of ISF to validate the suitability of the Nakajima test to describe the fracture in ISF.

4. Improve understanding of the effect of forming parameters and their interactions on the formability and fracture in the ISF process of grade 1 and 2 pure Ti.
5. Examine the feasibility of reconstructing a cranial plate from pure titanium using the ISF process.
6. Conduct a comprehensive study to investigate the heat treatment effect on the fracture mechanism and the microstructural changes of AMC sheet and examine the applicability of using ISF to form an AMC sheet.

1.4 Research methodology

To achieve the objectives, a series of tasks is planned as follows:

- The GTN model is developed with consideration of shear. The shear GTN damage model is implemented in Abaqus/Explicit via a VUMAT user subroutine. Tensile and shear tests are carried out to determine the parameters and to validate the modified GTN model experimentally. A digital image correlation (DIC) system is used to analyse the necking of the tensile and shear specimens. The data on the initial void volume fraction and those at nucleation, critical and fracture were obtained with a scanning electron microscope (SEM) and ImageJ software.
- The Nakajima test is used to construct the forming limit curve at necking and fracture. The results of the FLCF are compared with ISF to evaluate the ability of the Nakajima test to describe the fracture in ISF. Due to the fact that the original GTN model can be used to capture fracture occurrence at high stress triaxiality, and the shear modified GTN model was developed to predict the fracture at zero stress or even negative stress triaxiality, the Nielsen-Tvergaard model with regard to stress triaxiality is developed to predict the fracture under moderate stress triaxiality.
- Experiments and FE simulations are conducted to evaluate the influence of major ISF parameters on the formability and fracture of pure titanium (grades 1 and 2); then, the optimal parameters are used to investigate the feasibility of reconstructing a cranial plate using the ISF process.
- An aluminium /silicon carbide composite sheet (6092Al/SiCp) is used to obtain a fundamental understanding of the heat treatment effect on the fracture

mechanism, the microstructural changes and the interface between the Al-matrix and SiC particles in order to investigate the applicability of the ISF process to form the 6092Al/SiCp sheet. Changes in the microstructure of the 6092Al/SiCp and the topography of the fracture are investigated using SEM coupled with energy dispersive X-ray spectroscopy (EDS), transmission electron microscopy (TEM) and X-ray diffraction (XRD). Tensile tests with different strain rates ($8x10^{-5}$, $8x10^{-4}$, $8x10^{-3}$, $8x10^{-2}$ and 0.16 s^{-1}) are carried out to study the fracture toughness of the 6092Al/SiCp sheet and to find any correlation between the strain rate and heat treatment.

1.5 Thesis contributions

The contributions of this thesis can be summarized as follows:

- The GTN damage model with shear has been developed to comprehensively study fracture in SPIF for the first time, with particular attention on the effect of shear by using a combined approach of experimental testing for GTN parameters and SPIF processing for FE results validation.
- For the first time, the GTN damage model with consideration of stress triaxiality has been employed to construct the FLCF in the Nakajima test and in incremental sheet forming and to predict the ductile fracture with moderate stress triaxiality that is especially pertinent to the ISF.
- The experimental and FE results showed that the shear modified GTN model can predict the fracture accurately with Nakajima samples under uniaxial tension conditions due to low stress triaxiality and that the original GTN model is suitable for an equi-biaxial strain state (high stress triaxiality), whereas the stress triaxiality modified GTN model should be used for samples which have moderate stress triaxiality.
- The results of GTN based models (original GTN model, shear GTN model and stress triaxiality GTN model) allow detailed evaluation and insight into the effect of stress triaxiality on the facture mechanism under different strain state conditions.
- Better understanding has been achieved of the effect of three key forming parameters, namely the step size, feed rate and tool size, and their interactions on the formability and fracture in the ISF process of grades 1 and 2 pure Ti.

- The ISF parameters have different degrees of effect on the formability and fracture occurrence of pure titanium and the low ductility material e.g. grade 2 pure titanium is more sensitive to increases in the forming parameters.
- The SPIF can satisfactorily form a cranial plate with considerable lead time and cost benefits.
- Al_2Cu is usually formed in the Al-Cu alloy (2xxx and 2xx.x) after ageing when the percentage of Cu in the Al alloy is from 0.2% to 5.6%; the TEM and XRD proved that this phase could be formed with Al6092/SiCp composite when the percentage of Cu is high (1wt. %).
- O-condition annealing can reduce the detrimental effect of the intermetallic compounds in the interface region and improve the fracture toughness and ductility of the composite materials by reducing the amount of the intermetallic compound (Al_2Cu).
- After investigating the feasibility of using SPIF to form 6092Al/SiCp AMC sheets for the first time, the results show that the 6092Al/SiCp sheets can be satisfactorily formed after O-condition annealing.

1.6 Thesis structure

This thesis is presented in eight chapters with content summarized as follows:

The first chapter introduces a general background of the ISF processes with particular attention paid to the research challenges of ISF, the aims and objectives of the research, the methodology and the contributions of this work.

Chapter 2 provides a detailed review of the current state-of-the-art of the ISF process in terms of its technological capabilities and specific limitations with discussions on the formability and failure mechanics, as well as the forming parameters and their effects on the process. Particular attention is given to the effect of process parameters on springback and accuracy and surface roughness. This leads to a number of recommendations that are considered essential for future work.

The fundamental theory and key practical considerations in using FE to simulate ISF are provided in Chapter 3; these include the material constitutive model, failure criteria and non-linear FE solution methods. In addition, the effects of mass scaling, element size and friction coefficient are discussed with the support of cases studies.

In Chapter 4, a modified GTN damage model is developed with consideration of shear to predict ductile fracture in the ISF process. The modified GTN damage constitutive model with shear is implemented in Abaqus/Explicit via a VUMAT user subroutine. The results are compared to the original GTN model without shear and validated by experimental ISF testing.

In Chapter 5, FE analysis of the Nakajima test incorporating the GTN model is carried out to evaluate the formability of pure titanium in the ISF process. Particular attention is given to evaluate the capability of the GTN model to capture the fracture occurrence at different ratios of stress triaxiality and to assess the suitability of the Nakajima test to describe the fracture in ISF.

Chapter 6 presents a parametric study to examine the effects of ISF parameters on the formality and fracture of pure titanium grades 1 and 2. In addition, this chapter includes the construction of the cranial plate using FEM based on the modified GTN model and the predicted results are validated by ISF experimental work.

In Chapter 7, an AMC sheet with 17.5% volume fraction of silicon carbide (SiC) particles is used to obtain a fundamental understanding of the fracture mechanism, microstructure changes and the interface characterizations of Al and SiC particles after heat treatment. This work leads to an examination of applicability of using ISF to form AMC sheet.

Chapter 8, summarises the main conclusions of the research work based on the results gained in the previous chapters. Future recommendations are also outlined.

Chapter 2

LITERATURE REVIEW

2.1 Introduction

Incremental sheet forming is a relatively new flexible forming process. ISF has excellent adaptability to conventional milling machines and requires minimum use of complex tooling, dies and forming press, which makes the process cost-effective and easy to automate for various applications. In the past two decades, extensive research on ISF has resulted in significant advances being made in fundamental understanding and development of new processing and tooling solutions. However, ISF has yet to be fully implemented to mainstream high-value manufacturing industries due to a number of technical challenges, all of which are directly related to ISF process parameters. This chapter aims to provide a detailed review of the current state-of-the-art of the ISF process in terms of its technological capabilities and specific limitations, with discussions on the formability and failure mechanics, as well as the forming parameters and their effects on the process. Attention is also given to the effect of ISF process parameters on springback and accuracy and surface roughness. This leads to a number of recommendations that are considered essential for future research effort.

2.2 Formability in SPIF

In general terms, formability in sheet metal forming may be defined as the ability of a given metal to deform without exhibiting specific forms of failure. Formability in SPIF can be defined by the maximum wall angle ϕ (see Figure 2.1), and it is measured in terms of a tangent line from the unformed blank to the deformed part of the surface, determined by sine law, $t_f = t_i \sin(\pi/2 - \phi) = t_i \sin\alpha$, where t_i and t_f are the initial and final thicknesses of the part, respectively and α is the semicone angle [31]. Thus, ϕ_{max} is usually used as a parameter to measure whether the SPIF process is suitable for a given material and sheet thickness.

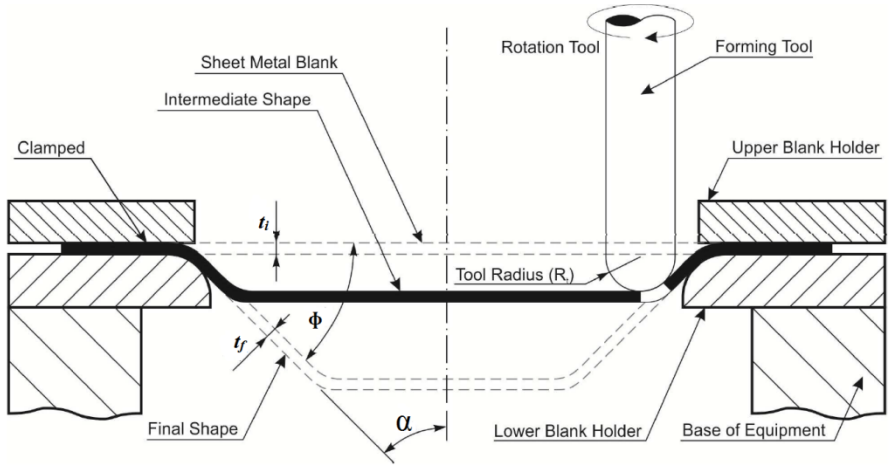


Figure 2.1 Schematic representation of a cross-sectional view of the rotationally symmetric SPIF process [36].

There are different opinions about the modes of deformation in SPIF. Based on experimental work and finite element (FE) simulation, some authors think that the deformation occurs due to shearing [37], whilst others believe it is through stretching [20]. In SPIF, a forming limit diagram (FLD) is used to describe the formability of materials. The forming limit curve (FLC) is usually employed to determine the limits of proportional straining before failure and is quite different from the corresponding one in traditional forming, as shown in Figure 2.2 [38].

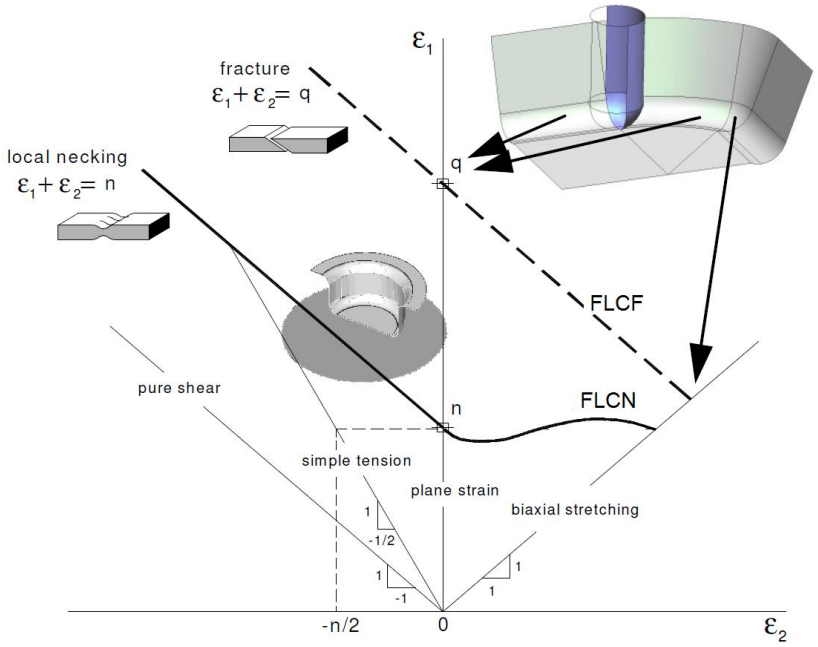


Figure 2.2 Forming limits diagram resulting from SPIF and traditional sheet forming [38].

One of the main limitations of ISF is thickness reduction. A double-pass forming method was proposed by Kim and Yang [39] to improve the formability of aluminium sheets in ISF. It was shown that the majority of deformation occurs by shear, which is an important factor to improve the formability. More uniform thickness strain distribution of the respective products is possible when using the double-pass forming method than with other methods e.g. single point incremental forming. Shim and Park [2] investigated the formability of aluminium sheet (Al 1050) in ISF, using a tool with a freely rotating ball. It was found that the formability of the sheet can be described by a straight line in the FLD. Forming limit diagrams were developed for ISF of 3003 aluminium sheet, using SPIF by Jeswiet and Young [16]. FLDs were defined according to five distinct product shapes: a hemisphere, a straight-sided cone, a hyperbolic-sided cone, a pyramid and a shape with five lobes. It was noticed that very high major strain of over 300 per cent can be achieved with SPIF. Han and Mo [40] developed a three-dimensional elasto-plastic finite element model to investigate the 08Al ISF process. All results were compared with those of experiments. Good agreement between simulated and experimental results in terms of the radial strain and thickness distribution was found. Furthermore, less thinning and more homogenous plastic strain and thickness distribution were achieved with reduced incremental step depth and increased tool size and wall angle. Jun-chao et al. [41] carried out numerical simulation and tensile tests to study the thickness distribution and mechanical property of a truncated pyramid (DC04 steel sheet). The results demonstrated that the minimum thickness was closely related to ISF tool diameter if a conventional tool path (profile tool path) was employed and its location was largely determined by the step size. Tensile test samples were taken from the formed pyramid. It was found that the plasticity of sheet material dropped suddenly while the strength rose. Junchao et al. [42] established a finite element model for a double-pass ISF. The blank used in the experiment was a DC56 steel sheet, which showed that a double-pass forming process enabled more uniform thickness distribution, largely due to the benefits from the increase of the total plastic deformation zone. Junchao et al. [43] devised a series of multi-pass ISF experiments to study the effect of the number of forming stages (n) and angle increments between two adjacent stages ($\Delta\alpha$) on the DC56 sheet formability. It was found that, with the increase of forming stages, the minimum thickness rises significantly and more uniform thickness distribution is accomplished. Moreover, the maximum thickness reduction drops initially and goes up as the value of $\Delta\alpha$ increases.

Titanium F67 grade 2 sheet was used by Silva et al. [44] to determine the thickness distribution of formed sheet by using SPIF. The measurement of thickness and true strain showed that the limit wall angle of the titanium sheet with 0.5 mm thickness is 47^{o}. In addition, the workpiece thickness is 0.35mm according to sine law, as compared to approximately 0.25 mm from experiment. There are many factors which affect the formability of materials. However, the main factors in the SPIF process include forming temperature, forming angle, step size, tool rotation, feed rate, tool size and tool path, and these will be considered in the following section.

2.2.1 Effect of process parameters on formability

2.2.1.1 Forming temperature

Studies have been undertaken to evaluate the effect of temperature on the formability of materials. A laser-based heating system was used by Duflou et al. [45], to create a heated spot in the moving contact zone between tool and titanium TiAl6V4 blank. The results showed that the formability of material was increased by laser-based heating. Ji and Park [46] attempted to use magnesium sheets in incremental forming at warm condition. It was found that with magnesium alloy, AZ31sheet formability increased as the temperature increased from 20 to 250°C. The use of an electrical current for heating hard-to-form sheet metal at the tool-blank interface was proposed by Fan et al. [47] for hot incremental forming, as shown in Figure 2.3. It was found that when the electric current was increased, the yield strength in the tool-blank contact zone was reduced, so the wall angle and formability of magnesium alloy AZ31 increased. Recently, Liu *et al*. published a paper on developing electricity-assisted ISF by using new forms of ISF tooling with cooling channels to form titanium Ti6Al4V sheets, which improved formability to this hard-to-form material [48].

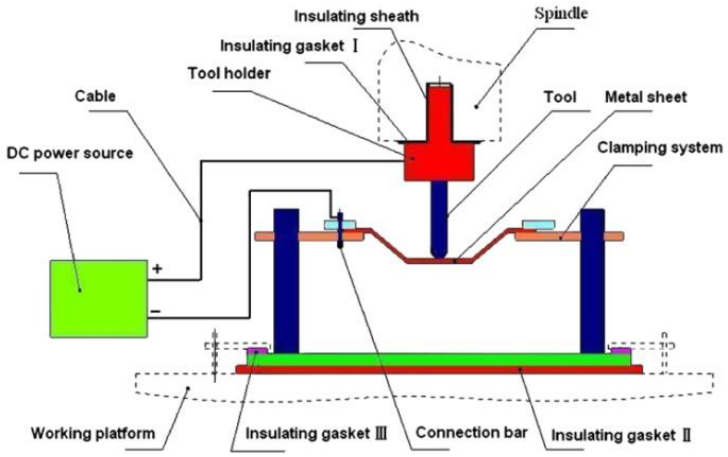


Figure 2.3 The principle of electric incremental forming [47].

Göttmann et al. [49] introduced a new concept for laser-assisted ISF, as shown in Figure 2.4. The tool path was programmed by the computer aided technology. Experimental results showed that the formability of the titanium grade 5 (TiAl6V4) alloy increased as compared to ISF of TiAl6V4 sheet at room temperature. Mosecker et al. [50] investigated the temperature effect on the microstructural evolution of the deformed workpiece (Ti Grade5 (Ti6Al4V)). They formed longitudinal pockets with different depths by using a laser-assisted ISF. It was found that without cooling, deformation at 850 °C led to the highest deformation depth accompanied by pronounced hardening of the material due to grain refinement. On the other hand, good results were yielded from cooling to a coarse globular microstructure with lower hardness and nearly homogenous thickness reduction. An apparatus was constructed by Adams and Jeswiet [51] to improve the formability of 6061-T6 Al employing SPIF process. This apparatus can be used to apply large direct current to the rotating tool. Several current setting and tool diameters were tested to determine the maximum wall angle. It was noticed that the formability increased at the same current density with different tool diameters, so the current density was considered to be a more important factor rather than the current magnitude. A general condition is that the formability improves with the increase of forming temperature, but hot ISF needs additional equipment (e.g. a heat source) so it is suitable to use hot ISF only in cases where the increased cost can be justified.

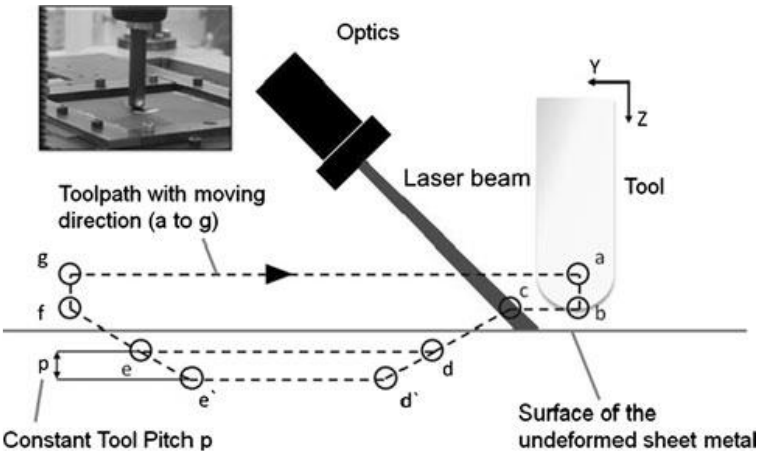


Figure 2.4 Experimental setup laser spot, forming tool and the procedure for the forming process [49].

2.2.1.2 Forming angle

In SPIF, the maximum forming angle is considered to be one of the most important criteria to measure the material's formability limit. Two experimental designs were presented by Ham and Jeswiet [28] to investigate the effects of forming parameters in SPIF on aluminium AA3003 formability. The results showed a small effect of the step size on the maximum forming angle within 1° of difference, whereas the material's thickness, tool diameter and interaction between the material thickness and tool size had a significant effect on maximum wall angle. Minutolo et al. [52] determined the maximum slope angle of the frustums of a pyramid and cone by forming aluminium 7075T0 sheet. The test program has led to evaluation of the maximum wall angle: 63° for a frustum pyramid and 66° for a frustum cone. An experimental study was undertaken by Bhattacharya *et al.* [29] to illustrate the effect of ISF process variables on the maximum wall angle of an Al5052 blank. Analyses of experimental results indicated that the formable angle decreased with increased tool size and incremental depth and decreased blank thickness, whereas feed rate did not have a significant effect on the formable angle. Radu [53] tested two geometries of parts and three thicknesses of metal blank in order to determine the maximum forming angle of a DC01 carbon steel sheet. It was possible to produce shapes with wall slope of up to 80° and a depth of up to 70 mm from sheet metal blanks no thicker than 1.2 mm by using a simple tool. The behaviour of brass 70/30 sheet under ISF conditions was addressed by Fritzen *et al.* [32], with the consideration of the following parameters: wall angle, step depth and tool path strategy. Experimental tests explained that the spiral tool path yielded a

greater forming angle as compared with the traditional tool path. It can be seen from the above investigations that many parameters have a big effect on the wall angle, e.g. tool diameter and tool path, although further study is needed in order to determine the range of their effects on the wall angle (e.g. step size and feed rate).

2.2.1.3 Incremental depth (step size)

The influence of incremental depth is still a debatable parameter. Theoretical investigation was carried out by Ambrogio et al. [54] to get a deeper understanding of the basic phenomena involved in SPIF. The analysis showed that a negative stress distribution occurs under the tool contact zone and tensile stresses on the walls of the formed part. These stresses decrease with decreased incremental depth. Ham and Jeswiet [28] studied the formability of aluminium AA3003 sheets in two new in SPIF and found that the incremental depth had a significant influence on the formability and that decreased step size improved the likelihood of the part to be formed. Kim *et al.* [33] studied the ISF process to produce a complex geometric shape (human face) by using FE simulation and Taguchi's method. Finite element method (FEM) simulation was implemented and evaluated from the historical strain and stress values of cold rolled steel. FE results based on the Taguchi array showed that the tool down step was identified as an important factor for improving the formability. The effect of some parameters, such as step size, on the formability of a commercially pure titanium blank was investigated by Hussain *et al.* [34] and the results proved that the formability decreases linearly as the step size increases. Experimental investigation by means of surface 3D digital image correlation was published by Decultot *et al.* [31] in forming of an AW-5086-H111-grade aluminium alloy. It was found that the workpiece formability was reduced with the increase of increment step size. An experimental study using aluminium Al3003-0 was undertaken by Duflou *et al.* [27] to measure the force in SPIF. It was noticed that the vertical step size had the least significant impact. According to the study by Fritzen *et al.* [32] to address the behaviour of 30/70 brass sheet in ISF. When the vertical step was decreased to 0.5 mm, there was a gain of 1° in the forming angle with a 100 mm depth without failure. It can be concluded that there is a gap of understanding regarding the influence of step size in ISF. Hence, more research needs to be carried out in order to find the relationship between step size and the formability of different materials.

2.2.1.4 Forming speed (rotation and feed rate)

Forming speed has a considerable influence on sheet formability with both rotational speed and feed rate considered important factors in SPIF. The relative motion between the tool and blank causes heat generated by friction. I|t is generally believed that the formability increases along with the forming speed due to heating effects. Ham and Jeswiet [28] presented two experimental designs to investigate the formability of aluminium AA3003 sheets in SPIF. Tool setups were at higher rotational speeds and thus generated more frictional heating in the contact zone, and it was found that the higher rotational speed improved formability. In addition, the blank formability is improved by reducing the feed rate. Producing dome geometry by SPIF was studied by Rattanachan and Chungchoo [55] to explain the effect of speed on the formability of DIN 1.0037 steel (St 37-2 steel). The results showed that the angular velocity of the tool had more influence on formability and that when tool rotational speed increased, the formability decreased. On the other hand, the tool feed rate had less influence on formability, with the results showing decreased formability at increased feed rate. A cold incremental forming process was carried out by Hussain *et al.* [34] in order to investigate the effects of some parameters on formability (maximum wall angle) of commercially pure titanium (Cp Ti) sheet. It was observed that an increase in the feed rate decreased the formability and that the relationship between feed rate and maximum wall angle was quadratic. Buffa *et al.* [30] proposed a method for enhancing the formability of materials in SPIF using high tool rotation speed. This technique was applied to poor formability materials at room temperature, e.g. aluminium AA1050-O, AA1050-H24 and AA6082-T6 sheets. The experimental results showed that there was an increase in drawing angle around 7.5° to 12.5°, as compared to conventional SPIF process. It can be clearly seen that the effects of tool rotation are debatable. Therefore, there is a clear need for further research to the effect of tool rotation on ISF formability to establish a quantitative relationship which would help provide a guideline for the optimum tool rotation and feed rate for a given material.

2.2.1.5 Tool size and shape

Tool size is an important factor effecting formability of materials in SPIF. Experiments have proven that a smaller tool radius enables a higher formability than can be achieved with a larger one. Furthermore, better support of sheet metal can be obtained with a large tool diameter, due to a bigger contact zone, and the amount of forming

force increases when the contact area increases between the tool and blank. In the case of a small tool radius, there is a highly concentrated zone of deformation that causes high strain and leads to better formability. Hussain *et al.* [34] evaluated the formability of a Cp Ti sheet in cold ISF process in order to investigate the effect of tool diameter on the formability. The tool diameter was varied over three levels, i.e. 8, 12, and 16 mm. It was found that by increasing the tool size the formability decreases to approximately follow a quadratic relation.

Using a finite element model to investigate ISF of 08Al sheet, Han and Mo [40] found that reduced incremental depth and increased tool size from 10 mm to 30 mm and wall slope angle tend to reduce axial stress and material thinning and lead to more homogeneous distribution of thickness and plastic strain. The effect of tool diameter on the thickness was studied by Jun-chao *et al.* [41]. They found that the tool size showed little correlation to the location of the minimum thickness, but when tool diameter increases with a spiral tool path, the thickness increases continuously (Figure 2.5). Moreover, the minimum thickness is closely associated with tool diameter if a conventional tool path is employed.

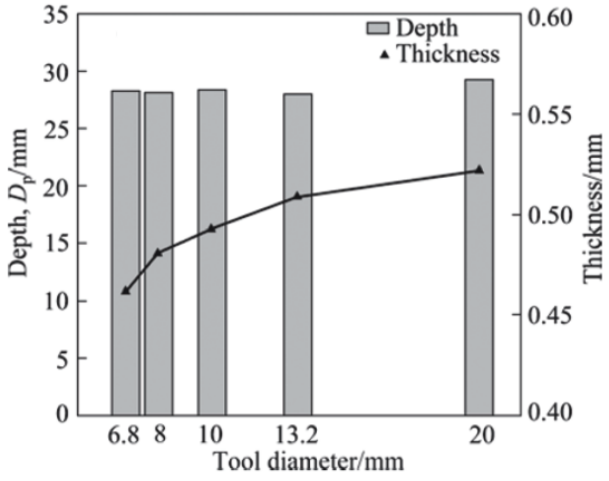


Figure 2.5 Minimum thickness and its location under condition of varying tool diameters [41].

Ham and Jeswiet [28] illustrated the effect of tool diameter on the maximum forming angle for SPIF of aluminium AA3003 sheets and found that higher formability occurred with smaller forming tools due to the concentration of friction heat at the forming tool tip.

A Box-Behnken design of experiment was used by Ham and Jeswiet [56] to develop the experimental plan and to analyse data. The results were presented as a response surface graph, which showed the factors affecting the forming limit. It has been shown that when comparing the influence of material type on average effective strain, with the AA6451 having the lowest average effective strain when tool diameter comparing to average effective strain, aluminium AA5754 seems to have no effect as the contour is flat. With aluminium AA645 sheet, the largest tool diameter (9.525 mm) generates lowest average effective strain, and the other tool sizes (4.7625 mm and 6.35 mm) have no effect on average effective strain.

A new oblique roller ball (ORB) tool has been developed by Lu et al. [57] to investigate the influence of friction on the material deformation and formability. Four grades of aluminium sheets were utilized in the experiments including AA110, AA2024, AA5052 and AA6111. A small hole in the sheet was drilled to study material deformation under both traditional rigid tool and the ORB tool. Experimental results showed that higher formability and smaller through-thickness shear are obtained with the ORB tool.

2.2.1.6 Tool path

Tool path generation is one of the most important factors that must be taken into account in ISF. It plays an important role in the final outcome, especially on thickness distribution of the formed product. Several types of tool paths were tested by Yamashita et al. [58] in order to determine the influence of the tool path on the deformation behaviour, using a finite element model (DYNA3D/explicit code). Depending on the formed part and thickness strain distribution for various tool paths, the travelling tool should be started from one of the corners of the product for a better shape. Otherwise, it is better for the tool to move in the horizontal and vertical directions simultaneously (i.e. in a helical manner) to get more uniform thickness distribution in the product. Mechanism of sheet metal in the ISF was presented by Zhou [59]. Due to the fact that the deformation of the blank occurs only around the tool tip and the contact area (deformation region) is subject to stretch deformation, the thickness of the deformed area of the sheet reduces and the surface area increases during the SPIF deformation. The purpose of sheet metal forming in steps is to produce the whole sheet deformation. From experimental results, in the case of the parallel line tool trajectory, a uniform thickness distribution of the deformed part is maintained and

correlates with that obtained by sine law the optimal tool path optimisation was determined by finite element method in corporation with a response surface method (RMS) and sequential quadratic programming (SQP) algorithm, by Azaouzi and Lebaal [60] in order to improve thickness distribution of an asymmetric part. It was observed that after the third iteration, the optimal solution provided an improvement of about 7% in terms of the uniform sheet thickness distribution (Figure 2.6).

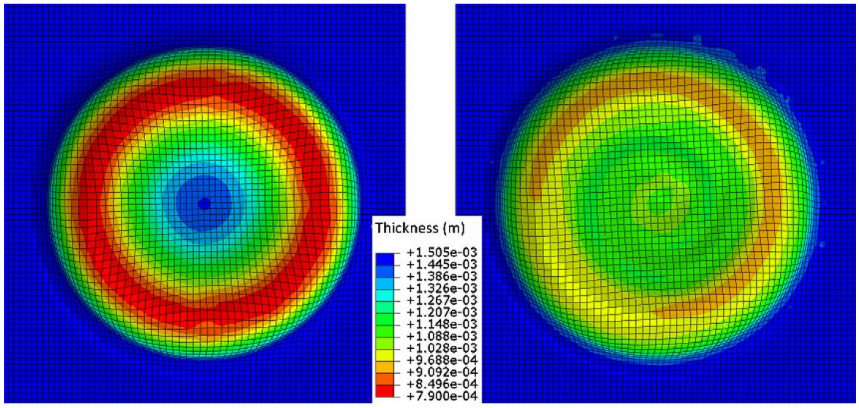


Figure 2.6 Comparison of the thickness distributions [60].

In order to overcome the problem related to inhomogeneous thickness distribution in aluminium AA1050-O part, an optimisation model was defined by Luigino *et al.* [13] to optimise tool path design by using a new trajectory according to the decremental slope differential of ±10°. Significant reduction in the localised thinning was observed when comparing the non-optimised tool path and the optimised one (Figure 2.7).

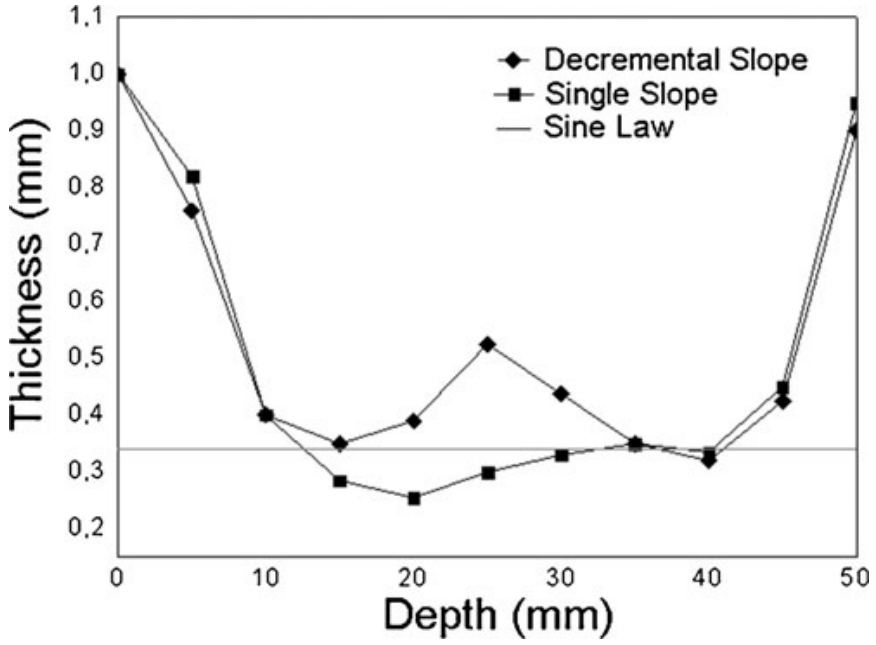


Figure 2.7 Sheet thickness distribution as a function of depth [13].

Experiments were carried out by Liu et al. [61] to investigate and understand the formability and forming process mechanism of aluminium AA7075-O sheets in SPIF process. No difference was noticed in formability when the same part was formed with helical and Z-level tool paths. In addition, the same resultant force was obtained with both tool paths, but the force curve was smoother with the helical tool path.

2.3 Deformation and failure mechanics in SPIF

In sheet metal forming, the failures occur due to a number of mechanisms including the following :(A) void nucleation and coalescence; (B) shear band formation and (C) necking instability [62]. So, to understand how failure develops in SPIF, deformation modes and states of strain and stress in the deformation zone should be known. In SPIF, there is more than one deformation mode, as shown in Figure 2.8, including the following: (A) plane strain stretching conditions in flat surfaces; (B) plane strain stretching conditions in rotational symmetric surfaces and (C) equal bi-axial stretching conditions at corners. Additionally, there are possibilities of other deformation modes between these modes [63].

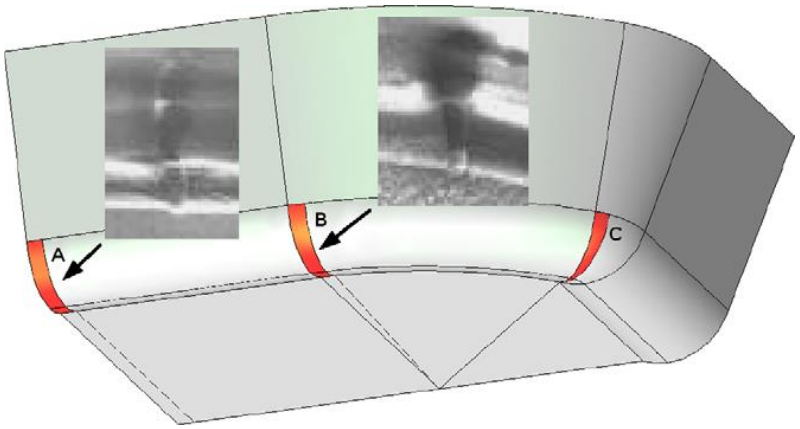


Figure 2.8 Instantaneous deformation zone and contact area between forming tool and workpiece during SPIF [63].

There are many ways to predict the onset of failure in sheet metal during forming processes, such as the FLD; forming limit stress diagram (FLSD); Müschenborn-Sonne forming limit diagram (MSFLD); and Marciniak-Kuczynski (M-K) forming limit diagram criteria [64]. However, the FLD is the most commonly used approach in predicting failure in the ISF. Using the deformation mode, many researchers have tried to investigate the difference between the failure mechanisms of traditional sheet metal forming and ISF so as to give a specific answer to the question, "Does necking occur before fracture in ISF?", or "Does fracture take place without necking?" Therefore, this section is focused on the most studied deformation and failure mechanisms and the effect of key variables on failure.

Stress triaxiality is used as a factor to consider the stress state's influence on failure modes, and strain represents one of the most important criteria to predict damage in SPIF. A theoretical model for the different modes of deformation commonly found in SPIF is built upon membrane analysis and ductile damage mechanics by Martins *et al.* [63]. Experimental observations show that fracture is not preceded by localized necking, and the crack develops under tensile meridional stresses acting under stretching conditions (Figure 2.9).

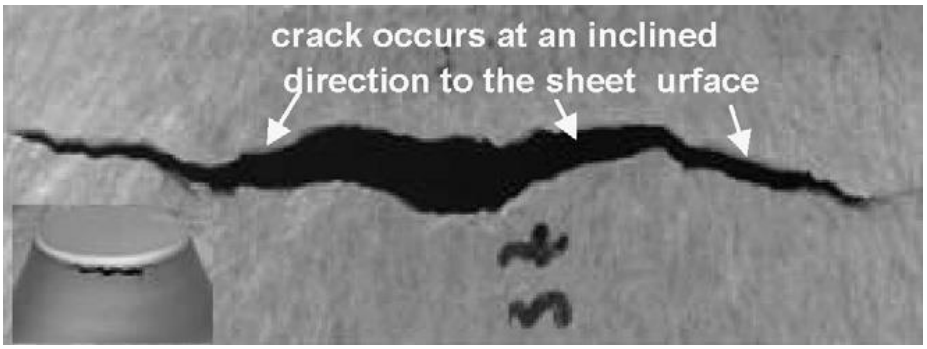


Figure 2.9 Experimental evidence that SPIF is limited by fracture without necking [63].

Another analytical model of SPIF was presented by Silva *et al.* [20] depicting membrane analysis and the experimental observation of the smear mark in the contact zone between the tool and sheet. This model proved that the cracks in SPIF were initiated by meridional tensile stresses but not by plane shearing stresses as shown in Figure 2.10.

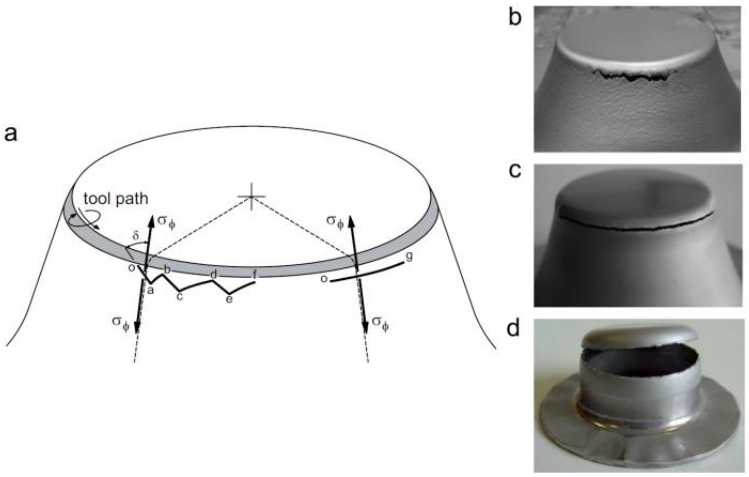


Figure 2.10 Crack propagation in SPIF: (a) schematic illustration of the typical crack propagation path in SPIF; (b) circumferential zigzag crack propagation path; (c) circumferential straight crack propagation path; and (d) circumferential straight crack propagation path in a rotational symmetric part obtained by conventional deep-drawing [20].

Specially prepared copper sheets were utilized by Jackson and Allwood [22] to experimentally examine the deformation mechanism of the ISF (SPIF and TPIF) and the accuracy of the sine law for prediction of wall thickness. The experimental results show that, firstly, the deformation in both SPIF and TPIF happens in two planes: the

first one perpendicular to the tool direction and the other parallel to the tool direction. Stretching and shear occurred in the first plane, and shear in the second plane. Secondly, the high percentage of stretching and shear in the first plane accounts for differences between the sine law and measured wall thickness in SPIF and TPIF. Finally, the mechanisms of SPIF and TPIF differed from a mechanism of pure shear. Experimental work using a surface 3D digital image correlation approach was carried out by Decultot *et al.* [31] to show that the fracture occurred in the uniaxial stretching domain. To predict the occurrence of failure in the an aluminium AA5052 sheet, Malhotra et al. [65] used explicit finite element analysis (FEA) with a damage-based fracture model, in which failure envelope depended on the hydrostatic pressure and the Lode angle. It was noted that the damage evolution was controlled by local bending around the tool and through-the-thickness shear. A fracture model combined with finite element analyses to predict the occurrence of fracture in SPIF was carried out by Malhotra *et al.* [21] for two shapes, a cone and a funnel. An aluminium AA5052 sheet was used in this study. It was found that both through-the-thickness shear and local bending of the sheet around the tool had an effect on fracture in the SPIF technology. By using a newly developed solid-shell element, a preliminary study of the stress state was carried out to evaluate a near-to-failure SPIF cone by Guzmán and Habraken [66], for aluminium AA3003-O sheet. The results showed that the Lode angle can be used with Voce or Swift hardening, and it is able to capture the stress state change during SPIF. Furthermore, an experimental and numerical study was undertaken by Xu et al. [67] to investigate the effect of through-the-thickness shear on the formability of aluminium AA5052-H32 sheet in SPIF. A fracture model was developed to simulate a 70° cone by SPIF and deep drawing. As a result, the fracture depth of the cone produced by SPIF was bigger than that of the same cone formed by deep drawing. Therefore, the through-the-thickness shear in deep drawing can be neglected as it is not significant as compared to that obtained in SPIF. In addition, the higher value of through-the-thickness shear in SPIF raises the value of the reference fracture strain, which results in lower damage accumulation. As a result, the through-the-thickness shear in SPIF is considered as a positive factor to material formability when it is within a certain range.

Fang et al. [68] proposed an analytical model from their study to investigate the deformation mechanism and fracture behaviour in the SPIF technology. Both the

bending effect and the strain hardening were considered based on the equilibrium approach. The result showed that the deformation takes place mainly in a meridional direction and small amounts of deformation occur in the circumferential direction. These deformations occur not just in the contact area but also on the inclined wall, and the fracture always occurs on the outer surface of the wall at the transition point between the contact and non-contact zones. Modified Mohr-Coulomb (MMC) damage model was implemented in Abaqus/Explicit via user subroutine (VUMAT) to predict the ductile fracture in SPIF. According to the Lode angle parameter and stress triaxiality, it was found the loading path of SPIF is non-linear as well, the MMC model with non-linear damage accumulation can predict the SPIF fracture location accurately while there was 10% error in fracture depth prediction [69]. FE simulation was employed to analyse the deformation of SPIF. The results showed that the SPIF part deform under three deformation modes e.g. stretching, shearing and bending [70]. An analytical model have been developed with the consideration of strain hardening and bending to study the deformation stability and fracture in ISF process of aluminium grads, AA1100 and AA5052. It was found the bending mechanism has a significant effect on the deformation stability as well as the fracture occurs based on the material's ductility and deformation stability [71].

It is clear from the above discussion that there is not a unified theory for failure in SPIF; due to the contradicting views on the effect of shear on fracture, some researchers confirm its important role in fracture while others oppose this view by others. Therefore, future work should focus on the fracture mechanism in ISF so that a unified model may be developed to accurately predict fracture in SPIF.

2.3.1 Application of a forming limit diagram

Depending on crack morphology and thickness measurements along the cross-section of the parts manufactured by SPIF, plastic deformation is revealed by uniform thinning until fracture, since there is no experimental evidence of necking taking place. Therefore, the forming limit curve at the necking (FLCN) for traditional sheet metal forming is not applicable to describe SPIF failure. Forming limit curve at fracture (FLCF) can be used to predict the fracture in ISF [38, 72]. Most of the FLCs in ISF at fracture take the shape of a straight line with a negative slope in the first quadrant of the FLD. Ductile fracture criteria used in bulk forming processes are utilized to describe the FLD at fracture. The main idea of ductile fracture criteria is that the

fracture happens when the maximum damage value of sheet metal exceeds a critical damage value (CDV)[73]:

$$\int_0^{\varepsilon_f} F(process\ parameters)d\varepsilon = CDV \tag{2.1}$$

where ε_f is the effective strain at fracture and F is a function of the process parameters. Allwood *et al.* [37] proved that the formability of ISF is higher than that for conventional sheet metal forming by comparing them using a paddle forming process with the same geometry. They noted that the forming limit of ISF is increased under uniform proportional load when through-thickness shear is presented. Based on ductile damage mechanics, Martins *et al.* [36] investigated the forming limit of aluminium AA1050-H111 sheet in SPIF. It was demonstrated that neck formation did not precede fracture. Therefore, the conventional FLC is not applicable when describing failure. Instead, a fracture FLD should be employed. Finite element method, combined with circle grid analysis, was used by Araújo et al. [74] in order to explain failure by cracking at the critical geometric features of facial implants and to assist in the overall design of a titanium grade 2 sheet. The fracture limit curves by cracking are characterised by means of a straight line with a slope equal to −0.8 and a maximum drawing angle of approximately 60°. In experimental testing, the maximum forming angle of titanium grade 2 has a rather low value, because the side walls that surround and support the region of the sheet where the implant is located tend to crack and fail at a rather low angle. Several tests were developed for aluminium AA1050-O sheets, aiming to achieve different straining conditions to determine FLDs for the ISF process. It has been shown that ISF may be characterised by a local stretching and FLC which is quite different from a conventional one.

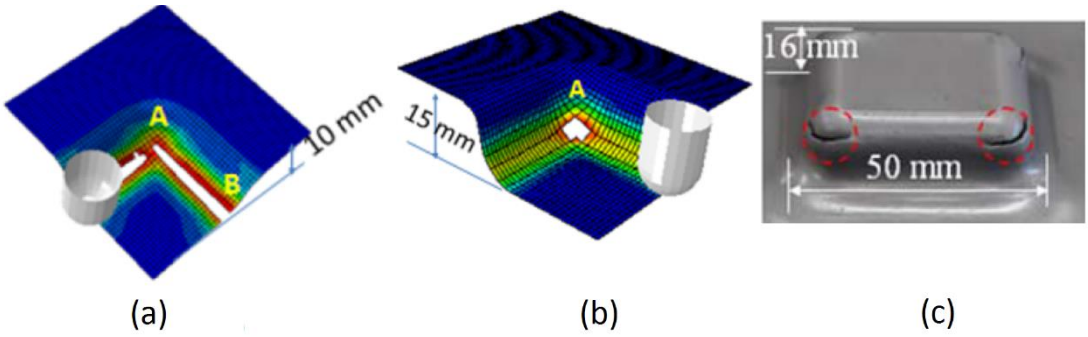


Figure 2.11 Comparison of FEM and experimental work: (a) FEM based on MMFC to establish FLD, (b) FEM with regard to tool dimension to establish FLD, and (c) experimental work [75].

FEM simulation was coupled with FLD criterion by Nguyen and Kim [75] to predict the failure in the ISF process using 1 mm cold rolled steel sheet. The FLCF constructed from the modified maximum force criterion (MMFC) was first utilised to predict ductile fracture in an ISF simulation test, then the FLCF was established with the consideration of tool dimension effect. Therefore, the wall angle of a square shape was changed to determine its effect on fracture height and obtain the FLCF. It is clearly seen from Figure 2.11 that the FLCF based on the MMFC is inaccurate, whereas there is a strong correlation when the FLCF is established according to tool diameter. In the case with a tool diameter = 12 mm, feed rate = 600mm/min and incremental depth = 1mm, the maximum wall angle of a complex shape is lower than 68.2°. Stretching, stretch-bending and SPIF tests were carried out by Centeno et al. [76] to experimentally analyse the formability of an aluminium AA2024-T3 sheet. A Nakajima test was used to determine the FLD, and the FLCF was put to the test by evaluating the failure strains of stretch-bending and the SPIF. According to Figure 2.12, it is clear that the fracture strains in stretch-bending tests with cylindrical punch are similar to those obtained with the Nakajima test (FLCF). On the other hand, the fracture strains in the SPIF are clearly above FLCF, which means that the bending effect controlled by the ratio of the initial sheet thickness to the tool radius might not be enough to explain the formability in SPIF.

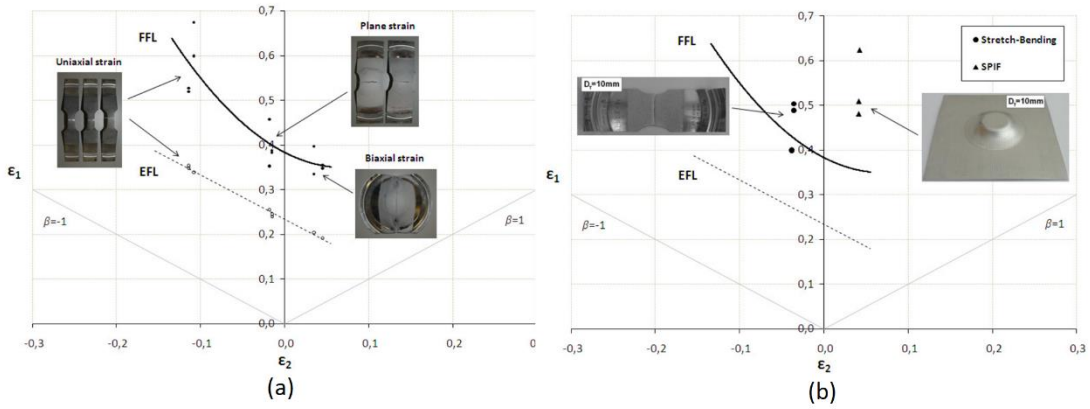


Figure 2.12 Forming limit diagrams: (a) Conventional FLD. (b) Fracture strains in SPIF and Stretch-bending for a tool diameter of 10mm [76].

Plasticity concepts and ductile fracture mechanisms were used by Isik *et al.* [23] to analyse the FLCF, and to obtain the shear fracture forming line (SFFL). Then, an experimental methodology was proposed by using SPIF, torsion and plane shear tests to determine the values of the in-plane strains at the onset of fracture. It has been found that there is a good agreement between FLCF established by means of tensile and conventional sheet formability tests and the FLCF constructed by SPIF test on conical and pyramidal truncated specimens (Figure 2.13). Also, a fair agreement between experimental and theoretical fundamentals was used to construct SFFL. The deformation mechanism and fracture behaviour of double point incremental forming has been investigated based on the membrane analysis and experimental work. It was found that by using different supporting force and tool shift the FLCF can be increased as compared with SPIF [77]. The FLCF was constructed under proportional loading (tensile test) and non-proportional loading (SPIF test). It was found the shape and value of FLCF in SPIF differ from the one of tensile test [69]. Stress-based forming limit diagram combined with maximum shear stress diagram criterion was introduced to predict the fracture in ISF process. This approach showed a good correlation between the prediction and experimental data [78].

There are two important considerations that need further clarification in FLCF of SPIF. It is necessary to prove, firstly whether the Nakajima test is able to capture the fracture occurrence in the SPIF or SPIF test and can it be used to establish FLCF, and secondly, whether the FLCF is a straight line in all types of materials or there are some materials which have the FLCF as a curve, as shown in Figure 2.12. Also, there is a knowledge

gap regarding the influence of through-thickness stress on the necking and fracture limit. Therefore, further investigations are needed.

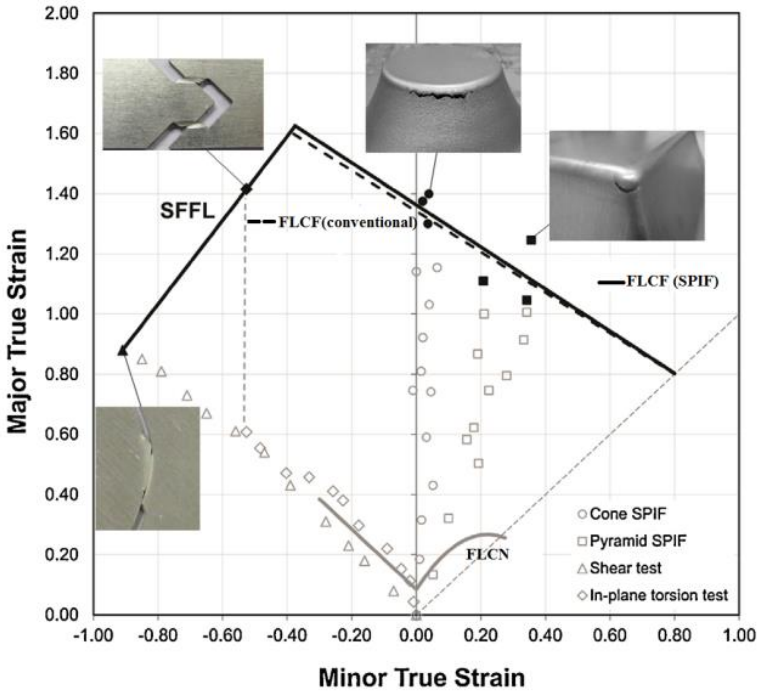


Figure 2.13 Determination of the fracture loci (FLCF and SFFL) from the experimental strains at fracture that were obtained from the SPIF and shear tests [23].

2.3.2 Effect of forming tool on deformation and failure

Depending on the tool diameter, failure can be predicted; e.g., in the case of large tool diameters, there is an increase in the amount of forming force because of the increase in contact area between the tool and sheet, and this area can fail due to the high stresses compared to another contact area with a small tool diameter. In addition, different types of tools and friction conditions between the tool and sheet play an important role in developing a failure. A tool containing a freely rotating ball was developed and applied by Shim and Park [2] to characterize the formability of fully annealed AA1050 sheets. The results showed that a near equi-biaxial stretching develops at a corner, while a near plane-strain stretching develops along the straight side, and the deformation of near equi-biaxial stretching is greater than near plane-strain stretching, so the cracks occur mostly at the corners. Numerical simulation was used to determine the condylar surface by Valentin et al. [79] in order to obtain the component of the titanium sheet (Ti-6Al-4V) by ISF. It was noted that the maximum value of strains and stresses equivalent or principal, and sheet thinning appeared across the tool trajectory

along the circumference with the bigger tool diameter (6 mm). One of the newest methods to produce a knee condylar surface by ISF was developed by Oleksik et al. [80]. CpTi sheet forming was examined using numerical simulation. It was identified that the maximum values of sheet thinning and principal strains appeared across the punch trajectory on the circumference with the biggest diameter. Furthermore, the sheet thickness was a parameter with the greatest effect among the studied parameters. Silva et al. [81] revisited failure in SPIF and presented a new understanding of the effect of process parameters, such as tool size, that helped researchers to propose a new unified view on formability limit and fracture in SPIF. Aluminium AA1050-H111 sheets were used in this study. The research work allowed determination of a critical threshold for the ratio of sheet thickness and tool radius of the tool (incremental tool ratio) that distinguishes between fracture with and without prior necking, as shown in Figure 2.14. Failure in SPIF was revisited by means of experimental analysis by Centeno *et al.* [24]. This investigation explained the effect of process parameters, such as forming tool radius on the formability of SPIF of stainless steel AISI304. Nakajima test was performed and compared with SPIF and stretch-bending test to measure the effect of bending in FLD strains. The results showed that in SPIF, the enhancement of formability above the FLCN increased as tool size decrease up to values around 150% with tool diameter of 6mm, while in the stretch-bending it remained around 30% for both tool diameters (10 and 20 mm). Also, it was noted that with small tool size, the fracture strains in stretch-bending were located near to FLCF produced from Nakajima test, but in SPIF the fracture strains were placed above it.

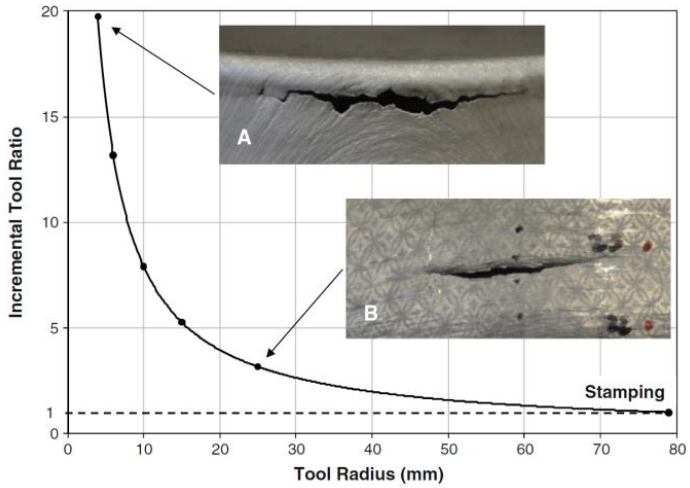


Figure 2.14 Incremental tool ratio (r_{part}/r_{tool}) as a function of tool radius for the SPIF of truncated conical shapes [81].

2.4 Springback and accuracy in SPIF

After forming operation, when the forming loads are removed, an undesirable shape change occurs due to "springback". Such a springback deformation leads to deviations from the desired shape. In traditional sheet metal forming, the contact area between the forming tools and sheet throughout the forming processes is large, and the springback is obtained when the tools are removed. Consequently, efforts were made to investigate the springback after removing the loads. On the other hand, in ISF the contact area between the tool and sheet is small and usually the deformed parts need to be cut to produce the final shape. Therefore, there are three types of springback in ISF: the first happens simultaneously with the displacement of the tool, which is called a continuous local springback. The second is a global springback that occurs when the loads are removed and put is dismounted from the clamps; and the last is a global springback which takes place after trimming (if done) [82]. In the SPIF process, there are many factors affecting springback values, e.g. tool path, sheet thickness, feed rate, spindle speed, tool size and step size. Some effects of these parameters are outlined below.

2.4.1 Effect of process parameters on springback and accuracy

2.4.1.1 Tool path

Accurate prediction of springback is essential for the design of tool path in ISF, so that it can be used to compensate for the springback value by the modification of the tool path. Elastic springback in an aluminium AA1050-O sheet was evaluated and compensated by Ambrogio et al. [83]. It was noted that some errors appeared along the oblique walls in the experiment generating a curvature on the straight sides. This phenomenon is due to the elastic springback, the effect of which is lower in comparison to the edges, where the geometrical stiffness is higher than in other areas, so a numerical/ experimental procedure was developed to limit the shape defects. An FE model based on shell element was proposed by Dejardin et al. [84] to analyse the springback effects in aluminium sheet. It was demonstrated through experiments and FEA that the springback, characterized by means of the cut rings method, can be accurately predicted by using the shell element associated with a suitable tool path. Han et al. [85] developed a coupled closed loop algorithm with a finite element method to simulate a 08Al sheet metal part. Using the wavelet transform combined with a fast

Fourier transform, the closed loop algorithm of the tool path was constructed. The results showed that the algorithm could predict an ideal profile of a processing track, and the error of springback was effectively eliminated. A finite element model was developed by Essa and Hartley [86] to modify the final stage of the tool path. The results showed that the extension of the tool path across the base of the sheet reduces the pillow effect at the sheet centre. Fu et al. [87] published another research study, based on the wavelet and fast Fourier transforms, to develop an algorithm for closed loop tool trajectory taking springback into account. However, the tool path were corrected based on the data of the springback shapes after unloading. It was found that the tool path correction algorithm with Fourier and wavelet transforms was reasonable. Lu et al. [88] presented a new feature-based tool path generation algorithm for ISF technology. Better geometric accuracy can be obtained by using this feature-based algorithm, especially for the cases of non-symmetrical parts without a supporting die. Future work should focus on new algorithms that take into account the effect of materials' properties and forming parameters in order that it can be used to compensate for springback after trimming.

2.4.1.2 Forming parameters

Recent researches indicate that there are five factors, namely sheet metal thickness, feed rate, spindle speed, tool size and incremental depth that affect springback. Oleksik *et al.* [80] employed a numerical simulation method for producing the knee condylar surface by using ISF to form Cp Ti sheet. The results showed that the global springback value increased with the increase of the tool size and decrease of the step size and sheet thickness. Springback and its effect on geometrical and dimensional accuracy of ISF technology were investigated by Vahdati et al. [89] and an analytical model was obtained to select the appropriate process parameters for reduced springback. It was found that increases of tool diameter, feed rate, spindle speed and sheet thickness with a reduction in vertical step size can lead to the reduction of springback, independently. Junchao *et al.* [43] utilized a DC56 sheet to establish a FEM for multistage ISF technology and experimental verification. It was found that, when the number of forming stages increases, the springback becomes larger, in contrast to a single pass process, due to the accumulation of springback during each forming stage. Furthermore, it was noticed that the magnitude of springback was not related to the incremental wall angle, while the number of forming stages was determined (Figure

2.15). Future work should study the effect of forming parameters on springback in descending order depending on its effect.

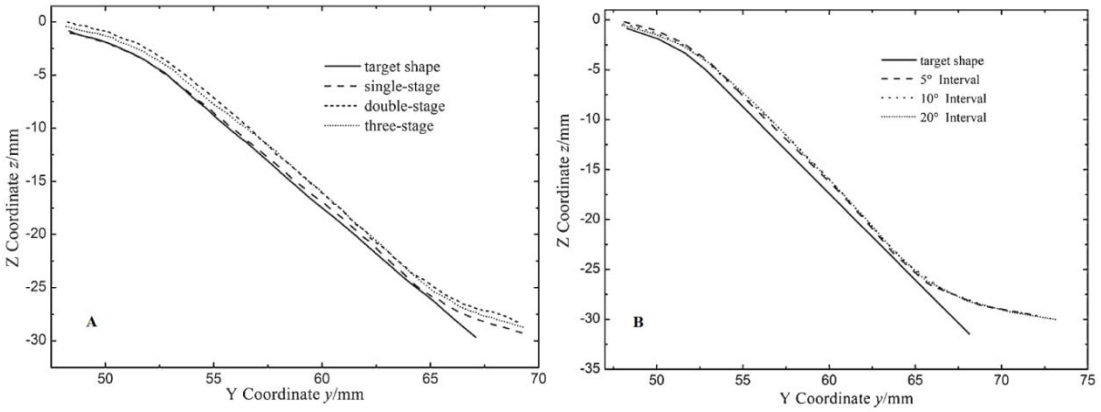


Figure 2.15 Sectional profiles for (a) different forming processes and (b) different angle intervals [43].

2.4.1.3 Tensile force

Three components of force are created during the ISF process, two in the horizontal plane (F_x and F_y) and another one in the vertical direction (F_z). These forces could be increased or decreased based on the ISF parameters; e.g. the forming force increases by increasing the step size. Thus, selecting suitable forming parameters helps reducing the amount of forming force to generate less degree of springback. A laser beam was used by Duflou *et al.* [45] to create a heat spot in the moving contact zone between the tool and sheet (A15182 and 65Cr2). The results showed that a moving heated system is able to reduce process force in SPIF. By achieving reduced stress levels and reduced springback, an improved accuracy in ISF can be realised. Pohlak et al. [90] investigated the effect of residual stresses on the geometry of the formed part. It was found that increasing stretching force helps to achieve a more accurate part, as shown in Figure 2.16. However, if stretching force is very high, it causes additional problems due to sheet necking. Annealing method was proposed by Zhang et al. [91] to anneal the SPIF part under the constraint of blankholder. This method can reduce the spring back that occurs when the deformed part is released from the clamping device. In this field, different types of heat treatment should be used to reduce the residual stresses and to obtain a part with a lesser degree of springback.

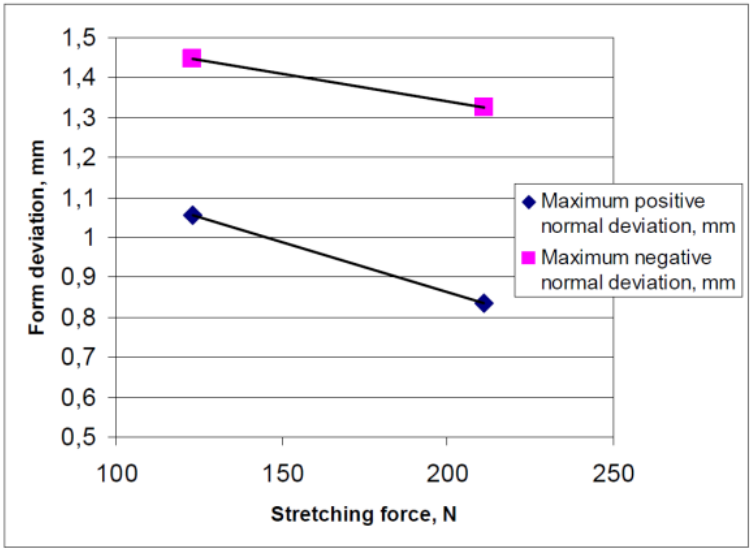


Figure 2.16 Form deviation and stretching force relationship [90].

2.5 Surface roughness in SPIF

Surface roughness or surface finish is a measure of the texture of a part's surface. It can be expressed by the vertical deviations of a real surface compared to the typical form. There are many different roughness parameters in use, but in ISF, average roughness (R_a) and the parameter of maximum roughness (R_z) are utilized more than the other parameters to determine the values of roughness. Many papers have been published in this field, and all of these papers aimed to achieve reduced surface roughness in ISF. Several parameters were considered to select suitable values in order to achieve a better surface finish, e.g. tool rotation, forming tool, tool path, step size and forming angle.

2.5.1 Effect of process parameters on surface roughness

2.5.1.1 Tool rotation and advancement

Tool rotation has a significant effect on surface quality; the roughness values depend on the direction of tool rotation and the speed of rotation. In addition, XY advancing (feed rate) affects the surface roughness. Tool rotation, advancement in XY and Z advancement (step size) were changed by Silva *et al.* [44] to produce pieces of varying size and complexity in the shortest time and of the highest quality. It was noted that the feed rate below 1200 mm/min and incremental depth of 0.2 mm produced rough surfaces as compared to that obtained at a much higher speed of 8400 mm/min, for SAE 1008 steel to achieve an acceptable roughness. The applicability of numerical

technique was examined by Yamashita *et al.* [58] for incremental forming of the steel sheet. It was discovered that the surface of the formed pyramid was smoother for a deeper product, due to the fact that the sheet was subjected to a stronger stretching force from a large stroke of the travelling tool in the vertical direction during the process.

Cerro et al. [92] summarized their work from experimental tests and FEM simulation to evaluate the surface roughness of Al 1050-0 sheet in both the tool advancing (feed rate) and in the perpendicular directions (step size). It was shown that the roughness values were always lower in the tool advancing direction than in the perpendicular one. In the first case, the surface roughness was 0.3 µm, and in the second case 0.6 µm. Nevertheless, surface roughness can fall by reducing the axial step size (Figure 2.17). A study was carried out by Durante et al. [93] in order to evaluate the effect of tool rotation, in terms of speed and direction, in ISF processing of aluminium AA7075-T0 sheets. It was pointed out that roughness values differed depending on whether the tool was rotating or not by using a rotating tool as compared with a non-rotating one. The surface roughness value is reduced by less than 10% (Figure 2.18).

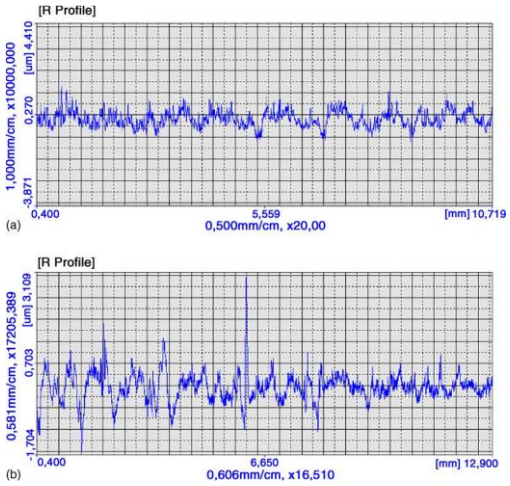


Figure 2.17 Typical roughness profiles measured in: (a) advancing tool direction (mean value around 0.3µm) and (b) perpendicular direction (mean value around 0.6 µm) [92].

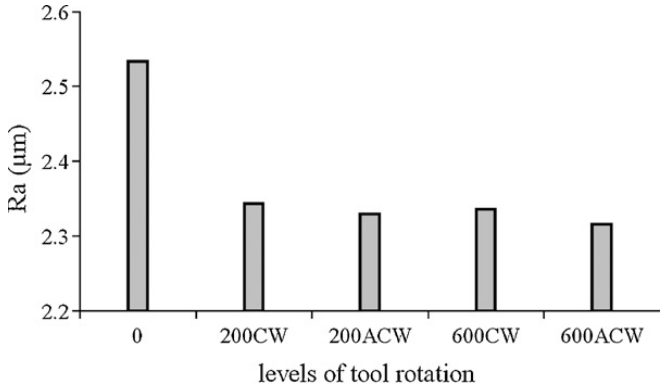


Figure 2.18 Roughness for different levels of tool rotation [93].

Hamilton and Jeswiet [94] investigated the effect of high feed rate and rotational speeds in SPIF processing of Al3003-H14 sheets. Three criteria were used to examine the formed sheet external non-contact surface roughness (orange peel effect), thickness distribution and sectional microstructure. A model for an equivalent combinatory roughness was created based on Ra and Rz roughness and forming parameters. It was shown that shape factor (a formation of forming angle/tool diameter and incremental depth) had a strong effect on an equivalent roughness as shown in Figure 2.19. However, grain structure and thickness distribution remained similar to lower speed forming.

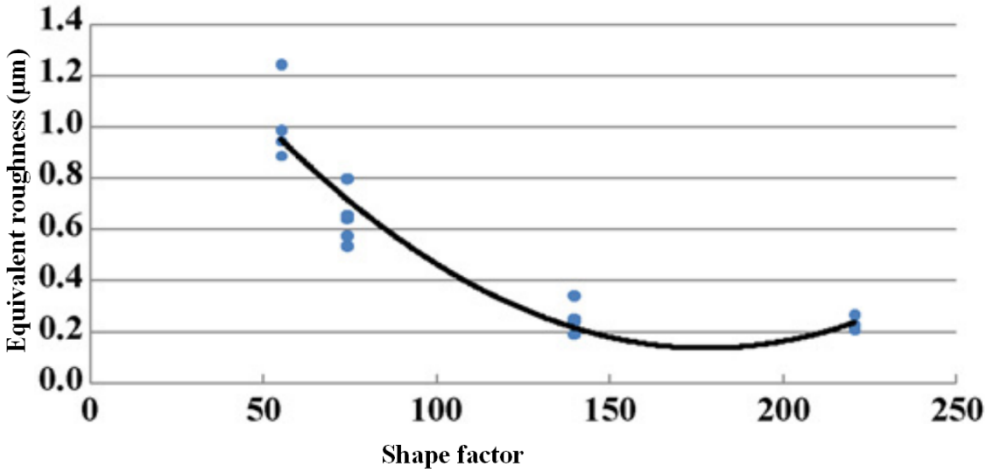


Figure 2.19 Sensitivity of roughness to the shape factor [94].

2.5.1.2 Tool size and material

Both forming tool material and tool size play an important role in the final surface roughness. Therefore, some researchers tried to select the most suitable material and tool diameter to get a better surface finish. Ham et al. [95] used two tools: one was

acetal tipped, and the other was a carbide tool to characterize the topography of surfaces created by forming aluminium sheet. It was found that the surface roughness and the degree of anisotropy of the surface depended on the forming tool material. The acetal tool did not appear to burnish the surface with which it had contact during forming and thus achieved a less rough surface than using a conventional forming tool. Also, the acetal tool produced a surface that was more cosmetically consistent with unformed sheet metal than the carbide tool. Experimental research was presented by Oleksik et al. [96] to study surface quality of the medical implants used for the partial resurfacing of the femoral condylar surface of the knee. The parts made of titanium (Ti-6Al-4V) were manufactured by SPIF. The roughness of the punch was reduced to improve the surface finish of the part. It was found that the roughness of the interior surface was Ra=0.34µm, which was comparable with the initial roughness of the titanium sheet (Ra=0.25µm). Furthermore, the quality of the final part was influenced mainly by the roughness of the tool and friction between the tool and sheet surface but not by the tool diameter. In addition, the external surface of the part (the surface which was not processed) was not affected during the forming process. An experimental study was carried out by Bhattacharya *et al.* [29] to study the effect of ISF process variables on the surface finish of Al5052. It was found that the surface roughness decreased with an increase in tool size for all incremental depths (Figure 2.20). Traditional rigid tool and oblique roller ball (ORB) tool were used by Lu *et al.* [57] to investigate the effect of friction on the surface finish. The results showed that better surface finish can be obtained with the ORB tool.

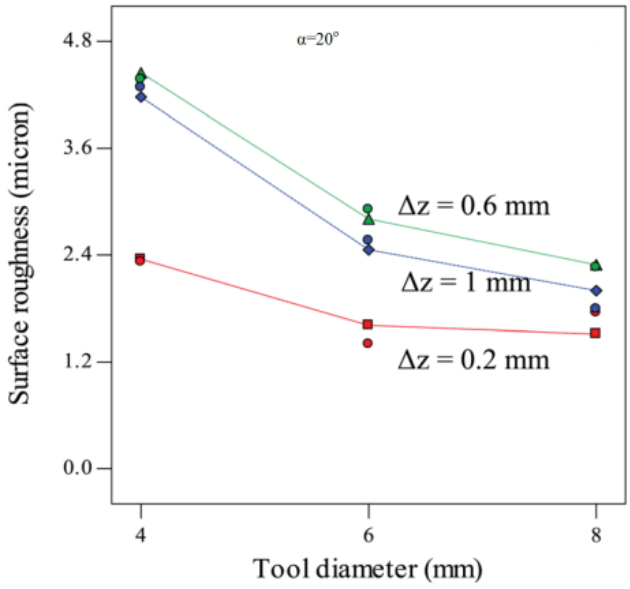


Figure 2.20 Variation of surface finish with tool diameter at different incremental depths [29].

2.5.1.3 Tool path

Depending on the strategy of the tool path, a high surface quality can be obtained. A new feature-based tool path generation algorithm for ISF technology was presented by Lu *et al.* [88]; in this algorithm, tool trajectory was created according to the specified critical edges. A better surface finish can be produced at the critical edges by using the feature-based algorithm as compared to the conventional ISF tool path method. This is true for certain non-horizontal edges on the parts. A dedicated program which uses the coordinates from the profile milling code and converts them into a helical tool path with continuous feed in all three directions was offered by Skjoedt et al. [97], who found that scarring was eliminated when using a helical tool path.

2.5.1.4 Step size

Incremental step size has a significant influence on the surface quality in the sense that greater incremental depth can lead to a low surface quality. A white light interferometry scan was used by Hagan and Jeswiet [98] to perform surface roughness tests of CNC ISF using various incremental depths. A relationship between incremental depth and peak-to-valley roughness was defined. It found that the maximum peak-to-valley height increases exponentially as the step size is increased; in depth increment tests, the average roughness values appear to follow the same trend as that of peak-to-valley. Attanasio *et al.* [15] used a coordinate measuring machine

(CMM), with precision of 3.8µm, to evaluate the surface quality of the door handle (FeP04 steel sheet). As shown in Figure 2.21, incremental depth and maximum scallop height have a great effect on surface waviness. Surface waviness drops when low step size values are utilized, even though good results are obtained on inclined walls as compared to flat or near-flat ones. Low values of scallop parameters (less than 0.1 mm) produce a more homogeneous surface finish in terms of part quality. To study the effect of ISF process variables on the surface finish of Al5052, an experimental study was carried out by Bhattacharya *et al.* [29]. The results showed that the surface quality decreases first with increases in step size depth up to a certain angle, and then increases.

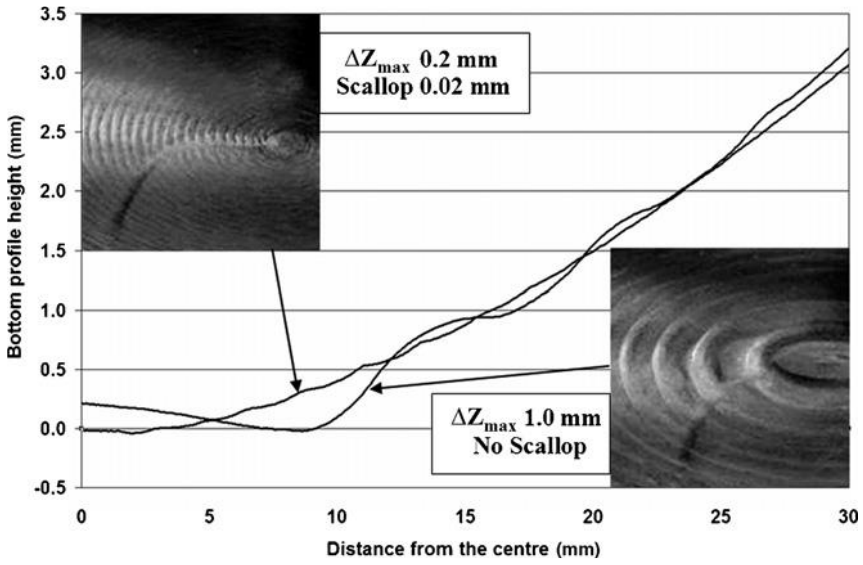


Figure 2.21 Bottom profiles measured on the best and the worst performing samples [15].

2.5.1.5 Forming angle

Forming angle is usually used as a measure for the formability and surface finish, because when the wall angle is changed, the roughness values change, due to the change of the stretching values in the part wall. So, when forming angle increases, the stretching increases and a good surface finish may be obtained. However, the high wall angle causes failure, so it should be selected carefully. By using different process variables, Bhattacharya *et al.* [29] conducted an experimental study to investigate the effect of ISF on surface quality of Al5052. They found that the surface quality increases with the increase in wall angle. Hot ISF was investigated by Ambrogio et al. [99]. In their study, three lightweight alloys, including aluminium AA2024-T3,

magnesium AZ31B-O and titaniumTi6Al4V, were formed by SPIF using continuous current in order to achieve local heating. The results showed that the surface quality deteriorated by increasing the forming angle. Titanium F67 grade 2 sheet for medical implant was formed by SPIF, and internal and external roughness was measured by Daleffe et al. [100]. The roughness of three sheets was measured with a changing angle of 45°, 47° and 48°. Roughness in the unformed sheet was 2µm. It was proven that, on the part of the sheet which came into contact with the tool, roughness was 5.19µm greater than that on the opposite side where it has 4.50µm, as shown in Table 2-1.

Table 2-1 Roughness results [100].

Measured faces	45° (µm)		47° (µm)		48° (µm)		Flat sheet Rm (µm)
	Face ext.	Face int.	Face ext.	Face int.	Face ext.	Face int.	
1	4.10	6.60	5.45	5.50	5.35	4.10	2.00
2	4.60	5.30	5.20	6.10	5.25	4.80	
3	3.30	5.15	4.20	3.90	4.60	5.30	
4	4.60	4.40	3.10	5.30	4.30	5.90	
Mean roughness (Rm) (µm)	4.15	5.36	4.48	5.20	4.87	5.02	

2.6 Summary

Many papers have been published in this field which share one aim, namely to understand the mechanisms of SPIF and to obtain a part of sufficient quality and accuracy without defects. By presenting an overview of the state of the art of the SPIF process, with a particular attention on the effects of ISF process parameters, conclusions and recommendation for future work can be made in the following areas.

2.6.1 Formability

- Full formability of hard-to-form materials can be used with hot ISF.
- More uniform thickness can be achieved with double or multi-pass forming.
- SPIF achieves higher strain compared to traditional sheet metal forming.
- Maximum principal strain and sheet thinning appear across the tool trajectory on the circle circumference with the large tool size.
- Forming angle increases when using a small tool size with a helical tool path.

- The influence of step size as a process parameter is still debatable; some researchers claim that the step size does not affect formability, while others believe that an increased step size has a negative effect on formability.
- Better formability is obtained when increasing the rotational speed and decreasing the feed rate of the tool.
- Tool diameter has little effect on the location of minimum thickness, but it seems that an increased tool diameter with a helical tool path has a positive effect on the even thickness distribution.
- More uniform thickness can be achieved with a helical tool path and parallel line type tool trajectory.

2.6.2 Deformation and failure mechanics

- It can be determined from the membrane analysis and experimental observations that fracture is not preceded by localized necking and that a crack develops in the meridional direction under tensile stresses acting under stretching conditions.
- Local bending and through-thickness shear have an effect on fracture in the SPIF.
- The probability of fracture increases with large tool sizes as compared to small ones.
- Fracture mostly occurs at the corner of the part due to the fact that near equi-biaxial stretching is greater than near plane-strain stretching.

2.6.3 Springback and accuracy

- Springback can be reduced by using an algorithm to compensate for the springback and modify the tool path.
- Increasing tool diameter, feed rate, spindle speed and sheet thickness and reducing vertical step size can lead to a reduction in springback.
- Springback can be decreased with an increase of the tensile force in the wall of the deformed part.

2.6.4 Surface roughness

- Both tool rotation and advancement have an effect on surface quality; the surface roughness is reduced by using a rotating tool as compared with the use

of a non-rotating one. On the other hand, roughness values are always lower in the tool advancing direction than in the perpendicular one.

- Surface roughness increases with the increased tool size.
- Parts without scarring can be obtained by using a helical tool path.
- Greater incremental depth can lead to low surface quality.

2.7 Recommendations for future work

In light of extensive research on ISF processes, there are a number of research questions still to be answered. Thus, future work is needed in the following areas:

- There are different opinions about the deformation modes in ISF based on both experimental work and finite element simulation. Some researchers think that deformation occurs due to stretching [20], whilst others believe it is largely due to a combined of through-thickness shear and stretching or through-thickness shear and local bending around the tool [21, 22]. Therefore, a new model of deformation could be developed to determine whether the deformation occurs due to shearing or through stretching.
- Many parameters have a big effect on the wall angle, e.g. tool diameter and tool path, and future work is needed to quantify the effects of the step size and feed rate.
- There is a knowledge gap regarding the influence of step size on the ISF, so future work should focus on its effect for different materials. Furthermore, establishing a relationship between the step size and material types is a possible focus.
- Future work on the effect of tool rotation may be made in the following areas. Firstly, the effect of tool rotation on ISF formability depending on sheet metal type should be studied; secondly, there should be a focus on finding a relationship between tool rotation and feed rate; finally, a table of suitable tool rotations and feed rates may be developed as a guide for some important materials used in ISF processes.
- There is a lack of a unified theory for the failure in SPIF. Thus, it is highly desirable that a new theoretical model can be constructed to predict fracture in SPIF, using a wide range of process variables, such as wall angle, step size, tool rotation and feed rate.

- A study on the effect of material anisotropy on the location of fracture in SPIF is recommended.
- There are two important questions which need to be clarified in the FLCF of SPIF. The first is whether the Nakajima test is able to capture the fracture occurrence in the SPIF, or if a SPIF test should be used to establish FLCF. The second is whether the FLCF is a straight line in all types of materials or there are some materials which have the FLCF curved, as shown in Figure 2.12.
- Further investigation should be carried out into the effect of initial sheet thickness to tool radius ratio (t_o/R) on the FLCF, and whether it is enough to describe FLCF in SPIF.
- Until today, there has been no work carried out to investigate the applicability of ISF to form discontinuous reinforced materials e.g. aluminium matrix composite. Thus, future work should focus on examining the applicability of ISF to form new materials.
- It is highly desirable to develop a new algorithm to predict springback with the consideration of the effect of materials' properties and forming parameters to compensate the springback after trimming.
- There is a considerable scope of looking into using different types of heat treatment to reduce the residual stresses and obtain a part with a lesser degree of springback.
- The surface finish and dimensional accuracy of an ISF part could be improved by using different algorithms to generate the tool path, several types of lubricant and new tool designs and materials.

CHAPTER 3

FINITE ELEMENT SIMULATION OF THE INCREMENTAL SHEET FORMING

3.1 Introduction

The prime objective of the finite element method is to obtain an approximated solution for complex engineering problems which are difficult to solve analytically. A widely used commercial FE package, Abaqus is built upon several algorithms with different computational costs. An in-depth understanding of these algorithms and practical considerations of using their functionalities is very important in order to develop a suitable model and to select appropriate methods for accurate and efficient FE solution of a particular problem.

In sheet metal forming processes, finite element analysis assists in the design of the product by predicting the material deformation and predicting forces, stresses, and strains that are required to execute the forming operation.

Single Point Incremental Forming (SPIF) is a challenging process to simulate due to the fact that a large number of elements are required and the forming tool travels along a relatively long path. Large deformations are produced by direct contact between the tool and workpiece which adds to the dual-nonlinearity of the problem. Abaqus offers two methods for solving non-linear problems: implicit and explicit. The implicit method obtains accurate results at high computational cost when compared with the explicit method.

The purpose of this chapter is to discuss a number of key issues that are relevant to the FE simulation of ISF; including the material constitutive model, strain hardening, failure criteria, non-linear solutions, and contact and boundary conditions. A number of case studies were chosen to evaluate the validity and effectiveness of using different algorithms and simulation parameters to simulate a particular SPIF process.

For the present work, an explicit solver is used with a mass-scale approach to speed up the computational time because the implicit solver usually leads to convergent problems and significant computational time.

3.2 Material constitutive model

The plasticity yield surface is an important criterion, due to the fact that it defines the critical stress levels at which plastic deformation occurs. Stress space is divided into two domains: elastic and plastic. In metal forming processes, both elastic and plastic stresses may be present. Abaqus supports more than one yield criterion, e.g. the Von-Mises and Hill yield criteria. The Mises yield criterion is used to define isotropic yielding, while the Hill yield criterion is utilized to define anisotropic yielding [64, 101]. Von-Mises criterion assumes that the properties of materials do not change with orientation and this can be expressed by means of the principal stress components as [102]:-

$$\sigma_y = \sqrt{\frac{1}{2}\left[(\sigma_1 - \sigma_2)^2 + (\sigma_1 - \sigma_3)^2 + (\sigma_2 - \sigma_3)^2\right]} \tag{3.1}$$

Whereas Hill yield criterion can be expressed as:-

$$\sigma_y = \sqrt{F(\sigma_2 - \sigma_3)^2 + G(\sigma_3 - \sigma_1)^2 + H(\sigma_1 - \sigma_2)^2 + 2L\sigma_{23}^2 + 2M\sigma_{31}^2 + 2N\sigma_{12}^2} \tag{3.2}$$

Where F, G, H, L, M and N material constants in the Hill yield function are calculated using anisotropy calculations and can be expressed in terms of six yield stress ratios: R_1, R_2, R_3, R_{12}, R_{13} and R_{23} according to the following equations [64, 103]

$$F = \frac{1}{2}\left(\frac{1}{R_2^2} + \frac{1}{R_3^2} - \frac{1}{R_1^2}\right), G = \frac{1}{2}\left(\frac{1}{R_1^2} + \frac{1}{R_3^2} - \frac{1}{R_2^2}\right),$$
$$H = \frac{1}{2}\left(\frac{1}{R_1^2} + \frac{1}{R_2^2} - \frac{1}{R_3^2}\right), \tag{3.3}$$
$$L = \frac{3}{2R_{23}^2}, M = \frac{3}{2R_{13}^2}, N = \frac{3}{2R_{12}^2}$$

$$R_1 = R_{13} = R_{23} = 1, \quad R_2 = \sqrt{\frac{r_{90}(r_0 + 1)}{r_0(r_{90} + 1)}}, \quad R_3 = \sqrt{\frac{r_{90}(r_0 + 1)}{r_{90} + r_0}},$$
$$R_{12} = \sqrt{\frac{3r_{90}(r_0 + 1)}{(2r_{45} + 1)(r_{90} + r_0)}} \tag{3.4}$$

where r_o, r_{45},and r_{90} are the anisotropy factors in direction of 0, 45, 90 degree.

3.3 Strain hardening of materials

When the material is subjected to plastic deformation under external loading, the stress required to obtain further deformation after the yield point increases. This phenomenon is called strain hardening, also referred to as work hardening. More than one rule was proposed to describe the strain hardening in material e.g. isotopic hardening, kinematic hardening and combined isotropic and kinematic hardening. The yield surface changes uniformly in all directions in isotropic hardening, which means the yield stress increases in all stress directions as plastic straining occurs. Isotropic hardening is useful for cases involving large plastic straining or where the straining at each point is essentially in the same direction in the strain space throughout the analysis. Figure 3.1 shows the isotropic hardening of a uniaxial stress-strain curve with non-linear hardening. With isotopic hardening, the accumulated equivalent plastic strain using Von Mises model takes the form [104, 105]:

$$\bar{\varepsilon}^p = \int_0^t \sqrt{\frac{2}{3}\dot{\varepsilon}^p : \dot{\varepsilon}^p}\, dt \tag{3.5}$$

The isotropic strain hardening in the Von Mises model is defined as a function of accumulated plastic strain:

$$\sigma_y = \sigma_y(\bar{\varepsilon}^p) \tag{3.6}$$

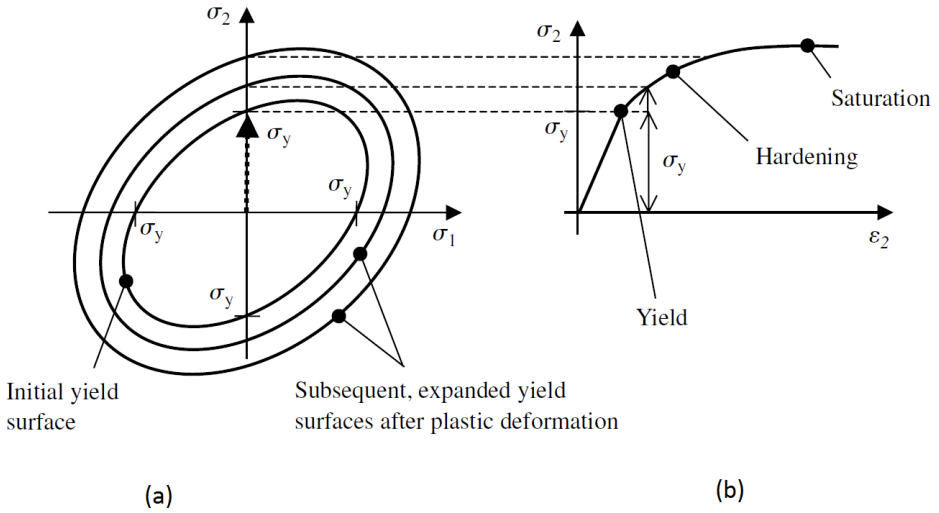


Figure 3.1 Isotropic hardening: (a) yield surface and (b) the corresponding uniaxial stress–strain curve [104].

If the loading of the material monotonically increases, it can be assumed that any hardening which occurs during the deformation is isotropic [104]. However, if the material is subjected to plastic tension followed by compression the material yield stress in the reverse loading is less than the initial yield stress. This phenomenon is called the Bauschinger effect [106]. The kinematic hardening rule is used in order to simulate the Bauschinger effect in the materials. With kinematic hardening, the yield surface preserves its orientation and shape but merely translates in the stress space, as shown in Figure 3.2. It is clear from the figure that, if the material is loaded to point 1 (yield point), then the load is reversed until point 2 (yield point of reverse loading), the elastic region of the reverse loading is smaller than that for initial loading due to kinematic hardening. The yield function describing the Von Mises yield surface depends on the location of the surface in the stress space. The initial yield surface (Figure 3.2) is translated by |x| under applied loading. The stress in the kinematic hardening is determined relative to the new surface [104]. The kinematic hardening yield function is written in terms of tensor stresses as follows:

$$\sigma_y = \sqrt{\frac{3}{2}\,(s_{ij} - x_{ij})(s_{ij} - x_{ij})} \tag{3.7}$$

where x_{ij} is the hardening parameter and is often known as the back-stress and s_{ij} is a deviatoric stress tensor.

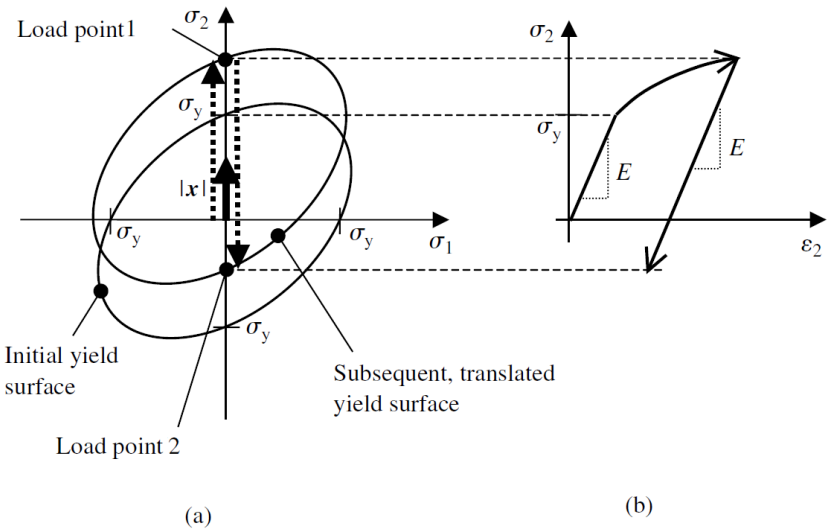


Figure 3.2 Reversed loading with kinematic hardening: (a) the translation of the yield surface and (b) the resulting stress–strain curve which shows the Bauschinger effect [104].

In the case of cyclic placidity, the materials show both kinematic and isotropic hardening. In the individual cycle, the Bauschinger effect (kinematic hardening) is represented, but after a large number of cycles, isotropic hardening is observed so that the peak of stresses (tension or compression) increases from one cycle to another. Therefore, in such cases, the combined kinematic and isotropic hardening rule should be used to predict the real behaviour of material hardening [104]. Figure 3.3 illustrates combined kinematic and isotropic hardening with the strain imposed resulting in cyclic plasticity.

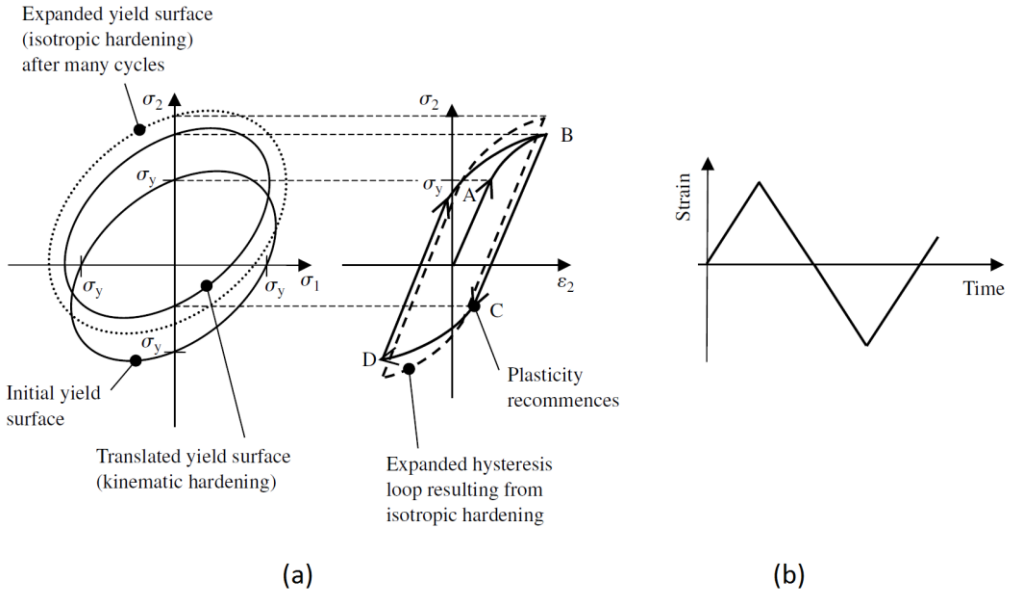


Figure 3.3 Combined kinematic and isotropic hardening: (a) yield surface with resulting stress–strain curve and (b) strain imposed resulting in cyclic plasticity [104].

Work hardening can be specified in Abaqus/Explicit as isotropic hardening, including Johnson-Cook (J-C) hardening, kinematic hardening and combined kinematic and isotropic hardening. In this work, isotropic hardening is used to simulate the hardening behaviour in pure titanium sheet during ISF. When isotropic hardening is defined, yield stress and plastic strain can be given in a table; the yield stress is interpolated from this table of data and remains constant for plastic strains exceeding the last value given in the tabular data. Johnson-Cook's hardening law is suited to modelling the high-rate deformation of many materials, including most metals, and is considered a particular type of isotropic hardening when the yield stress is given as an analytical function of equivalent plastic strain, strain rate, and temperature [64].

3.4 Failure criteria

A typical part made by sheet metal forming may undergo damage due to a number of mechanisms including ductile fracture due to void nucleation; growth and coalescence; shear fracture due to shear band localisation, and necking instability. Abaqus offers a number of damage models such as the ductile damage model (Hooputra's ductile damage) [107], the Johnson-Cook damage model [108] and the shear damage model (Hooputra's shear damage) [107] to predict the onset of damage in ductile materials. The Hooputra damage models (ductile and shear damage model) predicts damage based on microscopic strains and stresses. Hooputra's ductile damage assumes the fracture equivalent plastic strain ($\overline{\varepsilon}_{df}$) is a function of stress triaxiality and strain rate (Eq. (3.8)) while Hooputra's shear damage is based on the assumption that the fracture strain ($\overline{\varepsilon}_{sf}$) is a function of the shear stress ratio and strain rate (Eq. (3.9)).

$$\overline{\varepsilon}_{df}\left(\eta, \dot{\overline{\varepsilon}}\right) = \frac{\varepsilon_d^+ \, sinh[c(\eta^- - \eta)] + \varepsilon_d^- \, sinh[c(\eta - \eta^+)]}{sinh[c(\eta^- - \eta^+)]} \tag{3.8}$$

where ε_d^+ and ε_d^- correspond to the fracture equivalent plastic strain for equi-biaxial tensile and equi-biaxial compressive deformation, respectively. η^+ and η^- are the stress triaxiality in equi-biaxial tensile deformation state (2/3), and in equi-biaxial compressive deformation state (-2/3), respectively. c is the orientation dependent parameter.

$$\overline{\varepsilon}_{sf}\left(\theta_S, \dot{\overline{\varepsilon}}\right) = \frac{\varepsilon_S^+ sinh[f(\theta_S - \theta_S^-)] + \varepsilon_S^- \, sinh[f(\theta_S^+ - \theta_S)]}{sinh[f(\theta_S^+ - \theta_S^-)]} \tag{3.9}$$

$$\theta_s = \frac{1 - k_s \eta}{\emptyset} \tag{3.10}$$

$$\emptyset = \frac{\tau_{max.}}{\sigma_{eq}} \tag{3.11}$$

where ε_S^+ and ε_S^- correspond to the shear fracture equivalent plastic strain for equi-biaxial tensile and equi-biaxial compressive deformation, respectively. The shear stress ratio parameters θ_S^+ and θ_S^- correspond to the values of θ_S at $\eta = \eta^+$ = and $\eta = \eta^-$, respectively. f is the orientation dependent parameter, k_s is a material parameter and $\tau_{max.}$ is maximum shear stress.

The ductile fracture criterion combined with shear band (Hooputra model) is considered uneconomical model due to a large numbers of experiments e.g. tensile test, three-point bending, Erichsen's cupping test and shear test are required to

determine the fracture parameters under different deformation states (plane strain, equi-biaxial strain etc.) . Furthermore, this model can only predict the fracture initiation and does not give any information about the direction or rate of fracture propagation [107].

The Johnson-Cook damage model can be used to predict the onset of fracture only in cases of high strain rate deformation and temperature. The J-C model is considered a special case of ductile damage criterion in which the value of fracture equivalent plastic strain ($\bar{\varepsilon}_f$) is related to the stress triaxiality (η) and it is defined as the following:

$$\bar{\varepsilon}_f = [d_1 + d_2 e^{-d_3 \eta}] \left[1 + d_4 \ln\left(\frac{\dot{\bar{\varepsilon}}}{\dot{\varepsilon}_0}\right)\right](1 + d_5 T) \tag{3.12}$$

where d_1-d_5 are J-C damage parameters measured at room temperature and $\dot{\varepsilon}_0$ is the reference strain rate. T is the nondimensional temperature. The constant J-C damage parameters (d_1-d_5) are determined with high stress triaxiality [109]. Therefore, the J-C model cannot predict the fracture at zero stress or even negative stress triaxiality (shear state) [109].

In the ductile fracture criterion combined with shear band (Hooputra model) and J-C damage model, the fracture is started when the following condition is satisfied:

$$\sum \frac{d\bar{\varepsilon}}{\bar{\varepsilon}_f} = 1 \tag{3.13}$$

where, $d\bar{\varepsilon}$ is the increment in equivalent plastic strain, which is updated at every analysis increment and $\bar{\varepsilon}_f$ is the fracture strain under current conditions.

Depending on the sheet thickness, Abaqus is able to predict damage initiation (necking). Abaqus supports four criteria for predicting the onset of local necking instability in sheet metal forming: the forming limit diagram (FLD), forming limit stress diagram (FLSD); Müschenborn-Sonne forming limit diagram (MSFLD); and Marciniak-Kuczynski (M-K) criteria.

In this thesis, the FLD is used to evaluate the formability and fracture in SPIF. The FLD plots forming limit strains in the space of principal strains, as shown in Figure 3.4.

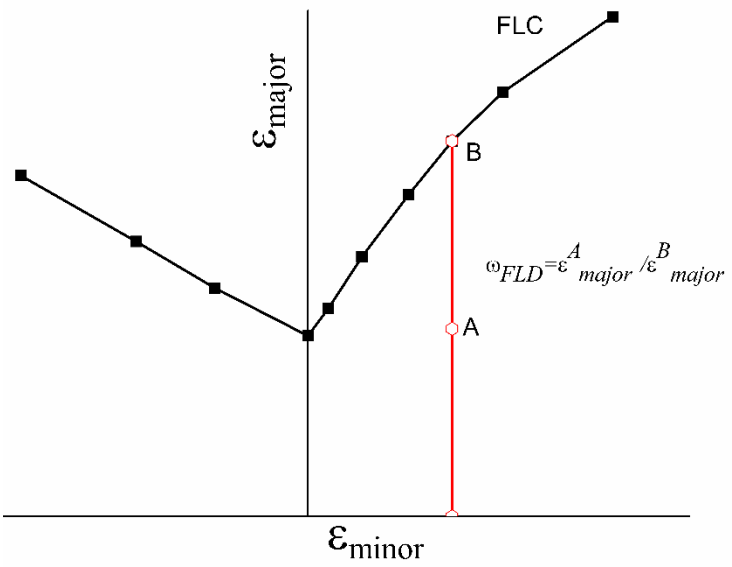


Figure 3.4 Forming limit diagram [64]

In Abaqus, when FLD damage initiation is used to predict the failure, FLC should be defined in a tabular form by giving the major principal strain at damage initiation as a tabular function of minor principle strain. The damage initiation criterion for the FLD is given by the condition $\omega_{FLD} = 1$, where the variable ω_{FLD} is a function of the current deformation state and is defined as the ratio of the current major principal strain, $\varepsilon_{major,}$ to the major limit strain on the FLC, which is evaluated at the current values of the minor principal strain, ε_{minor}, temperature, tem. , and predefined field variables, *f*:

$$\omega_{FLD} = \frac{\varepsilon_{major}}{\varepsilon^{FLD}_{major}(\varepsilon_{minor,tem,f})} \tag{3.14}$$

For example, for the deformation state given by point A in Figure 3.4, the damage initiation criterion is evaluated as

$$\omega_{FLD} = \varepsilon^{A}_{major} \Big/ \varepsilon^{B}_{major} \tag{3.15}$$

If the value of the minor strain lies outside the range of the specified tabular values, Abaqus will extrapolate the value of the major limit strain on the FLC by assuming that the slope at the endpoint of the curve remains constant [64].

From the above discussion, both the Hooputra and J-C models have some limitations. Therefore, in this thesis, a modified Gurson–Tvergaard-Needleman (GTN) damage model [110] will be developed in consideration of shear and stress triaxiality to predict ductile fracture in the ISF process due to void nucleation and coalescence. The

modified GTN damage constitutive model with shear and stress triaxiality will be implemented in Abaqus/Explicit via a VUMAT user subroutine. Furthermore, the FLD (forming limit curve at necking (FLCN) and fracture (FLCF)) will be constructed based on the modified GTN damage model and the FLCF will be used to predict the onset of fracture in the ISF process.

3.5 Non-linear solution method

FEM simulation of the SPIF process is very complicated due to the complex model and long movement of the forming tool. Several algorithms for dynamic analysis are offered by Abaqus, i.e., the dynamic/implicit and dynamic/explicit methods. The equation of motion in the implicit algorithm is based on direct-integration, so that the integration operator matrix must be inverted and a set of nonlinear equilibrium equations must be solved at each increment. However, the dynamic/explicit method uses the central-difference operator, and the global mass and stiffness matrices need not be formed and inverted due to the fact that displacements and velocities are calculated in terms of quantities that are known at the beginning of the increment. This means each dynamic/explicit increment is relatively inexpensive as compared to the increments in the implicit integration scheme [64].

The algorithm for the implicit dynamic procedure is defined by Hilber et al. [111, 112] thus:

$$M\ddot{u}^{(i+1)} + (1+\alpha)ku^{(i+1)} - \alpha ku^{(i)} = F^{(i+1)} \tag{3.16}$$

where M is the mass matrix, k the stiffness matrix, F the vector of applied loads and u the displacement vector:

$$u^{(i+1)} = u^{i} + \Delta t\dot{u}^{(i)} + \Delta t^{2}((^{1}/_{2} - \beta)\ddot{u}^{(i)} + \beta\ddot{u}^{(i+1)}) \tag{3.17}$$

and $$\dot{u}^{(i+1)} = \dot{u}^{(i)} + \Delta t((1-\gamma)\ddot{u}^{(i)} + \gamma\ddot{u}^{(i+1)}) \tag{3.18}$$

with $$\beta = \frac{1}{4}(1-\alpha^{2}), \quad \gamma = \frac{1}{2} - \alpha, \quad \frac{1}{3} \leq \alpha \leq 0 \tag{3.19}$$

By default in Abaqus, $\alpha = -0.05$ is chosen as a small damping term to quickly remove the high frequency noise.

The explicit central-difference operator satisfies the dynamic equilibrium equations at the beginning of the increment, t; the accelerations calculated at time t are used to

advance the velocity solution to time $t + \Delta t/2$ and the displacement solution to time $t + \Delta t/2$. Based on the explicit central-difference integration rule, the equations of motion for the body are [64]:

$$\dot{u}^N_{(i+\frac{1}{2})} = \dot{u}^N_{(i-\frac{1}{2})} + \frac{\Delta t_{(i+1)} + \Delta t_i}{2} + \ddot{u}^N_{(i)}, \qquad \mathrm{u}^{\mathrm{N}}_{(i+1)} = u^N_i + \Delta t_{(i+1)} \dot{u}^N_{(i+\frac{1}{2})} \quad (3.20)$$

where u^N is a degree of freedom (a displacement or rotation component) and the subscript i refers to the increment number in an explicit dynamics step. The central-difference integration operator is explicit in the sense that the kinematic state is advanced using the known values of $\dot{u}^N_{(i-1/2)}$ and $\ddot{u}^N_{(i)}$ from the previous increment [64].

The time increment should be extremely small, so thousands of increments are required to obtain accurate results from the explicit method. The size of the increment is determined by the stability of time [64]:

$$\Delta t \approx \frac{L_{min.}}{C_d} \quad (3.21)$$

where L_{min} is the smallest element dimension in the mesh, and C_d is the dilatational wave speed of material.

$$C_d = \sqrt{\frac{\lambda + 2\overline{\mu}}{\rho}} \quad (3.22)$$

where ρ is the density of the material and λ and $\overline{\mu}$ are Lamé's elastic constants; in an isotropic, elastic material, the effective Lamé's constants can be defined in terms of Young's modulus, E, and Poisson's ratio, ν, by

$$\lambda = \frac{E\nu}{(1+\nu)(1-2\nu)} \quad (3.23)$$

$$\overline{\mu} = \frac{E}{2(1+\nu)} \quad (3.24)$$

In this work, the dynamic/Explicit algorithm is used due to the fact that the computational cost of the CPU is proportional to the FE model size and does not alter as significantly as in the dynamic/implicit method.

3.6 Mass scaling

SPIF is considered a quasi-static process because it is done with low tool velocity. To complete a quasi-static SPIF process in real time, a huge amount of computation time is necessary due to the small time steps in the dynamic/explicit solver. In Abaqus, time scaling and mass scaling are used to convert the real problem to a virtual problem with a different time scale. Thus, the main role for the scaling factor is to speed up the finite element solution. If a large scaling factor is utilized, this may cause incorrect results, especially for stress, due to the increase in the dynamic effect [64, 113]. Unfortunately, no threshold is given for the scale factor. Since the energy ratio changes with time and can differ in various subdomains, the total kinetic to total internal energy can only give limited information to choose the scaling factor. A typical rule for testing the scaling factor is that the total kinetic energy should be less than 4%-10% of the total internal energy [62, 64, 114].

3.7 Contact and boundary conditions

Surface to surface contact conditions between the forming tool and upper surface of the sheet, between the blankholder and the upper surface of the sheet and between the lower surface of the sheet and inner surface of the backing plate, are used to analyse the tool and workpiece contact in the SPIF. The friction behaviour is modelled using Coulomb's friction law, with friction coefficient μ_1 between the blank and the forming tool and μ_2 between the blank and backing plate and between the blank and blankholder.

Since the force and displacement are the same at all points in the rigid body (forming tool, blankholder and backing plate), a reference point is chosen to which the boundary conditions can be applied; hence, in this work, the backing plate is fixed in all axes, the rigid forming tool is fixed in all rotational degrees of freedom, and the blankholder is fixed in all axes - except the vertical axis - in order to apply the holding force; here, a 50 KN holding force was applied to the reference point of the blankholder. In a numerical simulation, there is more than one way to define the tool path, e.g. position vs time, velocity vs time, or acceleration vs time. In this work, position vs time is considered in Abaqus/Explicit to define the tool path in SPIF.

3.7.1 Contact algorithms

Contact is considered a difficult aspect in non-linear FE problems, especially with the metal forming problems, due to three main aspects of contact modelling: the changing area of the surfaces that are in contact; the fact that contact force due to penetration is calculated according to the normal direction of the surface; and the calculation of the tangential force caused by friction [115]. Two algorithms for modelling contact and interaction problems are provided by Abaqus/Explicit: the general contact algorithm and contact pair algorithm. The general contact algorithm involves very simple definitions of contact with very few restrictions on the types of surface. The contact pair algorithm has more restrictions on the types of surface involved and also requires more careful definitions of contact [64].

The master and slave surfaces should be defined when the contact is analysed. The master surface is that with a rigid body (hard material) e.g. the forming tool, blankholder and backing plate in SPIF, whereas the slave surface is a deformable surface (e.g. the blank). Abaqus supports two kinds of contact weighting method: pure master-slave surface weighting and balanced master-slave surface weighting. In the first method, only the penetrations of slave nodes into the master surface will be resisted and there is no restriction for the master surface to penetrate into the slave surface. On the other hand, the second method applies the pure master-slave weighting twice, reversing the surfaces on the second pass, which minimises the penetrations of the contact bodies.

To enforce contact constraints Abaqus/Explicit utilizes two different methods [64]:

1. The kinematic contact algorithm uses a kinematic predictor/corrector contact algorithm to strictly enforce contact constraints (for example, no penetrations are allowed).
2. The penalty contact algorithm has a weaker enforcement of contact constraints but allows for the treatment of more general types of contact.

3.7.2 Friction model

Coulomb's friction law is a common friction model utilized in Abaqus to describe the interaction between two contacting surfaces. The tangential motion starts when the frictional shear stress reaches a critical value (τ_c), which is defined by

$$\tau_c = \mu P \tag{3.25}$$

Where μ is the coefficient of friction and P is the normal contact pressure. There is no relative motion between the contact surfaces (sticking) if the shear stress is below τ_c, while relative motion (slipping) takes place when the frictional shear stress reaches its critical value [64, 115].

3.7.3 Tool paths in ISF

A CNC milling machine is often used to perform the SPIF process, so in order to form the part with the CNC machine, a CAD model should be created by using a CAD/CAM system and these CAD models are utilized for devising the tool path. The CAD package CREO parametric 3.0 is used to create the CAD model and tool path for SPIF in this work. The CREO generates the tool path as a G-code program, which has many variants, e.g. G01 (linear interpolation), G02 (clockwise circular interpolation) and G03 (counter-clockwise circular interpolation), and these variants are followed by the coordinates of the tool centre point.

CREO is usually used for the metal cutting process by a CNC machine but it is also suitable for the SPIF process. Figure 3.5 shows a CAD model and tool path for a truncated cone created by CREO parametric 3.0. Surface milling is chosen to generate a tool path in the SPIF process, which is defined by the inner surface of the truncated cone, with the upper and lower edges as two closed-loop cutting lines.

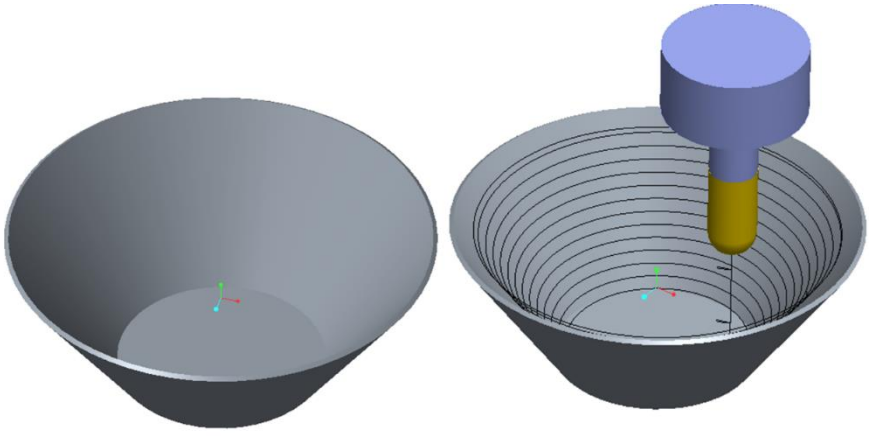


Figure 3.5 Steps for creating a tool path by using a CREO parametric 3.0

In SPIF, there are two approaches for generating the tool path: profile and helical, as shown in Figure 3.6. The profile path is characterised by a continuous feed rate in the

X-Y direction of the deformed blank. The feed rate in the Z-direction is in the same angular position in the XY-plane along a line down the side of the sheet. Poor surface finish is obtained with a profile path; moreover, a peak occurs in the vertical forming force as the tool steps down [62]. However, to eliminate these problems, a helical path is selected instead of a profile path. The helical path gives a continuous feed rate in all three directions.

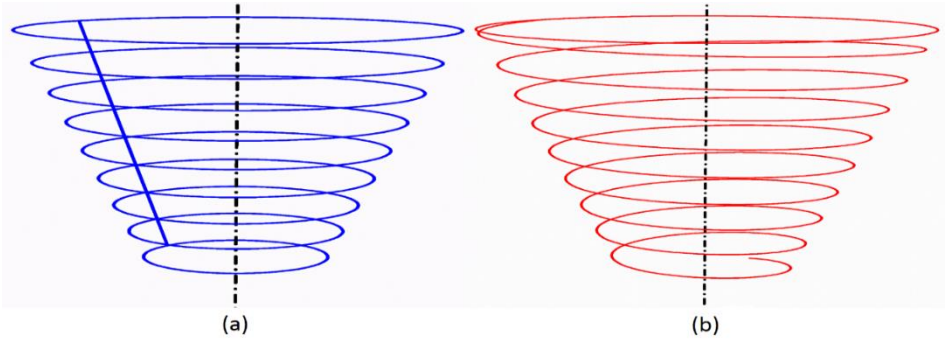


Figure 3.6 SPIF tool path: (a) profile tool-path and (b) helical tool-path

The implementation of an ISF tool path in Abaqus is very complex as compared to other sheet metal forming processes, e.g. the deep drawing process, in which the tool moves in one direction. In contrast, in ISF, the tool moves in three dimensions simultaneously to deform the sheet. The G-code program cannot be given directly to Abaqus as it includes the coordinates of (x, y and z) with many variants, while in Abaqus, the tool path should be defined as position vs time. Therefore, a MATLAB script was developed to convert the G-code to x-y-z data; then, the distance between each of the two points P1 (x_i, y_i, z_i) and P2 (x_{i+1}, y_{i+1}, z_{i+1}) is determined using equation (3.26).

$$D = \sqrt{(x_{i+1} - x_i)^2 + (y_{i+1} - y_i)^2 + (z_{i+1} - z_i)^2} \tag{3.26}$$

The required time to move the tool from one point to another is determined by dividing the distance (D) by the average feed rate of the forming tool.

There is more than one way in Abaqus to define the tool movement for the SPIF. The "smooth step" definition is used to obtain the quasi-static simulation and to avoid jumps or peaks in the tool velocity and acceleration. The smooth step definition method defines the amplitude, a, between two consecutive data points (A and B),

$A(t_i, P_A)$ and $B(t_{i+1}, P_B)$ as follows:

$$a = P_A + (P_B - P_A)\xi^3(10 - 15\xi + 6\xi^2)\ for\ t_i \leq t \geq t_{i+1} \quad (3.27)$$

Where $\xi = \frac{(t-t_i)}{(t_{i+1}-t_i)}$

The above function is such that $a = P_A$ at t_i, $a = P_B$ at t_{i+1} , and the first and second derivatives of a are zero at t_i and t_{i+1}. This definition is intended to ramp up or down smoothly from one amplitude value to another [62, 64, 114].

3.8 Element type

Abaqus/Explicit has many elements in its library; the choice of element type has a big influence on the simulated results, so that an appropriate element should be selected based on the need. Two factors should be considered when the element is selected: the degree of accuracy and the computational time. Each element in Abaqus has a unique name which distinguishes the characteristics of the element; in this work, the three-dimensional hexahedral element C3D8R (continuum, 3D, 8-node, reduced integration element) was selected to mesh the pure Ti sheet in the ISF process. This element can be employed for linear and nonlinear analyses involving plasticity, large deformation and contact. In Abaqus/Explicit, fast and cheap calculations can be achieved using reduced-order integration of the element matrices, but this integration scheme has a drawback with first order reduced integration element (C3D8R) in stress/displacement analyses; namely, it can result in shape distortion (hourglassing). Hourglassing can be minimized by using fine meshes. The forming tool, blankholder and the backing plate were modelled as an analytical rigid body. The rigid bodies are very frequently utilized in FE simulation as these bodies cannot deform during the deformation process; moreover, the computational time of rigid bodies is considered very efficient.

3.9 SPIF benchmark

A three-dimensional elasto-plastic model is set up for the simulation of the SPIF process. A FEM of the SPIF process is established based on Abaqus/Explicit, the developed numerical model of ISF is shown in Figure 3.7. Due to the nature of the SPIF process, there are dual nonlinearities (material and geometry) in the incremental material deformation, and the tool and workpiece contact zone. The finite element analysis in the SPIF is complicated and time consuming, because a large number of elements are used and the forming tool moves along a relatively long path.

In the FE model, a 0.7 mm thick pure titanium sheet with size 140 x 140 mm was meshed with 8-noded hexahedral elements using a reduced integration method (C3D8R). The material behaviour of the sheet metal is assumed to be isotropic elastic and plastic yielding, and the forming tool, blank holder and backing plate are regarded as rigid surfaces. Isotropic hardening is used to simulate the hardening behaviour in pure titanium grade 1 sheet during ISF. When isotropic hardening is defined, yield stress and plastic strain can be given in a table. Figure 3.8 gives the flow stress- plastic strain of the material at strain rate 0.00133 s^{-1} that is used in the FE simulation. Coulomb's friction law was applied with a friction coefficient of 0.1 to model the contact between the forming tool and blank and of 0.2 between the blank and other parts including the backing plate and the holder.

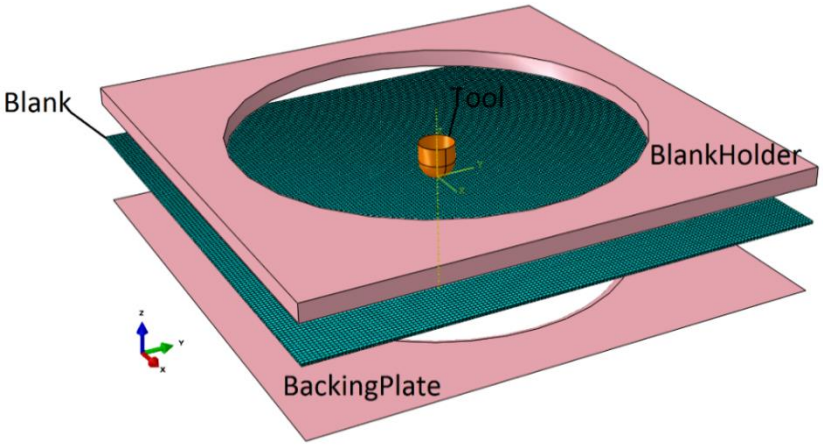


Figure 3.7 Configuration of FE model for SPIF process.

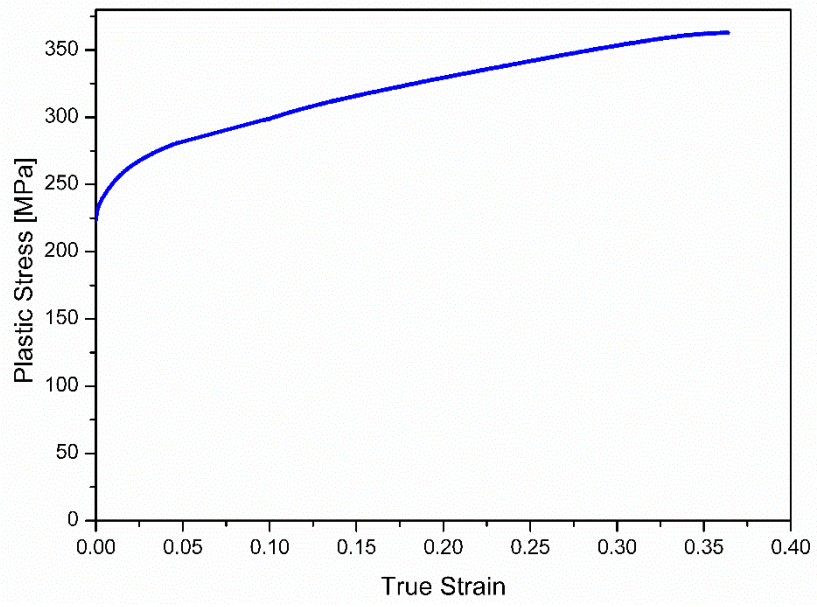


Figure 3.8 Flow stress of pure Ti grade 1.

To study the effect of simulation parameters on the FE results, 45° truncated cone is executed with a 116 mm major base and a final depth of 30 mm. The SPIF test is carried out with a 10 mm hemispherical forming tool and 0.2 mm step size with a 1000 mm/min feed rate (see Figure 3.9).

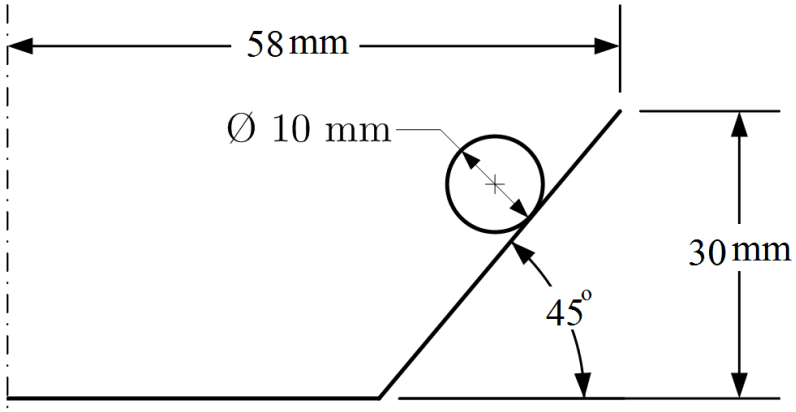


Figure 3.9 Geometric shape of the truncated cone.

3.10 Numerical results

3.10.1 Influence of meshing density

The element should be small in size to ensure that the nodes of the master surface (rigid tool) do not penetrate the mesh of the slave surface (deformed body) during contact. Meshing density has a significant effect on predicting accurate results. However, using a very small element size means that the computational time to do the analysis will be increased due to the fact that a stable increment time is strictly dependent on the element's length for explicit integration.

In order to study the optimum mesh size to be used for the simulation of SPIF, six element lengths (2, 1, 0.8, 0.6, 0.5, and 0.4mm) with three layers of elements through the thickness were chosen. The material characteristics of 0.7 mm thick pure Titanium are reported in Table 3-1;

Table 3-1 Mechanical properties of grade 1 pure titanium.

Yield stress	Ultimate tensile stress	Young's modulus	Poisson's ratio	Density
223.49 MPa	363 MPa	108 GPa	0.34	4505kg/m^3

In this work, equivalent plastic strain distribution is used to predict a suitable element size. Figure 3.10 shows the contour of equivalent plastic strain distribution on the final product of ISF with two different element sizes. It is noted from the figure that the

equivalent plastic strain in the transition zone between the top and bottom surfaces and inclined wall increases with increased element length (2 mm), while low values of strain with more uniform distribution can be achieved with a small element (0.5 mm)

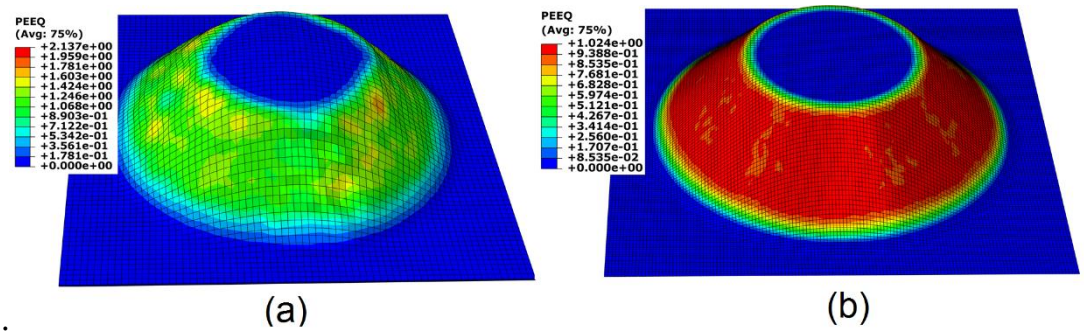


Figure 3.10 Equivalent strain distribution: (a) element length = 2mm and (B) element length = 0.5mm.

Figure 3.11 shows the equivalent plastic strain distribution with different mesh sizes. It is clear from the figure that with a smaller element size, the increment in equivalent plastic strain can be captured earlier than that with larger element sizes. It can be concluded that using a solid element with reduced integration means each element has one integration point in the middle; hence, if a large element is used, the possibility of capturing the peak of an equivalent plastic strain is less than when using a small element. In this investigation, the element length was reduced by using trial-and-error in order to get two element sizes with the same peak of equivalent plastic strain. Then, a larger length was selected to save time. However, a length of 0.5 mm was chosen for this investigation. The FE simulation of SPIF was run on a high performance computing (HPC) system using 48-core. The required time to complete the simulation with mass scaling was approximately 120 hours.

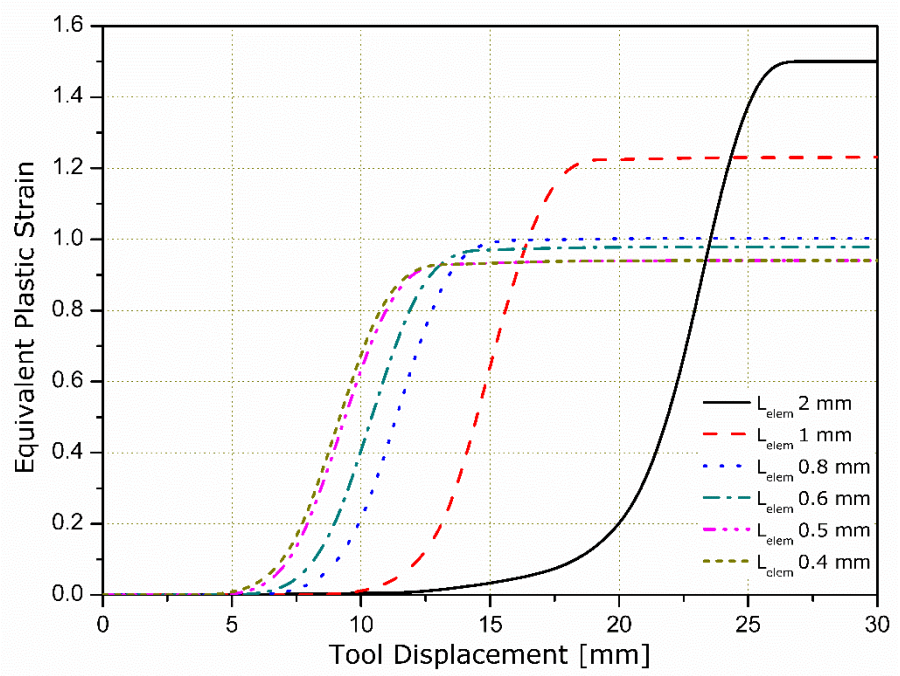


Figure 3.11 Comparison of equivalent strain for different meshing densities.

To check the validity of the SPIF simulation, the FE thickness was compared with experimental SPIF thickness, as shown in Figure 3.12. The SPIF simulated results of 0.5 mm element are consistent with one of the actual experiments.

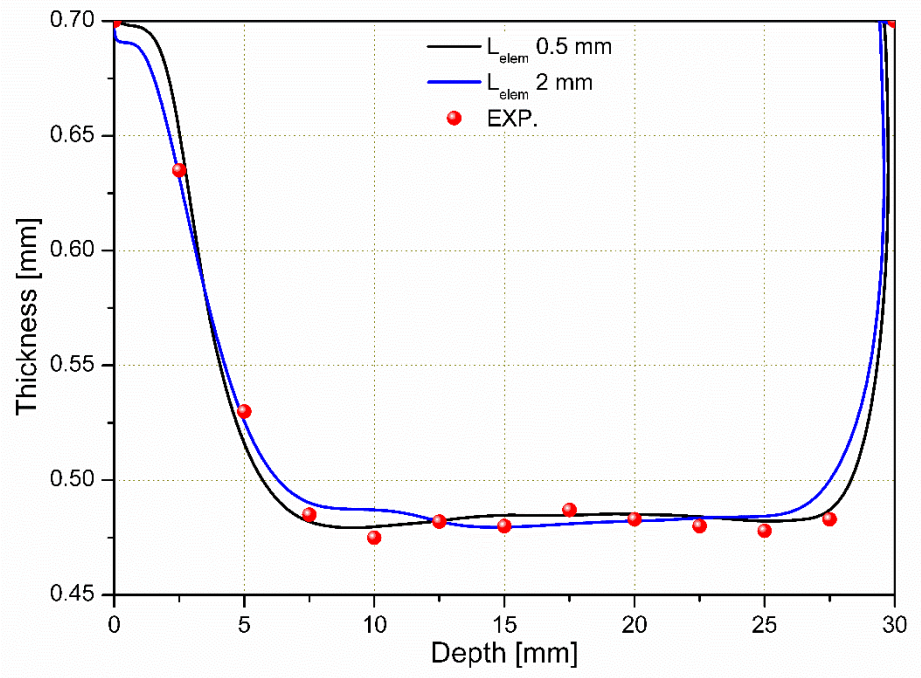


Figure 3.12 Comparison between numerical and experimental thickness distribution.

3.10.2 Influence of mass scale

To save computation time in Abaqus/Explicit, mass scaling techniques have been widely employed; however, these techniques can yield poor results if a large scaling factor is used due to the increase in dynamic effects. Typically, the kinetic energy should remain less than 4%-10% of the internal energy for the whole model.

To introduce mass scaling into a model, two types of mass scaling are available in Abaqus/Explicit: fixed and variable. In this work, variable mass scaling is selected as it is most useful when the stiffness properties that control the stable time increment change significantly during each step. When using this type of mass scaling, a desired minimum stable time increment is defined and a mass scaling factor is automatically calculated and applied, as required, throughout the step.

Unfortunately, no threshold is given to decide how much scaling is permissible. Therefore, three stable time increments ($\Delta t = 2*10^{-4}$, $2*10^{-5}$, and $2*10^{-6}$ s) were chosen to identify which one would provide acceptable accuracy compared to the desired geometry, with relative values between kinetic and internal energy less than 4% to 10%.

The output of the explicit FE analyses for a high value for the stable time increment ($2*10^{-4}$s) leads to highly non-uniform deformation of the part, as shown in Figure 3.13 (a), with high values of equivalent plastic strain, while lower values of equivalent plastic strain with uniform distribution can be achieved with a low stable time increment, e.g. $2*10^{-5}$ s and $2*10^{-6}$ s (see Figure 3.13 (b and c)).

Figure 3.14 shows the history of the dynamic energy with different stable time increments. It can clearly be seen that, with stable time increments of $2*10^{-4}$ s and $2*10^{-5}$ s, the kinetic energy exceeded 10% of the internal energy, while with another stable time increment ($2*10^{-6}$s), the relative values of energy are less than 4%. Moreover, for $\Delta t = 2 \times 10^{-6}$s a good match is obtained between the final product and the desired geometry of the cross-section, as shown in Figure 3.15, when compared with stable time increment $\Delta t = 2*10^{-4}$s and $2*10^{-5}$s. The desired shape is simply the ideal geometry formed by the tool path during the process, without taking material behaviour into account. Based on the equivalent plastic strain distribution, the final product geometry and the relative values between the kinetic and internal energy, $\Delta t = 2*10^{-6}$s was chosen for all the simulations in this thesis.

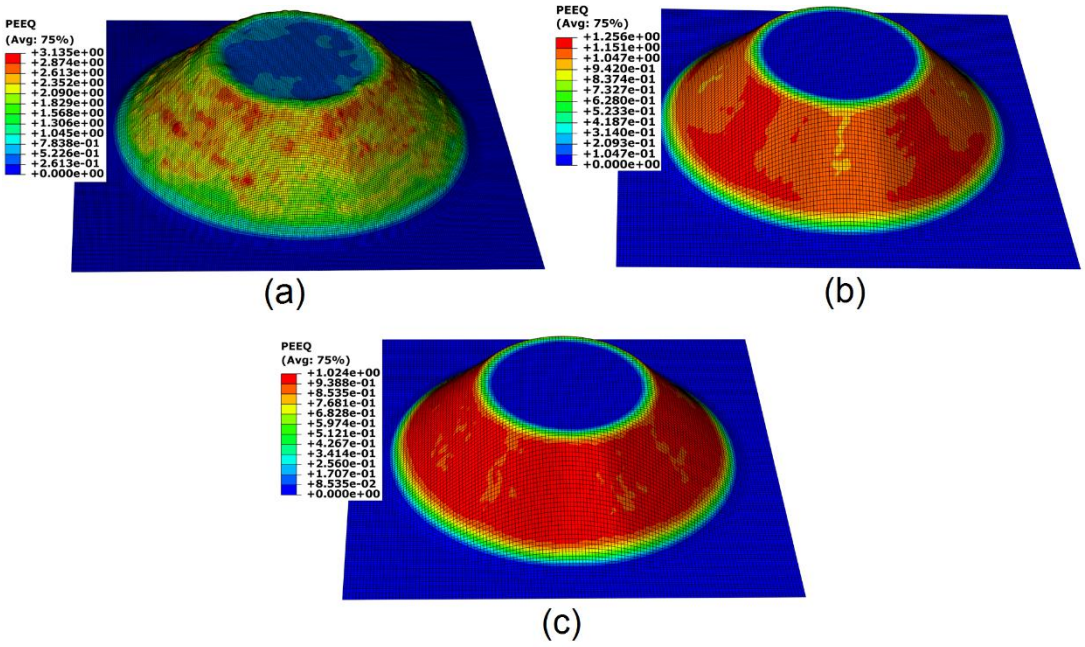


Figure 3.13 Distortion of final product with different stable time increments: (a) Δt 2E-4 s, (b) Δt 2E-5 s and (c) Δt 2E-6 s.

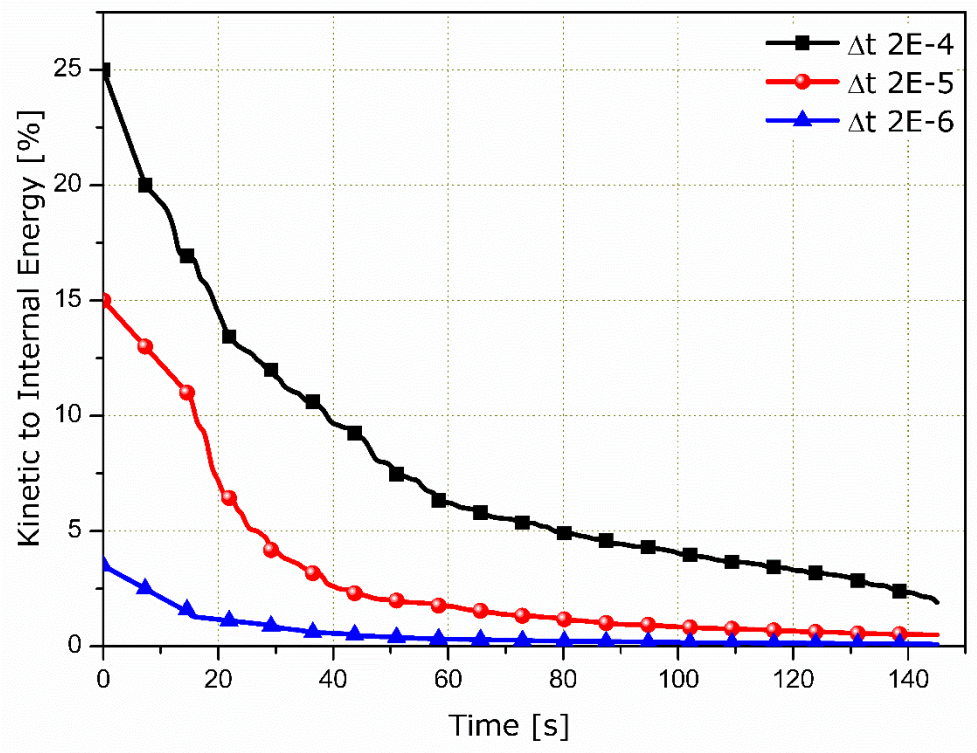


Figure 3.14 The ratio of kinetic and internal energy for the ISF process.

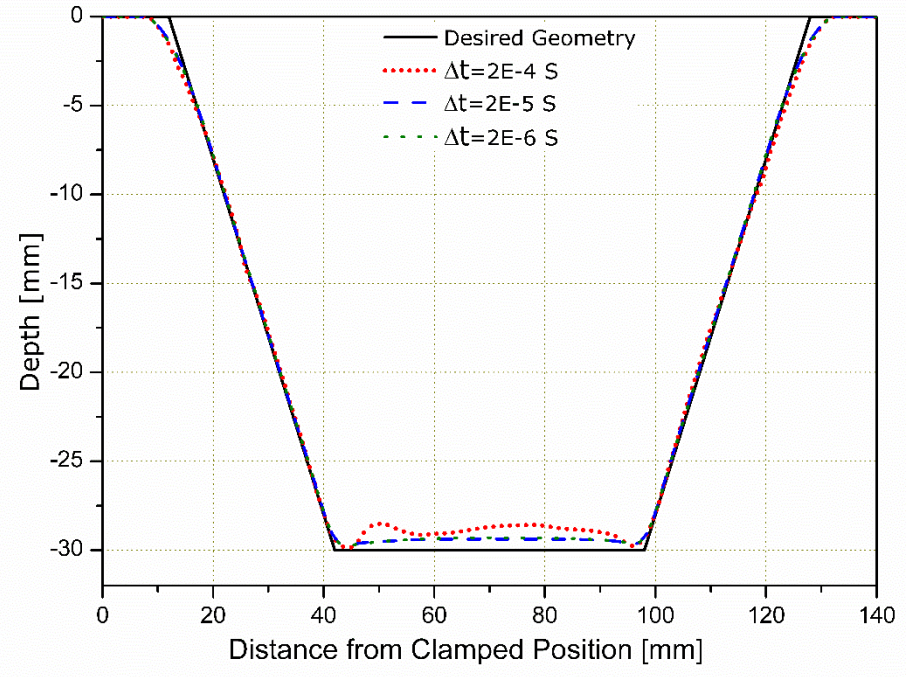


Figure 3.15 Product geometry comparison.

3.10.3 Influence of friction coefficient

In most of the sheet metal forming process, low friction is favoured. In the SPIF process, a certain level of friction is required between the forming tool and the sheet to transfer the stresses onto the forming tool and allow some stretching of the sheet. In order to investigate the effect of friction on the FE model of the SPIF process, an identical truncated cone, as in Figure 3.9, was simulated with different values of friction coefficient (μ = 0.05, 0.1, 0.15, 0.2, and 0.25) at the interface between the forming tool and 0.7 mm thick pure Ti sheet. The step size was set to 0.2 mm with a 1000 mm/min feed rate.

The variation of the vertical ISF force with forming tool displacement under different frictional conditions is shown in Figure 3.16. It is seen that the ISF force increases after increasing the friction coefficient between the forming tool and the sheet. This means that the FE model of the ISF process is robust with reference to the friction, indicating that the change in friction coefficient can greatly alter the predictions.

The predicted thickness was compared with that of the experiment to illustrate the effect of friction coefficient on thickness distribution, as shown in Figure 3.17. It is clear therefore that more thinning can be achieved with a high friction coefficient (μ0.25).It can be seen that there is a good correlation in the thickness distribution of

the truncated cone between the simulated thickness obtained for friction coefficient of 0.1 and the experimental thickness. Friction coefficient equal 0.1 is chosen in this work to simulate the friction in SPIF between the forming tool and the sheet.

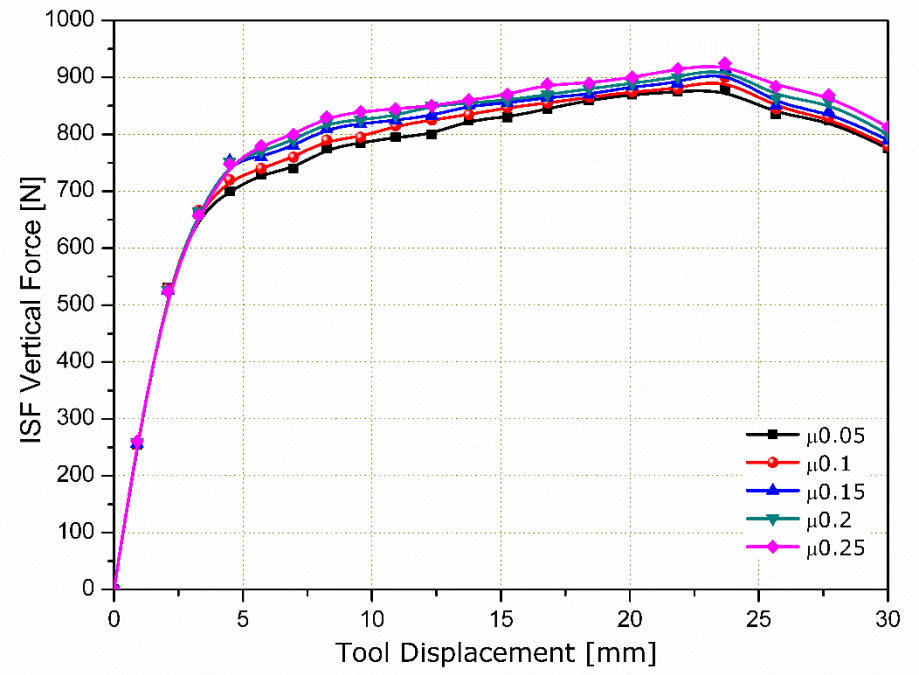


Figure 3.16 The effect of friction on the ISF load.

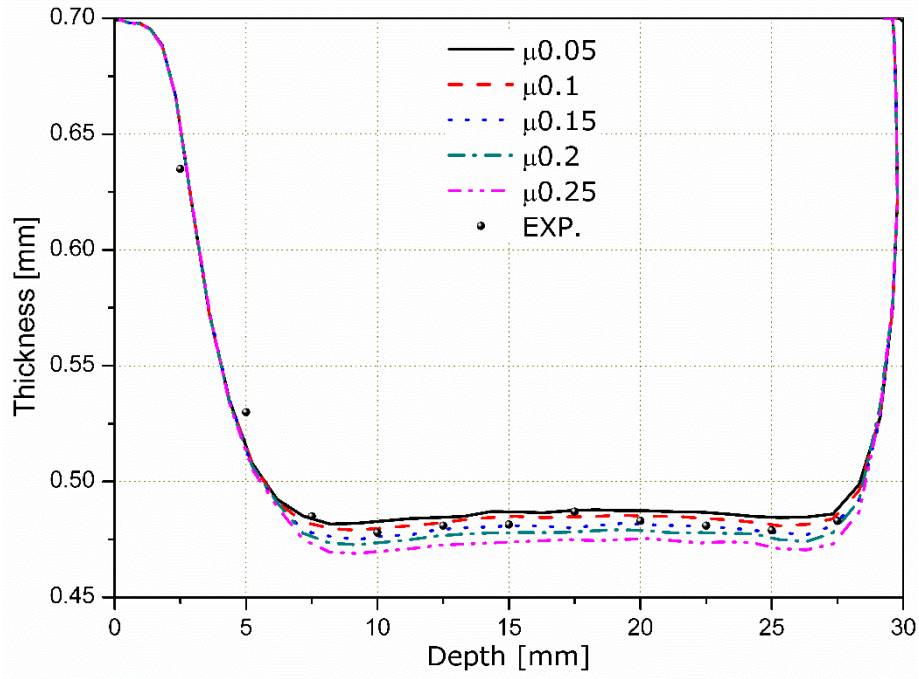


Figure 3.17 Thickness distribution with different friction coefficients.

3.10.4 Validation of SPIF simulation

To validate the SPIF simulation, the FE results were compared with the work of Manco et al. [116]. This was a two part work using the LS-Dyna FE simulation and experiments. A 1 mm AA1050-O sheet was used in the experiment, with mechanical properties as listed in Table 3-2.

Table 3-2 Mechanical properties of AA1050-O.

Yield stress	Ultimate tensile stress	Elongation at break	Power law
28MPa	76MPa	39%	$\sigma = 111\varepsilon^{0.14}\ (MPa)$

The final geometry is a truncated cone, with a 90 mm major base and final depth of 50 mm; a forming tool diameter of 12 mm, and an incremental depth of 1 mm per revolution were utilized with two wall angles of 60° and 70°. The SPIF simulated results by Abaqus are consistent with one of the actual experiments and the LS-Dyna software, with a percentage error of approximately 4%, as shown in Figure 3.18. This error can be explained by possible errors in both analyses and experiments. In the analyses, the possible errors are due to the lack of exact information about the material's properties and friction conditions, whereas in the experiments, the possible errors are due to variations in the measured blank thickness.

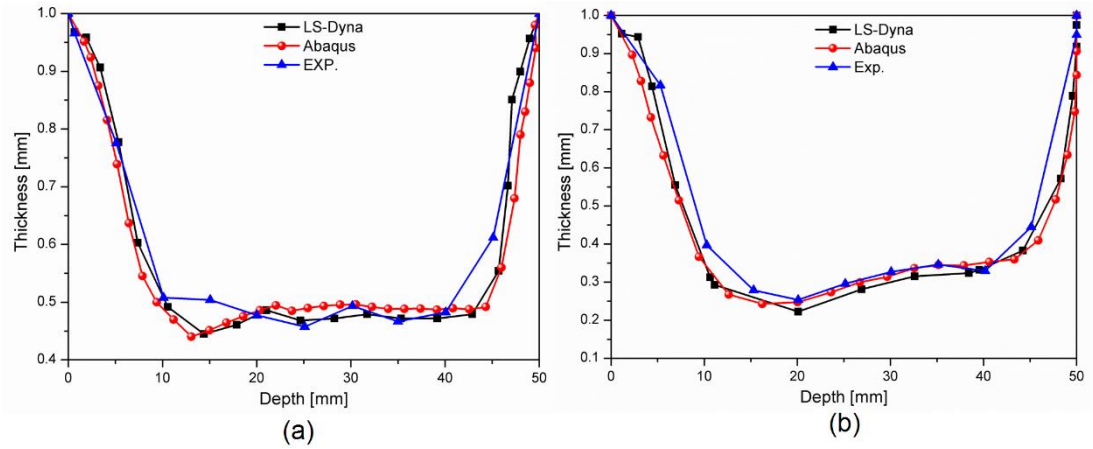


Figure 3.18 Comparison between experimental and numerical thickness distribution: (a) α=60° and (b) α=70°.

3.11 Conclusions

The main aims of this chapter was to develop a three-dimensional model using commercial finite element software Abaqus/Explicit to simulate the deformation of a pure titanium sheet metal blank during SPIF, then to study the effect of simulation parameters on finite element simulation results, e.g. element size, mass scaling factor and friction coefficient.

From the finite element simulation, it can be concluded that the element size affects the finite element results, especially in terms of equivalent plastic strain, so this should be selected carefully to get good results; the best length of element in the deformation area is 0.5 mm. The mass scaling factor may lead to error or failure of the explicit SPIF simulation due to the fact that kinetic energy can be raised if a high value of mass scaling is chosen. Furthermore, time consumption is greater if a small value of mass scaling is used; thus, a suitable value should be selected to produce a part with relative values between kinetic and internal energy of less than 0.4%-10%. This has been achieved with stable time increment of $2x10^{-6}$s. The FE model of SPIF is robust to changing as the change in friction coefficient can alter the predictions; in addition, the SPIF model for friction coefficient of 0.1 shows good prediction of sheet thickness when the results are compared with the experimental work.

CHAPTER 4

MODELLING OF DUCTILE FRACTURE IN ISF

4.1 Introduction

The fracture mechanism in incremental sheet forming (ISF) is still an unresolved issue due to contradicting views on the effect of shear on fracture in the ISF process. In this chapter, a modified Gurson–Tvergaard-Needleman (GTN) model is developed with the consideration of shear to predict ductile fracture in the ISF process due to void nucleation and coalescence with results compared with original GTN model without shear. The modified GTN damage constitutive model with shear was implemented in Abaqus/Explicit via a VUMAT user subroutine. Tensile and shear tests were carried out to determine the parameters and to validate the modified GTN model experimentally. The deformation of the tensile specimen was measured by using a digital image correlation (DIC) system to analyse necking and fracture of the tensile specimen. The data of initial void volume fraction and those at nucleation and fracture were obtained with a scanning electron microscope (SEM). Using the modified GTN model, finite element (FE) simulations were conducted to predict fracture of pure titanium sheets in ISF processing of two typical geometries, i.e. a truncated hyperbolic cone shape and a truncated hyperbolic pyramid.

In micromechanics based approaches to predicting fracture of ductile materials, a comprehensive study was carried out by Cao and co-workers [117] in developing Gurson-type models using a mixed velocity-pressure FE formulation to review and clarify the constitutive equations of Avaras and to give proof of the equality of tangent moduli proposed by Zhang and Govindarajan-Avaras. The results showed good accuracy of analytical formulation and the validity of the implementation for a mixed velocity-pressure FE formulation. On the other hand, Tekkaya and co-workers developed an ion beam slope cutting method to prepare the specimen from a notched tensile test specimen for SEM analysis for detailed examination of nucleation and growth of voids during the deformation of dual-phase steel DP600 [118].

A GTN yield criterion was developed utilizing Abaqus/Explicit via a user-defined material subroutine (VUMAT) by Chen and Dong, based on the Hill'48 yield model to predict the damage of anisotropic sheet [119]. Deep drawing of a cylindrical cup was taken as an example of sheet metal forming. It was concluded that the Hill'48-GTN plastic yield criterion provided a promising tool to predict the plastic behaviour and fracture in sheet metal forming. Kami et al. developed a Hill'48-GTN yield criterion to predict fracture in the deep drawing process of a rectangular box [120] and to construct a forming limit diagram of AA6016-T4 anisotropic sheet [26]. The FE results showed that the GTN model was able to predict fracture and to provide a realistic description of the material response in the whole forming process. Using a GTN constitutive model coupled with the Mori-Tanaka approach, Vrh et al. demonstrated the effect of stiffness degradation on the springback of the steel sheet drawn part [121]. The results showed that, when compared with the Demeri springback cup test, the stiffness degradation in material has a significant impact on the springback. Lievers et al. [122] presented a method to determine the void nucleation rate in the ISF process based on density changes using the original GTN model. Three automotive aluminium sheet alloys (AA5754, AA5182 and AA6111) were used to calibrate the void nucleation behaviour. This technique provides a large homogenous deformation area and avoids the large strain and stress gradient associated with smooth or notched tensile specimens. Smith et al. [123] attempted to evaluate the effect of shear on the fracture depth in the ISF process via LS-DYNA explicit software with a shear-modified GTN model proposed by Nahshon and Hutchinson. However, questions still remain regarding the role of shear and particularly its effect on the sheet formability in ISF processes. Therefore, the main motivation of this study is to develop a GTN based model and to investigate its accuracy and effectiveness in predicting the ductile fracture in ISF processing of typical truncated cone and pyramid shapes.

4.2 Fracture mechanisms in SPIF

Depending on the state of stress, damage in sheet metal forming occurs generally due to one or combination of the following mechanisms [124]:

- Ductile fracture (based on void nucleation and coalescence);
- Shear fracture (based on shear band formation).

The deformation modes and states of strain and stress in the deformation area should be known for detailed evaluation of fracture. The deformation mode in SPIF varies for

different locations in the deformed part, e.g., (A) plane strain stretching conditions in flat surfaces; (B) plane strain stretching conditions in rotational symmetric surfaces; and (C) equal bi-axial stretching conditions at corners. Additionally, there are possibilities of other deformation modes in ISF. Understanding the deformation and failure mechanisms in SPIF is of great importance for achieving improved formability. Furthermore, there will be added benefits for more in depth evaluation of the effect of localised deformation on the fracture mechanism in SPIF. Extensive research has been carried out to investigate deformation and fracture mechanisms in SPIF:

- Membrane analysis: Silva *et al.* [20], [63] employed membrane analysis of small element under plane strain condition in the transition area between the corner radius of a truncated cone and its inclined wall to explain ISF cracks triggered due to meridional tensile stresses.
- Through-thickness shear: Jackson and Allwood [22] used FE simulation to study the effect of through-thickness shear on the formability of SPIF. The results showed that the significant through-thickness shear occurring in the direction parallel to the tool motion could affect the formability. They demonstrated that the material in the contact zone tends to move in the direction of the tool displacement due to friction.
- Bending under tension (BUT): Emmens and van den Boogaard [125], [126] utilized the continuous bending under tension test to investigate this aspect of ISF. The results showed that the formability was proportional to the sheet thickness under constant bending radius. A relation between strain and elongation was developed and validated experimentally based on the assumption of localized deformation.

It is clear there are different opinions about the deformation modes in SPIF based on both experimental work and finite element simulation. Some researchers think that the deformation occurs due to stretching [20, 63], whilst others believe it is largely due to through-thickness shear and stretching [21, 22]. Therefore, more work needs to be done to understand the fracture mechanisms in SPIF processing of complex shapes.

4.3 GTN based micromechanics damage model

Several constitutive equations have been developed based on phenomenological criteria (continuum damage mechanics) or micromechanics criteria to model the

fracture of material under large plastic strain (ductile fracture). The continuum-based criteria have been built to employ a stress-strain relationship. The first phenomenological model within a consistent thermodynamic framework was developed in 1958 by Kachanov [127]. This model has been developed by Lemaitre [128] and Lemaitre and Desmorat [129] and it widely used to predict the fracture under pure shear state.

The micromechanics based damage model was built based on the fact the ductile fracture of metallic materials mostly occurs by the mechanism of nucleation, growth and coalescence of microvoids. A void can be nucleated from an inclusion or second phase particle by decohesion or cracking, and it grows due to the development of localised plastic strain under the application of tensile hydrostatic stresses. The amount of void in the material is defined as a ratio of the volume of voids to the total volume of the material. It is denoted by f and also referred to as the void volume fraction (VVF). The shape of the void is assumed to be spherical and it is scattered randomly in the material's matrix [130]. When the material is fully dense without any void, the f value is 0 or 1 if the material is completely void without any stress carrying capacity. When the space between two adjacent voids is small enough, the voids begin to coalesce and this leads to cracks and subsequent fracture of the material, as shown in Figure 4.1 [131, 132].This phenomenon can be analysed utilizing damage models taking into account the effect of microstructure defects by defining a relationship between particular failure stages and the strength of the material. The first micromechanics based damage model was proposed by McClintock [133] in 1968 to describe the growth of spherical voids in an elastoplastic matrix. Another micromechanics based model was developed in 1969 by Rice and Tracey [134] to investigate the evolution of spherical voids. The results of these models showed that the voids growth is governed by a combined role of plastic strain and stress triaxiality.

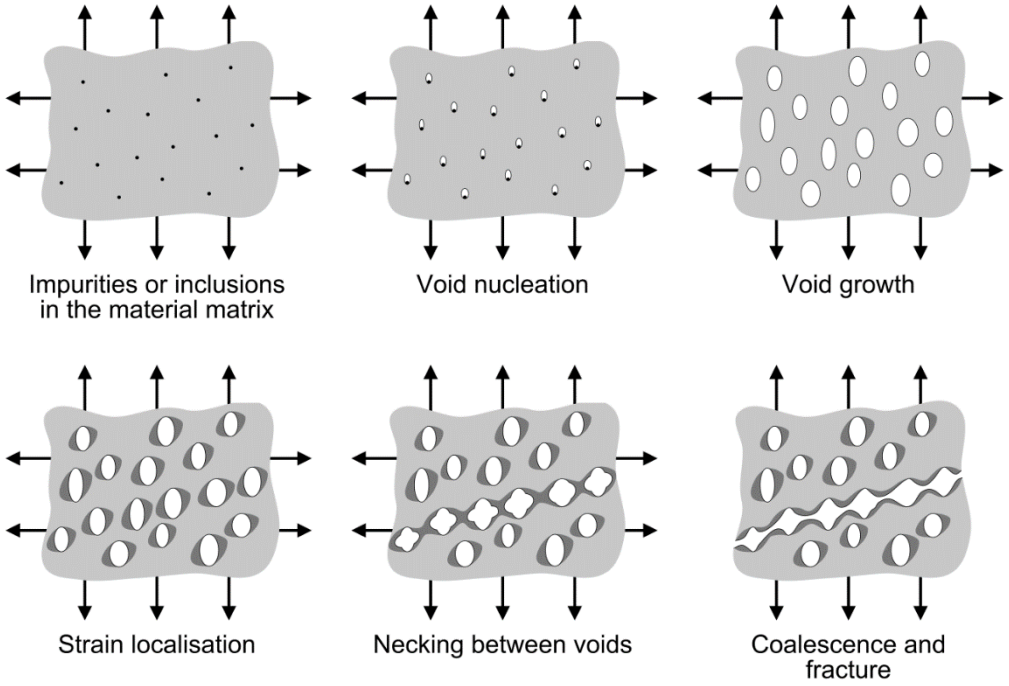


Figure 4.1 Schematic of the nucleation, growth and coalescence of voids. Adapted from [135].

Gurson's porous metal plasticity model [130], later modified by Tvergaard and Needleman (GTN) [110], is one of the most commonly used micromechanics based material damage models for the prediction of fracture.

Mises theory assumes that the hydrostatic stress component does not affect yield stress. Whereas ductile fracture in materials is completely due to void growth, e.g. porous materials harden in compression due to the closing of voids and soften under tension due to void growth, as shown in Figure 4.2 [64].

Hydrostatic stress causes dilatancy and influences the yield stress, as shown in Figure 4.3. With Mises material, $f=0$, the yield surface is a straight line, which means hydrostatic stress has no effect. However, when the void volume fraction increases, the yield surface gets smaller due to the fact that yielding occurs at lower values of equivalent stress [110, 136, 137].

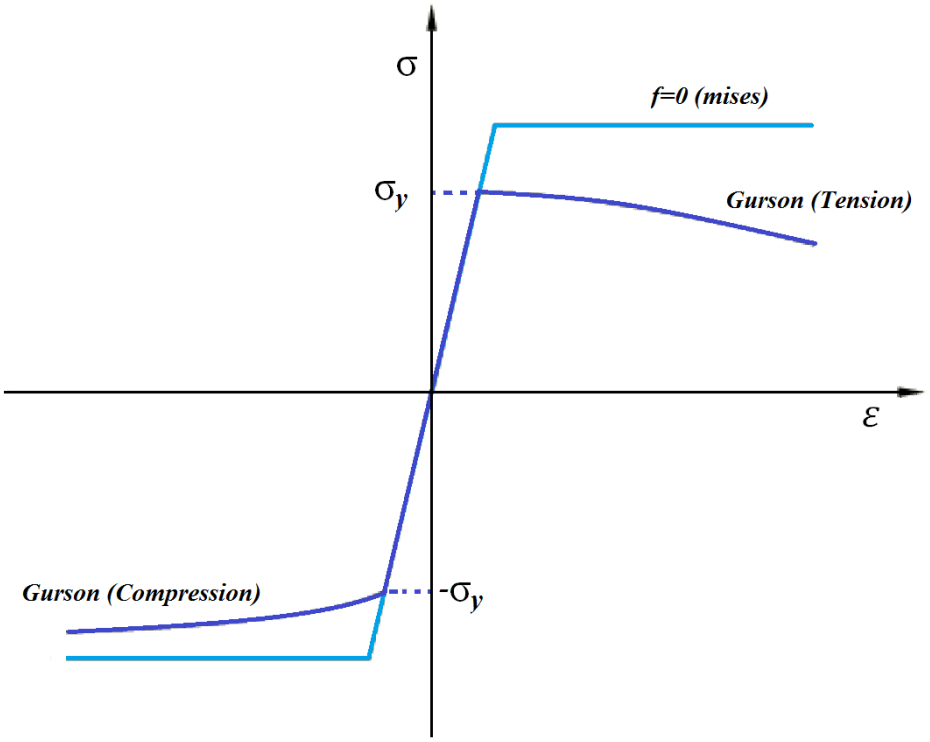


Figure 4.2 Comparing uniaxial behaviours of porous metals with Mises materials. Adapted from [64].

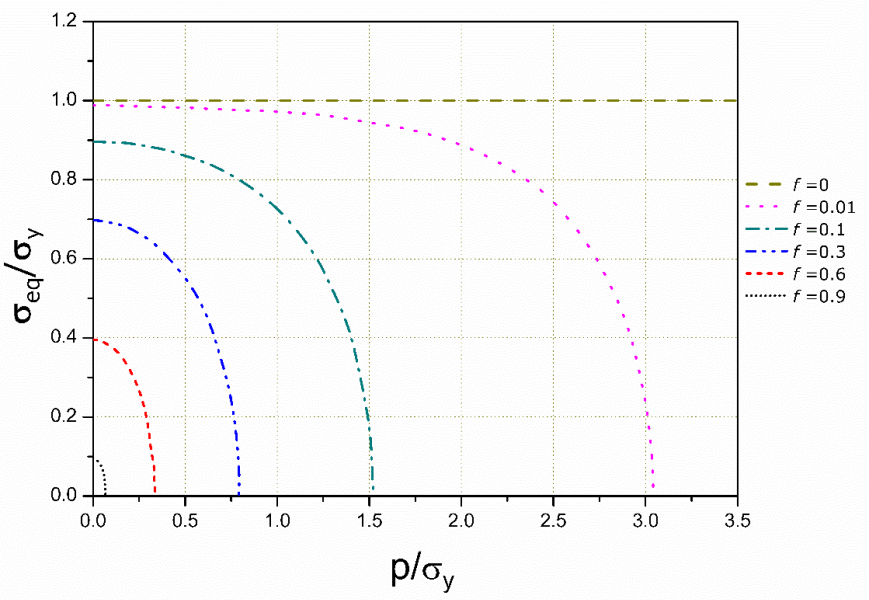


Figure 4.3 The dependence of yield surface on the hydrostatic stress for various values of void volume fraction. Adapted from [137].

In general, the flow of plastic solid porous material can be written in the form

$$\emptyset = (\sigma_y, p, \sigma_q, f) = 0 \tag{4.1}$$

and satisfying

$$\emptyset = \frac{\sigma_q^2}{\sigma_y^2} - 1 = 0 \; when \; f = 0 \tag{4.2}$$

where $\sigma_q = \sqrt{\frac{3}{2} S_{ij} S_{ij}}$ is equivalent to von Mises stress; $S_{ij} = \sigma_{ij} - \frac{1}{3}\sigma_{ii}$ is a deviatoric stress tensor; $p = -\frac{1}{3}\sigma_{ii}$ is the hydrostatic stress; σ_y is the flow stress of the undamaged material matrix; and σ_{ii} is the trace of the stress tensor.

The classical plasticity theory (the Von Mises theory) was extended by Gurson [130] to cover the effect of plastic dilatancy and pressure sensitivities of inelastic flow based on the observation that the nucleation and growth of voids in a ductile metal can be described macroscopically. The Gurson model was developed based on the assumption that the material has a spherical shape of voids in the matrix, and rigid-plastic limit analysis was employed to develop the yield condition

$$\emptyset = \frac{\sigma_q^2}{\sigma_y^2} + 2f cosh\left(\frac{3p}{2\sigma_y}\right) - 1 - f^2 = 0 \tag{4.3}$$

The Eq. (4.3) can be reduced to Von Mises solid when *f=0*.

The Tvergaad-Needleman modification (GTN model) [110] is considered as one of the most adopted variants of the Gurson's model. This model introduces a void volume fraction f^* and three constitutive coefficients q_1, q_2 and q_3 characterizing the interaction effects between voids. The yield function of the GTN model takes the following form:

$$\emptyset = (\frac{\sigma_q}{\sigma_y})^2 + 2q_1 f^* \cosh\left(-\frac{3q_2 p}{2\sigma_y}\right) - \left(1 + q_3 f^{*^2}\right) = 0 \tag{4.4}$$

Where $\emptyset$ is the non-dilatational strain energy; q_1, q_2 and q_3 are the constitutive parameters proposed by Tvergaard [138] to get closer agreement between the GTN model and the full numerical analyses of a periodic array of voids with suggested values of q_1=1.5, q_2=1.0 and q_3=2.25. The parameter f^* was introduced by Tvergaard-Needleman to account for the final material failure for void coalescence. This parameter is a function of the void volume fraction *f* and is specified as

$$f^* = \begin{cases} f & if \; f \le f_c \\ f_c + \dfrac{\overline{f}_F - f_c}{f_{f-f_c}}(f - f_c) & if \; f_c < f < f_f \\ \overline{f}_F & if \; f \ge f_f \end{cases} \tag{4.5}$$

where f_c denotes the critical value of the void volume fraction, and f_F is the final value of the void volume fraction when the material has completely lost its stress carrying capacity. The function of $\overline{f}_F$ is defined as

$$\overline{f}_F = \frac{q_1 + \sqrt{q_1^2 - q_3}}{q_3} \tag{4.6}$$

The increase in the initial void volume fraction f is defined as the sum of the increment due to void nucleation and void growth

$$df = df_{nucleation} + df_{growth} \tag{4.7}$$

The nucleation mechanism is considered to be dependent exclusively on the plastic strain of the matrix material and it is assumed that the voids are nucleated only in tension.

$$df_{nucleation} = A d\overline{\varepsilon}_m^p \tag{4.8}$$

$$\text{where } A = \begin{cases} \frac{f_N}{S_N\sqrt{2\pi}} e^{-0.5\left(\frac{d\overline{\varepsilon}_m^p - \varepsilon_N}{S_N}\right)^2} & if\ p \geq 0 \\ 0 & if\ p < 0 \end{cases} \tag{4.9}$$

The parameter A is defined as a function of the total equivalent plastic strain ε_m^p of the matrix material, f_N is the void volume fraction of the nucleated void; ε_N is the mean value of the normal distribution of the nucleation strain; and S_N is the standard deviation. $d\overline{\varepsilon}_m^p = \frac{\sigma : d\varepsilon^p}{(1-f)\sigma_y}$ is equivalent plastic strain.

$$df_{growth} = (1 - f) d\varepsilon_{ii}^p \tag{4.10}$$

where $d\varepsilon_{ii}^p$ is the trace of the plastic strain tensor.

4.4 Classification of GTN model parameters

The parameters involved in the GTN model can be classified into two groups. The first group is named "constitutive parameters" ($q_1, q_2\ and\ q_3 = q_1^2$) [139, 140] as suggested by Tvergaard [138]. The q_1 parameter has a big effect on the strength properties of materials; with a higher value of q_1, the strength of the material decreases, as shown in Figure 4.4 (a). This is because the softening phenomenon in the material due to void growth is dominating over matrix hardening [132]. The optimal value of q_1, according to Tvergaard, is 1.5. The second constitutive parameter, q_2, has an effect on the hydrostatic stress $p = -\sigma_{ii}/3$ sensitivity; with a high value of q_2, the yield limit

is significantly reduced. This is due to high softening through void volume growth, revealing the extermination of the strain hardening of the material matrix (see Figure 4.4(b)) and the typical value of q_2 is 1.0.

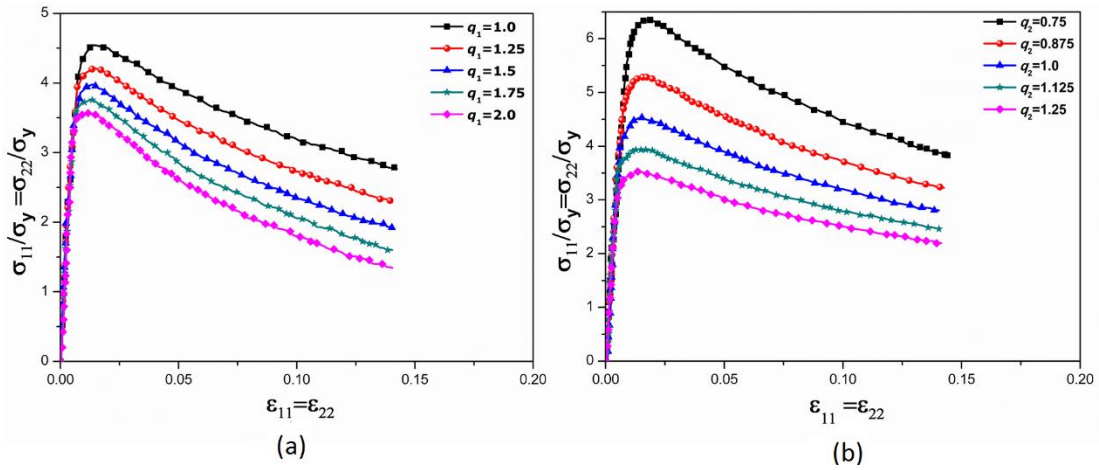


Figure 4.4 Influence of constitutive parameters q1 and q2 on nonlinear response of GTN constitutive law at $\varepsilon_{22}/\varepsilon_{11} = 1.0$ (a)$1.0 \leq q_1 \leq 2.0$; (b) $0.75 \leq q_2 \leq 1.25$. Adapted from [141].

The second group is called "material parameters" which are divided in two parts. Firstly, "initial material" parameters include the initial void volume (f_o) and the void nucleation parameters (f_N, ε_N and S_N). The initial void volume fraction has a bigger impact on the beginning of yielding than on the behaviour at high deformation levels, but the void volume fraction at nucleation (f_N) has a uniform influence on the material's behaviour in the softening regime. With the increase of f_N value, there is a small increase in the current void volume fraction, without significant variations of the void volume fraction [141]. Secondly, "critical parameters" are the critical void volume fraction (f_c) and final void volume fraction (f_f) at fracture. In this study these parameters are determined experimentally based on tensile test and SEM microscopic evaluation.

4.5 Shear mechanism

The GTN model has its limitations as it ignores the fracture mechanism due to shear. A number of papers have been published recently to develop modified GTN models by adding a function to capture the fracture at low stress triaxiality.

4.5.1 Xue's shear mechanism

Xue [136] proposed a function based on the void volume fraction, equivalent plastic strain ε_{eq} and the Lode angle θ_L (Lode angle is defined as smallest angle on the deviatoric plane between the projection of stress tensor and the line of pure shear). This mechanism was based on a cell structure subjected to a simple shear strain with a circular void at the centre. Xue's shear mechanism assumes that the increment in the void volume fraction obtained by shear effect is

$$df_{shear} = q_4 f^{q_5} g_0 \varepsilon_{eq} d\varepsilon_{eq} \tag{4.11}$$

For a 2D model, q_4=1.69 and q_5=0.5 with q_4=1.86 and q_5=1/3 for 3D problems, respectively; ε_{eq} is the total equivalent strain and g_0 is a parameter responsible for the inclusion of the Lode angle dependence on the shear mechanism, which can be defined as:

$$g_0 = 1 - \frac{6|\theta_L|}{\pi} \tag{4.12}$$

$$\theta_L = \tan^{-1}\left[\frac{1}{\sqrt{3}}\left[2\left(\frac{S_2 - S_3}{S_1 - S_3}\right)\right]\right] \tag{4.13}$$

where S_1, S_2 and S_3 are the deviatoric stress tensors in the principal directions.

4.5.2 Nahshon-Hutchinson's shear mechanism

The original GTN model predicts no increase in the growth rate of the void for low stress triaxiality $\eta = -p/\sigma_q$. Nahshon and Hutchinson [142] introduced an expression used to predict the increase in the rate of void due to low stress triaxiality, which is written as

$$df_{shear} = k_w \frac{f\omega(\sigma)}{\sigma_q} S : d\varepsilon^p \tag{4.14}$$

where $\omega(\sigma)$ is a function of the stress state and its value is calculated as:

$$\omega(\sigma) = 1 - \left(\frac{27 J_3}{2\sigma_q^3}\right)^2 \tag{4.15}$$

The value of ω lies in the range of $0 \leq \omega \leq 1$; for all axisymmetric stress states $\omega = 0$ and for all the states comprising of pure shear plus a hydrostatic contribution $\omega = 1$. k_w is a parameter producing the damage rate in shear loading, and J_3 is the third invariant of the deviatoric stress tensor $J_3 = \det(S)$.

The total void volume fraction after the additional contribution of the shear mechanism thus becomes

$$f_{total} = f_{initial} + (df_{nucleation} + df_{growth} + df_{shear}) \quad (4.16)$$

4.5.3 Lode angle dependency

The original GTN model can accurately capture the fracture at high stress triaxiality but no failure at zero or low stress triaxiality (pure shear). To distinguish the pure shear state and simple tension, a Lode angle dependency is utilized [143]. From the experimental observation, the simple shear fracture strain is less than the simple tension fracture strain [144]. The stress triaxiality effect cannot explain this observation due to the fact that the pure shear lacks hydrostatic tension stress. That decreases the ductility of materials when compared to the simple tension stress state. A phenomenological method is used to depict the Lode angle by introducing a Lode angle dependency function in the fracture envelope [136]. When the material is subjected to shear loading conditions, the damage accumulation is accelerated by the void shearing mechanism. The coalescence process is started when the void reaches a certain range. At this stage, inhomogeneous straining takes place in the cell structure and new voids tend to nucleate near the shortest ligaments between large voids at a high deformation point. However, the free distance between voids is reduced by the shear mechanism and leads to facilitation of the connection of the void in the shear direction (see Figure 4.5) [133, 136].

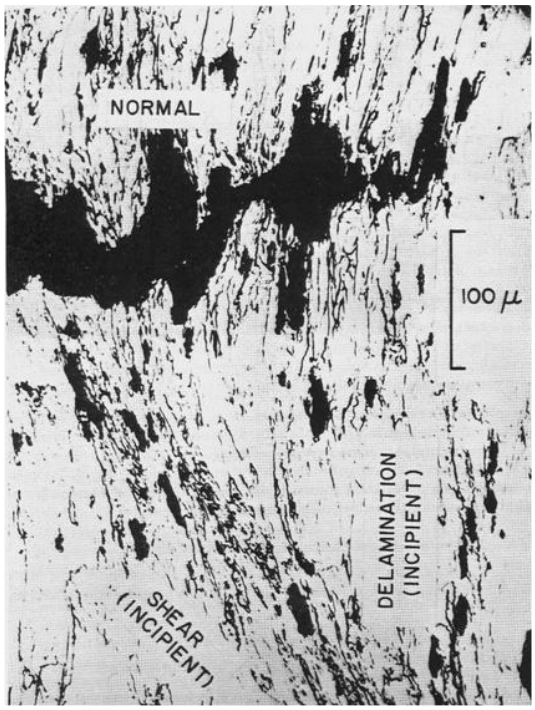


Figure 4.5 Normal fracture incipient delamination and shear fracture in the tensile specimen [144].

4.6 Implementation of the modified GTN model

The modified GTN damage model with shear consideration has been implemented in Abaqus/explicit through the material user subroutine VUMAT. The VUMAT subroutine begins by assuming the increment in the strain is purely elastic, and based on this assumption a trial stress is calculated before the yield function is checked. Thus if $\emptyset \leq 0$, the current state is elastic, it is necessary to update the stresses and exit; if not, the current state is plastic and the incremental plastic strain should be determined. Figure 4.6 shows the flow chart of the stress integration algorithm of the shear modified GTN model. In this work, predictor return algorithm is used to compute the increment in plastic strain ($d\varepsilon^p$) [145, 146] and is briefly summarized below.

The VUMAT begins by assuming the incremental strain is purely elastic and, based on this assumption, a trial stress is calculated. Hook's law is obeyed to determine the trial stress,

$$\sigma_{t+\Delta t}^{trial} = \sigma_t + 2\overline{\mu}\Delta\varepsilon_{ij}^{el} + \lambda\varepsilon_{ii}^{el}\delta_{ij} \tag{4.17}$$

where $\overline{\mu} = \frac{E}{2(1+\nu)}$ is a shear modulus and $\lambda = \frac{E\nu}{(1+\nu)(1-2\nu)}$ is the first Lamé parameter.

The equivalent stress is derived from deviatoric components, S_{ij},

$$S_{ij}^{trail} = \sigma_{ij}^{trial} + P \tag{4.18}$$

where $P = -\frac{\sigma_{ii}^{trial}}{3}\delta_{ij}$ is hydrostatic pressure

$$\sigma_q^{trial} = \sqrt{\frac{3}{2}S_{ij}^{trial}S_{ij}^{trial}} \tag{4.19}$$

The values of trial hydrostatic and equivalent stresses are used in the modified GTN model in Eq. (4.4) to check whether the plastic strain deformation occurs. If the current state is plastic, the incremental plastic strain is determined by:

$$d\varepsilon_{ij}^{p} = \Delta\lambda\frac{\partial\emptyset}{\partial\sigma_{ij}} \tag{4.20}$$

The equivalent plastic strain is defined by

$$\overline{d\varepsilon}^{p} = \sqrt{\frac{2}{3}d\varepsilon_{ij}^{p}d\varepsilon_{ij}^{p}} \tag{4.21}$$

The change in plastic consistency parameter $\Delta\lambda$ is:

$$\Delta\lambda = \frac{\emptyset}{V_{ij}D_{ik}V_{ik} - \xi_1 h_1 - \xi_2 h_2} \tag{4.22}$$

The definitions of ξ_1, ξ_2 and V_{ik} in terms of stress components are:

$$\xi_1 = \frac{\partial\emptyset}{\partial\varepsilon_{ij}^{p}} = -\frac{2H}{\sigma_y^3}\left[\frac{3}{2}\sigma_{ij}\sigma_{ij} - 0.5\sigma_{ii}^2\right] - \frac{Hf^*q_1\sigma_{ii}}{\sigma_y^2}\sinh\left(\frac{q_2\sigma_{ii}}{2\sigma_y}\right) \tag{4.23}$$

$$\xi_2 = \frac{\partial\emptyset}{\partial f} = 2q_1 cosh\left(\frac{q_2\sigma_{ii}}{2\sigma_y}\right) - 2q_3 f^* \tag{4.24}$$

$$V_{ik} = \frac{\partial\emptyset}{\partial\sigma_{ik}} = \frac{1}{\sigma_y^2}\left[3\sigma_{ik} - \sigma_{ii}\delta_{ik}\right] + \frac{f^*q_1q_2}{\sigma_y} sinh\left(\frac{q_2\sigma_{ii}}{2\sigma_y}\right)\delta_{ik} \tag{4.25}$$

The components of *h* values are found to be:

$$h_1 = \sqrt{\frac{2}{3}V_{ij}V_{ij}} \tag{4.26}$$

$$h_2 = (1 - f^*)V_{ii} \tag{4.27}$$

The elastic constant matrix is defined as:

$$D_{ik} = \begin{bmatrix} 2\bar{\mu}+\lambda & \lambda & \lambda & 0 & 0 & 0 \\ \lambda & 2\bar{\mu}+\lambda & \lambda & 0 & 0 & 0 \\ \lambda & \lambda & 2\bar{\mu}+\lambda & 0 & 0 & 0 \\ 0 & 0 & 0 & \bar{\mu} & 0 & 0 \\ 0 & 0 & 0 & 0 & \bar{\mu} & 0 \\ 0 & 0 & 0 & 0 & 0 & \bar{\mu} \end{bmatrix} \tag{4.28}$$

The tangent of the flow stress *H* is calculated by

$$H = \frac{\sigma_y - \sigma_y^{old}}{d\varepsilon^p} \tag{4.29}$$

After determination of the value of incremental plastic strain ($d\varepsilon_{ij}^{pl}$), this value is used to update the stress and void volume fraction by updating the equivalent plastic strain

$$d\bar{\varepsilon}_m^p = \frac{\sigma : d\varepsilon_{ij}^p}{(1-f)\sigma_y} \tag{4.30}$$

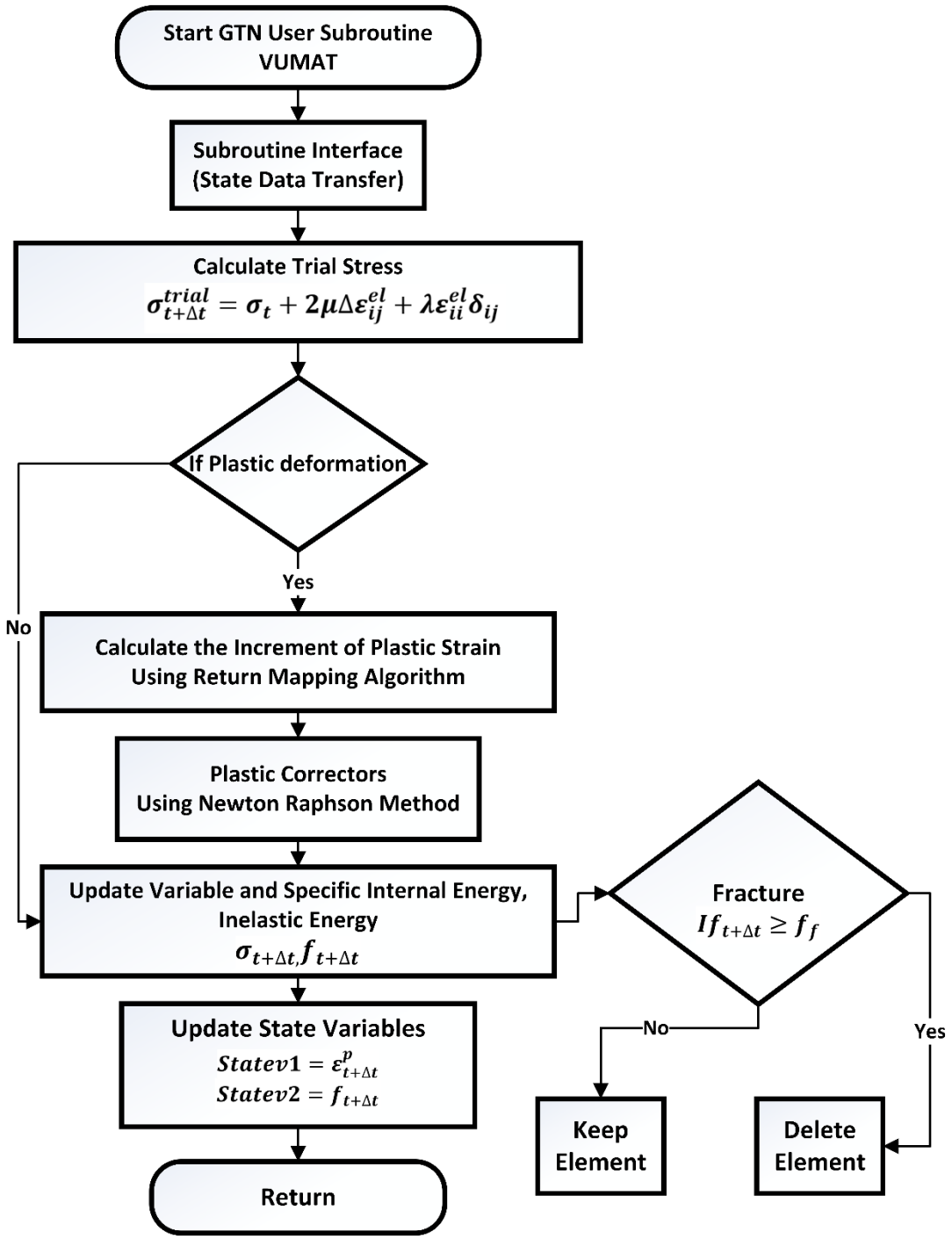


Figure 4.6 VUMAT subroutine flowchart of shear modified GTN model.

4.7 Experimental works

4.7.1 Tensile test

In order to simulate the SPIF process by using FEM, the mechanical properties of the sheet metal should be determined. In this work, an INSTRON testing machine was utilized and the specimen design was in accordance with British standard (BS EN

10002-1). Tensile specimens were obtained by using EDM cutting from 0.7 mm thick grade 1 titanium sheet. The reason for choosing the grade 1 pure titanium in this study is because it is commonly used in sheet forming of cranioplasty implants. The mechanical properties of the pure titanium are given in Table 4-1.

Table 4-1 Mechanical properties of pure titanium.

Yield stress	Ultimate tensile stress	Young's modulus	Poisson's ratio	Density
223.49 MPa	363 MPa	108 GPa	0.34	4505kg/m^3

To measure the displacement on the surface of the specimens during tensile tests, a Dantec Q-400 DIC (digital image correlation) system was used. DIC technique is used to obtain the deformation of a surface by comparison of two digital images of the surface before and after deformation by tracking the displacements of markers on the surface of the specimen. Figure 4.7 shows an example of random placements of markers, called a speckle pattern, which is produced by spraying paint. A CCD camera (Coupled Charge Device) is utilized to capture images during deformation process with light source and computer as shown in Figure 4.8. To determine the displacement after deformation these images are compared by searching for the best correlation between matrixes of pixels of images, which is called a subset. Optimization techniques are employed to find the best match between the subsets before and after deformation by searching the area of same light intensity distribution, assuming the light intensity does not change during deformation.

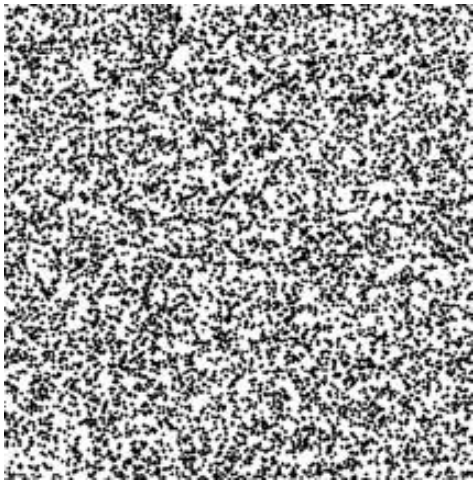


Figure 4.7 Typical example of random pattern on specimen surface.

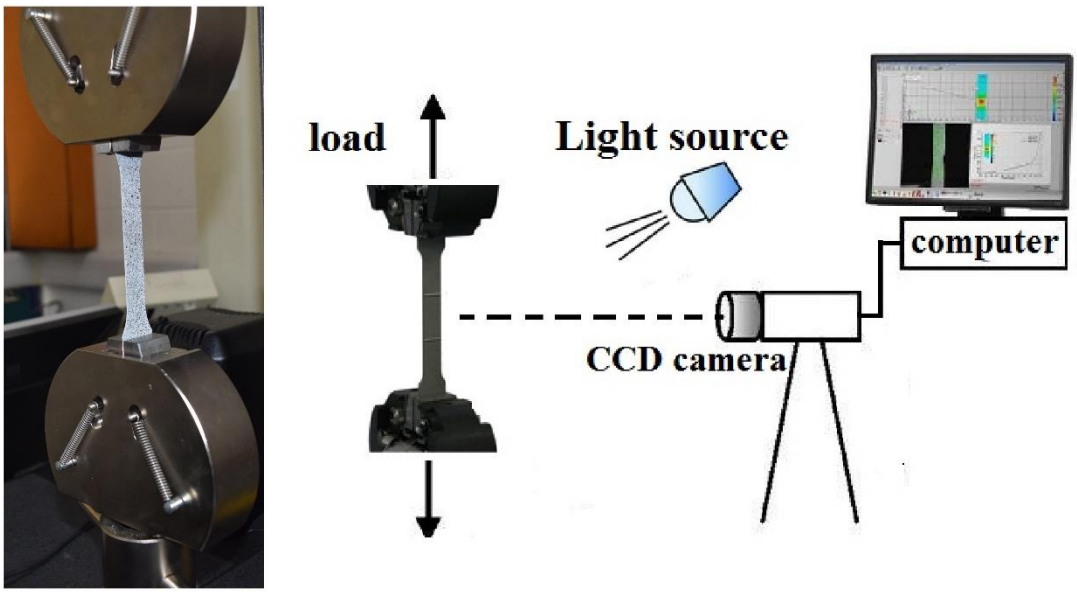


Figure 4.8 Experiment setup of digital image correlation.

4.7.2 Determination of GTN model parameters of Ti grade 1

To determine material parameters of the developed GTN model, a DIC system was used to measure the deformation and to evaluate necking and fracture along the tensile specimen. XL30 scanning electron microscope (SEM) was used to obtain the images of the microstructure and to determine the void volume fraction at different stages throughout the tensile test. To evaluate the heterogeneity of deformation and measure the displacement on the surface of the tensile specimens, several tensile tests were carried out. Figure 4.9 shows the load-displacement curve produced from the tensile test together with measured strain field using the DIC, and the locations to determine the GTN model parameters.

In SEM microscopic evaluation, the first step was to determine the primary void volume fraction by scanning the sheet before plastic deformation. The initial void volume fraction came from original voids, non-metallic inclusions and second-phase particles, as shown in Figure 4.10 (a). These inclusions were randomly distributed in the metal matrix. The initial void volume fraction f = 0.00138 was determined as a mean value of original voids and non-metallic inclusions. When the tensile specimen is subjected to plastic strain under external loading, the nucleation mechanism is started by void formation around the non-metallic inclusions and second-phase particles. It is difficult to predict the load where nucleation begins; therefore, the tensile test was stopped at different stages as shown in Figure 4.11 in order to scan the

sample to determine whether nucleation had started. In this study, nucleation started when the load reached 2.8KN.

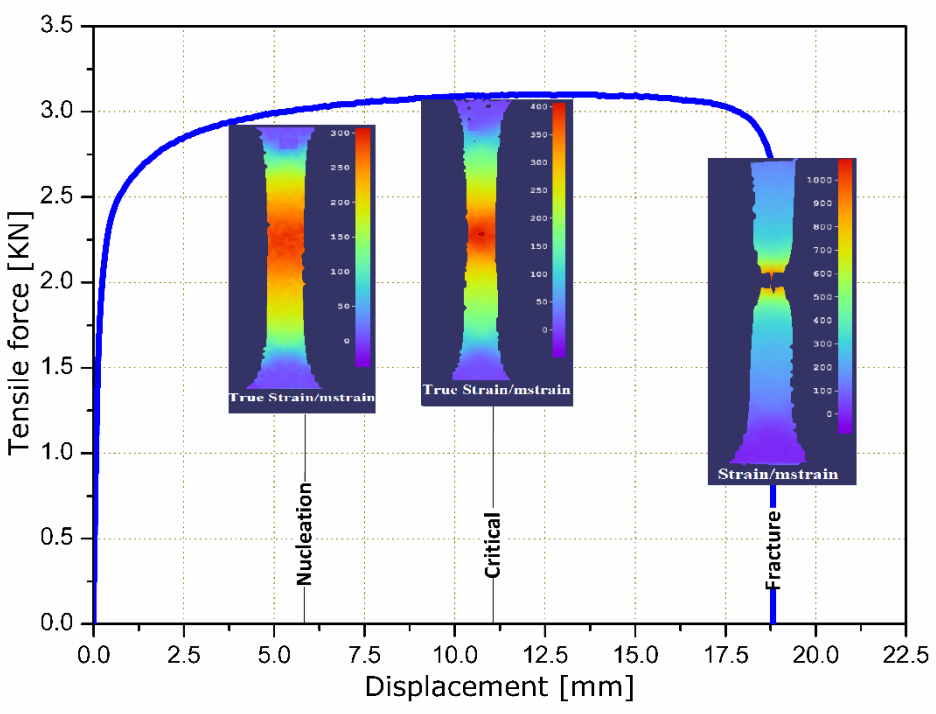


Figure 4.9 Load-displacement curve in tensile test.

Figure 4.10 (b) shows the volume fraction of the nucleated void (f_N=0.017) at a nucleation strain ε_N=0.3 and standard deviation S_N=0.1. When the load increases and reaches the maximum value of 3.04 KN and elongation of 11 mm, significant changes in the dimensions of the tensile specimen can be noticed. Furthermore, the material's load carrying capacity is gradually lost and the void volume fraction reaches the critical value f_c=0.2593 (Figure 4.10 (c)). When the elongation reaches 18.8 mm, the voids become bigger and tearing of the ligaments between enlarged voids causes fracture in the tensile specimen perpendicular to the tensile loading. The void volume fraction at fracture f_f is evaluated as 0.3025, as shown in Figure 4.10 (d). The damage parameters of grade 1 pure titanium are summarised in Table 4-2.

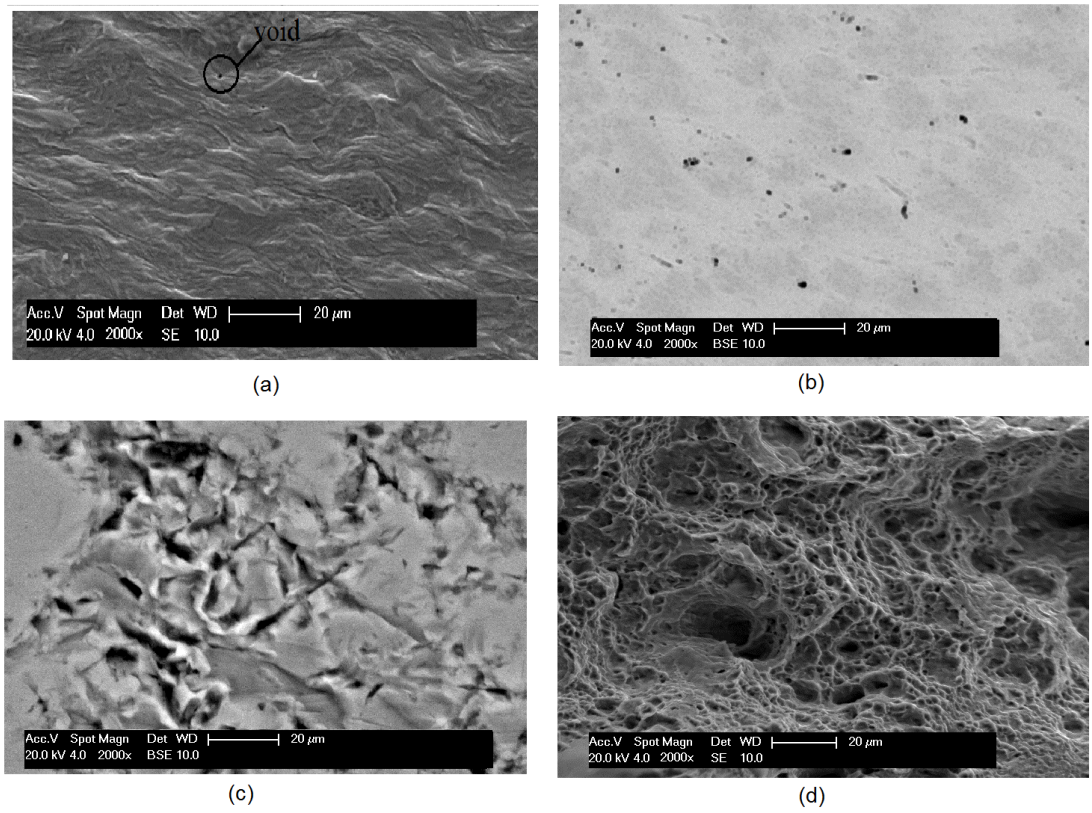


Figure 4.10 Microstructure of pure titanium at different stages throughout the tensile test: (a) before deformation (initial state), (b) at void nucleation state, (c) at critical stage and (d) fracture surface.



Figure 4.11 Tensile specimen under different displacements to determine the VVF at nucleation.

Table 4-2 Damage parameters of pure titanium.

f_o	q_1	q_2	f_N	ε_N	S_N	f_c	f_f
0.00138	1.5	1	0.017	0.3	0.1	0.2593	0.3025

4.7.3 Single point incremental forming test

As shown in Figure 4.12, SPIF tests for a truncated hyperbolic conical shape and a pyramidal geometry with varying forming angles were also carried out to evaluate the fracture mechanism of both shapes under ISF deformation conditions. These tests were carried out with an incremental depth equal to 0.2 mm per revolution and tool diameter of 10 mm. The tool is rotation free with a feed rate of 1000 mm/min for both the truncated cone and truncated pyramid.

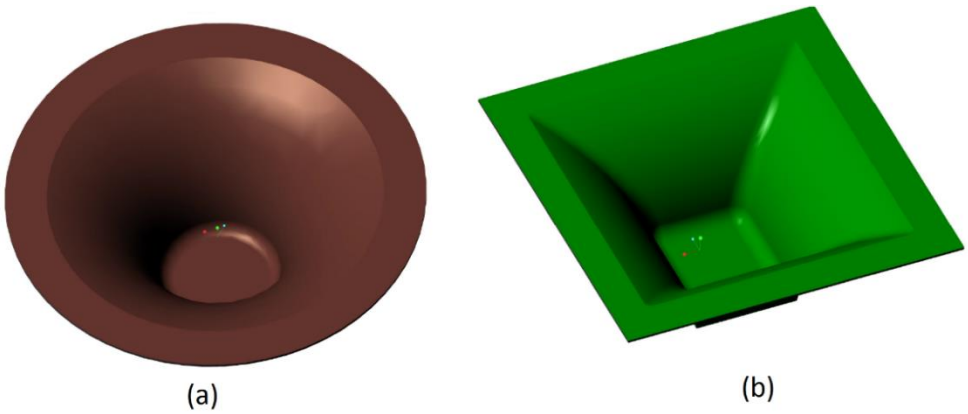


Figure 4.12 Geometries obtained by using SPIF: (a) cone; (b) pyramid.

A HURCO CNC milling machine (VM10) was employed to carry out the SPIF tests at ambient temperature for a hyperbolic truncated cone and hyperbolic pyramid shape. The sheet was fastened using a special fixture assembled on the CNC milling machine. The setup of SPIF process and formed parts are shown in Figure 4.13. A hemispherical tool is utilised for performing the SPIF test. The forming tool was set not to rotate in this work for all the SPIF tests. In the experimental test of ISF, a lubricating grease (Rocol RTD compound) was applied to the interface between the forming tool and sheet in order to reduce friction. The CNC milling machine was stopped manually after the occurrence of fracture and the depth up to the fracture is measured utilising digital height gage (see Figure 4.14), and this depth was unitized to determine the corresponding wall angle (maximum wall angle) of SPIF parts at fracture. The maximum wall angle is determined based on the slope of fracture point by comparing the slop of fracture point with the typical profile of the deformed part.

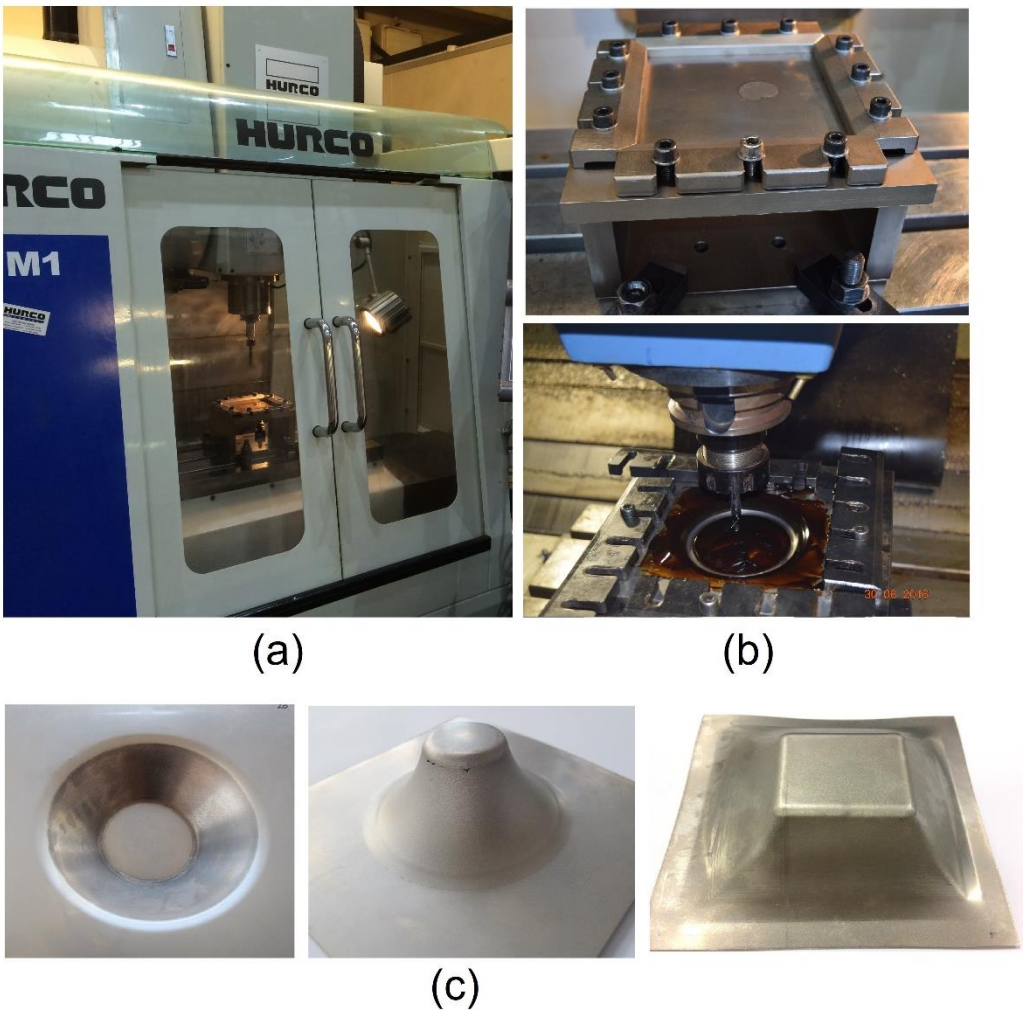


Figure 4.13 SPIF experiments and formed titanium parts: (a) CNC milling machine, (b) the fixture used to fix the sheet and (c) parts produced by SPIF process.

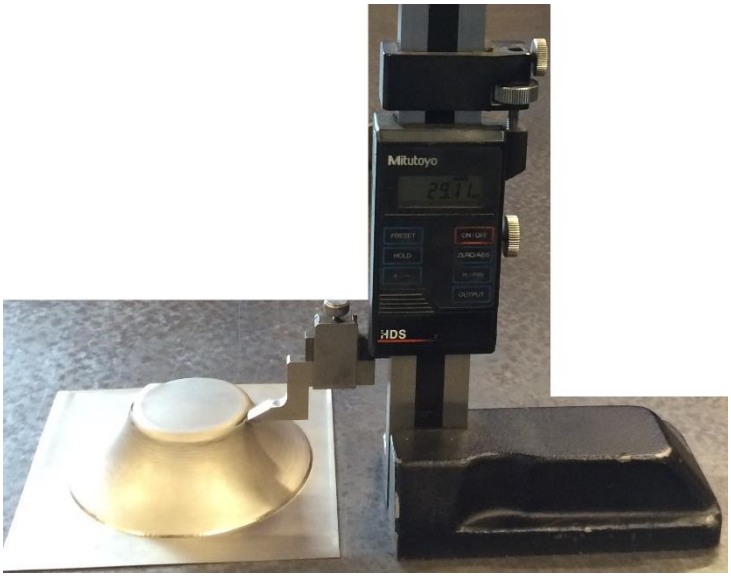


Figure 4.14 Measuring fracture depth by digital height gage.

4.8 Validation of the modified GTN model

4.8.1 Benchmark tests on single element

Two 3D models were used to validate the shear modified GTN model implanted in the VUMAT user subroutine. Firstly, a hydrostatic tensile stress state (Figure 4.15(a)) is utilized to verify the equivalence between the original Gurson model (the porous metal plasticity model in Abaqus constitutive model libraries Mises-GTN/Explicit) and the shear modified GTN model. Under this loading condition, the Abaqus and VUMAT results should be the same. Secondly, a pure shear stress loading condition (Figure 4.15(b)) is used to explain the difference between the original Gurson model (Abaqus) and the developed modified GTN model. The shear model was compared with the analytical model to illustrate the relevance of the results.

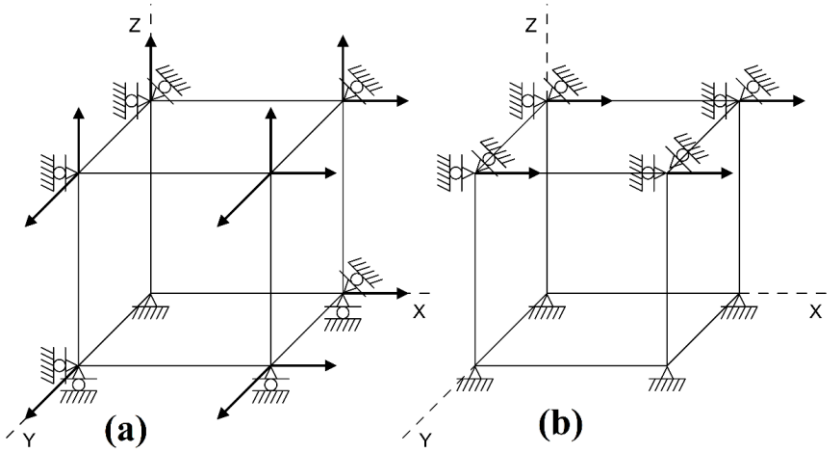


Figure 4.15 Boundary conditions for: (a) hydrostatic tension, (b) shear stress.

4.8.1.1 Hydrostatic tension

A single cube-shaped element of pure titanium with initial dimensions of 0.5 mm was used to do the validation. The mechanical properties and damage parameters of modified GTN model of pure titanium are reported in Table 4-1 and Table 4-2 respectively. A 3D hexahedral element with 8 nodes and reduced integration (C3D8R) was used to validate the hydrostatic tension test. The same input parameters were employed in both models from the standard Abaqus GTN function and the shear modified GTN model implemented by VUMAT user subroutine.

Figure 4.16 shows the void volume fraction and axial stress as a function of axial strain; the results show a perfect agreement between the Abaqus based Gurson model

and the modified GTN model with the consideration of shear using VUMAT subroutine.

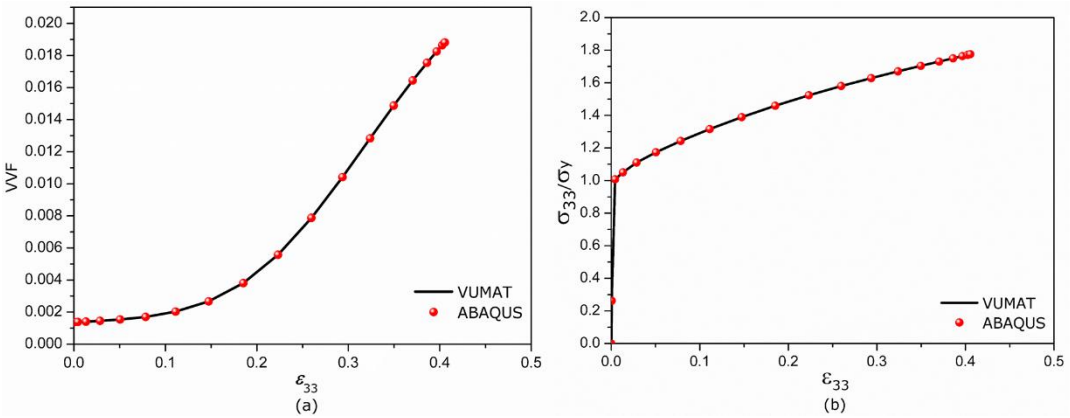


Figure 4.16 Results of the simulation of a hydrostatic tensile test as a function of axial strain: (a) void volume fraction (b) axial stress.

4.8.1.2 Pure shear stress

An identical cube as in the previous section was subjected to a shear force on the upper surface in the X-direction (Figure 4.15 (b)), and the same material properties were employed to those in the hydrostatic tension test. An analytical model was used to illustrate the relevance of the results. However, to simplify the analytical model, the increase in the void volume fraction due to nucleation was neglected; furthermore, the material failure based on void growth was not taken into account ($f^*=f$).

In pure shear loading, the equivalent plastic strain and equivalent plastic strain rate are defined by equations (4.31) and (4.32), respectively [147].

$$\varepsilon^p = \frac{2}{\sqrt{3}}\varepsilon_{12}^p \tag{4.31}$$

$$\dot{\varepsilon}^p = \frac{2}{\sqrt{3}}\dot{\varepsilon}_{12}^p \tag{4.32}$$

The void volume fraction evolution is expressed as a function of equivalent strain.

$$f^* = f = k_w f \varepsilon^p \qquad \text{For} \quad f<f_c \tag{4.33}$$

By integrating Eq. (4.33) the expression of void volume fraction becomes

$$f = f_o e^{k_w \varepsilon^p} \tag{4.34}$$

With q_1, q_2, and q_3 equal to 1, the yield function Eq. (4.4) is reduced to

$$\sigma_q = (1-f)\sigma_y \tag{4.35}$$

Substituting the strain hardening law (Ludwik law $\sigma_y = \sigma_{yo} + k\varepsilon^{p^n}$) into the yield function Eq. (4.35) and dividing the Ludwik function by σ_y, the ratio of $^{\sigma_q}/_{\sigma_y}$ as a function of equivalent strain is obtained as

$$\frac{\sigma_q}{\sigma_y} = (1 - f_o e^{k_w \varepsilon^p}(1 + \frac{k}{\sigma_y}(\varepsilon^p)^n) \tag{4.36}$$

Figure 4.17 illustrates the void volume fraction and equivalent stress as a function of equivalent plastic strain. It is clear from the figure that there is a perfect agreement between the results from the analytical prediction and the modified GTN model with consideration of shear.

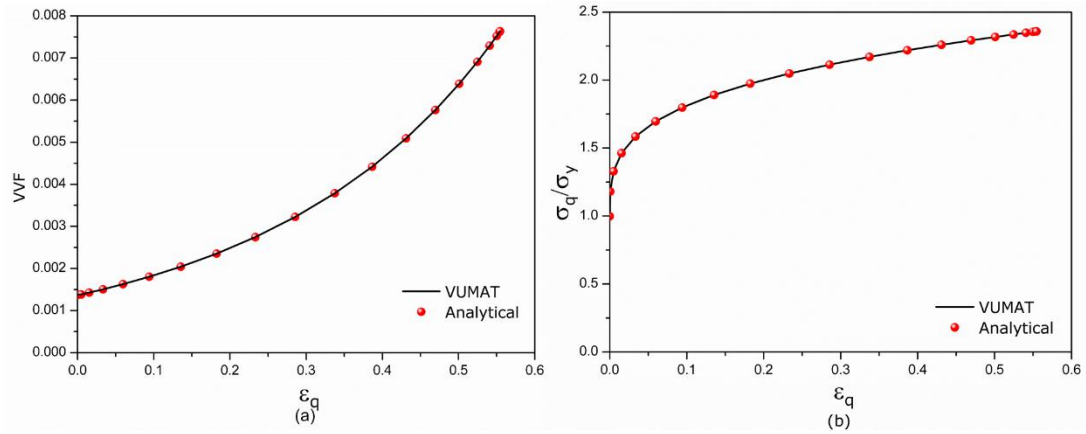


Figure 4.17 Results for shear stress simulations as a function of the equivalent strain: (a) the void volume fraction and (b) the effective stress.

4.8.2 Influence of meshing density

Meshing density has a significant effect on predicting accurate results. A common approach is to use refined mesh with small element size in FE simulation. However, using a very small element size means that the computational time could be increased quadratically due to the increase of the total number of degrees of freedom. In FEM simulation, failure prediction using the Gurson model is significantly influenced by mesh size as this model causes strain softening prior to fracture [107]. Small element size is required to capture correct deformation pattern and the real shape of fracture e.g. cup-cone failure mode [110, 148]. Soyarslan et al. [149] noted the localization band and fracture behaviour are highly dependent on mesh refinement when GTN model is used to predict the fracture with the consideration of the softening material response.

In order to select the optimum mesh size to accurately predict the fracture with modified GTN model simulation of sheet metal, six element lengths (1.2, 1, 0.8, 0.7, 0.5 and 0.25mm) were chosen to simulate the tensile test case as summarised in Section 4.7.1. The total number of elements for each mesh refinement is, as a consequence, 6923, 8594, 11288, 13721, 24668 and 83723, respectively. Element deletion technique was used to model the fracture in the sheet. A 3D hexahedral element with 8 nodes and reduced integration (C3D8R) was used to predict the fracture in the sheet with GTN model.

In this work, equivalent plastic strain distribution and force–displacement curve are used to evaluate the effect of element size. Figure 4.18 shows the equivalent plastic strain history in the fracture zone with different mesh sizes. It is noted from the figure that with a smaller element size the increment in equivalent plastic strain can be captured earlier than with larger element sizes. This is particularly true, when reduced integration element was chosen in FE simulation as only one integration point was used to sample strain and stress results of an element. However, as the element size is sufficiently small, FE simulation would converge to the same strain result as in the case of 0.25 mm and 0.5 mm mesh size in this study as shown in Figure 4.18 and Figure 4.19.

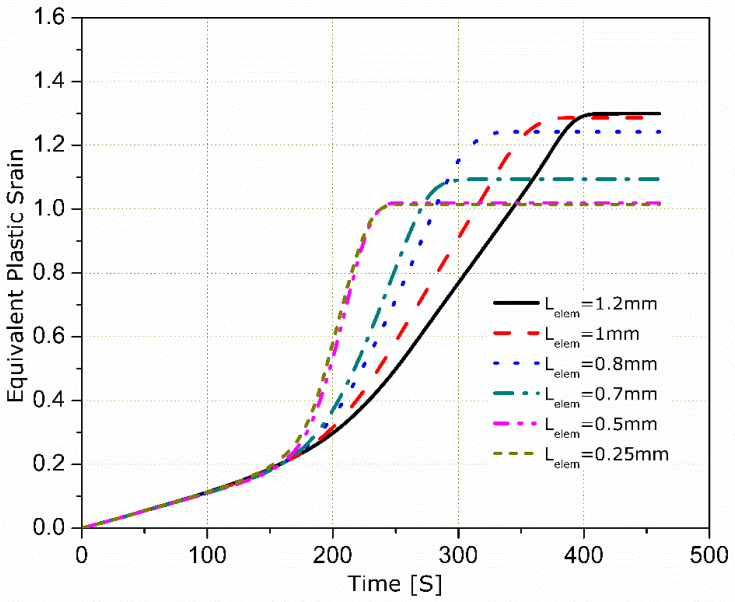


Figure 4.18 Comparison of equivalent plastic strain for different mesh sizes.

Figure 4.19 shows the load-displacement curves of FE results as compared to experimental testing to help choose a suitable mesh size for FE simulation of the

studied SPIF processes using the modified GTN model. Fracture may be captured experimentally and numerically from force-displacement curve when necking occurs as the force reached its maximum and starts to drop. It is observed from the figure that the loss of load carrying capacity occurs in the model with sufficiently small element size first. This is because the FE model with smaller element size is able to more accurately predict the strain values and the void volume fraction (VVF) using the modified GTN models and hence the drop of load carrying capacity and the fracture of the specimen under tensile loading condition. A good correlation between the experimental and FE simulation load-displacement curves is observed for both 0.25 and 0.5 mm element sizes. Therefore, an element size of 0.5 mm was chosen in this investigation.

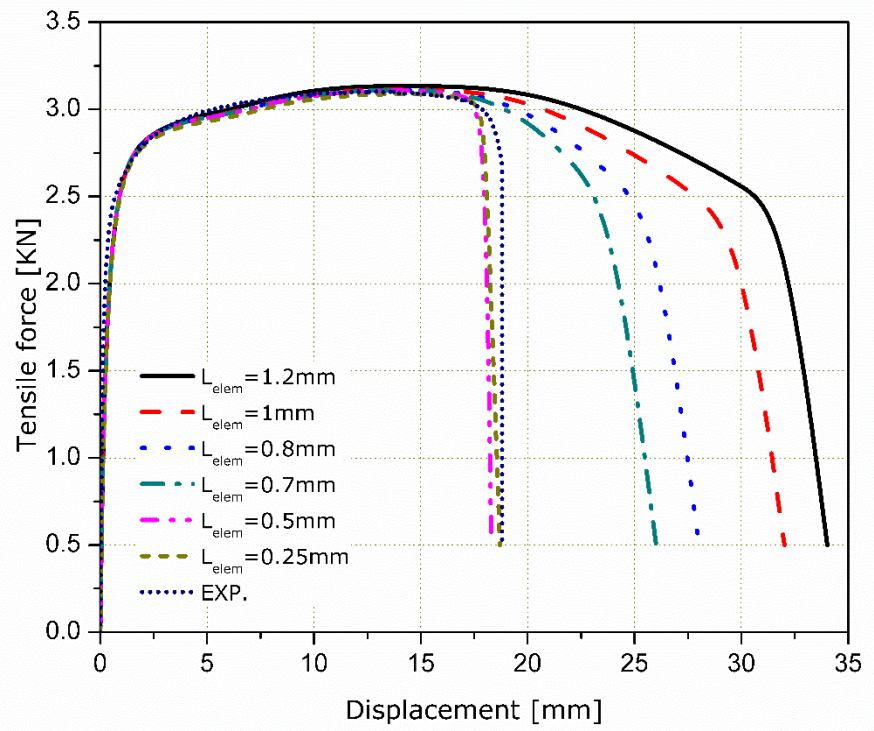


Figure 4.19 Load-displacement curves for different mesh sizes and comparison with experimental data.

4.8.3 Validation of the modified GTN model under tensile and shear conditions

Two experimental tests were conducted with DIC to validate the modified GTN model by comparing predicted fracture results with and without consideration of shear. As shown in Figure 4.20, under tensile condition, the load and displacement results

showed no effect of shear when comparing the experimental results with GTN models with and without the effect of shear.

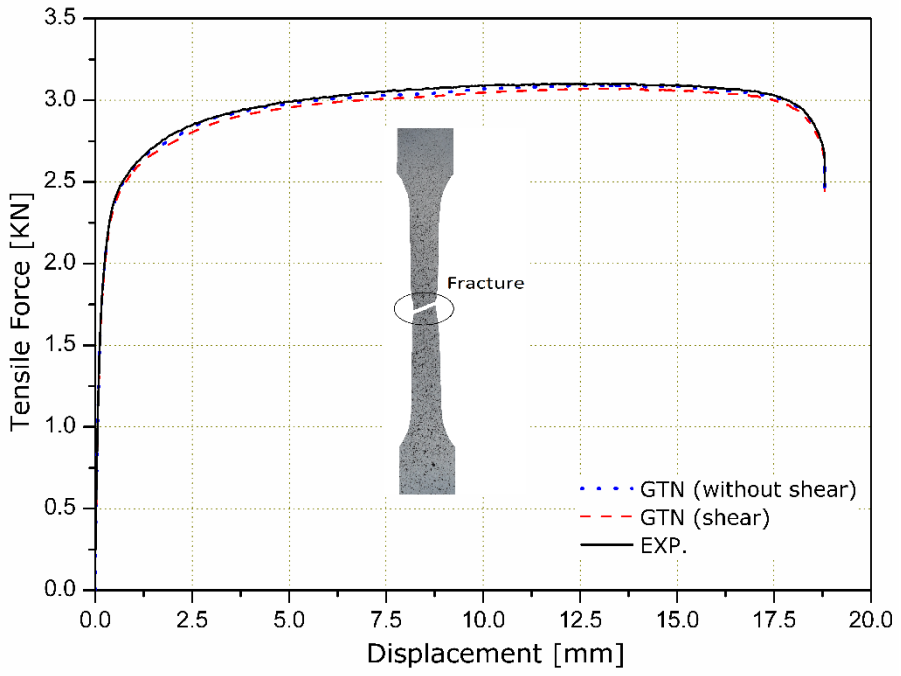


Figure 4.20 Comparison of force-displacement curves of experimental tensile test with the GTN models, with and without shear.

Shear tests were also employed to validate the modified GTN model with the shear effect to predict the fracture in the case under shear loading. Various shear sample geometries were suggested in the literature to enhance the knowledge of the material behaviour under shear, e.g. shear sample proposed by Miyauchi [150], standard shear sample (ASTM B831) and twin bridge shear sample [151]. In this study the shear sample was designed according to ASTM B831 and performed on an INSTRON testing machine. However, through the shear tests buckling occurred in the shear zone due to the small thickness of the sample (0.7 mm) suggesting that the pure titanium with this thickness cannot resist buckling. Therefore, a modified ASTM sample [23] was used in this study as shown in Figure 4.21. The modified ASTM sample was used to reduce the tendency of buckling caused by additional moments in the shear zone. In pure shear test, the value of hydrostatic pressure is very small or zero compared to the equivalent stress at fracture zone [152]. As shown in Figure 4.22, the simulated fracture is a direct result of shear as the fracture line is parallel to the tensile loading. To further illustrate the suitability of the modified ASTM sample in shear testing, the

stress triaxiality of the shear sample was less than 5% at the fracture location as compared to a value of 0.35 for standard tensile condition as shown in Figure 4.23.

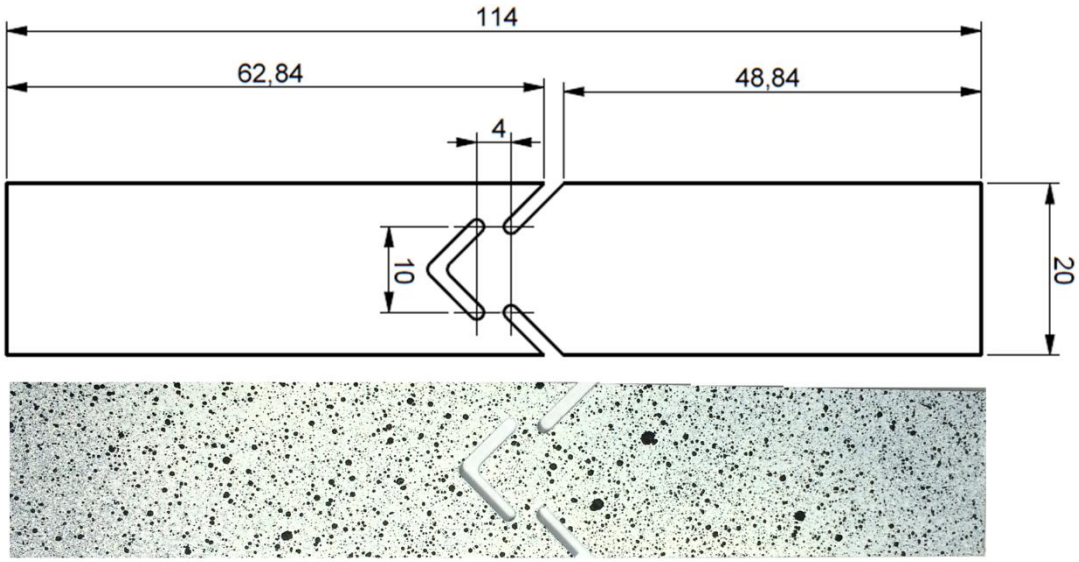


Figure 4.21 Specimen geometry for the modified ASTM shear test.

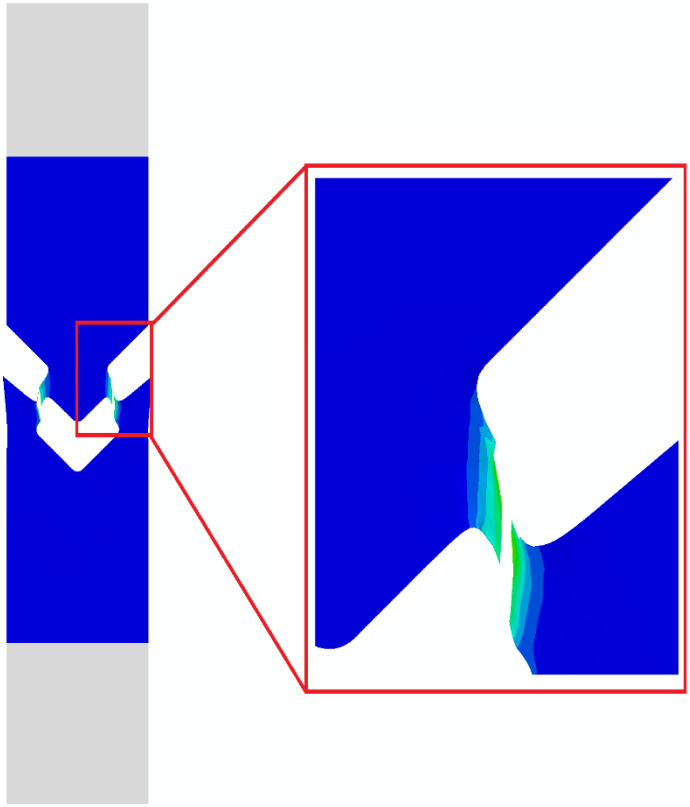


Figure 4.22 Fracture shape in pure shear test (equivalents strain distribution).

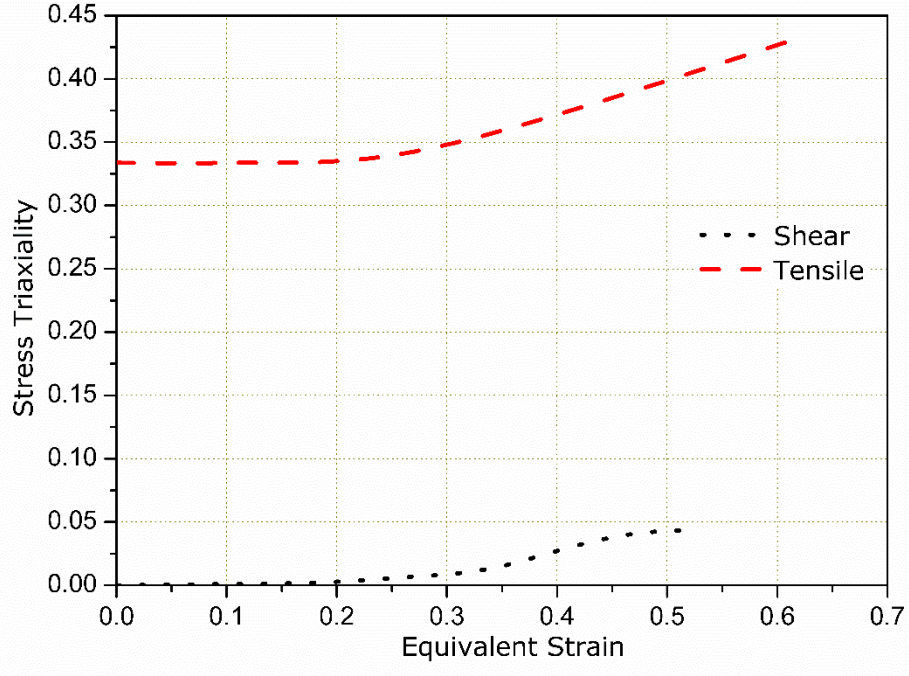


Figure 4.23 Evolution of stress triaxiality for the shear and tensile test.

In this investigation, fracture is established from a force-displacement curve, where necking is considered to occur as the force reaches its maximum value and starts to drop. Figure 4.24 shows the comparison between experimental and simulation results. Same displacement (5.3mm) was applied in both the FE model and the experiment. It is noted from the figure that fracture occurs at 3.9 mm using the modified GTN model with shear effect and at 4.1 mm in the experiment but no fracture occurs towards the end of elongation when the GTN model without shear is used. Although the shear modified GTN model predicts an earlier fracture by a small margin as compared to experiment, this result clearly indicates that the developed GTN model with shear is more capable to predict fracture under shear loading conditions.

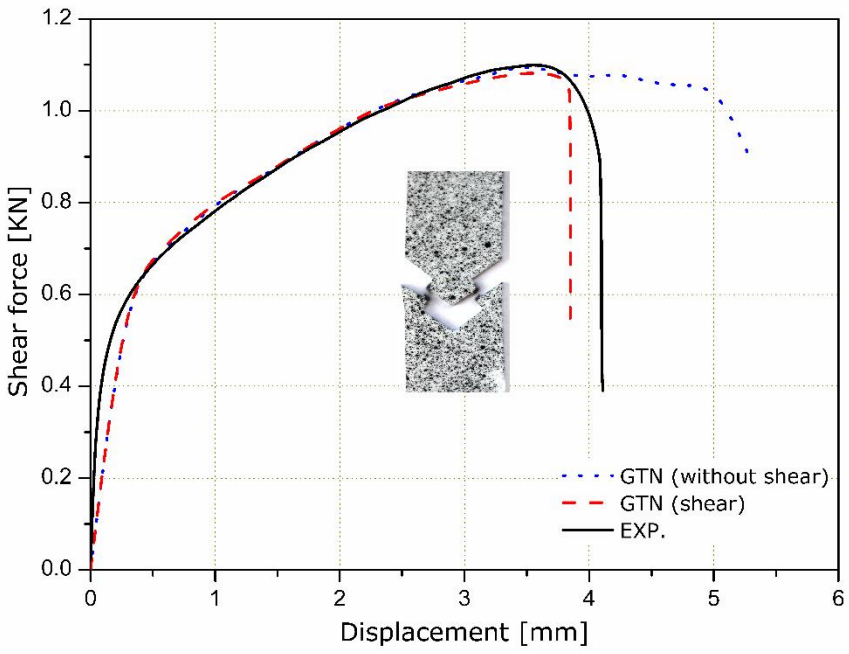


Figure 4.24 Comparison of force-displacement curves of experimental shear test with GTN models, with and without shear.

4.9 SPIF of hyperbolic cone and pyramidal shapes

SPIF tests for a truncated hyperbolic conical shape and a pyramidal geometry with varying forming angles were also carried out to evaluate the fracture mechanism of both shapes under ISF deformation conditions. These tests were carried out with an incremental depth equal to 0.2 mm per revolution and tool diameter of 10 mm. The tool is rotation free with a feed rate of 1000 mm/min for both the truncated hyperbolic cone and truncated pyramid. A hyperbolic profile was selected to test the fracture in SPIF; this part was designed with varying wall angles from 22^{o} to 80^{o}, as shown in Figure 4.25.

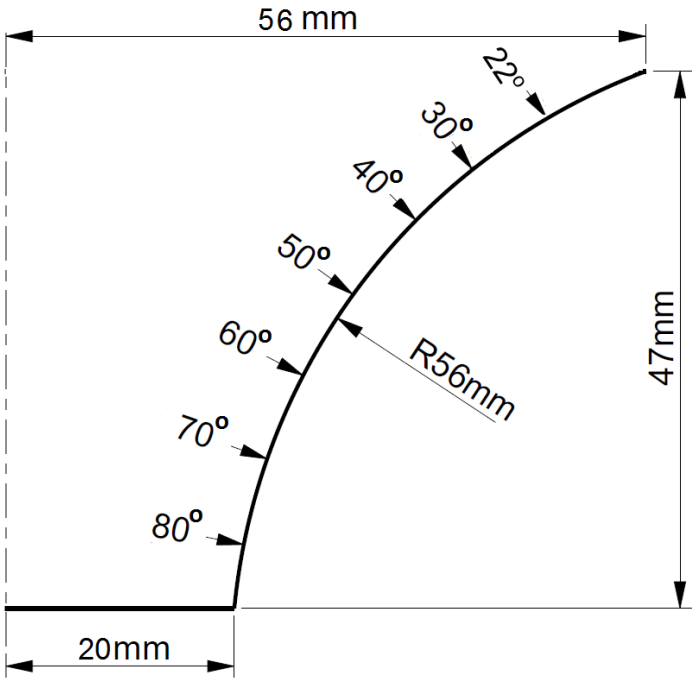


Figure 4.25 Geometric shape of hyperbolic profile.

The explicit algorithm in Abaqus with the shear modified GTN model implemented through VUMAT was employed to simulate SPIF of a pure titanium sheet with dimensions 140 x140 x0.7 mm. In the simulation of the SPIF process, the tool, backing plate and the blankholder were modelled as analytical rigid surfaces. The blank was modelled as a deformable body with an eight node brick element (C3D8R). Displacement vs time was used to define the tool path in SPIF.

Since the shear modified GTN model was used to predict the fracture occurrence in the FE simulation, it is important to investigate the distribution of VVF on the part during deformation. Figure 4.26 shows the distribution of VVF obtained by FE simulation along the achievable depth. It is noted from the figure that the value of initial VVF before deformation was 0.00138 (Figure 4.26 (a)) and it is increased when the tool moves down along the defined tool path. The highest values of VVF are always in the transition area between contact and noncontact zones on the outer surface. It can be concluded that the voids are nucleated only in the tension state. Moreover, in the transition area, maximum thinning occurs which leads to increased VVF due to an increase in stretching by meridional stress. In the FE simulation, the distribution of VVF is almost uniform in the early stages of the SPIF process but it tends to localize during the process. The VVF accumulation leads to sudden fracture in the part when its value reaches 0.3025, as shown in Figure 4.26 (e and f).

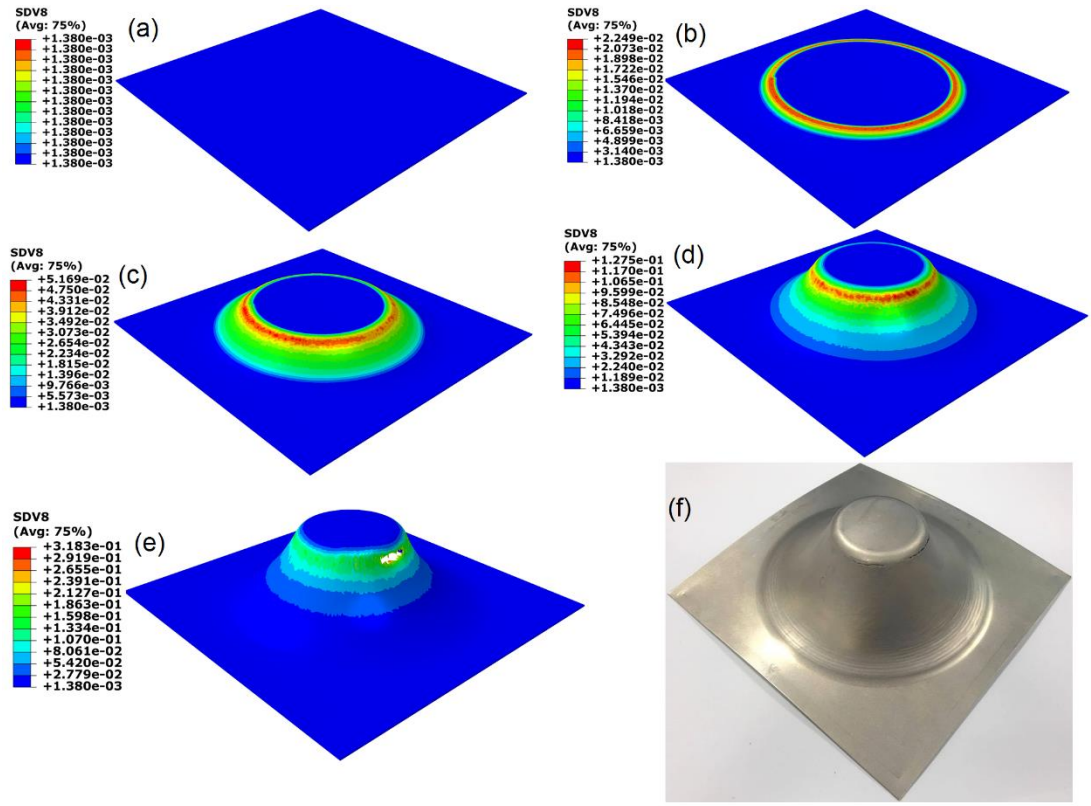


Figure 4.26 Distribution of the void volume fraction (SDV8) obtained by numerical simulation of a SPIF process with different depths.

In order to evaluate the void volume fraction and major strain in the sheet after fracture, five neighbouring elements were selected, one of which was in the fracture (unsafe zone) and others on one side of the fracture (safe zone) as shown in Figure 4.27. Figure 4.28 compares the evolution of the VVF at the defined locations. As can be seen in the figure, in the early deformation stages, the VVF grows uniformly until 118s when these curves begin to separate from each other and increase rapidly over a short period. This means that the VVF starts to grow when the stretching in the wall increases and reaches a certain value. However, the value of the VVF in element A is equal to or more than the final value of the VVF (0.3025), which is determined experimentally by SEM, so this element is deleted from the FE model, as shown in Figure 4.27. Element B is located in the critical zone with a VVF value of 0.22, which is close to the critical experimental value (0.2593). The other elements (C, D and E) remain in the safe zone and their VVF values are well below the critical value.

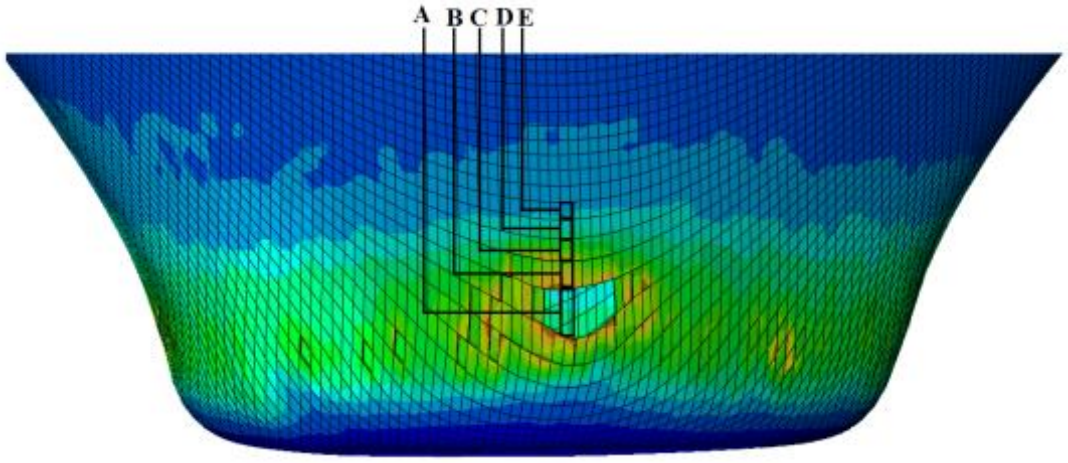


Figure 4.27 Location of selected elements on the FE model.

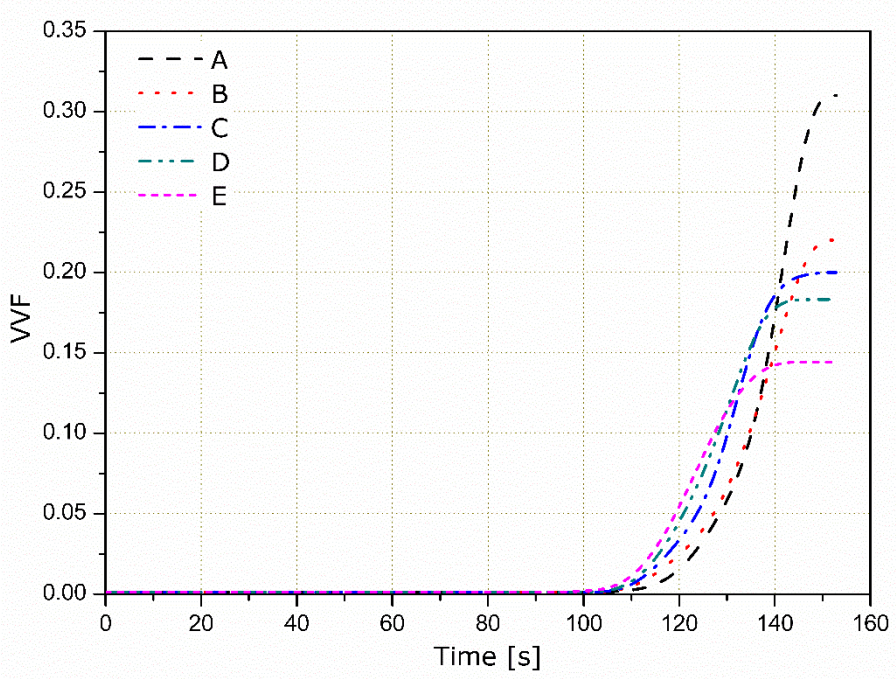


Figure 4.28 Evolution of void volume fraction during the SPIF process.

The major strain may be used as a criterion to detect the onset of fracture in the sheet metal forming process. Figure 4.29 shows the increase of major strain with the time of the same elements used to evaluate the VVF. It is evident from the figure that the distribution of major strain shows the same trend as the VVF distribution.

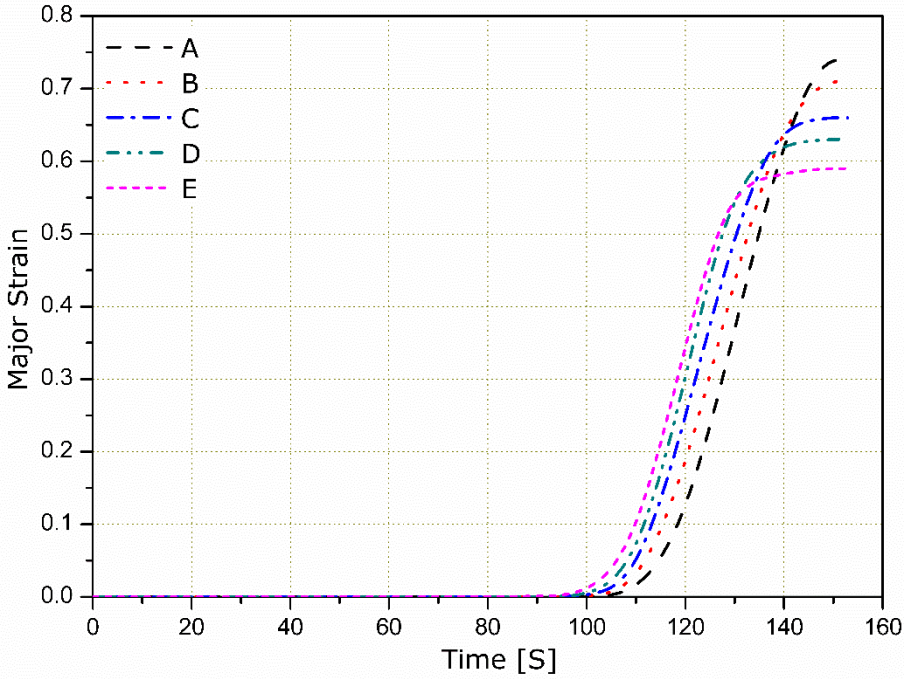


Figure 4.29 Evolution of major strain during the SPIF process.

Nahshon-Hutchinson's shear mechanism is used in the present work to study the effect of shear on the fracture in SPIF. Two jobs were run with one using the original Gurson model (porous metal plasticity model Mises-GTN/Explicit) and the other using the shear modified GTN model via the VUMAT subroutine. Figure 4.30 represents a comparative illustration of the effect of the shear mechanism on the VVF growth during SPIF. It is evident from the figure that the VVF reaches the fracture value earlier by using the modified GTN model with shear than that without the consideration of shear, which indicates that the shear mechanism accelerates fracture occurrence in SPIF.

To validate the results obtained from the original GTN model and modified GTN-model with the consideration of shear, the FE results were compared with experimental work, as shown in Figure 4.31. To ensure the repeatability of the results, experimental test of the SPIF process was repeated three times and the average value is taken. The SPIF simulated results were consistent with experiments suggesting that the modified GTN model is capable of capturing the fracture in SPIF.

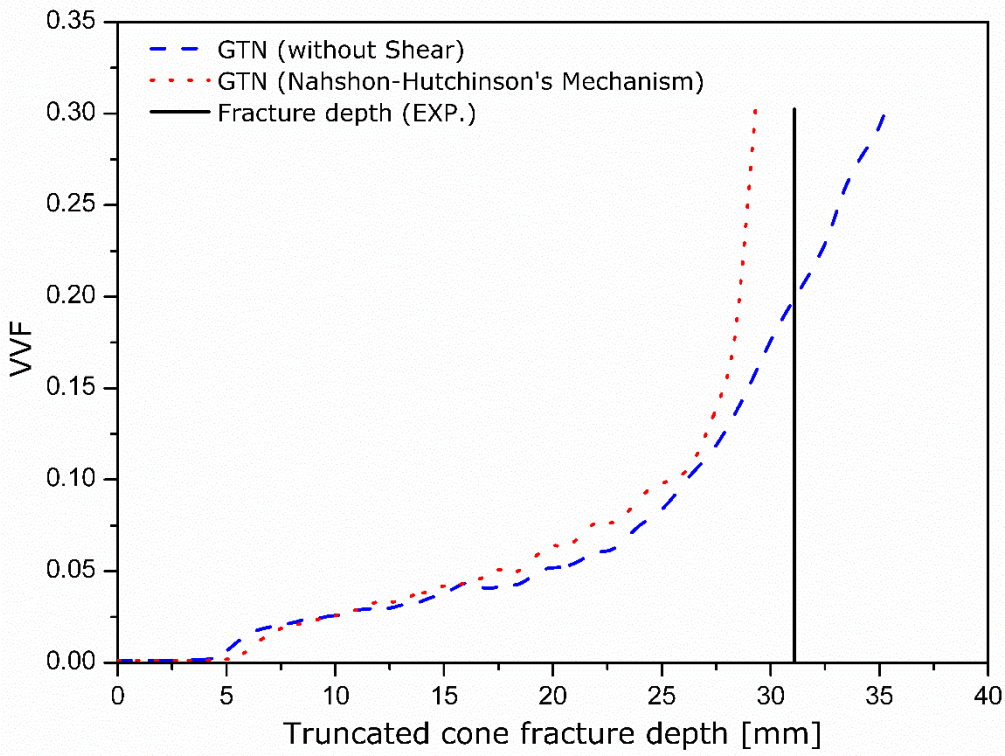


Figure 4.30 VVF reuslts for forming a hyperbolic shape using GTN models with and without shear.

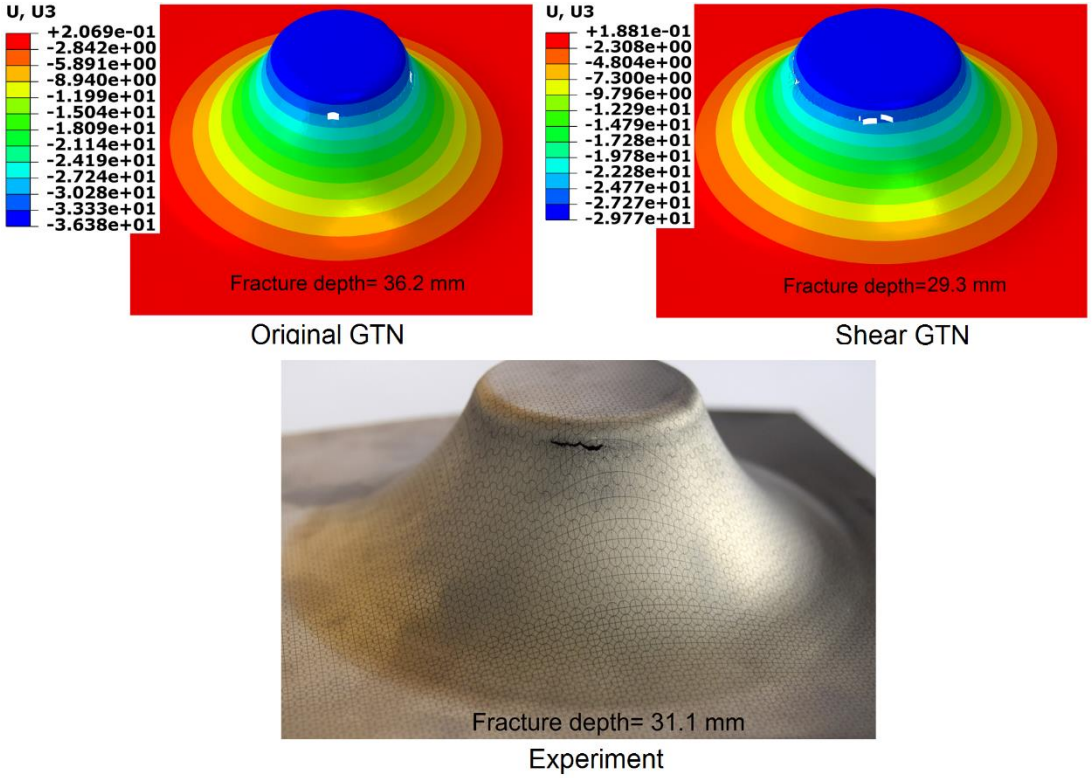


Figure 4.31 Simulated results obtained from the original and shear modified GTN model in comparison with the actual forming experiment of the hyperbolic shape.

For the case of the pyramidal shape, the same GTN model parameters and SPIF procedure were used as for the hyperbolic shape. The reason of making two different shapes is to study the ability of the modified GTN model to predict fracture at different strain states from two different shapes. In particular, with the hyperbolic shape the plane strain stretching is created but with the pyramidal shape both plane strain stretching and biaxial strain stretching are present. Figure 4.32 shows the predicted VVF values for both GTN models. It is clear from the figure that the fracture occurs earlier with the consideration of shear and it is closer to experimental result. It can be concluded that the shear clearly plays a role in the stretching along the meridional direction to develop the fracture in SPIF.

As shown in Figure 4.33, the fracture occurred at the corner area of a depth of 28.64 mm, 25.5 mm and 26.7 for the original GTN model, the GTN model with shear and the experimental testing, respectively. The FE simulation of shear modified GTN model was in a good agreement with experiments. The fracture is developed at corner area due to biaxial stretching deformation at the corner as compared to a plane strain stretching along the straight side.

From SPIF tests of both shapes, the hyperbolic shape can achieve a higher forming angle than the pyramidal shape. The maximum wall angle of the truncated cone hyperbolic shape at fracture was 68.4^{o} and the pyramidal shape achieved a maximum wall angle of 61.2^{o}. This suggests that fracture in SPIF is also dependent upon the stress states.

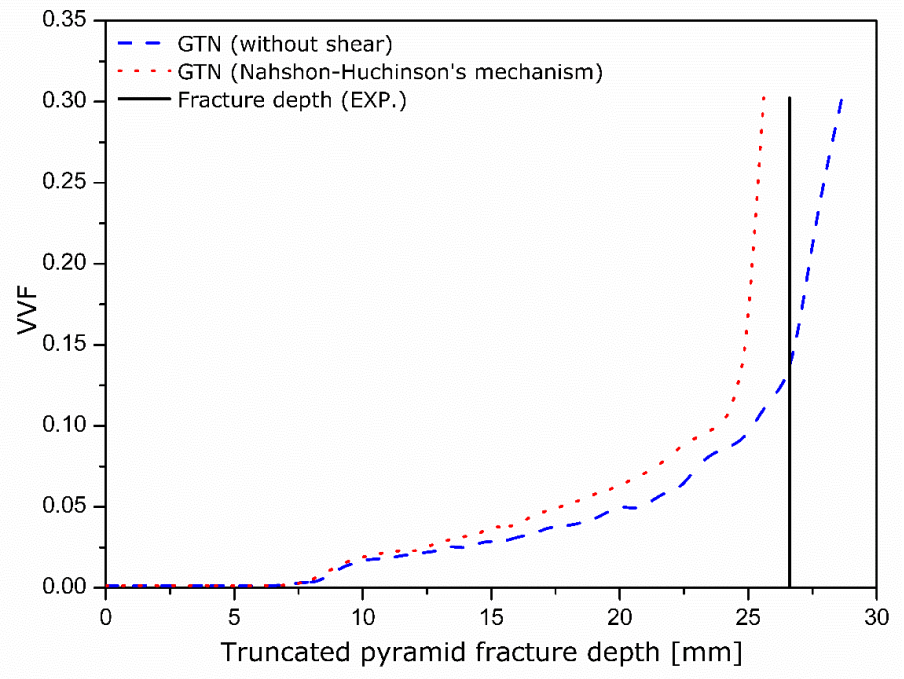


Figure 4.32 VVF results for forming a truncated pyramid using GTN models with and without shear.

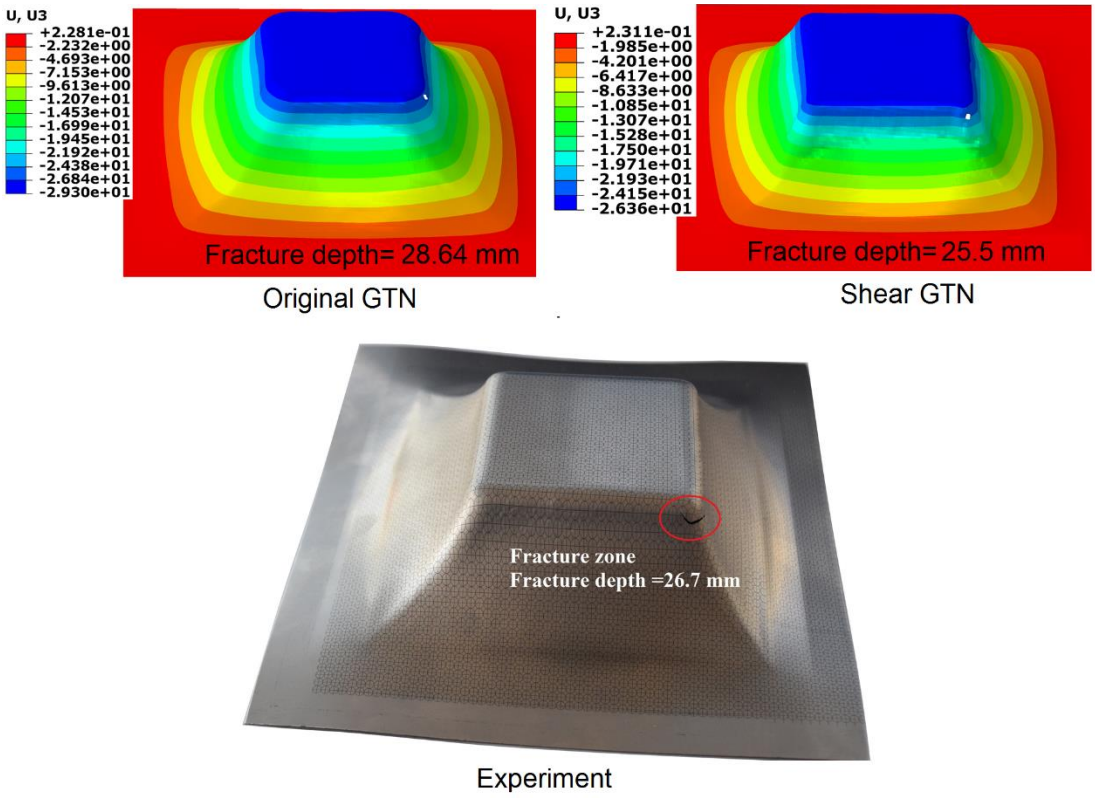


Figure 4.33 Simulated results obtained from the original and shear modified GTN model in comparison with the actual forming experiment of the truncated pyramid.

4.10 Conclusions

In the original GTN model the increment of void volume fraction is measured based on the nucleation and growth of voids. In this study, a Nahshon-Hutchinson type shear mechanism was incorporated in the GTN model to take into account of the effect of shear on the evolution of void volume fraction. The modified GTN model was implemented via Abaqus/Explicit to study the effect of shear on the fracture occurrence in ISF. The FE results obtained from the GTN based models were validated by ISF experimental results.

The damage parameters of GTN model were determined by using a DIC system to evaluate the necking and instability along the tensile specimen and SEM to scan the affected zone of the tensile specimen and ImageJ software to analyse the images of SEM and to determine the parameters of the modified GTN model. Based on the results obtained, the DIC and SEM are considered an effective means to derive the modified GTN model parameters.

Two experimental tests (tensile and shear test) were conducted to determine the ability of the shear modified GTN model to predict the damage under shear loading. The results showed that the modified GTN model (VUMAT) with shear improved the modelling accuracy of fracture over the original GTN model under shear loading conditions.

In comparison with experimental testing, shear modified GTN damage model showed a good agreement regarding the occurrence of ISF fracture for both shapes (truncated hyperbolic cone shape and a truncated hyperbolic pyramid). The results also show that shear plays a role under meridional tensile stress to accelerate fracture propagation in ISF processes.

CHAPTER 5

FORMABILITY IN IN CREMENTAL SHEET FORMING

5.1 Introduction

A forming limit diagram (FLD) is commonly used as a useful means for characterizing the formability of material in sheet metal forming processes. In this chapter, the Nakajima test is used to construct the forming limit curve at necking (FLCN) and fracture (FLCF). The results of the FLCF are compared with incremental sheet forming to evaluate the suitability of the Nakajima test to predict the fracture in ISF. Tests were carried out to construct the FLD at necking and fracture to cover the strain states from uniaxial tension to equi-biaxial tension with different stress triaxialities - from 0.33 for uniaxial tension to 0.67 for equi-biaxial tension. Due to the fact that the Gurson–Tvergaard-Needleman (GTN) model can be used to capture fracture occurrence at high stress triaxiality, and the shear modified GTN model (Nahshon-Hutchinson's shear mechanism) was developed to predict the fracture at zero or even negative stress triaxiality, the original GTN model and shear modified GTN model may be not suitable to predict the fracture in all samples of the Nakajima test as some samples are deformed under moderate stress triaxiality. In this study, the fracture limits are compared using the original GTN model, shear modified GTN model and Nielsen-Tvergaard model with to the consideration of stress triaxiality. To validate the ability of these models, and to assess which model is more accurate in predicting the fracture with different stress triaxialities, finite element simulations of the Nakajima test were compared with experimental results and recommendations drawn on the applicability of the Nakajima test to characterise the fracture during ISF.

The FLD for SPIF is usually employed to determine the limits of proportional straining before failure and is quite different from the corresponding diagram for traditional sheet forming such as deep drawing or hydroforming. The experimental results showed that the distribution of the sheet thickness is uniform in the cross-section of the parts produced by ISF up to the fracture, without necking before the fracture. Based on these

results, the FLCN for traditional sheet metal forming is not suitable for ISF. Consequently, the FLCF is utilized to predict the fracture during the ISF process [37]. The shape of the FLCF is a straight line with a negative slope for most materials and it is located in the first quadrant of the forming limit diagram. Figure 5.1 illustrates the typical modes of deformation when a sheet element is subjected to proportional loading. In Figure 5.1, the forming limit curves FLCN and FLCF are stated for a strain ratio of the true minor strain ε_2 to the true major strain ε_1, $\rho = \varepsilon_2/\varepsilon_1$ and this ratio takes different values for different paths of strain e.g. $\rho=1$ for biaxial tension and $\rho=0$ for plain strain [73, 153, 154].

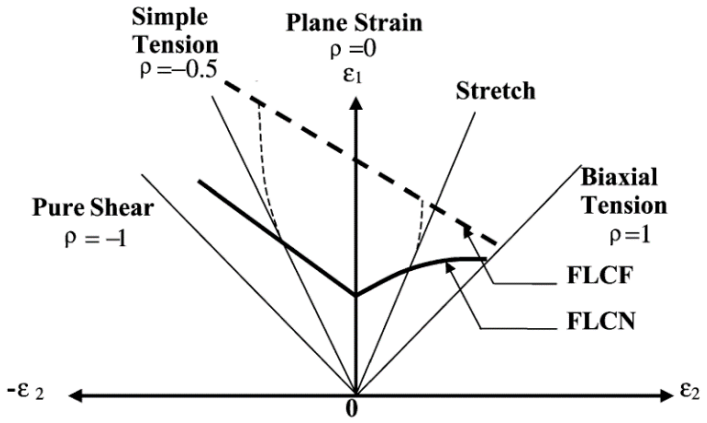


Figure 5.1 Schematic diagram showing the FLCN and FLCF [73].

Ozturk and Lee [155] constructed the FLD using the ductile fracture criteria of Hill, Mises, Cockcroft and Latham as well as Oh et al. models. They proved the ability of these models to accurately predict the fracture in the tension-compression region (left hand side) of FLD, although the prediction was not accurate in the tension-tension region (right hand side) of FLD. The original GTN model was utilized by Uthaisangsuk et al. [156] to simulate the FLD and forming limit stress diagram (FLSD). The investigation showed that the FLD was not suitable for the complex sheet metal forming process and that, with a multi-step forming process, the FLSD is more accurate than the FLD. Furthermore, the original GTN model showed acceptable prediction of the fracture. The original GTN model was employed by Parsa *et al.* [25] to predict the FLD for aluminium monolayer and sandwich sheets. The results showed a good correlation between the experiments and the original GTN model, especially in a biaxial strain state, due to the high stress triaxiality ratio created by this state. The Nakajima test was carried out by Min et al. [157] to plot the FLD and FLSD for an

aluminium alloy (AA) 5052-O1 sheet. The fracture in the Nakajima test was predicted using the original GTN model, which showed good agreement with the experimental Nakajima test for all strain states. The original anisotropic GTN model was implemented in ABAQUS/Explicit by Kami *et al.* [26] to construct the FLD of an anisotropic aluminium sheet using the Nakajima test. The result of the original anisotropic GTN model showed a better correlation with the experimental Nakajima test, especially in the biaxial tension strain state.

An experimental methodology was proposed to determine the FLCF using a SPIF, torsion and shear test. It is noted that the FLCF constructed by a conventional sheet test, e.g. the Nakajima test, is identical to that constructed from ISF tests on pyramidal and conical truncate parts [23]. The major strain at fracture in ISF was located above the Nakajima's forming limit curve at fracture when small tool dimeter was used [24].Tensile and hydraulic bulge tests were utilized to establish the FLCF for multi-stage SPIF. The results showed that the FLCF can be successfully employed to determine the forming limit of multi-stage SPIF. In addition, the overall strains obtained in multi-stage SPIF are higher than the FLCN established by the hydraulic bulge test [158].

It is clear from the literature that the original GTN model has been used to simulate the Nakajima test in order to construct the FLCN. The results showed that there was a good correlation between the FE prediction and experiments, especially in the biaxial strain state [25, 26] due to the high stress triaxiality ratio created by this state. However, the ability of the Nakajima test to describe the fracture in ISF is still debatable; some researchers claim that the test is identical to that constructed from ISF tests on pyramidal and conical truncate parts [23], while others proved that the major strain at fracture in ISF is located above the Nakajima's forming limit curve at fracture when a small tool dimeter is used [24]. Thus, in this chapter, for the first time, the GTN damage model with consideration of stress triaxiality is used to construct the FLCF in the Nakajima test and in incremental sheet forming and to solve the problem of fracture prediction with moderate stress triaxiality that is especially pertinent to the ISF. In addition, the results of the FLCF of Nakajima test are compared with ISF to evaluate the ability of the Nakajima test to describe the fracture in ISF.

5.2 Stress triaxiality modified GTN model

In the GTN model, the initial void volume fraction increases due to the nucleation of new micro-voids (Eq. (4.8) and the growth of the old voids (Eq. (4.10) so this model can be used to predict the fracture under a high triaxiality ratio (η). Therefore, the GTN model was modified by Nahshon and Hutchinson [142], as defined in Eq.(4.14), to predict the fracture at zero stress triaxiality (shear state) or even negative stress triaxiality. Thus, in the shear modified GTN model, the increment in the void volume fraction is determined based on the micro-voids' nucleation, growth and shear mechanisms.

According to the above discussion, the original GTN model works in the range of high stress triaxiality while the shear modified GTN model can predict the fracture under low stress triaxiality. Therefore, Nielsen and Tvergaard [159] further developed the shear extension of GTN model by Nahshon and Hutchinson to consider the effect of stress triaxiality in the regions of moderate stress triaxiality by adding a stress dependent factor Ω (η), The values of this factor lie between one at low stress triaxiality and zero at high stress triaxiality. Therefore, the function of the stress state becomes

$$\omega_o = \omega(\sigma)\Omega(\eta), with\ \Omega(\eta) = \begin{cases} 1, & for \quad \eta < \eta_1 \\ \dfrac{\eta - \eta_2}{\eta_1 - \eta_2}, & for \ \eta_1 \le \eta \le \eta_2 \\ 0, & for \ \eta > \eta_2 \end{cases} \qquad (5.1)$$

where ω(σ) is given by Eq.(4.15), $\eta_1 < \eta_2$.

After this addition, the stress triaxiality modified GTN model can work in the same way as the original GTN model if $\eta > \eta_2$, and as the shear modified GTN model if $\eta < \eta_1$. Thus this extension can capture the failure at different values of stress triaxiality.

5.3 Experimental works

5.3.1 Nakajima test

Nakajima test is a stretching process up to fracture and is used to predict the forming limit diagram. The tools used in this test include a hemispherical punch, die and blankholder. Figure 5.2 shows the Nakajima test configuration according to BS EN ISO 12004-2. The experimental setup and formed specimen of Nakajima test is shown in Figure 5.3.

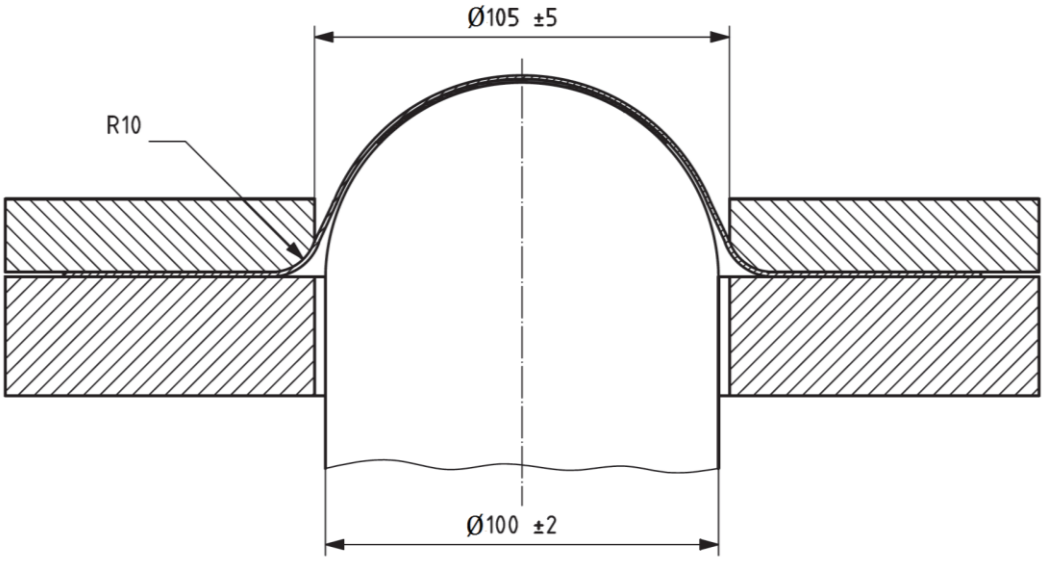


Figure 5.2 Illustration of the cross section of the tool used for Nakajima testing [89].

The spark-erosion method is utilized to produce the final shape of the specimen because it does not cause cracks in the sample's edges. More than one specimen is required for the description of a complete forming limit diagram from uniaxial to equi-biaxial tension. In this work, five geometries of pure Ti grade1 with a sheet thickness of 0.7 mm were examined with three repetitions. The sample dimensions are illustrated in and Figure 5.4 and Table 5-1. Prior to the formability test, acetone was used to clean the sample, after which grease and PVC of 1 mm thickness were applied to the contact surface as a lubricant to reduce friction between the punch and specimen. The test was with a punch velocity equal to 1.2 mm/s.

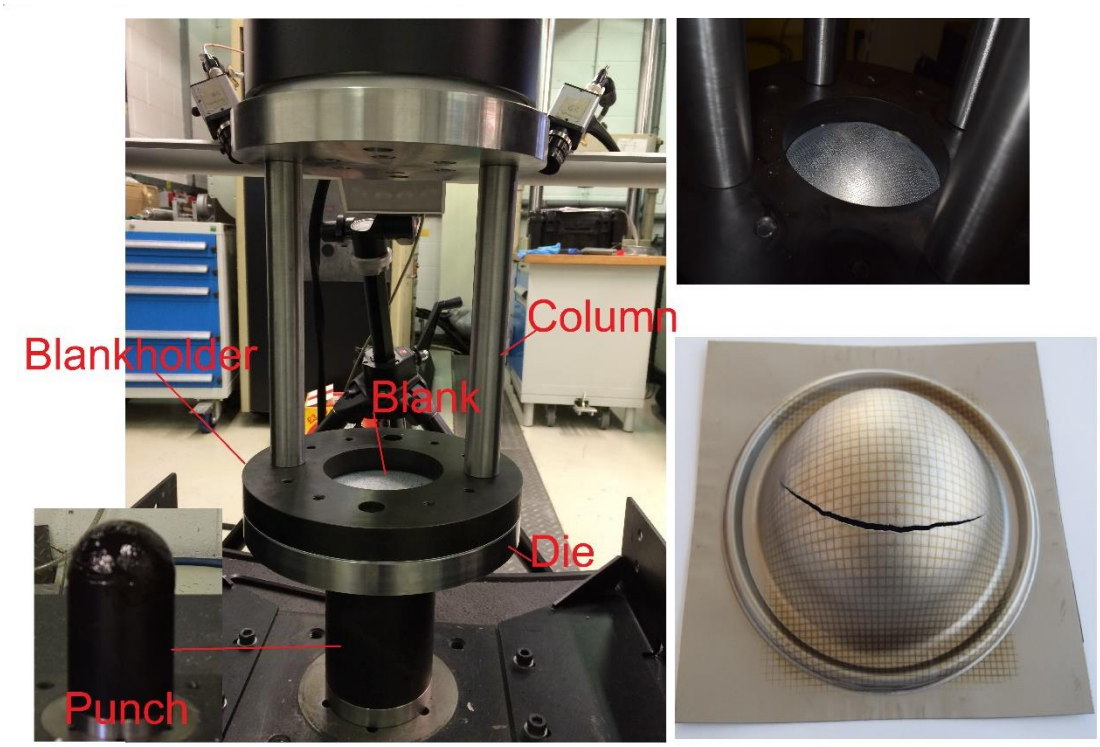


Figure 5.3 Nakajima test equipment and deformed specimen.

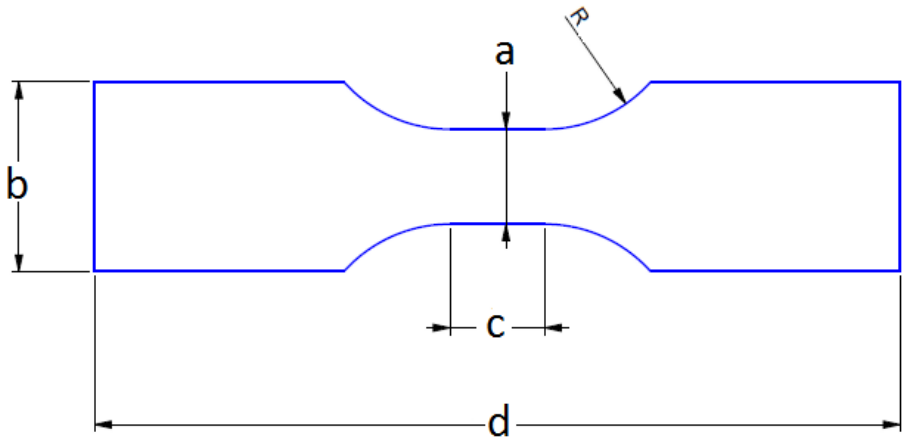


Figure 5.4 Dimensions of different FLD samples prepared for experiments.

Table 5-1 The dimensions of Nakajima test specimens.

Parameters	Sample 1	Sample 2	Sample 3	Sample 4	Sample 5
a	20	60	90	130	170
b	40	80	120	170	170
c	20	20	20	0	0
d	170	170	170	170	170
R	30	30	30	50	-

The technique utilized to obtain the forming limit curve at necking (FLCN) included electrical chemical etching to print a grid of circles with a 2 mm initial diameter on the

surface before the stretching process, and measuring the major and minor axis dimensions of the ellipses that resulted from the plastic deformation. The values of strain are computed from equation (5.2) (see Figure 5.5) [81]:

$$\varepsilon_{major} = \ln(\frac{a}{d_o}), \qquad \varepsilon_{minor} = \ln(\frac{b}{d_o}) \tag{5.2}$$

where d_o represents the original diameter of the circle and a and b are the major and minor axes of the ellipse

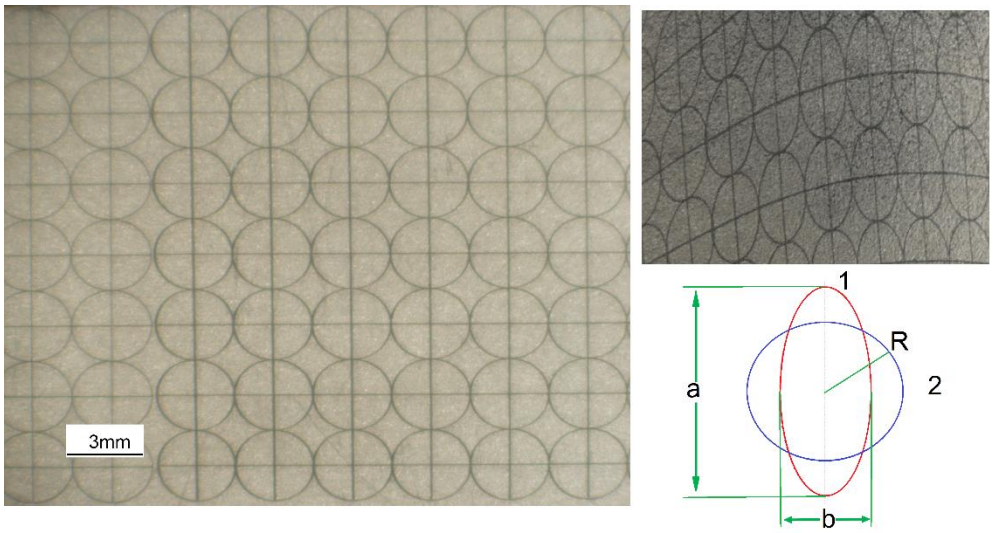


Figure 5.5 Circular grid patterns, (a) before deformation and (b) after deformation.

In addition, the optical deformation measurement with the digital camera was used to evaluate the major and minor strain distributions on the outer surface of the blank. The procedure for establishing the FLCF began by measuring the thickness at fracture in several places along the crack in order to obtain the average thickness strain. Average thickness strain was evaluated on both sides of the fracture. By using the grid pattern, the average minor strain was evaluated along the fracture, and by using volume constancy, the major strain was determined as follows:

$$\varepsilon_{major} = -(\varepsilon_{minor} + \varepsilon_{thickness}) \tag{5.3}$$

5.3.2 Single point incremental forming

The proposed experimental method to establish the forming limit curve at fracture (FLCF) makes use of SPIF. The SPIF test was carried out to form truncated conical and pyramidal geometries with varying forming angles from 22° to 80° (Figure 4.25). The truncated cone and truncated pyramid allow construction of the FLCF directly

from the experimental measurement of major and minor strains at fracture under plain strain and biaxial stretching conditions. To measure the strain state, the circle grid analysis was utilized using a similar methodology to the Nakajima test. Figure 5.6 shows the deformed circles on the hyperbolic truncated cone and hyperbolic truncated pyramid of grade 1pure Ti.

These ISF tests were done with an incremental depth equal to 0.2 mm per revolution and tool diameter of 10 mm. The tool is rotation free with a feed rate of 1000 mm/min. To ensure the repeatability of the results, the SPIF process was repeated three times and the average value was taken.

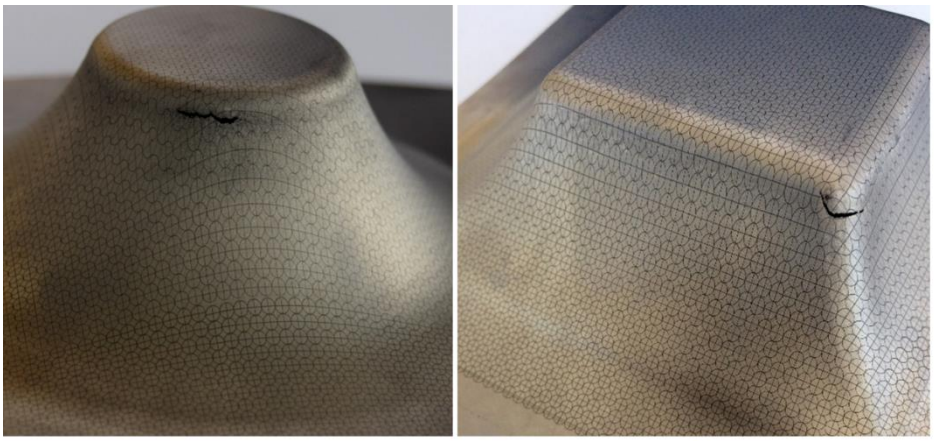


Figure 5.6 The distorted grid on the deformed SPIF parts: (a) hyperbolic truncated cone shape and (b) hyperbolic truncated pyramid shape.

5.3.3 Thickness and strain measurement

In order to study the thickness and strain distribution within the SPIF process and Nakajima test, a grid pattern of 2 mm initial dimeter was printed on the blank sheet by using laser and electrical chemical etching as shown in Figure 5.5. In order to measure the thickness distribution on the deformed wall along the depth, the deformed parts were sectioned from the middle for two parts by using a water jet as shown in Figure 5.7. Digital micrometre and optical microscope were used to measure the deformed wall thickness and the changes in the grid circles during the deformation.



Figure 5.7 The sample of divided hyperbolic truncated cone.

5.4 Finite element simulation

Abaqus/Explicit was used to implement the shear modified GTN and stress triaxiality modified GTN models as a materials user subroutine (VUMAT). A return mapping algorithm was then utilized to determine the increments in plastic strain ($d\varepsilon^{p}$) [145, 146]. Figure 5.8 shows the FE model of the Nakajima test performed on a specimen with a width of a=90 mm. The mesh size was 0.25 mm in the affected zone with three layers of elements through the thickness. In both the Nakajima test and SPIF simulation, the punch, die and the blankholder were modelled as an analytical rigid surfaces. While, the blank was modelled as a deformable body with an eight node brick element (C3D8R). In FE simulation, displacement vs time was used to define the tool path in SPIF and the movement of the punch in the Nakajima test. In Nakajima test, Coulomb's friction law was applied with a friction coefficient of 0.05 to model the contact between the punch and blank and of 0.2 between the blank and other parts including the die and the blankholder.

The Nakajima test was carried out in two steps. In the first step, a 50 KN holding force was applied to the reference point of the blankholder. In the second step, the holding force remained constant and the punch moved down in the vertical direction. In this investigation, the Nakajima test was run five times with different dimensions, as shown in Table 5-1, to cover a wide range of strain states from uniaxial to equi-biaxial tension. Minor and major strains were recorded at the end of each job corresponding to a point on the FLD.

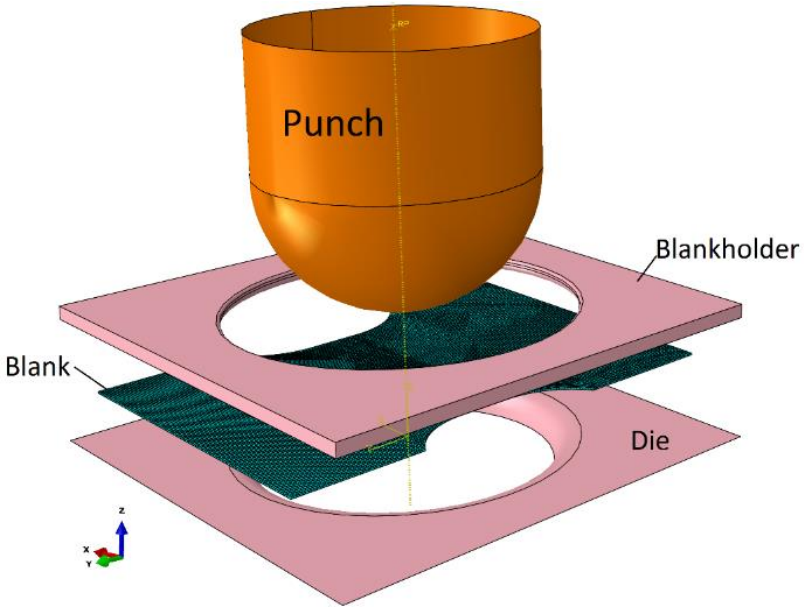


Figure 5.8 Finite element model of Nakajima test.

5.5 Results and discussion

5.5.1 Nakajima test

The level of major strain at fracture in different strain states is illustrated in Figure 5.9. It is evident that relatively high major strain concentrations were present in the fracture zone of the stretched piece as a result of excessive bending.

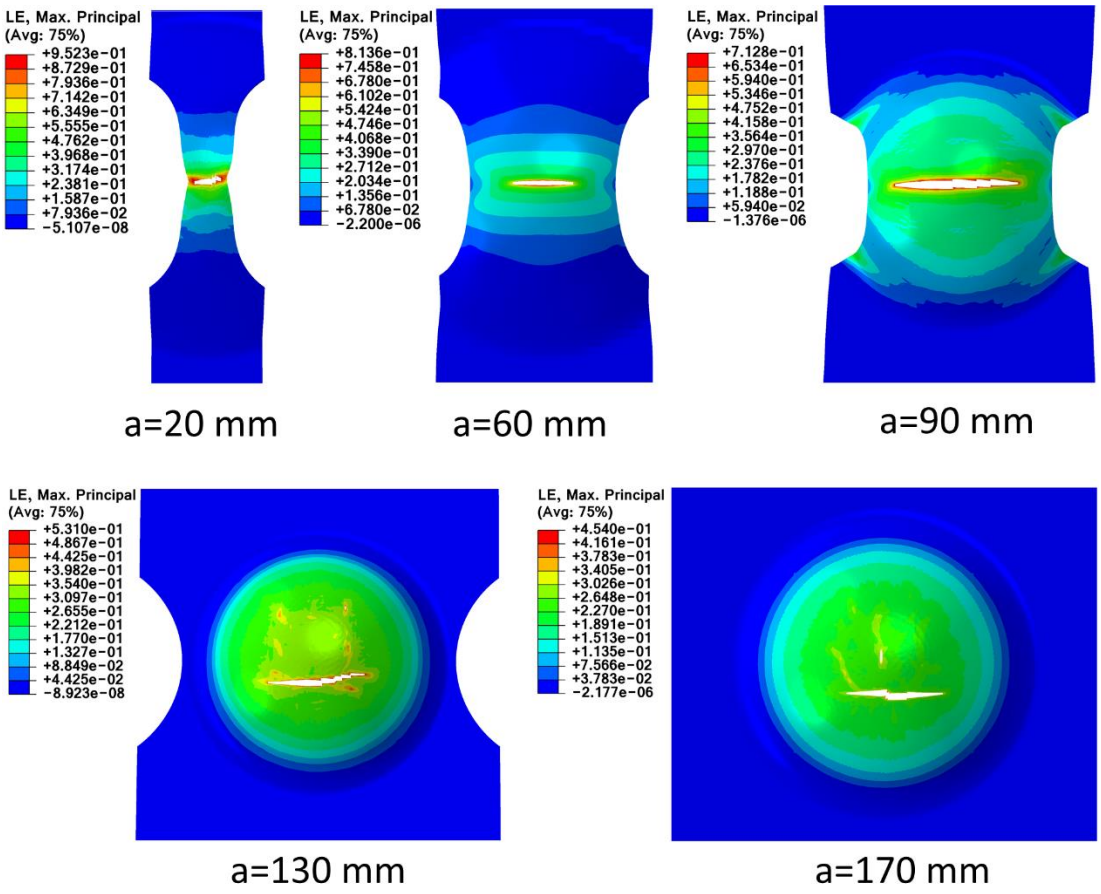


Figure 5.9 Major strain distributions during the Nakajima test simulation in different strain states.

Figure 5.10 illustrates the distribution of major and minor strains in all samples of the Nakajima test. From the figure, it can be seen that the ratio between the minor and major strain is -0.5, -0.11, 0.03, 0.901 and 1 for specimens with a width of a=20, 60, 90, 130 and 170 mm, respectively. Based on these ratios, the samples are enough to cover all strain states from uniaxial tension (strain ratio =-0.5) to equi-biaxial tension (strain ratio= 1) and the specimens with a width of a=20, 90 and 170 mm corresponded well to strain states of uniaxial tension, plain strain and equi-biaxial tension, respectively.

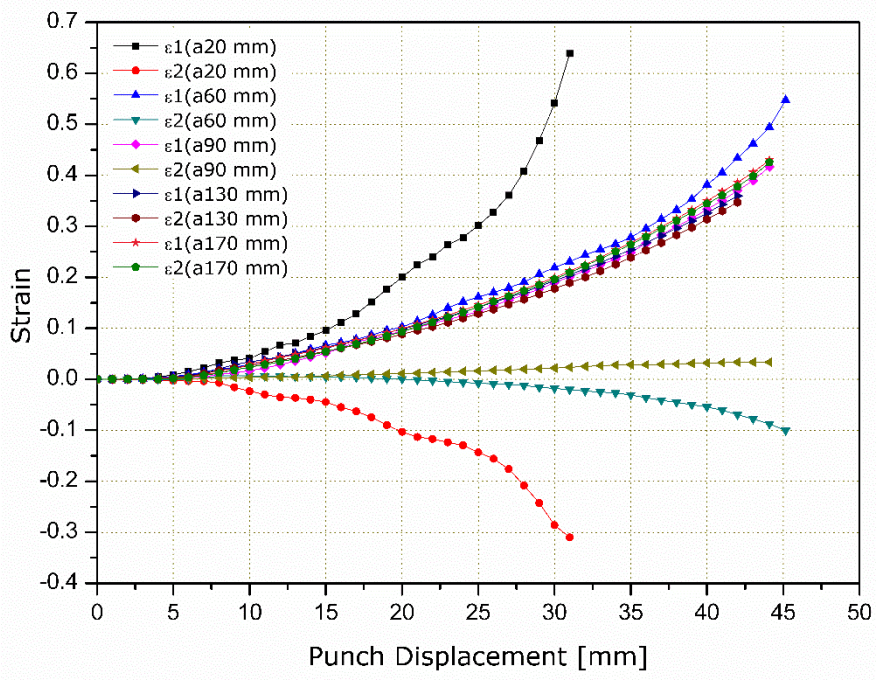


Figure 5.10 Distribution of major and minor strain in Nakajima test specimens.

To describe the complete FLCN and FLCF, five geometries were used to cover all the strain states from uniaxial tension to equi-biaxial tension and these samples were experienced different stress triaxialities, as shown in Figure 5.11. From the figure, it is clear that stress triaxiality was not constant during the deformation of each sample. Therefore, the average value of stress triaxiality was taken as a reference of each sample and was 0.39, 0.5, 0.57, 0.63 and 0.66 for samples with a width of a=20, 60, 90, 130 and 170 mm, respectively. Based on these results, stress triaxiality appears to change from one sample to another; in the Nakajima test, it also changed in the same sample. Therefore, the effect of stress triaxiality on the fracture occurrence should be taken into account when the GTN model is used to evaluate the fracture in the Nakajima test.

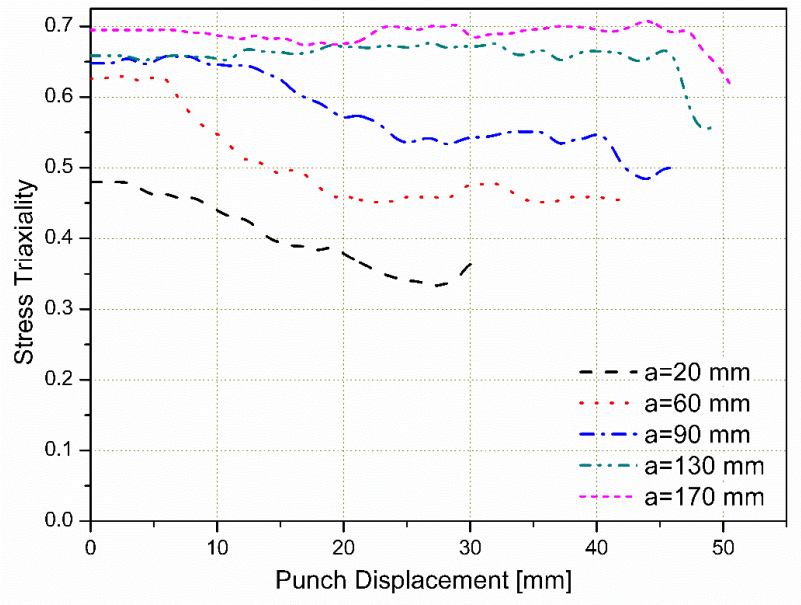


Figure 5.11 Evaluation of stress triaxiality in Nakajima test specimens.

Major strain at fracture was measured using FE models (the original GTN, shear modified GTN and stress triaxiality modified GTN) and from experimental tests for all Nakajima samples to validate and examine these models. Figure 5.12 (a) shows the distribution of major strain on all FE models, as well as the experimental tests for samples with a width equal to 20 mm (uniaxial tension). It is clear from the figure that there is a good correlation between the shear modified model and experimental curve; this correlation is due to the fact that the value of stress triaxiality is normally considered low (0.39) and the Nahshon-Hutchinson's shear mechanism was added to capture the fracture at low stress triaxiality, but the original GTN model cannot predict the void's growth within this range of stress triaxiality and coalescence is postponed. Specimens with a width of 60 and 90 mm have moderate stress triaxiality; therefore, both the original GTN model and shear modified GTN model cannot accurately predict the value of the major strain at fracture, as shown in Figure 5.12 (b and c); this is due to the fact that the original model and shear modified model do not work with a moderate ratio of stress triaxiality. However, the stress triaxiality modified GTN model is considered the best choice to use when moderate stress triaxiality is generated during the deformation as this model can accommodate the effect of stress triaxiality. The ratios of stress triaxiality in specimens with widths of 130 and 170 mm are normally considered high at 0.63 and 0.66, respectively. With this range of stress triaxiality, the original GTN model can predict the fracture occurrence accurately, as shown in Figure

5.12 (d and e). Therefore, based on the above results for processes under different stress triaxialities, e.g. the Nakajima test, it is better to use the GTN model which considers the range of stress triaxialitise such as the Nielsen-Tvergaard stress triaxiality extension of the GTN model which can be used to select either the original GTN model, the shear modified GTN model, or a stress triaxiality modified GTN model.

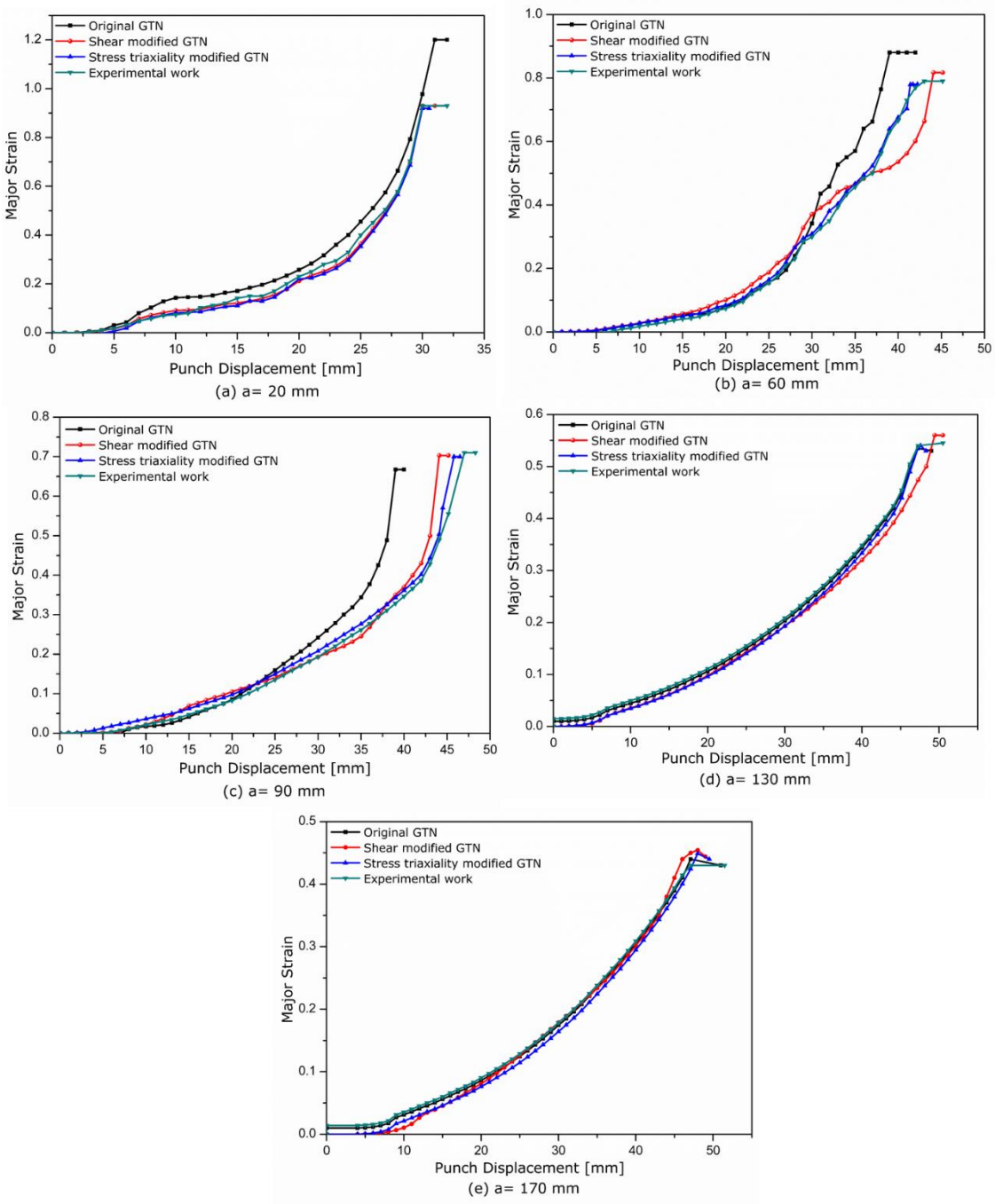


Figure 5.12 Evaluation of major strain in the fracture region of Nakajima specimens.

The predicted fracture depth (FD) for Nakajima test specimens with different widths was validated by the experimental depth, as shown in Figure 5.13 and Figure 5.14. It is clear that the fracture depth shows a good correlation between simulations using Abaqus/ Explicit with the stress triaxiality modified GTN model and the experimental measurements.

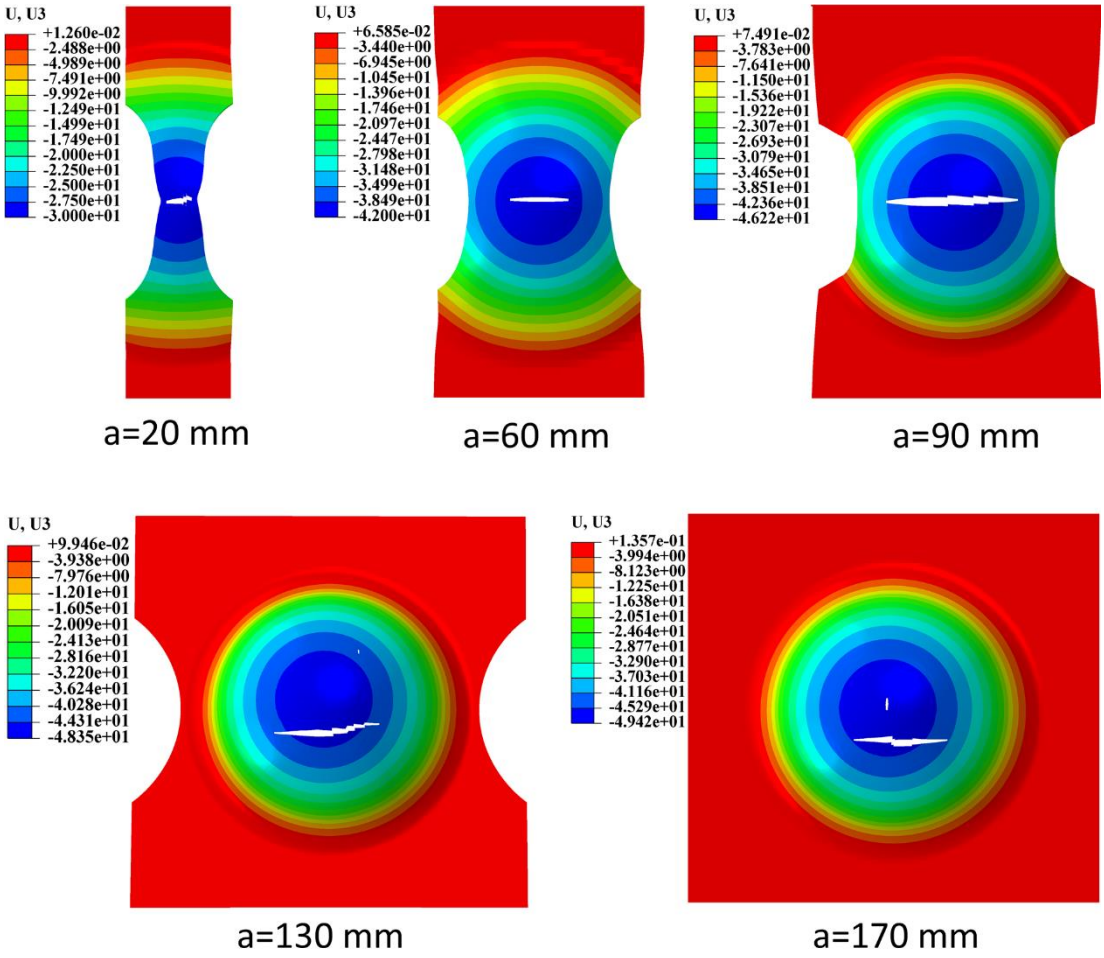


Figure 5.13 Fracture depth of simulated Nakajima test specimens with different widths obtained for the stress triaxiality modified GTN model.

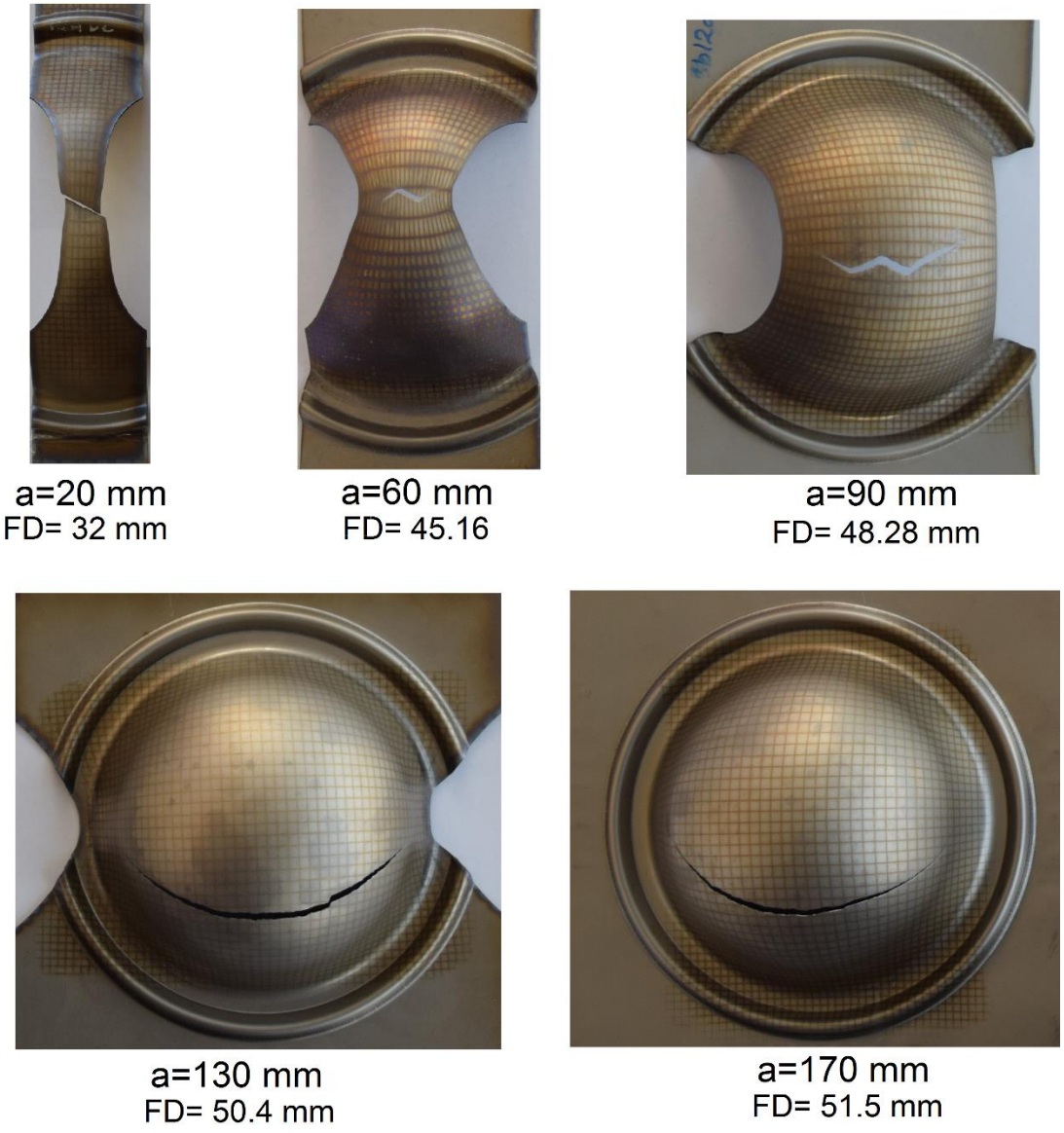


Figure 5.14 Fracture depth of Nakajima test specimens with different widths.

5.5.2 Single point incremental forming

The stress triaxiality modified GTN model was used to simulate the SPIF process for two shapes (hyperbolic truncated cone and hyperbolic truncated pyramid) due to the ability of this model to predict fracture occurrence with different stress triaxialities. The distribution of the major strain in SPIF parts is illustrated in Figure 5.15. In the hyperbolic truncated cone shape, the major strains are concentrated on the wall of the SPIF part in the transition area between the contact and non-contact zones, whereas in the hyperbolic truncated pyramid, it is concentrated at the corner of the part.

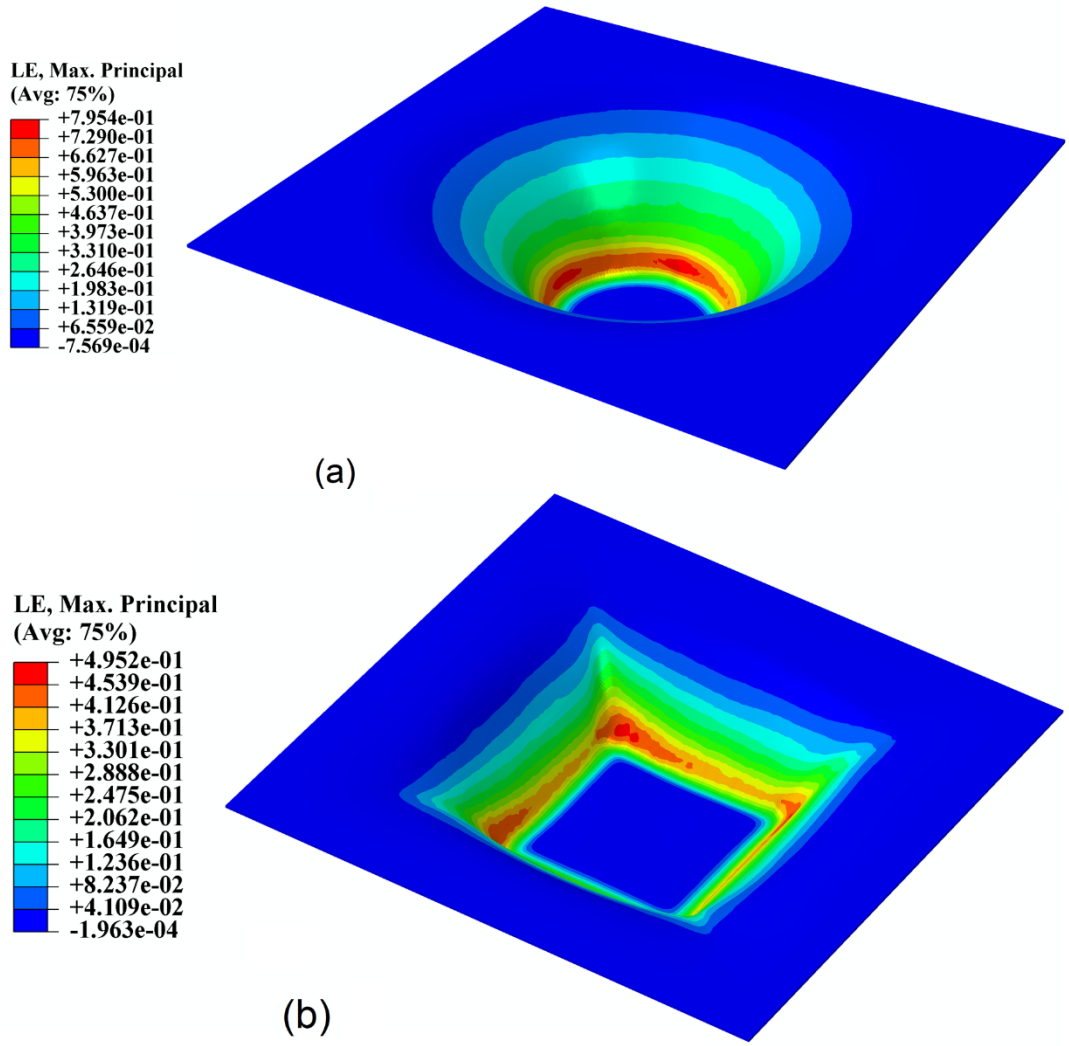


Figure 5.15 Comparison of major strain concentration in (a) hyperbolic truncated cone and (b) hyperbolic truncated pyramid shape.

The values of major and minor strains for both shapes were recorded, as shown in Figure 5.16, and the ratios of strain ($\rho = \varepsilon_2/\varepsilon_1$) were 0.05 and 0.87 for the hyperbolic truncated cone and hyperbolic truncated pyramid shape, respectively. These ratios were validated experimentally by measuring the major and minor strain at fracture in SPIF for both shapes. Figure 5.17 shows the deformed grid at fracture; it is observed from the diagram of the hyperbolic truncated cone shape that there is a big change on one axis of the circular grid, whereas the change in the other one is small, meaning there is an increase in major strain, while the minor strain remains unchanged (plain strain). It is also observed with the hyperbolic truncated pyramid shape that there is uniform distortion in the grid at fracture and that the ratio is close to 1 (equi-biaxial strain). Based on these ratios of strain, the hyperbolic truncated cone is deformed under

plain strain conditions and the corner of the hyperbolic truncated pyramid part is deformed under equi-biaxial strain. Therefore, two points can be recorded in the first quadrant of FLD; these points are used to validate the capability of the Nakajima test to describe the formability of SPIF process.

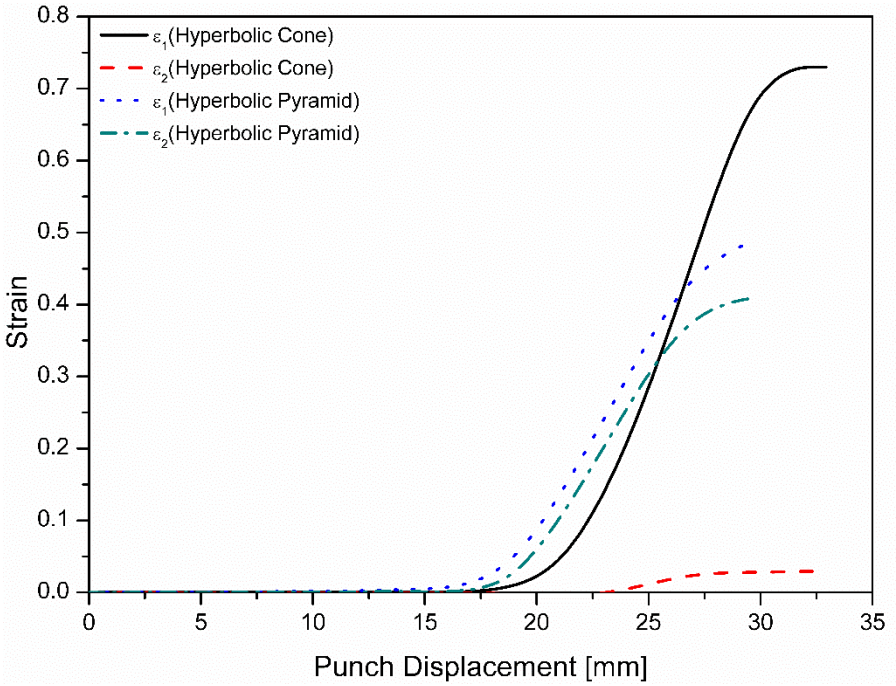


Figure 5.16 History of major and minor strain in the hyperbolic truncated cone and hyperbolic truncated pyramid shape.

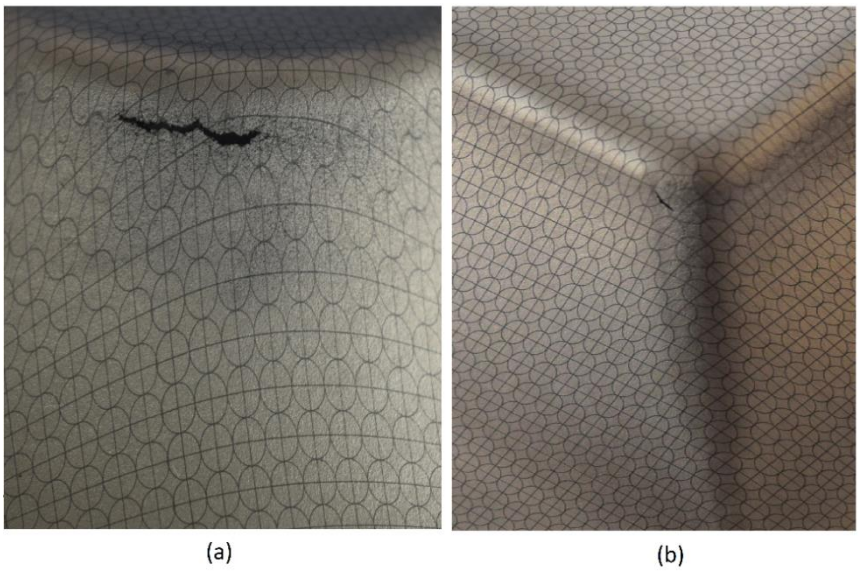


Figure 5.17 The distorted grid on the deformed SPIF parts: (a) hyperbolic truncated cone shape and (b) hyperbolic truncated pyramid shape.

The values of major strain in both shapes were compared with the experimental SPIF test to validate the ability of the stress triaxiality modified GTN model to accurately predict the values of major strain at fracture, as shown in Figure 5.18. The results show that major strain in the hyperbolic truncated pyramid shape increases earlier than in the hyperbolic truncated cone due to the fact that the fracture develops in the corner of the hyperbolic pyramid shape under equi-biaxial stretching, whereas plain strain stretching appears in the hyperbolic cone shape. The SPIF-simulated results by Abaqus, using the stress triaxiality modified GTN model, are consistent with those of the actual experiments for both shapes.

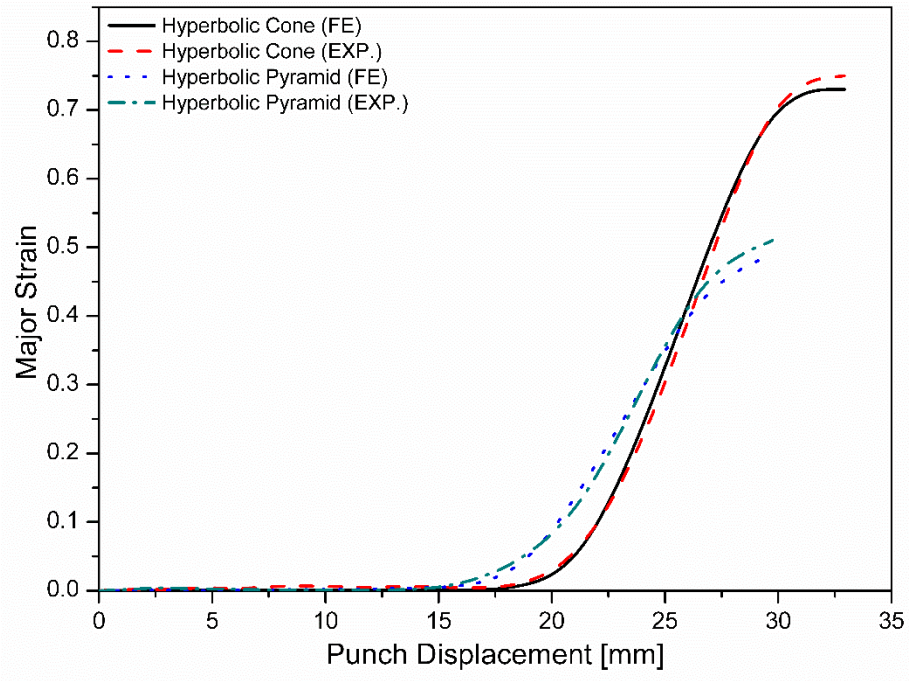


Figure 5.18 History of major strain in the fracture region of SPIF in both the hyperbolic truncated cone and hyperbolic truncated pyramid shapes.

5.5.3 Forming limit diagram

The experimental Nakajima test was conducted at ambient temperature with specimens of widths 20, 60, 90, 130 and 170 mm; the test was stopped when a crack occurred in the sample. The FLCN was established by measuring the major and minor strain in the necking region, while the FLCF was determined by measuring the major and minor strains in the fracture region and then plotting them in the major and minor strain space, as shown in Figure 5.19. It can be seen from the figure that the FLCF takes the shape of a straight line with a negative slope in the first quadrant of the FLD. The numerical FLCN and FLCF results for pure titanium showed a good agreement

with the experimental results. The SPIF process was used to validate the FLCF obtained by the Nakajima test. It can be noticed that the major strain at fracture in SPIF for both tests, i.e. the truncated cone and truncated pyramid, is located above the FLCF. This is due to the stress state being induced as the tool moves in SPIF, indicating that the part produced by SPIF has higher formability than traditional sheet metal forming.

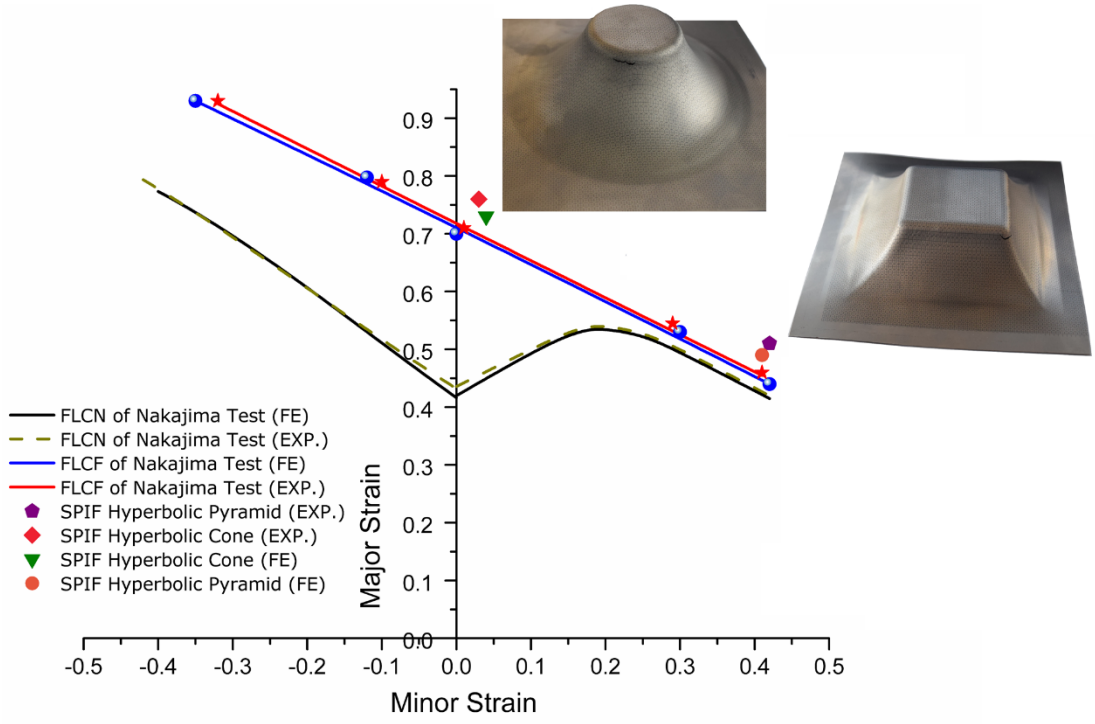


Figure 5.19 Forming limit diagram for 0.7 mm thick grade 1 titanium sheet.

5.6 Conclusions

In this chapter, FE analysis of the Nakajima test incorporating the GTN based models was carried out to evaluate the formability of pure titanium in the ISF process. The GTN based models were implemented via Abaqus/Explicit to determine the fracture occurrence in the Nakajima and ISF tests. Particular attention was given to validation of the applicability of the GTN model to capture the fracture occurrence at different ratios of stress triaxiality and to evaluate the suitability of the Nakajima test to describe the fracture in the ISF. A comparative investigation was also carried out by using experimental tests to validate the FE results of the GTN model.

The experimental and FE results showed that the shear modified GTN model could predict the fracture accurately with samples under uniaxial tension condition due to low stress triaxiality and the original GTN model is suitable for an equi-biaxial strain state (high stress triaxiality), whereas the stress triaxiality modified GTN model should be considered for samples which have a moderate stress triaxiality. The numerical and experimental FLCF of pure titanium from the Nakajima test showed good agreement with the experimental and numerical results of ISF. Therefore, the Nakajima test can be applied to establish the FLCF, which can be utilized to describe the formability the SPIF test of conical and pyramidal truncated specimens.

CHAPTER 6

ISF PARAMETRIC STUDY

6.1 Introduction

The quality of an ISF product is affected by various factors, e.g. sheet material, step size, feed rate, tool size and lubricant. To produce an ISF part of sufficient quality and accuracy without defects, optimal parameters of the ISF process should be selected. In this chapter, experiments and FE analyses were conducted to evaluate the influence of major forming parameters including the step size, feed rate and tool size on the formability and fracture of pure titanium. This is followed by using optimal parameters to investigate the feasibility of reconstructing a cranial plate from 0.7 mm grade 1 pure titanium using the ISF process. Two types of pure Ti (grade 1 and 2) were used to evaluate the sensitivity of the material type to forming parameters. GTN damage constitutive model with stress triaxiality consideration is used to predict ductile fracture in the ISF process due to void nucleation, growth and coalescence.

Many studies have been performed to evaluate the optimal parameters of the ISF process. Uniform plastic strain and thickness distribution can be obtained by reducing the step size and increasing the tool size and wall angle [40]. When the conventional tool path (constant step depth) is used, minimum thickness was noted which was closely related to the tool size, and its location was largely determined by the incremental depth (ΔZ) [41]. The stresses in the contact region between the tool and the sheet and in the wall of the ISF part can be reduced by decreasing the step size [54]. Through an experimental investigation to measure the forming force in ISF, it was noted that the step size has little effect on the formability of the ISF process [27]. Two experiments were carried out to demonstrate the effect of ISF parameters. The first experiment showed that the step size had an effect on the ISF formability and that the likelihood of the part to deform was enhanced by decreasing the step size. In the second experiment, the results showed a small effect of step size on the maximum wall angle [28]. Many investigations have proved that an increased step size has a detrimental effect on the ISF formability [29, 31-34].

High ISF formability can be achieved when a smaller tool size is used rather than a large tool size [28, 29, 34, 56]. This is because with a small tool size, a highly concentrated zone of deformation is generated with a high strain which leads to enhanced formability. On the other hand, a bigger contact zone created by a large tool size leads to an increased forming force and reduced formability. The maximum value of the principal strain and sheet thinning was noted across the tool's trajectory on the circumference with the biggest tool diameter [81]. The major strain at fracture in ISF was located above the Nakajima's forming limit curve at fracture (FLCF) when lower tool dimeter is used [24]. The effect of feed rate is considered insignificant as compared to the effect of tool size and step size [29]. Furthermore, the feed rate has less effect on formability than the tool's rotational speed [30]. However, the formability of ISF can be altered by changing the feed rate. For example improved formability of the ISF part can be achieved using low feed rate [28, 34, 35]. It appears from the literature that there is a lack of detailed understanding and even opposing views on the effect of ISF process parameters, such as the step size and feed rate on fracture occurrence in ISF. Some researchers claim that the effect of step size and feed rate are considered insignificant [27-30], while others believe that an increased step size and feed rate has a negative effect on formability [28, 29, 31-35]. It also appears that most attention has been paid to studying the effect of ISF parameters using FE simulation without consideration of ductile fracture criteria. Therefore, future work is needed to provide a better understanding of the effect of ISF parameters.

The purpose of this chapter is twofold; the first one is to investigate the effect of three key forming parameters, namely the step size, feed rate and tool size, and their interactions with the formability and fracture in the ISF process of pure Ti grade 1 and 2 using experimental testing and FE analysis incorporating the GTN moodel for ductile fracture prediction. Secondly, since every patient for cranioplasty surgery requires a unique cranial plate to be manufactured, the traditional forming process would require to design and manufacture a custom positive and negative die for each particular patient resulting in a significant amount of lead time and cost. Therefore, ISF is a promising technique that could be developed as an alternative manufacturing approach for cranial plates with considerable lead time and cost benefits due to the fact that it does not require any high capacity press or dies of a specific shape. The optimal

parameters from the parametric study of ISF process are used to investigate the feasibility of manufacturing titanium cranial plate using the ISF process.

6.2 Experimental testing

6.2.1 Materials characterizations

The materials properties and GTN damage model parameters of grade 1 pure Ti were determined as summarised in section 4.7. As grade 2 pure titanium sheets are also commonly used in cranioplasty and other implant applications, the materials properties and GTN damage model parameters of grade 2 pure Ti are determined as well. To determine the material properties of pure titanium grade 2, specimens were machined and tested according to British standard specification (BS EN 10002-1). EDM was used to obtain the tensile specimen from 0.8 mm thick grade 2 pure titanium sheet. The specimens were loaded until fracture occurred. The tensile test was carried out at cross head speed 0.1mm/s ($\varepsilon = 0.00133\ s^{-1}$), using an INSTRON testing machine. To measure the displacement on the surface of the specimens during the tensile tests, a Dantec Q-400 DIC (digital image correlation) system was used. The mechanical properties of the pure titanium grade 2 are summarized in Table 6-1.

Table 6-1 Mechanical properties of pure titanium 2.

Yield stress	Ultimate tensile stress	Young's modulus	Poisson's ratio	Density
367.5MPa	473.1MPa	107 GPa	0.34	4505 (Kg/m^3)

To predict the effect of feed rate on the formability and fracture of incremental sheet forming using FE analysis, tensile tests for both types of pure Ti are performed at three strain rates (0.00133, 0.04 and 0.08 s^{-1}). The fractured specimens of grade 1 and 2 pure Ti at different strain rates are shown in Figure 6.1. It is seen from the figure all samples were broken in ductile manner due to the fact that there is a necking in the fracture region. Moreover, the strain rate had a significant effect on the fracture elongation of both types of pure Ti and this elongation is increased with the decreased strain rate value. Figure 6.2 shows the true stress-true strain curves of grade 1 and 2 pure Ti at different strain rates. From the figure, it is observed that the ultimate tensile strength is increased and fracture elongation decreased with increased strain rate for both types of pure Ti.

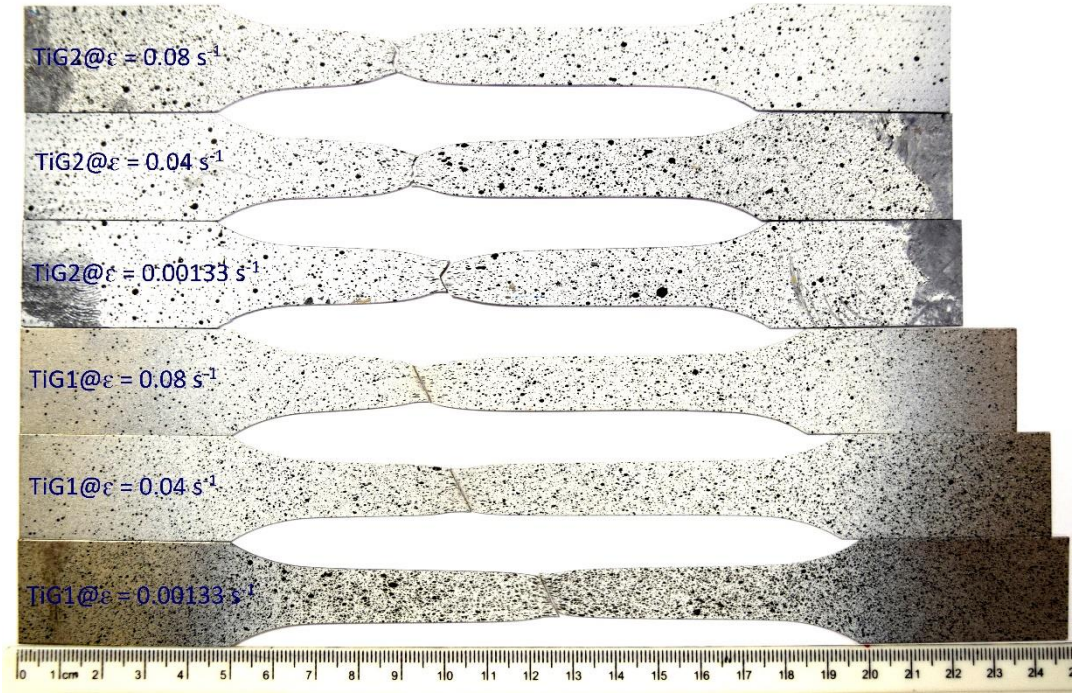


Figure 6.1 Fractured tensile specimens.

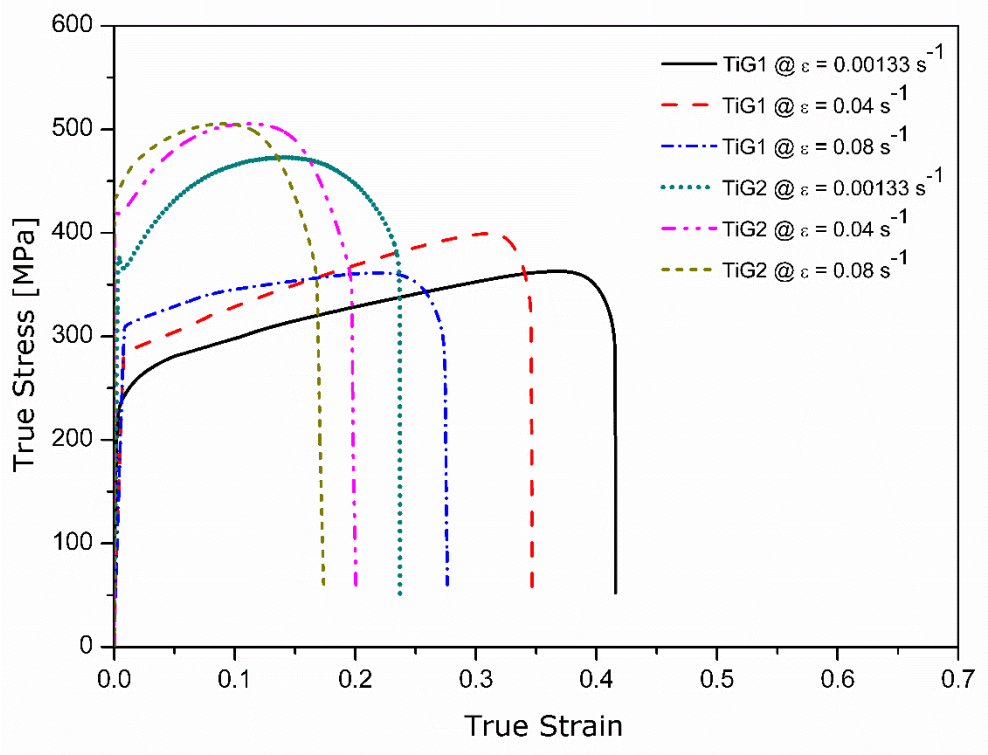


Figure 6.2 True stress true strain curves for grade 1 and 2 pure titanium deformed at different strain rates.

To determine the void volume fraction values of grade 2 pure Ti at the initial and following stages of deformation, i.e. nucleation, critical and fracture, a tensile test was run with the use of digital image correlation to determine the exact position of the

maximum deformation region on the tensile specimen. Then this region was cut and scanned under a scanning electron microscope to evaluate the nucleation and the growth of the voids in the Ti matrix. Figure 6.3 shows at which load and displacement stage the nucleation begins and this is followed by the critical and fracture positions in the load-displacement curve for both grade 1 and 2 pure Ti specimens. The nucleation of voids (f_N) is started after the yield point and before the maximum stress (maximum load). Unfortunately, no threshold is given for nucleation. Therefore, the tensile test was stopped at different displacements in order to scan the sample under SEM to check whether nucleation had started. The critical value of VVF (f_c) is determined when the tensile force reaches the maximum value and the necking is started in the samples. After the necking in the tensile sample voids get bigger and tearing of the ligaments between enlarged voids causes fracture in the tensile specimen. The fracture value of VVF (f_F) is determined by scanning the fracture surface of tensile sample using SEM then ImageJ software is used to determine the percentage of voids in the fracture surface.

The SEM's images were analysed using ImageJ software to determine the quantitative values of VVF. Figures 6.4 to 6.7 explain the technique used to determine the VVF at different stages. The GTN model parameters for grade 2 pure Ti sheet are listed in Table 6-2.

Table 6-2 GTN damage model parameters of 2 pure titanium.

f_o	q_1	q_2	f_N	ε_N	S_N	f_c	f_f
0.0052	1.5	1	0.018	0.3	0.1	0.07853	0.11648

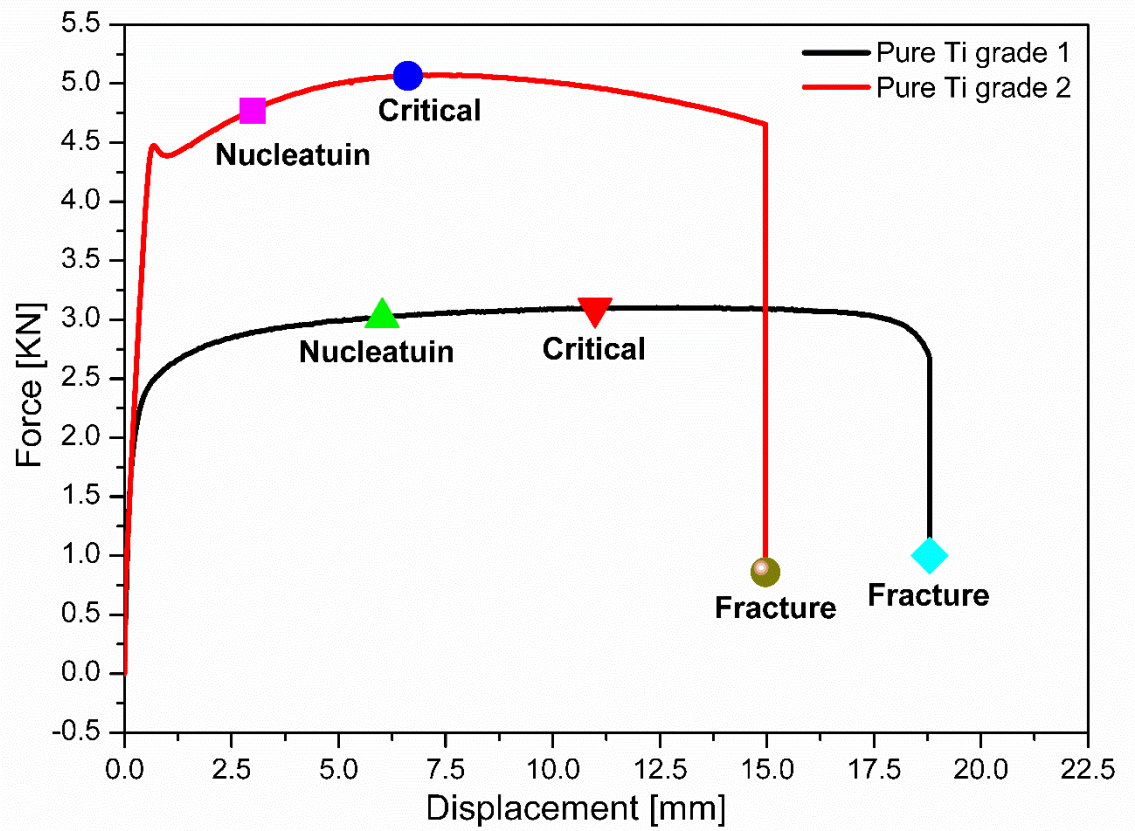


Figure 6.3 Load-displacement curves for pure Ti grade 1 and 2 showing the stages of determination of the GTN model parameters.

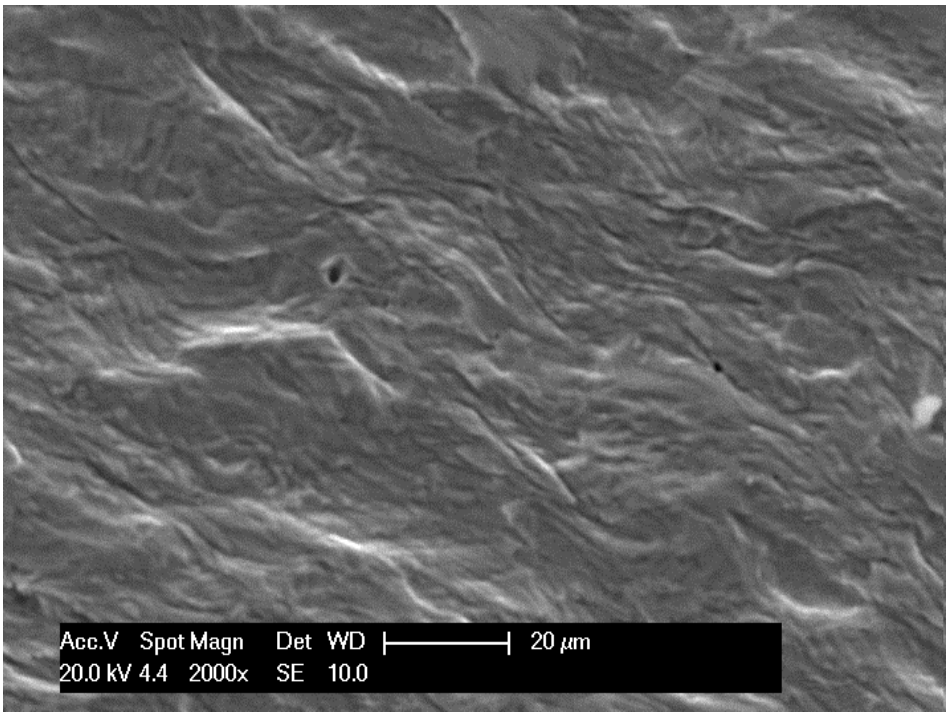
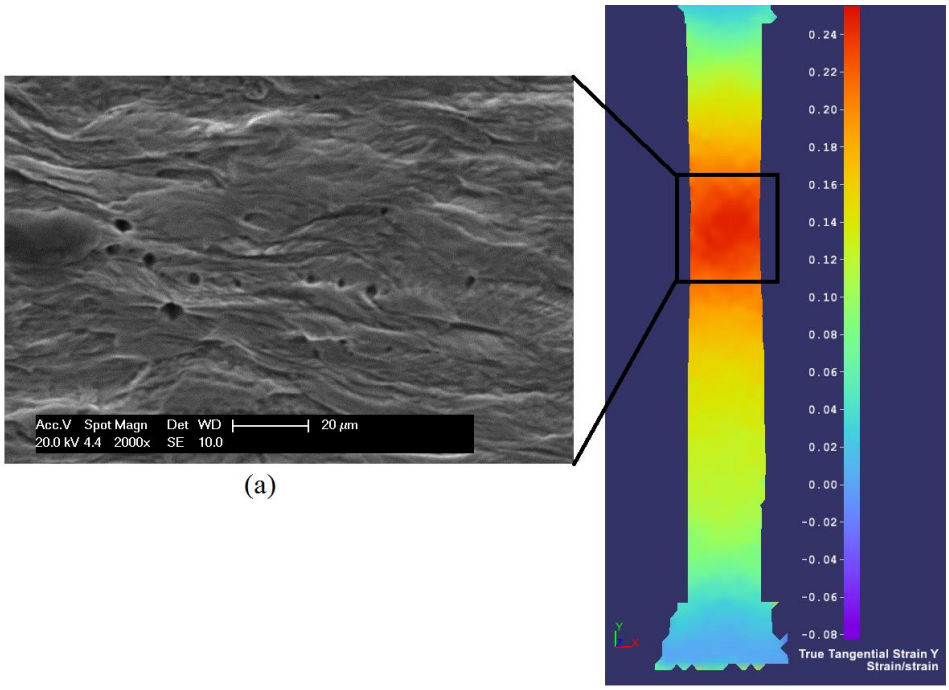
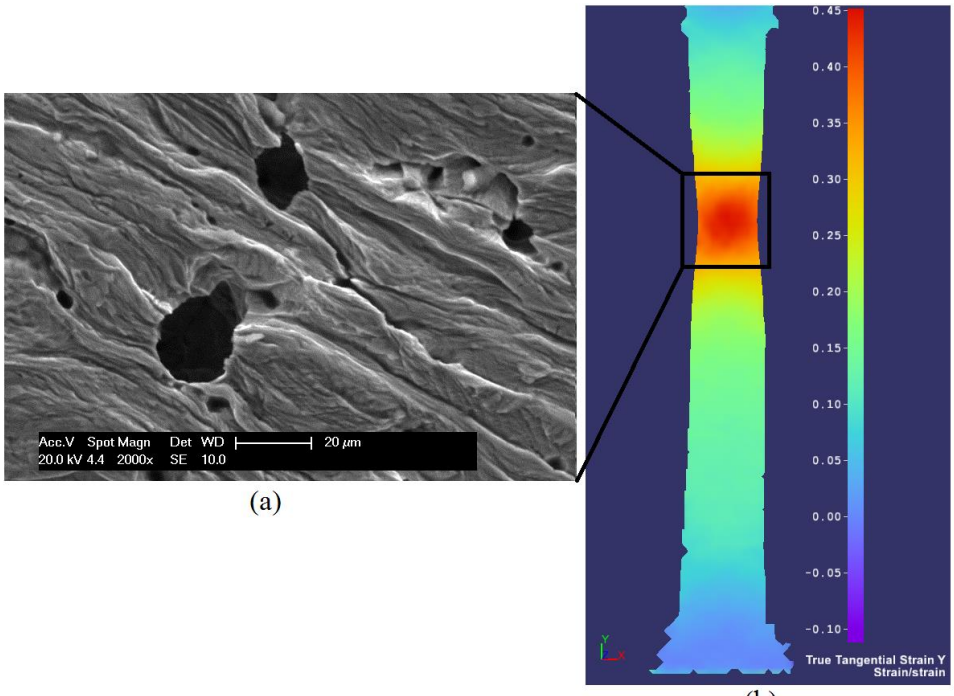


Figure 6.4 Microstructure of pure Ti grade 2 before deformation.



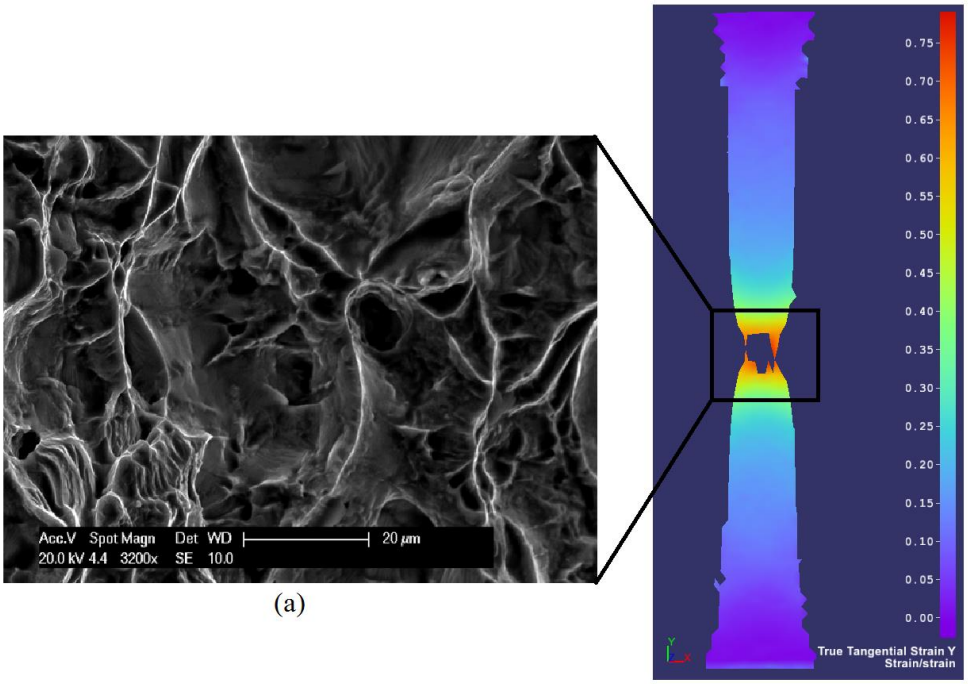
(a) (b)

Figure 6.5 Determination of void volume fraction at nucleation: (a) microstructure of pure Ti grade 2 showing the voids nucleation and (b) strain distribution from digital image correlation at nucleation.



(a) (b)

Figure 6.6 Determination of critical void volume: (a) microstructure of pure Ti grade 2 showing the voids at critical stage and (b) strain distribution from digital image correlation at necking.



(a) (b)

Figure 6.7 Determination of void volume fraction at fracture: (a) microstructure of pure Ti grade 2 showing the voids at fracture and (b) strain distribution from digital image correlation at fracture.

6.2.2 Design of Experiments

The CNC milling machine was employed to carry out the SPIF tests for a hyperbolic truncated cone shape with varying wall angles, as shown in Figure 6.8. The sheet was fastened using a special fixture assembled on the CNC milling machine. The blank size is 140 mm x 140 mm with a sheet thickness of 0.7 mm for grade 1pure Ti and 0.8 mm for grade 2 pure Ti. The tool path (G-code) was generated using a commercial CAD/CAM system. To evaluate the effect of ISF parameters on the formability and the fracture location of the grade 1 and 2 pure Ti hyperbolic truncated cone, three levels of values are employed as input for each parameter of ISF and their values are listed in Table 6-3. 7 test cases were performed to study the effect of process parameters on formability and fracture of ISF and each test was repeated three times to ensure repeatability of results and the average value is taken. This design showed sufficient consistence to capture the effects of studied process parameters with considerable lead time and cost benefits. The experimental ISF design is shown in Table 6-4; this design was used for both types of pure Ti.

Table 6-3 ISF parameters.

Factor	Level 1	Level 2	Level 3
Step size (mm)	0.2	0.4	0.6
Tool size (mm)	8	10	15
Feed rate (mm/min)	1000	2000	3000

Table 6-4 Design of Experiments.

Experiment No.	Step size [mm]	Feed rate [mm/min]	Tool diameter [mm]
1	0.2	1000	10
2	0.4	1000	10
3	0.6	1000	10
4	0.2	2000	10
5	0.2	3000	10
6	0.2	1000	8
7	0.2	1000	15

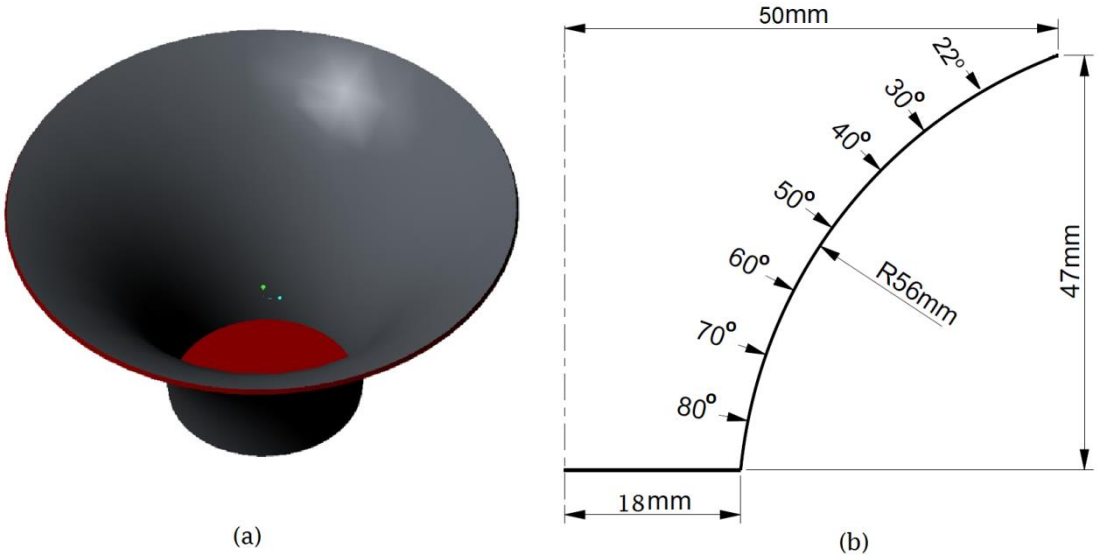


Figure 6.8 Geometric shape of a hyperbolic cone: (a) CAD model and (b) cross-section profile.

The SPIF test also was carried out to deform a hyperbolic truncated pyramid with the same profile as the hyperbolic truncated cone (Figure 6.8 (b)) in order to use, together with the hyperbolic truncated cone, to construct the forming limit curve at fracture (FLCF) to study the effect of ISF parameters on the fracture strain level. Two points were recorded in the first quadrant of the forming limit diagram: one in the plain strain zone from the hyperbolic truncated cone and another one from the biaxial strain zone from the hyperbolic truncated pyramid. These two points were used to determine the slope of the FLCF lines. The hyperbolic truncated pyramid ISF test was done with a

step size equal to 0.2 mm and tool diameter of 10 mm. The feed rate was set to 1000 mm/min with non-rotating tool.

The technique was used to construct the FLCF of ISF experimentally and included using a laser to print a grid of circles on the outer surface of the blank with a 2 mm initial diameter. These circles were changed to ellipses due to plastic deformation at the end of ISF testing. An optical microscope was employed to measure the minor axis dimension of the ellipses. The minor strain was determined using a plastic strain equation based on the initial diameter of the printed circle and the finial length of the minor axis of the ellipse. Thickness strain was evaluated on both sides of the fracture to get the average value of the thickness strain. The major strain was determined using volume constancy based on the minor and thickness strain.

6.3 FEA model

Abaqus/Explicit was used to establish a 3D FE model of ISF to study the effect of forming parameters on the formability and fracture in ISF. The truncated conical and pyramidal geometries with varying forming angles were taken as a benchmark in this work. The blank was modelled as a deformable body with 8-noded hexahedral elements and a reduced integration method (C3D8R). The sheet metal was assumed to be an isotropic elastic plastic material, and the forming tool, backing plate and blankholder were regarded as rigid surfaces. Coulomb's friction law was applied with a friction coefficient of 0.1 to model the contact between the forming tool and blank and of 0.2 between the blank and other parts including the backing plate and the holder. In this study, the GTN model which considers the effect of stress triaxiality is used to investigate the effect of ISF parameters including the step size, feed rate and tool diameter, on the deformation and fracture mechanism due to the fact that this model can predict fracture under different stress triaxiality conditions. In this chapter, the GTN model (VUMAT) is updated based on strain rate to study the effect of feed rate on the formability and fracture of ISF process. Isotropic hardening is used to simulate the hardening behaviour in both types of Ti during ISF. The true stress-strain data of pure Ti grade 1 was summarised as in Figure 3.8. Figure 6.9 gives the flow stress-plastic strain of the pure Ti grade 2 at strain rate 0.00133 s^{-1} that is used in the FE simulation.

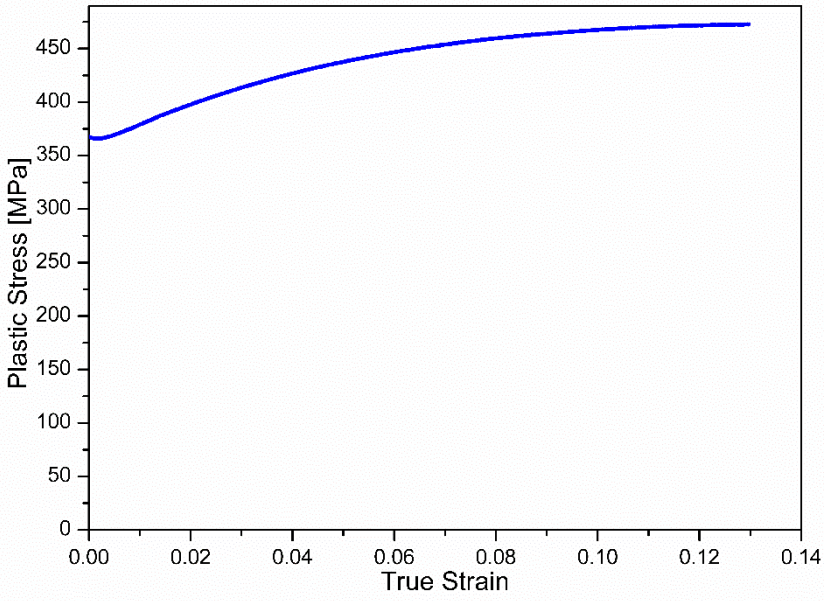


Figure 6.9 Flow stress of pure Ti grade 2.

6.4 Results and discussion

6.4.1 Effect of step size

The step size was set to three values: 0.2, 0.4 and 0.6 mm (Experiment Nos. 1, 2 and 3, respectively). The experimental and FE values of the maximum wall angle (fracture angle) and the fracture depth of the hyperbolic truncated cone under different step sizes are listed in Table 6-5. It is clear from the table that the influence of step size on the formability (maximum wall angle) and fracture depth of grade 1 pure Ti is small as compared to that of grade 2 pure Ti. The experimental wall angle of grade 1 pure Ti hyperbolic truncated cone increases by 0.85° when the step size is reduced from 0.6 mm to 0.2 mm, while the increase in the wall angle of grade 2 pure Ti is about 5°.

Table 6-5 Effect of ISF step size on the formability and fracture of grade 1 and 2 pure Ti.

Step size [mm]	Pure Ti grade 1				Pure Ti grade 2			
	Fracture depth [mm]		Fracture angle [°]		Fracture depth [mm]		Fracture angle [°]	
	FE	EXP.	FE	EXP.	FE	EXP.	FE	EXP.
0.2	31	32.2	69.45	70.83	13	14.46	47.74	49.83
0.4	30.5	32	68.91	70.62	11.7	12.9	45.92	46.26
0.6	29.5	31.4	67.81	69.98	11.2	11.8	42.47	44.74

To validate the capability of the GTN model with the consideration of stress triaxiality to predict the fracture depth accurately with different step sizes in the ISF process, the FE results were compared with those of the experimental test for grade 1 and 2 pure

Ti, as shown in Table 6-5 and Figures 6.10 and 6.11. From the table and the figures, it can be seen that there is a good correlation between the FEA using the stress triaxiality modified GTN model and the experimental data of the fracture depth and maximum wall angle. Figure 6.12 shows the variation of the vertical forming force with tool displacement using different step sizes for both grades of pure Ti. The figure reveals that the forming force increases with increased step size; this is due to the fact that stretching in the wall of the ISF part increases with greater step size and this also works to increase the stress level in the forming wall, as shown in Figure 6.13, leading to early fracture in the deformed part.

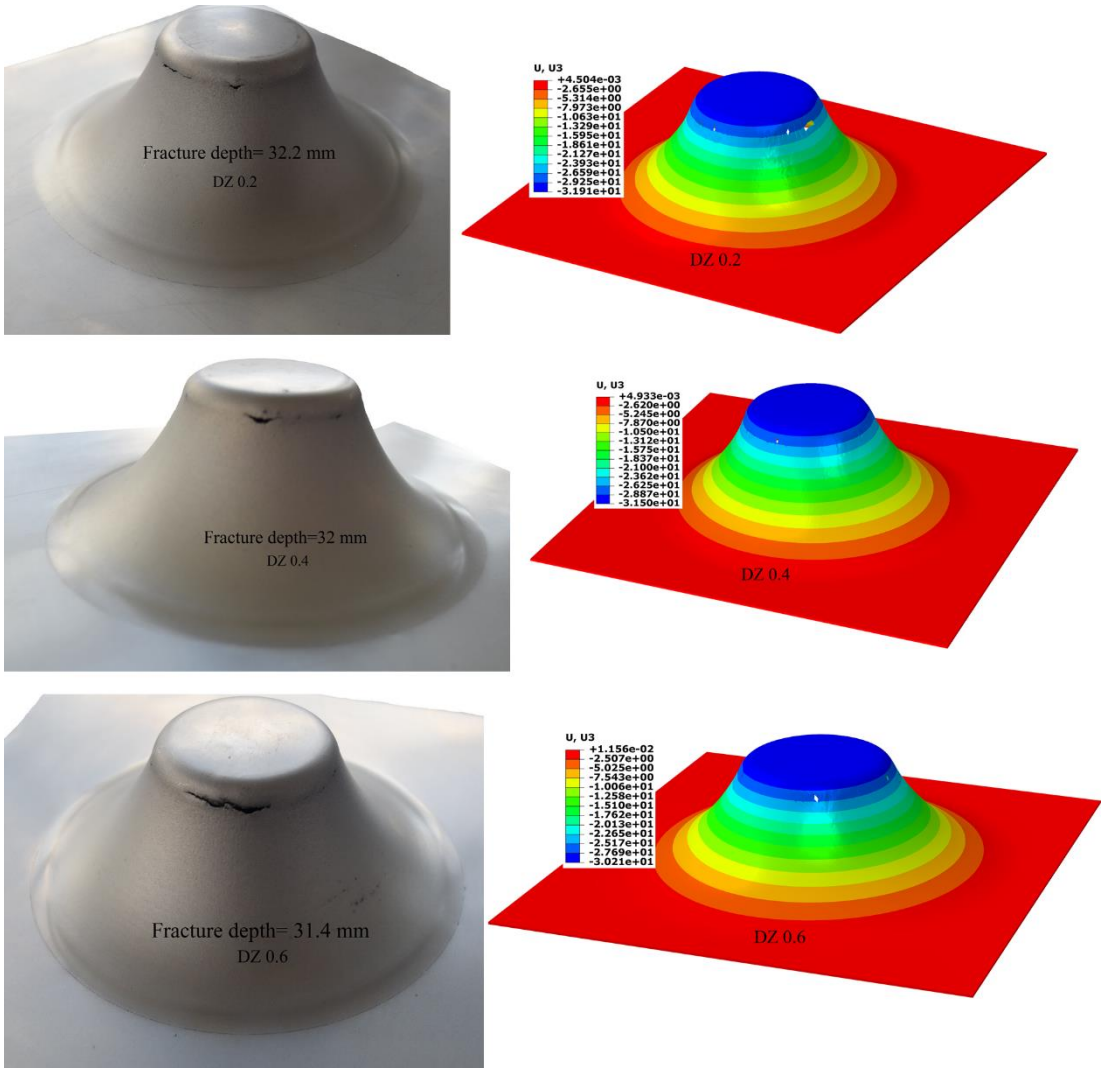


Figure 6.10 Simulated results obtained from the modified GTN model with stress triaxiality in comparison to the actual forming experiment of the pure Ti grade 1 hyperbolic cone shape with different step sizes.

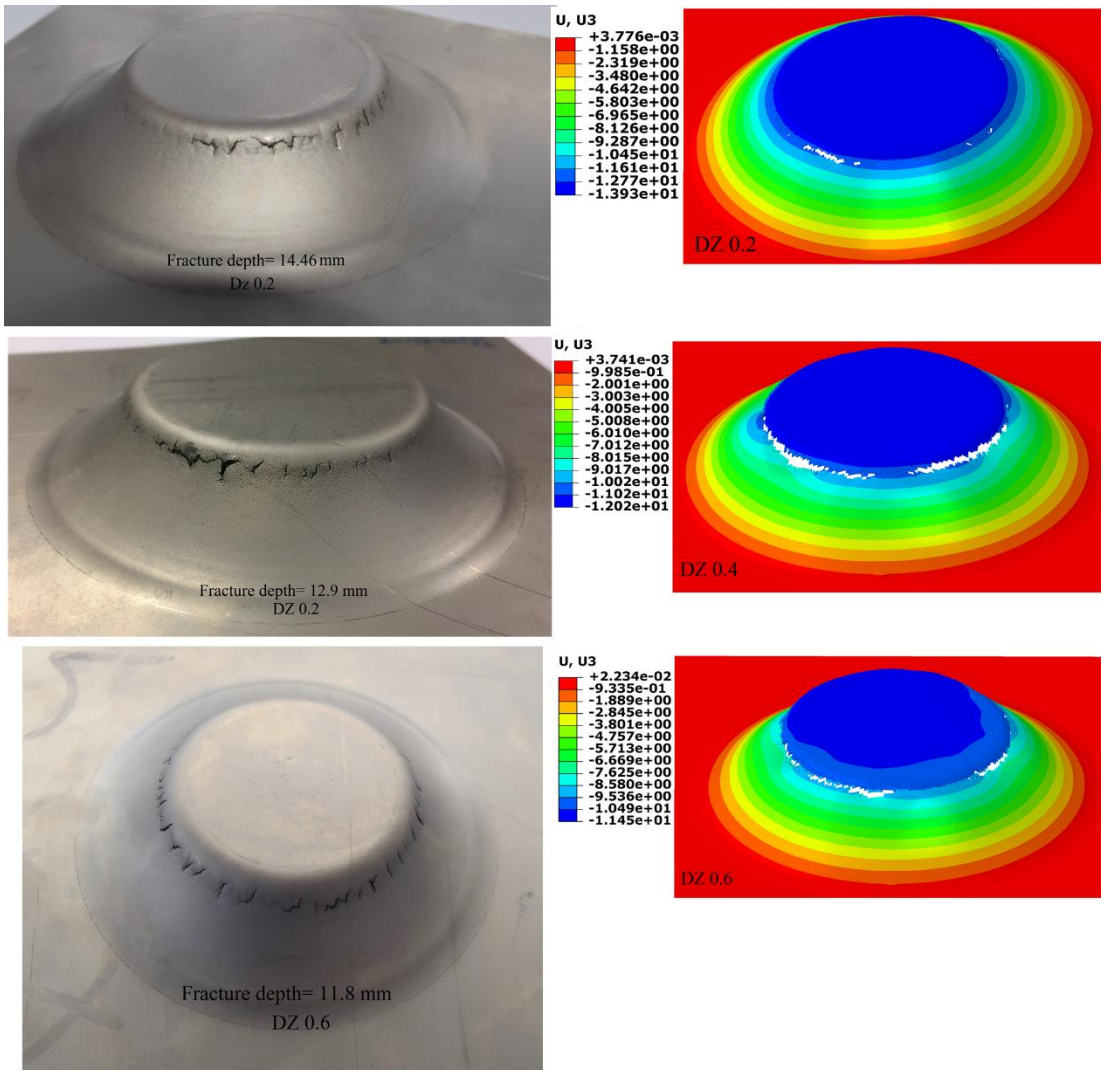


Figure 6.11 Simulated results obtained from the modified GTN model with stress triaxiality in comparison to the actual forming experiment of the pure Ti grade 2 hyperbolic cone shape with different step sizes.

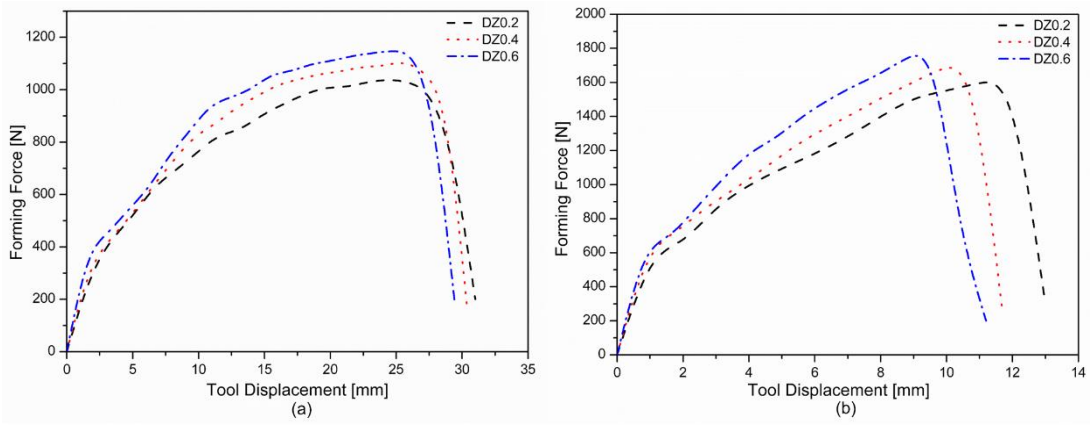


Figure 6.12 Comparison of vertical forming load for different step sizes (DZ): (a) pure Ti grade 1 and (b) pure Ti grade 2.

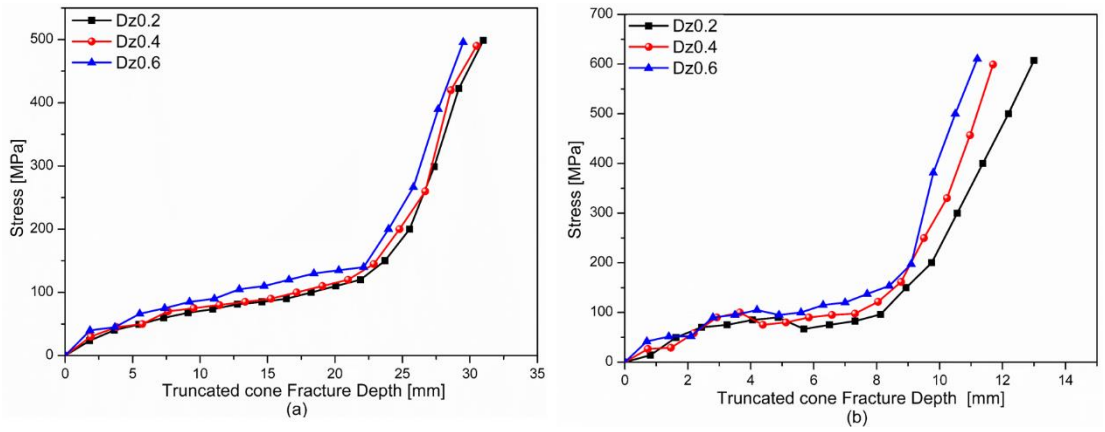


Figure 6.13 History of Mises Stress distribution for different step sizes (DZ): (a) pure Ti grade 1 and (b) pure Ti grade 2.

As the step size increases, the tensile stress in the forming wall increases and the level of fracture strain decreases. It is noted from the Figure 6.14 that the values of major strain decrease with increased step size for both types of pure Ti, but the percentage decrease is higher in grade 2 pure Ti. The increase in the tensile stress due to greater step size enhances the growth of the initial voids and the nucleation of new voids early on and, when the void volume fraction reaches a certain value (0.305 in grade 1 pure Ti and 0.116 in grade 2 pure Ti), fracture occurs, as shown in Figure 6.15. It is clear from the figure that there is a uniform growth of void volume fraction in the early stages of deformation with both grades of pure Ti until a certain depth; then, the void volume fraction curves begin to separate from each other with rapid growth, followed by a sudden fracture.

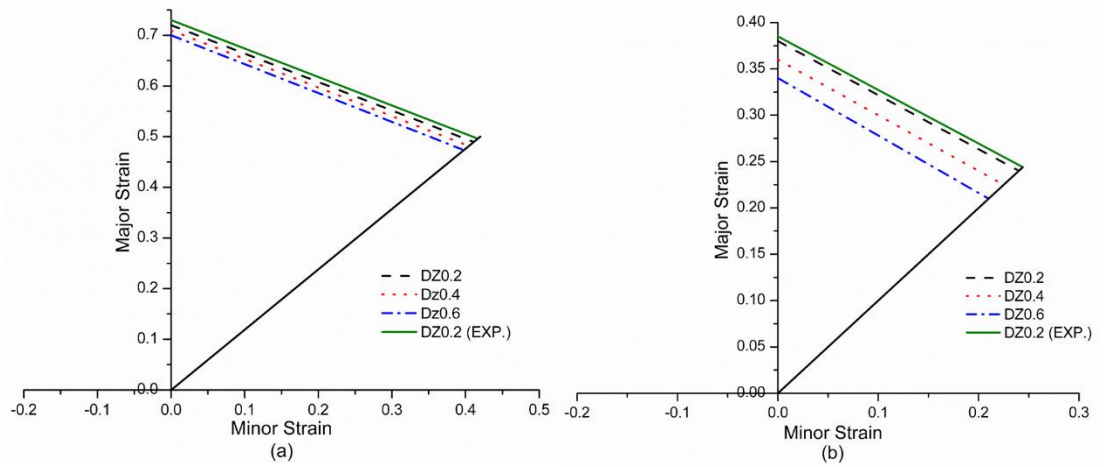


Figure 6.14 FLCFs for different step sizes (DZ): (a) pure Ti grade 1 and (b) pure Ti grade 2.

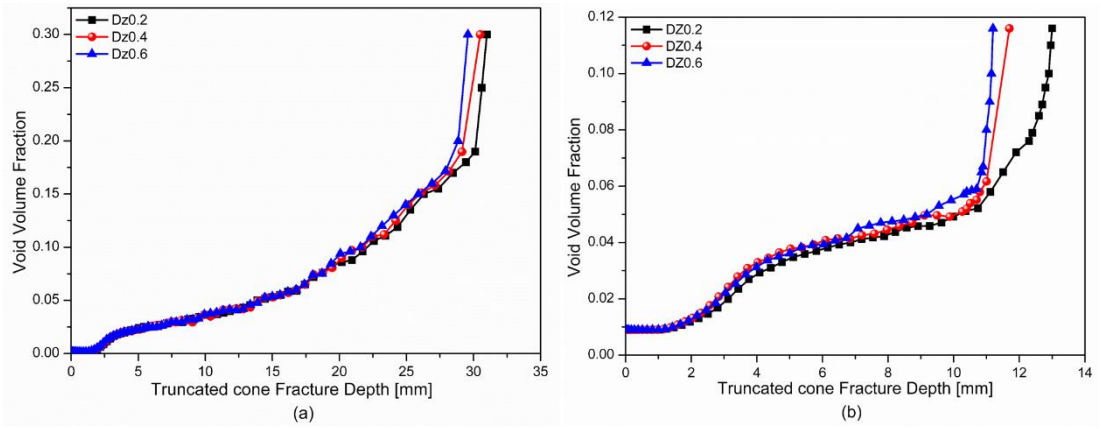


Figure 6.15 History of the void volume fraction obtained by numerical simulation of the ISF process with different step sizes (DZ): (a) pure Ti grade 1 and (b) pure Ti grade 2.

Figure 6.16 shows the effect of step size on the hyperbolic truncated cone thickness distribution at fracture. It is evident that the sheet thinning increases uniformly before reaching the maximum value (fracture thickness) in the transition region between the contact and non-contact zones. Also, it is clear that more thickness reduction can be achieved with a smaller step size as a larger wall angle can be achieved with a small step size.

In summary, it can be concluded that formability appears to be improved with a small step size rather than a large step size with both types of pure Ti because a large step size increases stretching in the wall of the ISF part, which leads to increase in the stress level and to enhancement of the growth of initial voids in the pure Ti matrix to reach the fracture value early.

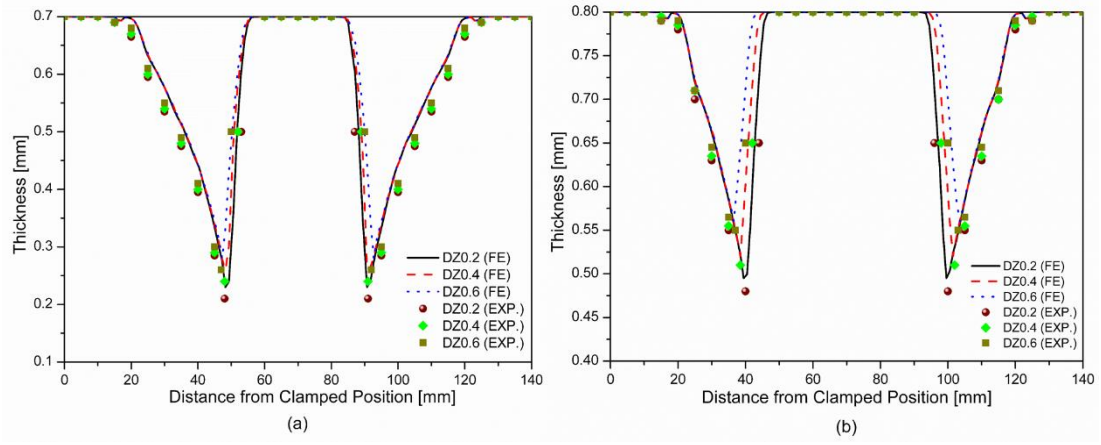


Figure 6.16 Thickness distribution for different step sizes (DZ): (a) pure Ti grade 1 and (b) pure Ti grade 2.

6.4.2 Effect of feed rate

Three feed rates were employed, i.e. 1000, 2000 and 3000 mm/min (Experiment Nos. 1, 4 and 5, respectively) to examine the influence of feed rate on the formability and fracture depth of grade 1 and 2 pure Ti for the hyperbolic truncated cone with a non-rotating tool. The experimental and FE data for the maximum wall angle and fracture depth of grade 1 and 2 pure Ti are reported in Table 6-6. From the table, it is evident that improved formability can be achieved with a low feed rate for both types of pure Ti. 2.73^{o} of experimental wall angle can be earned with grade 1 pure Ti when the feed rate is changed from 3000 mm/min to 1000 mm/min, while 6.1^{o} is earned with grade 2 pure Ti.

Table 6-6 Effect of ISF feed rate on the formability and fracture of grade 1 and 2 pure Ti.

Feed-rate [mm/min]	Pure Ti grade 1				Pure Ti grade 2			
	Fracture depth [mm]		Fracture angle [^{o}]		Fracture depth [mm]		Fracture angle [^{o}]	
	FE	EXP.	FE	EXP.	FE	EXP.	FE	EXP.
1000	31	32.2	69.45	70.83	13	14.46	47.74	49.83
2000	29.8	30.9	68.14	69.42	11	11.5	43.73	45.73
3000	28.7	29.7	66.92	68.1	9.9	10.5	41.95	43.74

The predicted fracture depth of the ISF process under different feed rates was validated by the experimental depth, as shown in Table 6-6 and Figures 6.17 and 6.18 . It is clear that the fracture depth shows a good correlation between simulations results using Abaqus/ Explicit using the stress triaxiality modified GTN model and the experimental measurements.

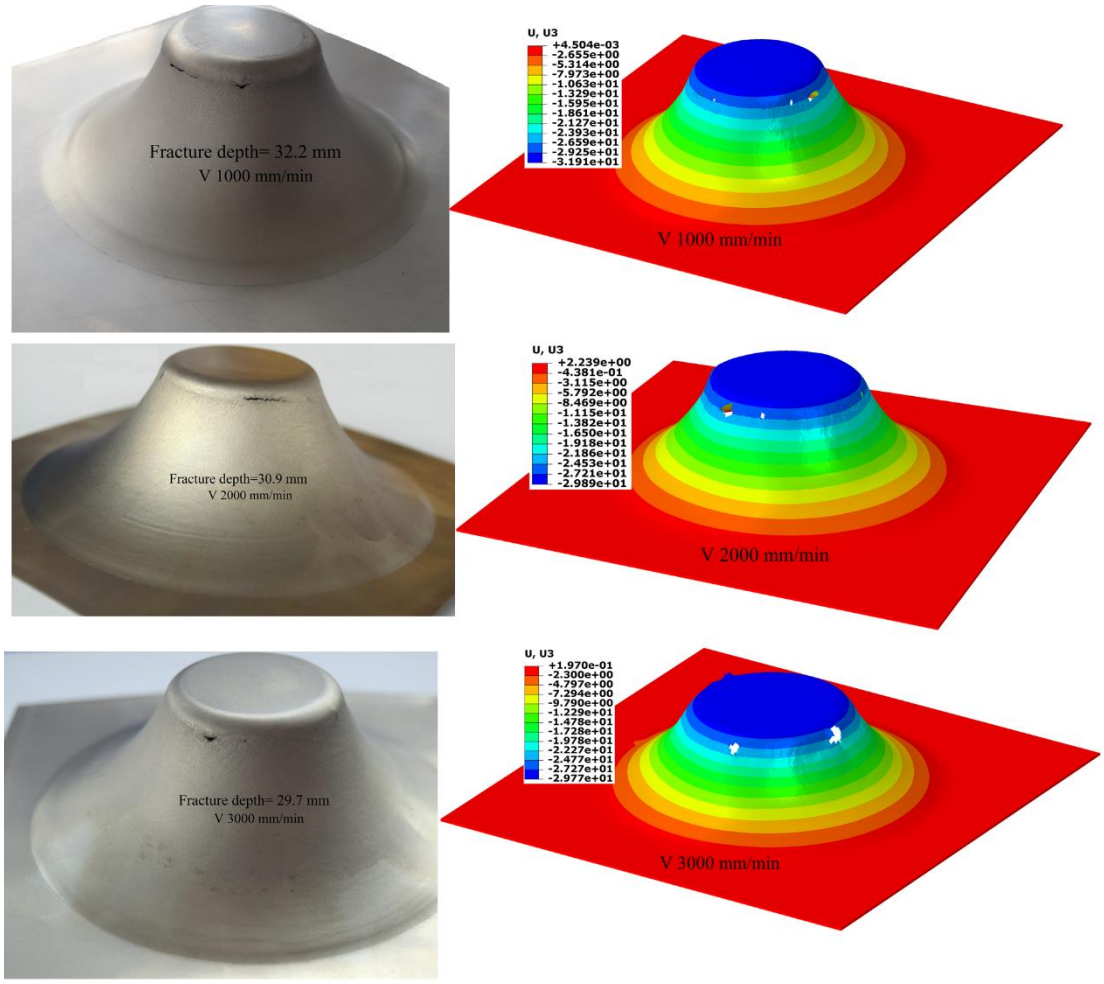


Figure 6.17 Simulated results obtained from the modified GTN model with stress triaxiality in comparison to the actual forming experiment of the pure Ti grade 1 hyperbolic cone shape with different feed rates.

Figure 6.19 shows the effect of feed rate on the vertical forming force. The figure reveals that the ISF force increases with increasing feed rate for both grades of pure Ti. This is attributed to higher strain rate levels; when the feed rate increases, the strain rate increases, as shown in Figure 6.20. It is well-known that high strain rate has a significant effect on fracture occurrence; when the strain rate increases, the fracture occurs early. From the mechanical properties of grade 1 and 2 pure Ti (Figure 6.2), it can be seen that grade 1 pure Ti is more ductile than grade 2 pure Ti. However, Table 6-6 and Figure 6.20 show grade 2 pure titanium is more sensitive to the feed rate, suggesting that the strain rate has a small effect in high ductility materials.

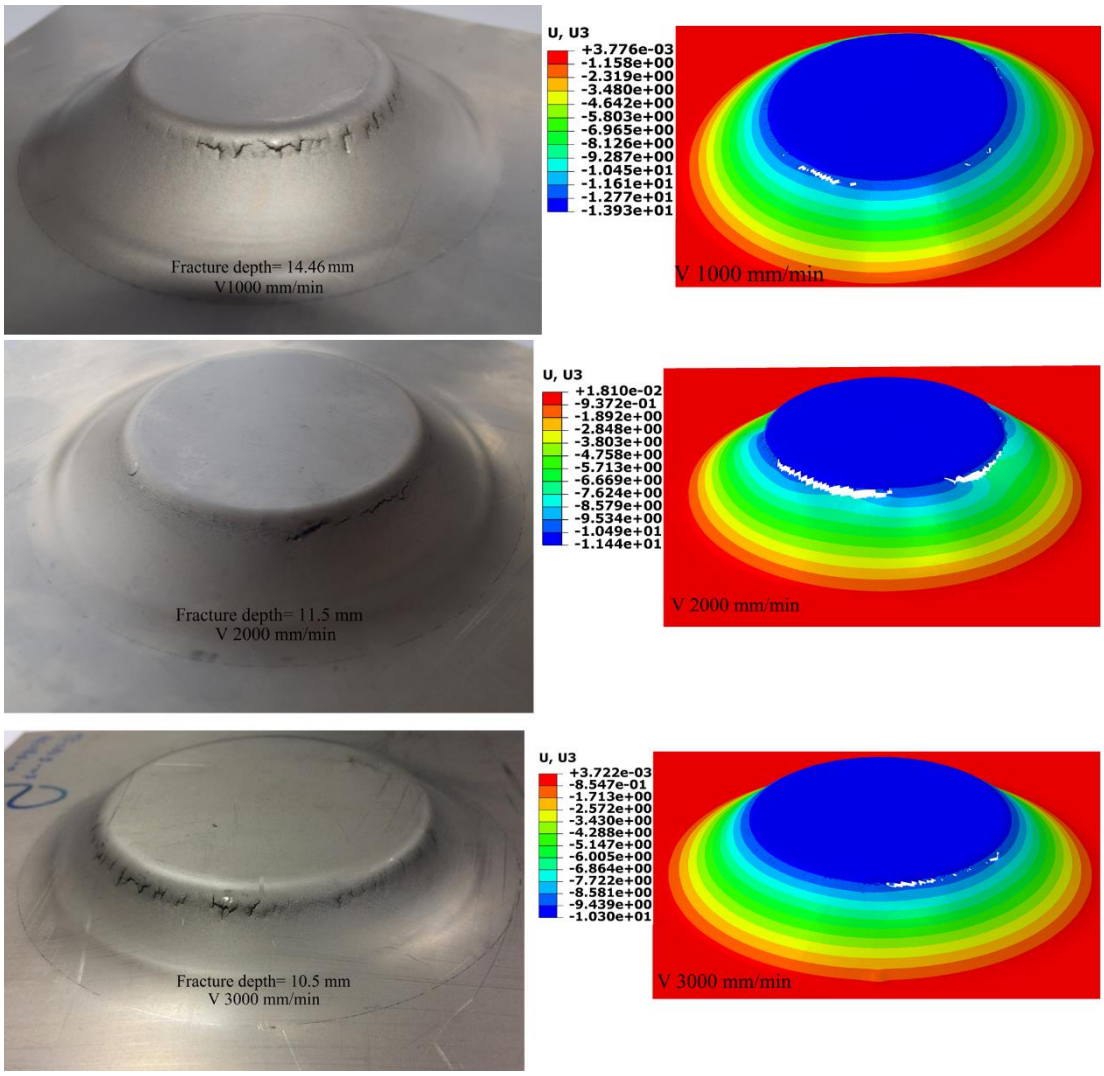


Figure 6.18 Simulated results obtained from the modified GTN model with stress triaxiality in comparison to the actual forming experiment of the pure Ti grade 2 hyperbolic cone shape with different feed rates.

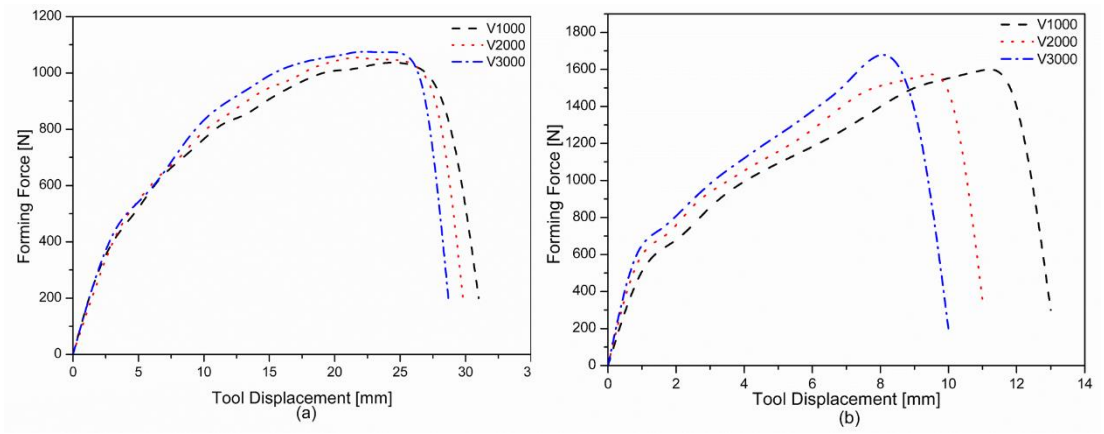


Figure 6.19 Comparison of vertical forming load for different feed rates (V): (a) pure Ti grade 1 and (b) pure Ti grade 2.

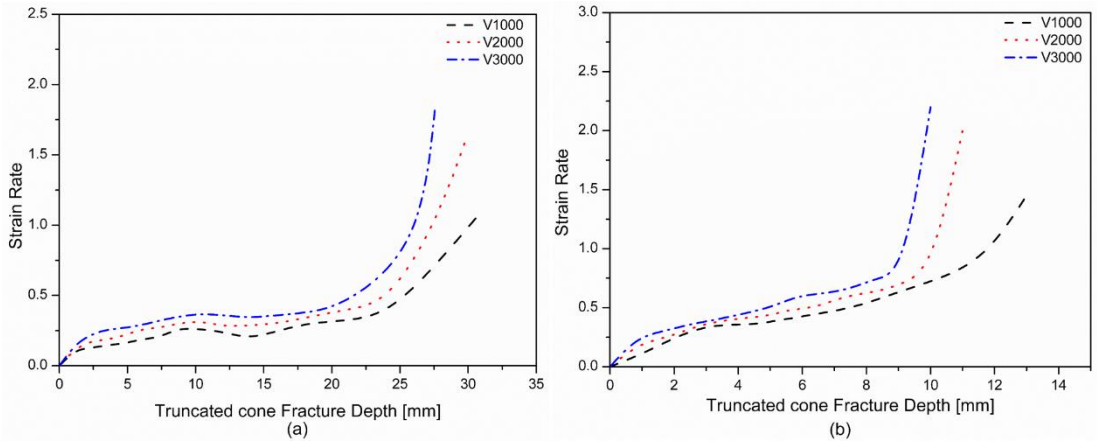


Figure 6.20 Strain rate history for different feed rates (V): (a) pure Ti grade 1 and (b) pure Ti grade 2.

With a high strain rate, the fracture is accelerated and the level of strain at fracture is reduced. Therefore, the FLCF is enhanced with a low feed rate, as shown in Figure 6.21. The value of major strain at fracture of grade 1 pure Ti changes from 0.675 to 0.72 when the feed rate changes from 3000 mm/min to 1000 mm/min, while the FLCF of grade 2 pure Ti changes from 0.34 to 0.38. The level of void volume fraction increases with the feed rate, as shown in Figure 6.22; this is because with a high strain rate, the forming force increases and this can help to generate new voids and encourage the initial voids to get bigger, leading to an increase in the value of the void volume fraction in the transition zone between the contact and non-contact zones, so fracture occurs earlier when the void volume fraction reaches a fracture value.

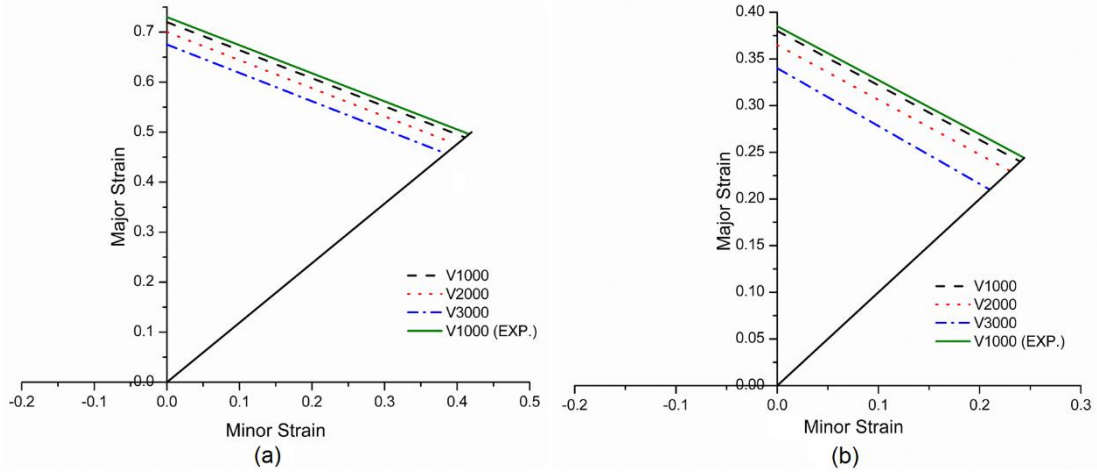


Figure 6.21 FLCFs for different feed rates (V): (a) grade 1 pure Ti and (b) grade 2 pure Ti.

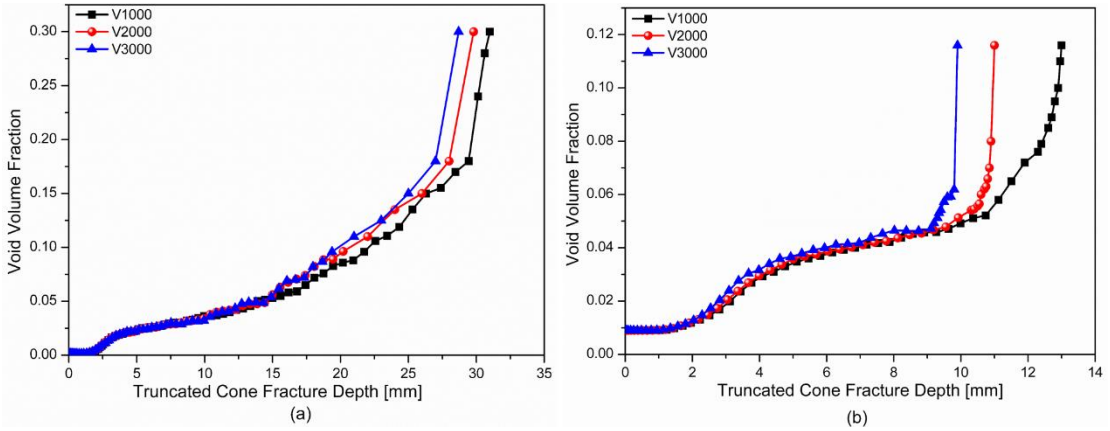


Figure 6.22 history of the void volume fraction obtained by numerical simulation of the ISF process with different feed rates (V): (a) pure Ti grade 1 and (b) pure Ti grade 2.

The predicted thickness was compared with that of the experiment to illustrate the effect of feed rate on thickness distribution. As shown in Figure 6.23, there is a good correlation in the thickness distribution of the hyperbolic truncated cone between the GTN model with the consideration of stress triaxiality and the measured thickness results from ISF experiments. It is shown that relatively high levels of sheet thinning can be achieved with a low feed rate (1000 mm/min) due to the fact that a high wall angle can be achieved with a low feed rate.

In summary, it can be concluded that the low feed rate to some degree postpones the fracture occurrence in both types of pure Ti, although its effect is greater in grade 2 pure Ti. It seems that stabilising effects are present with a low feed rate (low strain rate), which delays the acceleration of damage, as compared to the ISF test conditions of high feed rate.

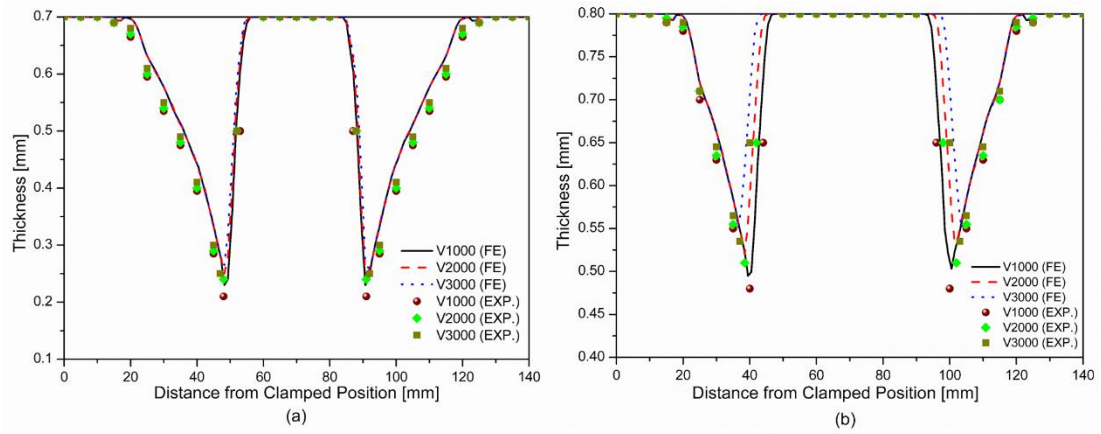


Figure 6.23 Thickness distribution for different feed rates (V): (a) pure Ti grade 1 and (b) pure Ti grade 2.

6.4.3 Effect of tool diameter

Three sizes of hemispherical head tool, 8, 10 and 15 mm (Experiment Nos. 6, 1 and 7) were utilized to evaluate the effect of tool diameter on the formability and fracture depth of grade 1 and 2 pure Ti. Table 6-7 summarizes the values of fracture depth and the maximum wall angle of the pure Ti grade 1 and 2 hyperbolic truncated cone. It is clear from the table that the formability and fracture are enhanced with small tool size. Therefore, the experimental wall angle of grade 1 pure Ti increases by 5.68^{o} when the tool diameter is changed from 15 mm to 8 mm, while 7.65^{o} is earned with grade 2 pure Ti .The fracture results show that the grade 2 pure Ti is more sensitive to the change of the tool diameter than grade 1 pure Ti.

Table 6-7 Effect of ISF tool size on the formability and fracture of grade 1 and 2 pure Ti.

Tool size [mm]	Pure Ti grade 1				Pure Ti grade 2			
	Fracture depth [mm]		Fracture angle [^{o}]		Fracture depth [mm]		Fracture angle [^{o}]	
	FE	EXP.	FE	EXP.	FE	EXP.	FE	EXP.
8	34.5	35.1	73	73.96	15	15.5	49.55	51.2
10	31	32.2	69.45	70.83	13	14.46	47.74	49.83
15	28.5	29.86	66.7	68.28	9.3	10	40.5	43.55

The depths of the ISF truncated cone predicted by Abaqus (stress triaxiality modified GTN model) for different tool sizes are consistent with those of the actual experiments for both pure Ti types, as shown in Table 6-7 and Figures 6.24 and 6.25.

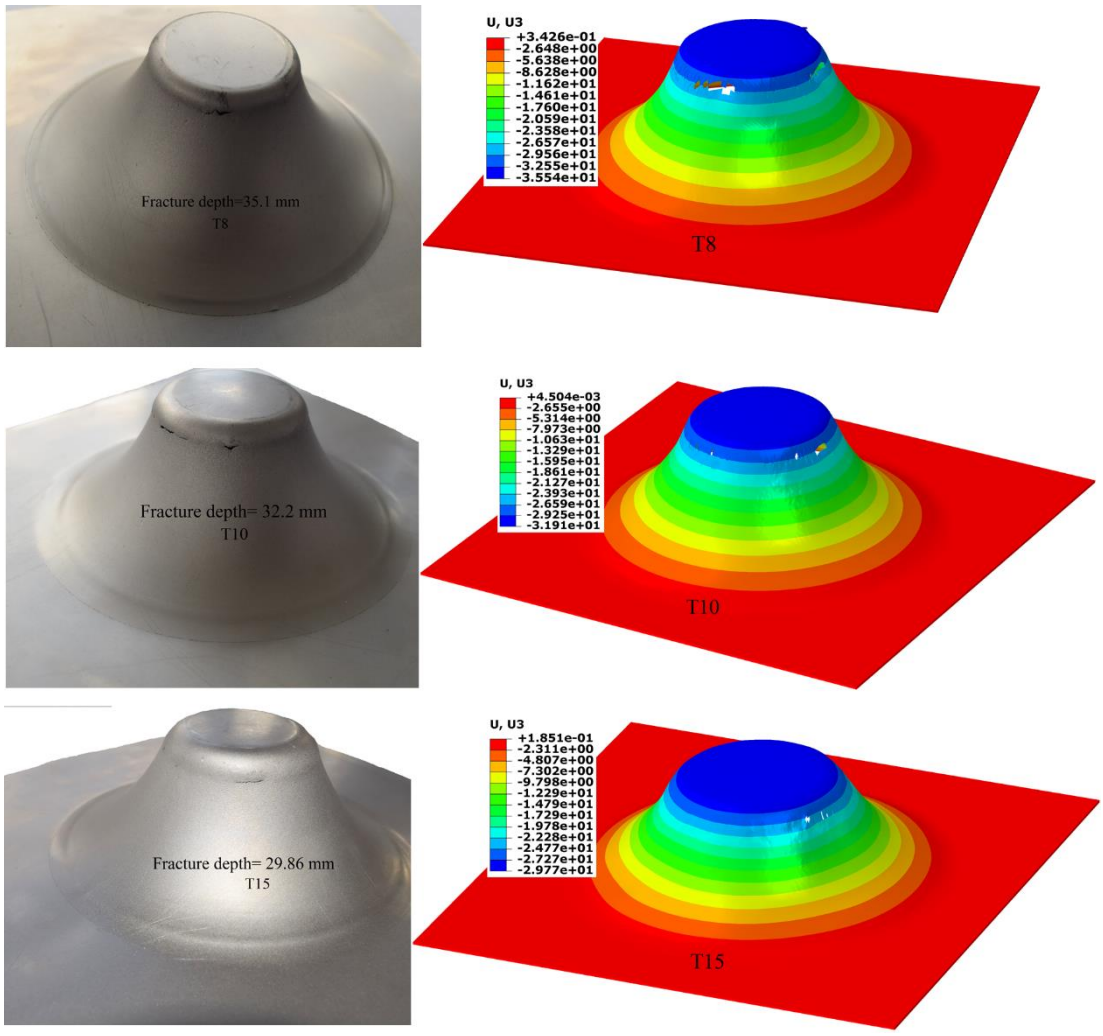


Figure 6.24 Simulated results obtained from the modified GTN model with stress triaxiality in comparison with the actual forming experiment of the pure Ti grade 1 hyperbolic cone shape with different tool sizes.

Figure 6.26 illustrates the effect of tool size on the vertical forming force of the ISF process. It is seen from the figure that the forming load increases with larger tool sizes for both types of pure Ti; this is due to a bigger contact zone being created with a large tool size and an increase in the forming force when the contact zone is bigger. With a smaller tool diameter, a more concentrated zone of deformation is generated in the tool/sheet contact zone and higher strain is to achieved, leading to improved formability. As shown in Figure 6.27, the value of the major strain at plane strain is 0.75, 0.72 and 0.67 for grade 1 pure Ti, and 0.4, 0.38 and 0.34 for grade 2 pure Ti with tool diameters of 8, 10 and 15mm, respectively.

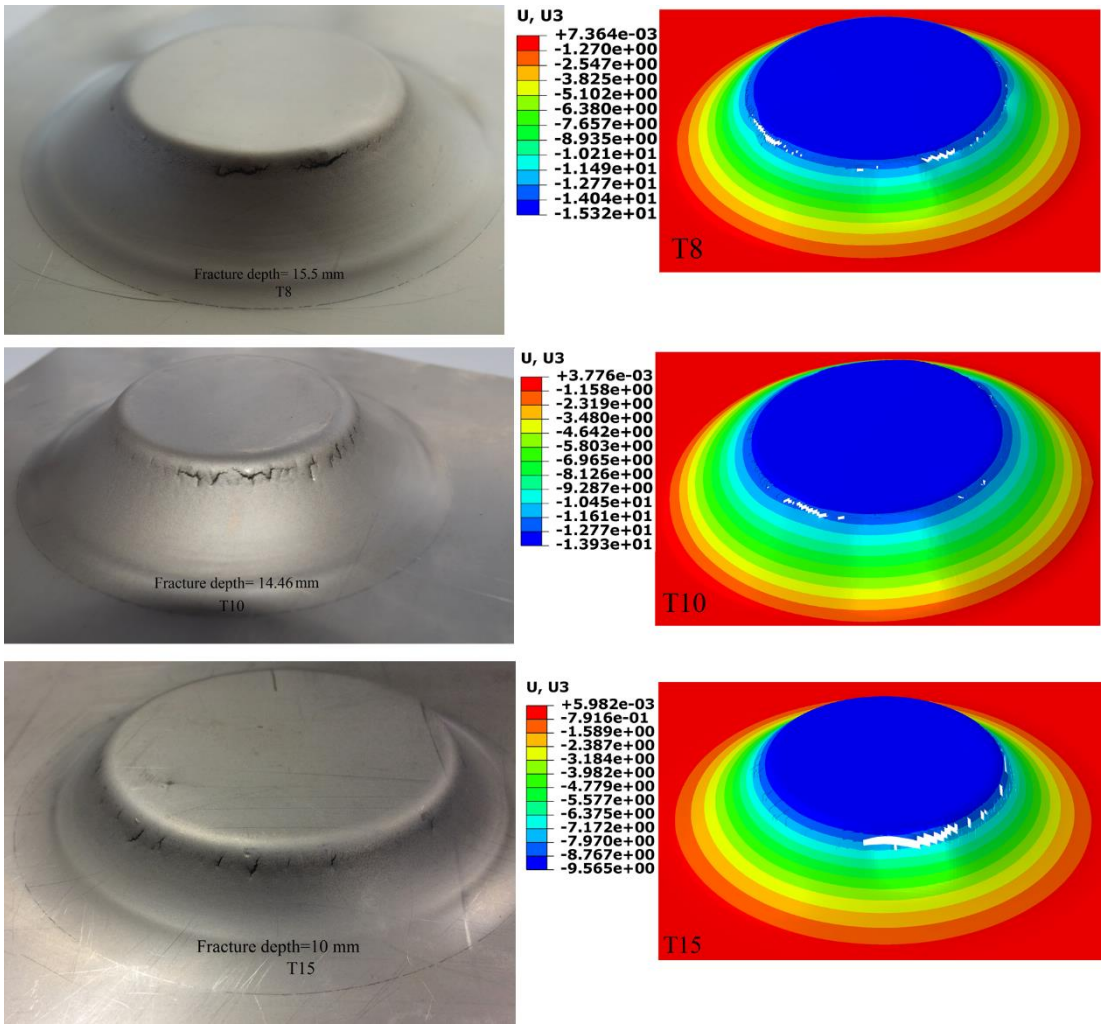


Figure 6.25 Simulated results obtained from the modified GTN model with stress triaxiality in comparison with the actual forming experiment of the pure Ti grade 2 hyperbolic cone shape with different tool sizes.

The growth of voids increases under high tensile forming force, resulting in accelerated fracture occurrence, as shown in Figure 6.28, suggesting that with a large tool size, the void volume fraction reaches the fracture value earlier. The predicted thinning was compared with the experiment to investigate the effect of tool size on thickness distribution and to validate the applicability of the stress triaxiality modified GTN model to predict the accurate thickness at fracture. Figure 6.29 shows the thickness distribution of grade 1 and 2 pure Ti with different tool sizes. It is noted that the significant thinning occurs with a small tool size due to a higher wall angle being achieved; that means with a small tool size fracture occurrence is delayed and formability is enhanced. The thickness results showed a good correlation between the prediction and experimental data.

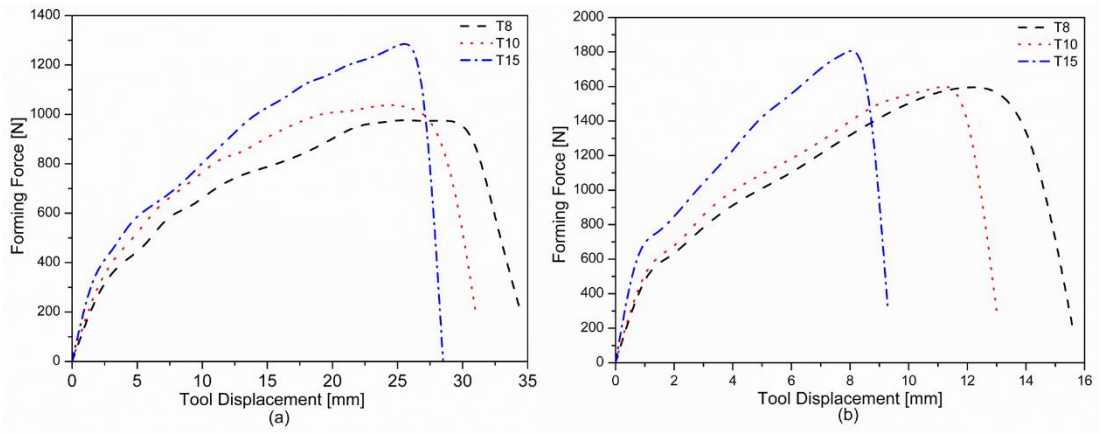


Figure 6.26 Comparison of vertical forming load for different tool sizes (T): (a) pure Ti grade 1 and (b) pure Ti grade 2.

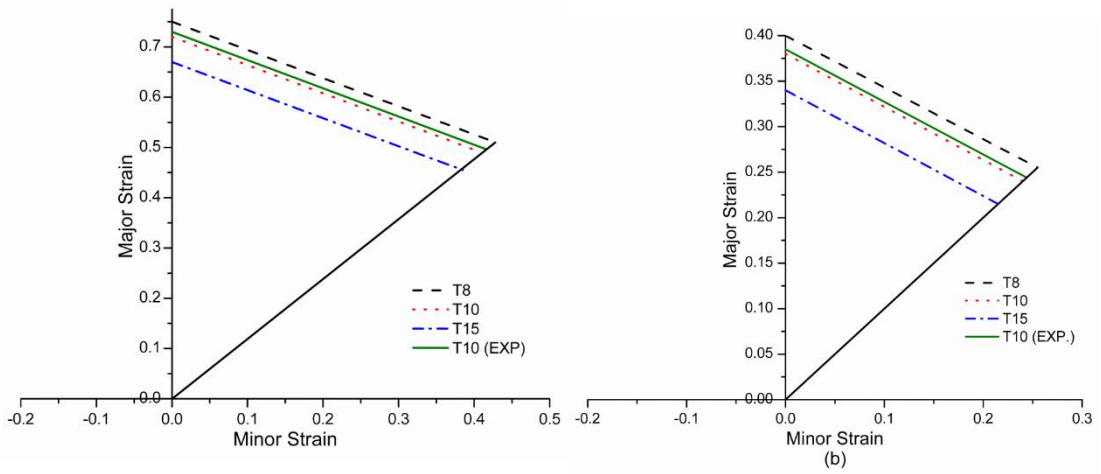


Figure 6.27 FLCFs for different tool sizes (T): (a) pure Ti grade 1 and (b) pure Ti grade 2.

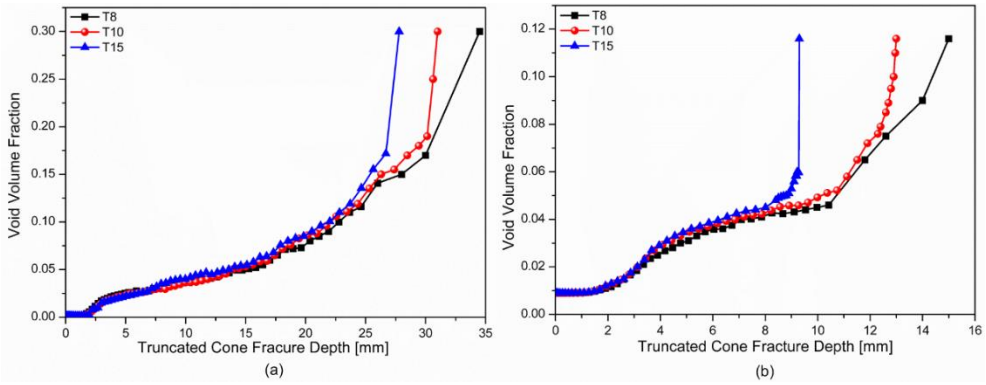


Figure 6.28 History of the void volume fraction obtained by numerical simulation of the ISF process with different tool sizes (DZ): (a) pure Ti grade 1 and (b) pure Ti grade 2.

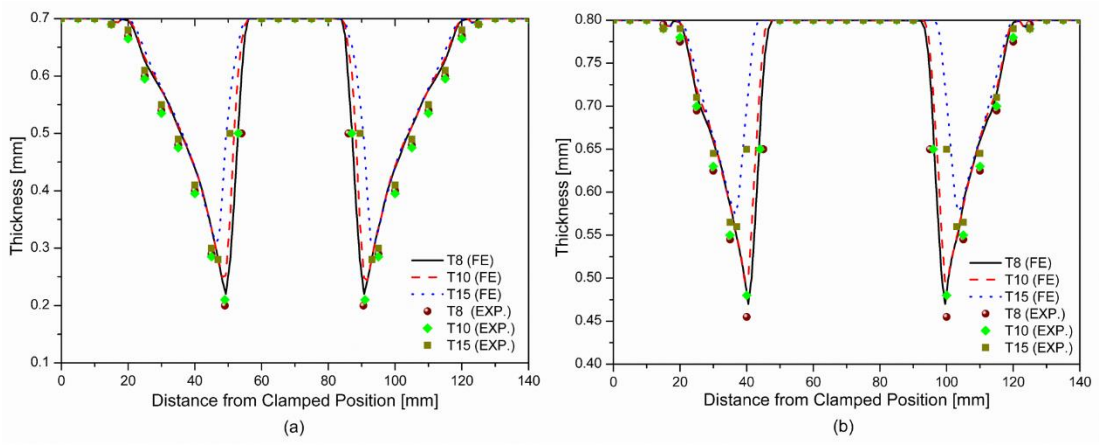


Figure 6.29 Thickness distribution for different tool sizes (T): (a) pure Ti grade 1 and (b) pure Ti grade 2.

6.5 Cranial plate reconstruction

In this section, the feasibility of reconstructing a cranial plate from 0.7 mm grade 1 pure titanium using the SPIF process is examined. To manufacture a cranial plate using the SPIF process, the tool path of a real cranial plate should be generated. Normally, the tool path of the simple parts of ISF is generated based on the freeform surface (CAD model). In cranioplasty, the CT scan is employed to generate a cloud of points for the patient's skull geometry, which is used to generate the CAD model of cranial plate as shown in Figure 6.30.

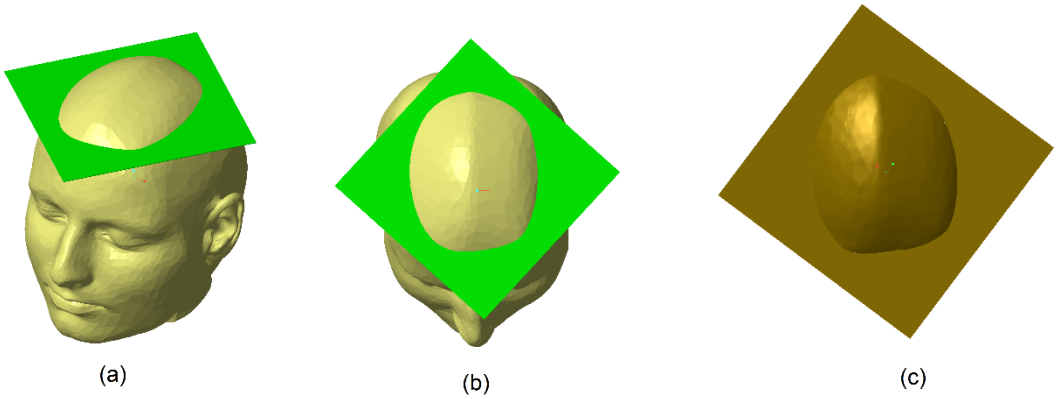


Figure 6.30 Geometric construction of a cranial plate: (a) skull model, (b) top view of the skull and (c) the CAD model of the cranial plate.

To generate a CAD model, a series of cross-sectional images of the patient's head are produced by using a CT scan; these images is combined with a computer programme to obtain a three dimensional CAD model. Based on the CAD model of the cranial

plate, a helical tool path was generated using a feature-based algorithm [88]. In this algorithm, the critical edges, e.g. the top and bottom edges, are detected; then, the contours are generated to be distributed between them. Theoretically, a better surface finish can be achieved using a feature-based approach as well as; more uniform thickness can be obtained with high geometrical accuracy. The generated tool path for the SPIF process of the cranial plate is shown in Figure 6.31.

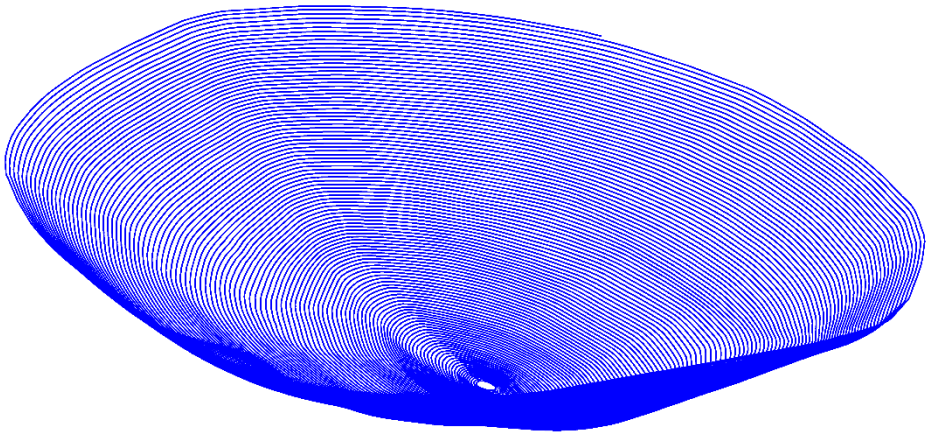


Figure 6.31 SPIF tool path generated for cranial plate forming.

According to the aforementioned parametric study of the SPIF process of a hyperbolic truncated cone, the best formability was achieved with a step size equal to 0.2 mm per revolution and a tool diameter of 8 mm. Moreover, the tool was non-rotating with a feed rate of 1000 mm/min. Therefore, these parameters are used in this work to generate the cranial plate (see Figure 6.32). Based on this feed rate, the time required to create the whole cranial plate is 18.5 mins, which is considered more efficient compared to conventional cranial plate manufacturing methods.

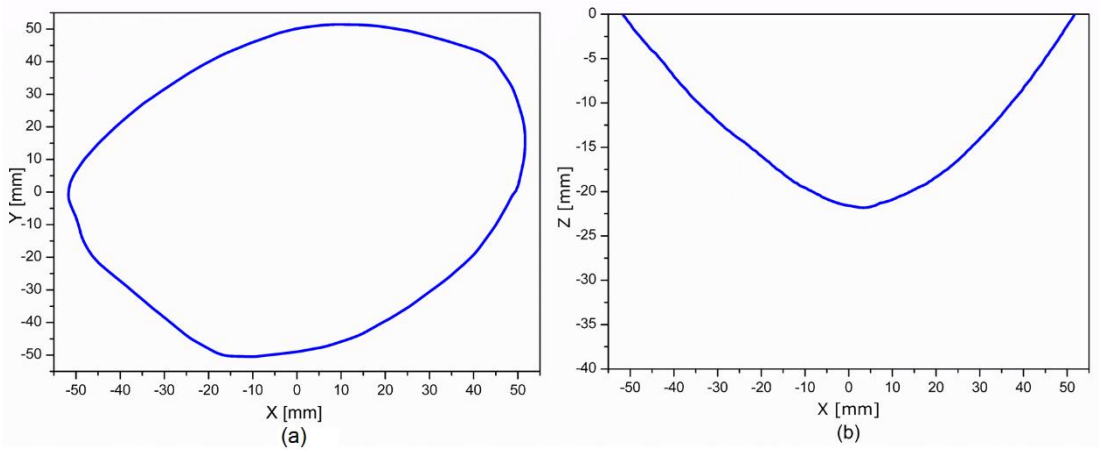


Figure 6.32 Cranial plate geometry: (a) X-Y plane and (b) X-Z plane.

FE analysis, incorporating the GTN model with consideration of stress triaxiality, was carried out to evaluate the formability of grade 1 pure titanium in the ISF process of the cranial plate. Figure 6.33 shows the FE model of the SPIF of the cranial plate forming. It is clear from the figure that a similar fixture to that of the SPIF of a truncated cone is used, except for the backing plate shape, which was customized. The mesh size was 0.5 mm with three layers of elements through the thickness.

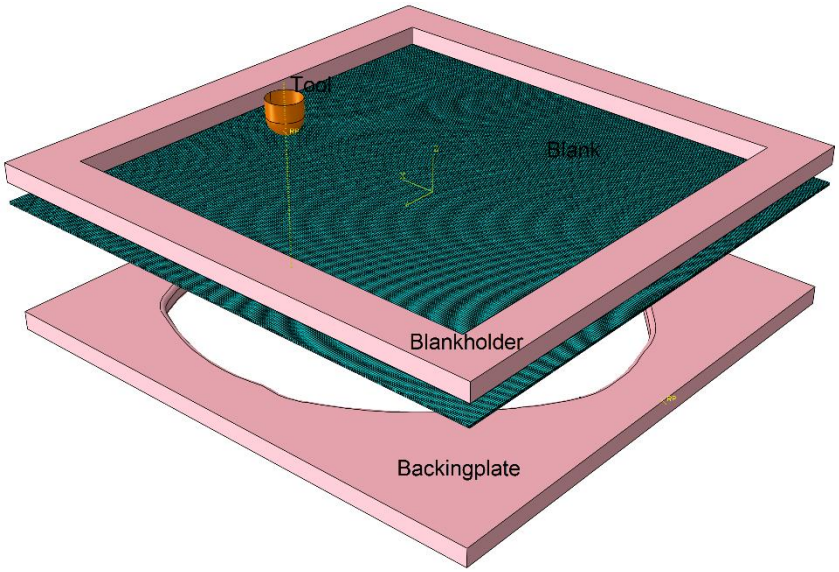


Figure 6.33 Finite element model of cranial plate forming.

A CNC milling machine was utilized to carry out the SPIF test of the cranial plate based on a defined helical tool path. Medical grade titanium sheet (grade 1 titanium) with dimensions of 140 x140 x0.7 mm was utilized for the SPIF test of the cranial plate. Lubricating grease (Rocol RTD compound) was applied to the interface between the forming tool and sheet in order to reduce friction. A customized backing plate was designed and manufactured based on the perimeter of the cranial plate, as shown in Figure 6.34, to ensure the geometric an accuracy of the finished cranial plate. The backing plate was fixed underneath the blank to support the blank through the ISF process. The setup of the SPIF process and formed cranial plate is shown in Figure 6.35.

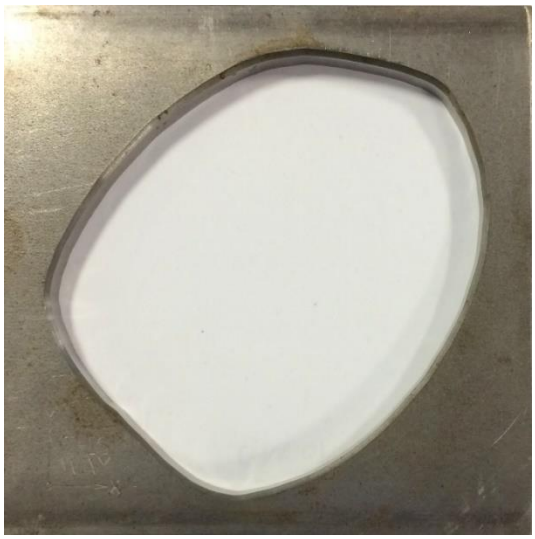


Figure 6.34 A customized backing plate to support the cranial plate during deformation.

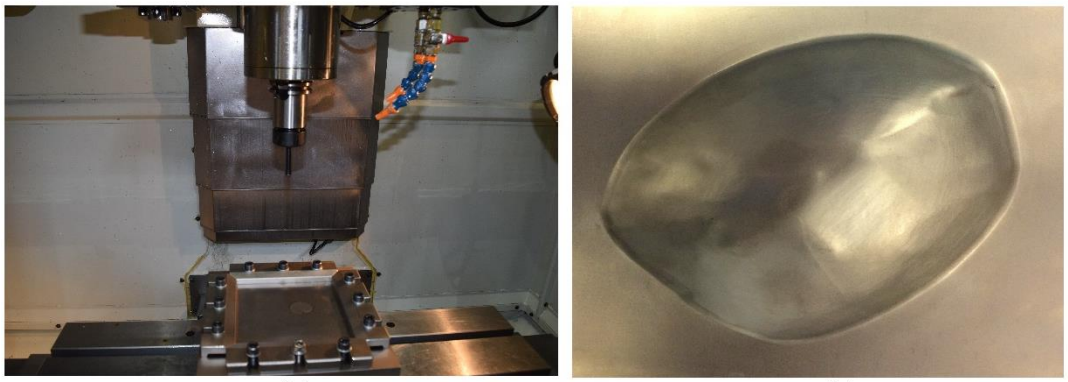


Figure 6.35 SPIF experiments of cranial plate forming: (a) SPIF experiment and (b) deformed cranial plate.

Figure 6.36 shows the distribution and evolution of equivalent plastic strain (SDV1) obtained by FE simulation following increasing depth of cranial plate. It is evident that relatively high strain concentrations were present at the edge of the cranial plate in the early stages of deformation and that is due to the largest wall angle of the cranial profile in the transition zone between the top of the sheet and cranial wall (edge of the cranial plate). The distribution of strain becomes more uniform with the progress of the ISF process due to the fact that changes in the wall angle become more gradual.

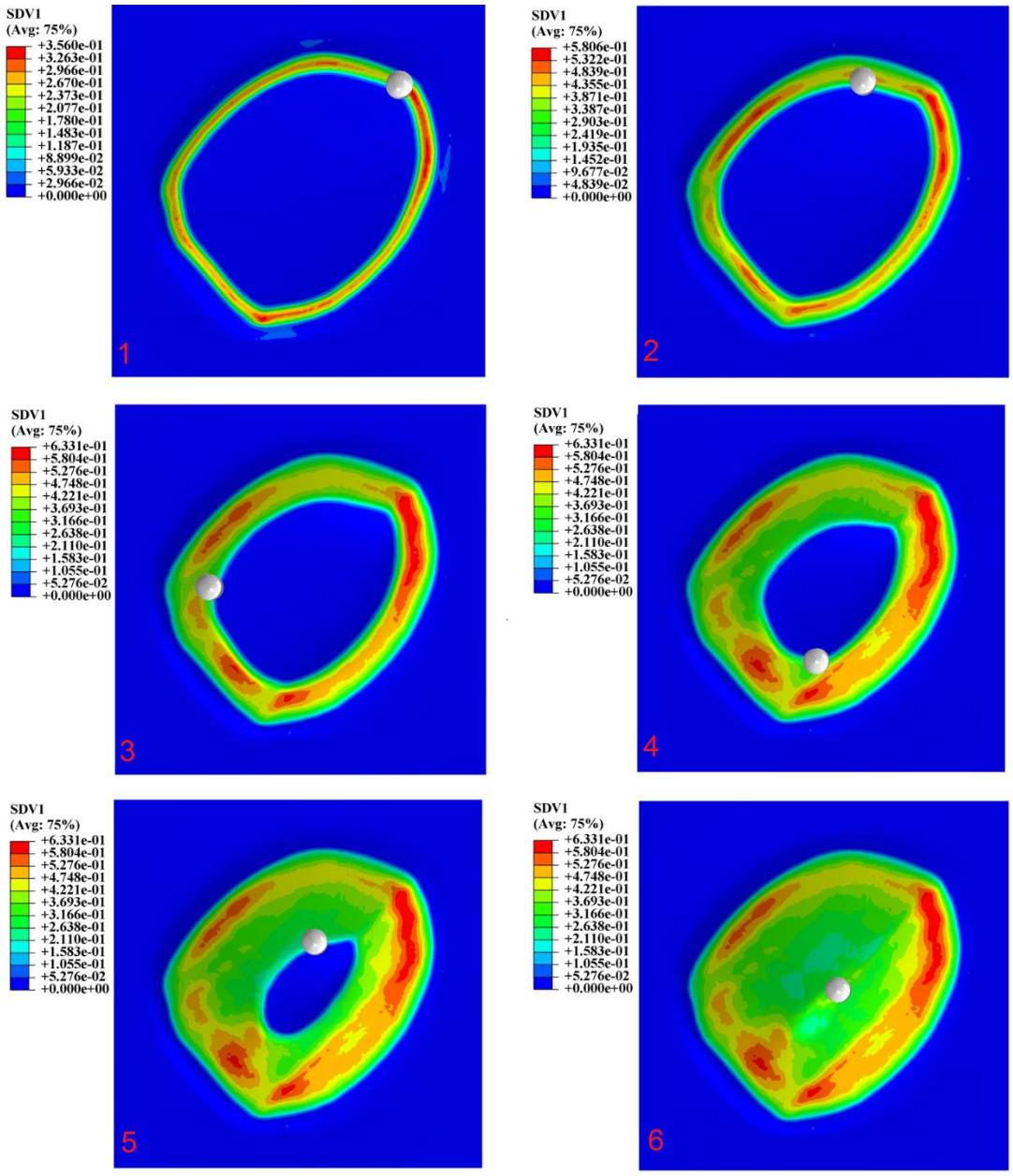


Figure 6.36 Distribution of the equivalent strain (SDV1) obtained by numerical simulation of cranial plate forming at different depths.

It is important to produce a cranial plate with less thinning as thinning could affect the cranial plate's stiffness. In this work, the thickness distribution of the finished cranial plate was measured along two cross-sections (X and Y), as shown in Figure 6.37.

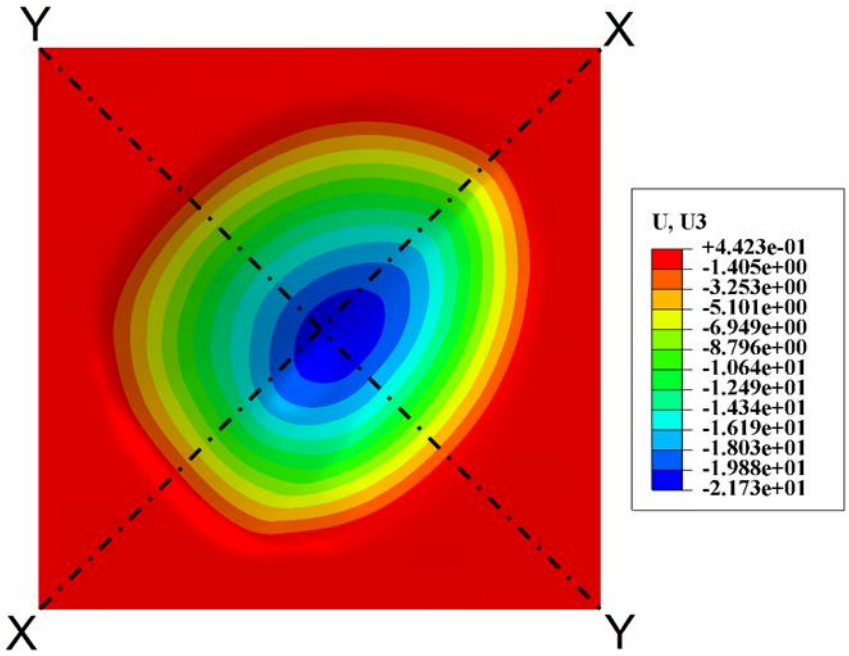


Figure 6.37 The final depth of the cranial plate with the location of cross-sections for thickness measurements.

The thickness distribution in both cross-sections can be seen in Figure 6.38; this figure plots predicted and experimental cranial plate thickness against the distance measured from the clamped position. It is noted from the figure that maximum thinning in the cranial plate wall occurs at the edge, which is due to the fact that the largest wall angle lies in this region, whereas less thinning is found at the bottom of the cranial plate since the wall angle gets smaller with the progress of cranial deformation. With an initial blank thickness of 0.7 mm, the minimum thickness in the deformed cranial plate is 0.56 mm and this is equivalent to a thickness reduction of 20%. This percentage thickness reduction is considered to be acceptable because the percentage thickness reduction at fracture for grade 1 pure titanium with the same ISF parameters is 68%, as explained in the section which discusses the effects of tool diameter. Therefore, this cranial plate is considered safe in the scope of thickness distribution.

The predicted thickness was compared with that of the experiment to validate the FE results, as shown in Figure 6.38. There is a good correlation in terms of the thickness distribution of the carinal plate between the GTN model with the consideration of stress triaxiality and the measured thickness results from the ISF experiments.

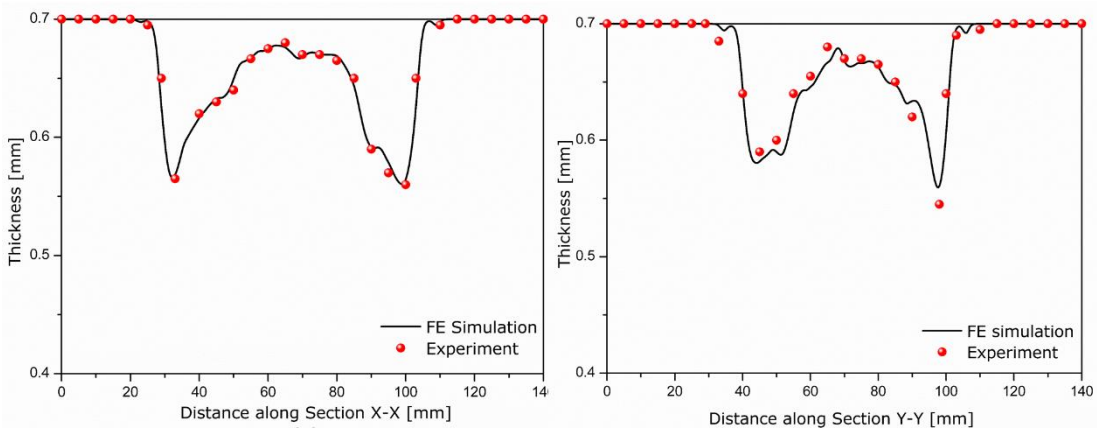


Figure 6.38 Thickness distribution along sections X-X and Y-Y.

Since this work uses the GTN damage model to predict the fracture and, in this model, the fracture is determined based on micro-void nucleation, growth and coalescence mechanisms, it is worth investigating the void volume fraction (VVF) distribution on the formed cranial plate. Figure 6.39 shows the VVF distribution along both sections (X and Y). It is clear from the figure that the VVF tends to localize during the early stages of the SPIF process and reaches maximum values, after which more uniform distribution can be obtained; this is attributed to high levels of stretching, which are associated with a high wall angle at the cranial plate edge. The VVF increases due to the growth of the existing voids and the nucleation of the new void. The maximum value of the VVF in the formed cranial plate is 0.0286, while the fracture VVF of grade 1 pure titanium is 0.3025, meaning that the pure titanium matrix of the finished cranial plate remains uniform and the void size is so small that it does not affect the strength and load bearing capability of the formed cranial plate.

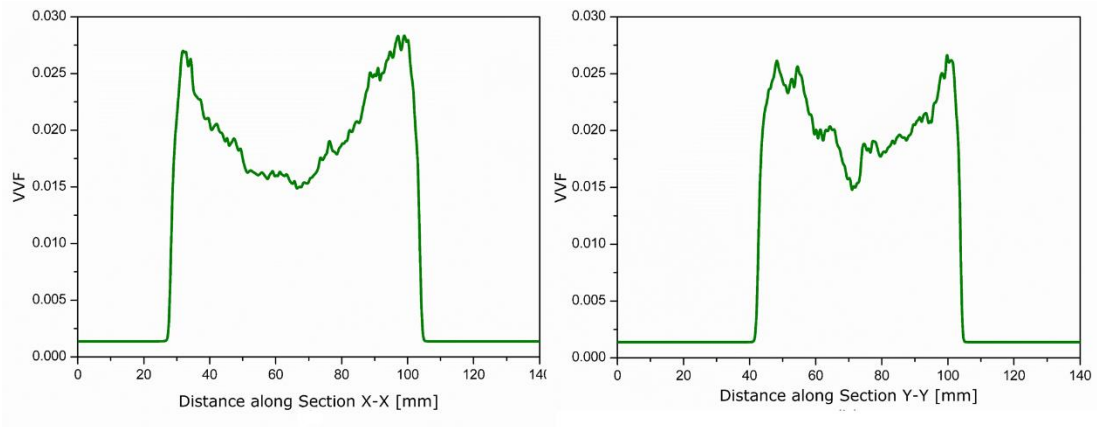


Figure 6.39 Void volume fraction distribution along sections X-X and Y-Y.

The forming limit curve at fracture (FLCF) is used in the SPIF process to represent the strain limit of the materials before the fracture occurs. In this work, FLCF is used to evaluate the major strain of the cranial plate and to check the safety of this cranial plate, as well as to determine under which state of strain the cranial plate is deformed. Figure 6.40 shows the major-minor strain distribution for the cranial plate in the FLCF plot of the SPIF process with forming parameters being: 8 mm tool diameter, 0.2 mm step size and 1000 mm/min feed rate. It is clear from the figure that the major-minor strain of the cranial plate under the fracture curve and all the strains are located in the safe zone; moreover, the minor strain is very small compared to the major strain, indicating that the cranial plate deforms under the plane strain condition. To determine quantitatively under which strain state the cranial plate is deformed, the major strain was compared with the minor strain, as shown in Figure 6.41, and the strain ratio was determined. It is clear from the figure that the minor strain remains close to zero through the cranial plate deformation process, while high values of major strain are obtained. Based on these data, the ratio between the true minor strain ε_2 to the true major strain ε_1 ($\rho=\varepsilon_2/\varepsilon_1$) was determined to be 0.0488, which proves that the cranial plate deforms in a plane strain state due to the strain ratio being close to zero.

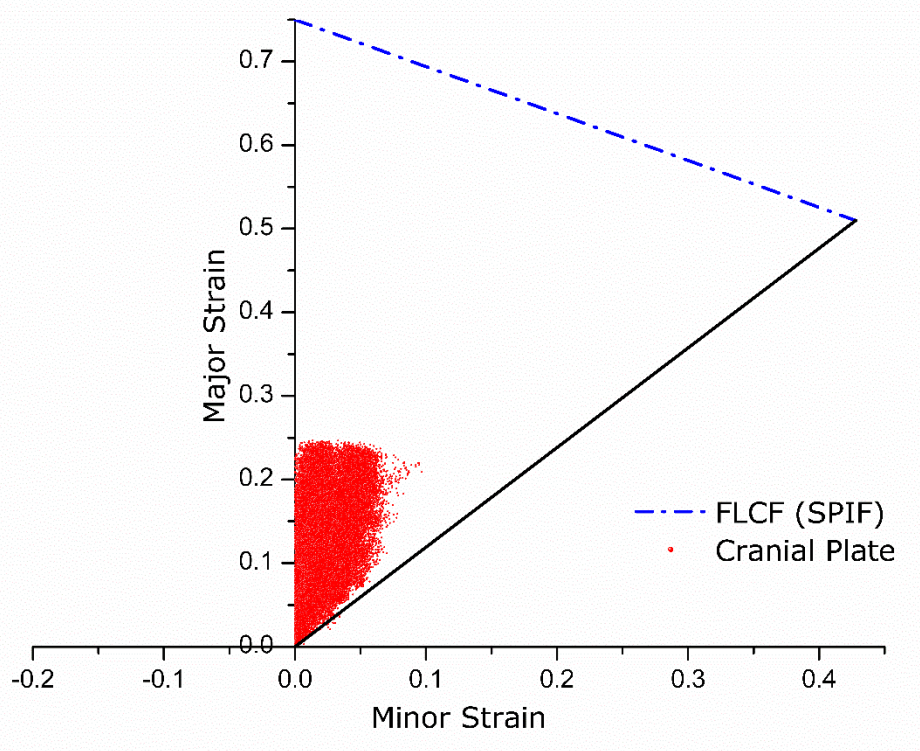


Figure 6.40 Distribution of major and minor strain in forming limit diagram.

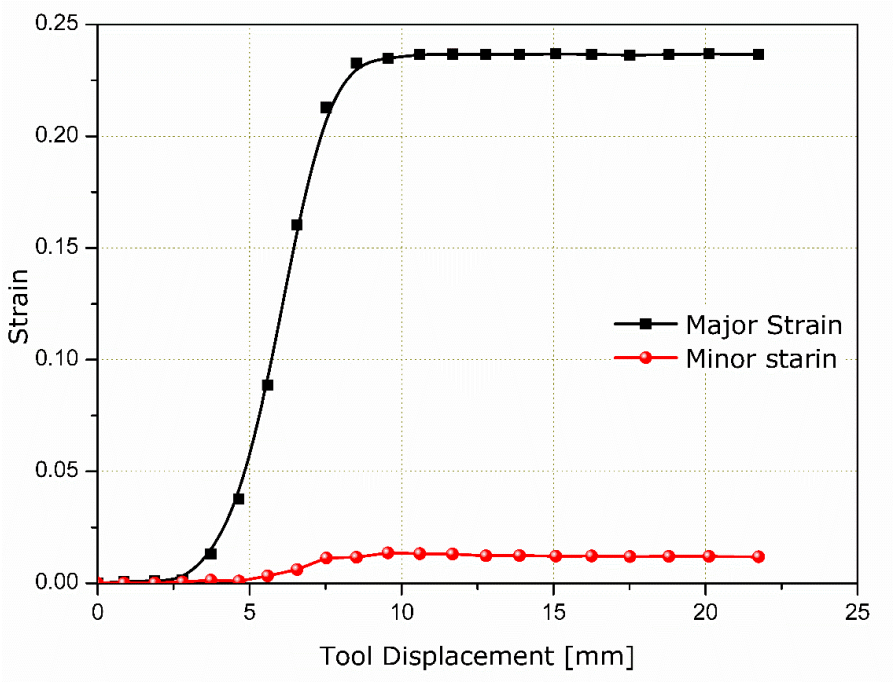


Figure 6.41 History of major and minor strain in cranial plate.

6.6 Conclusions

This chapter aims to provide a better understanding of the effect of three key forming parameters, namely the step size, feed rate and tool size, on the formability and fracture in the ISF process of grade 1 and 2 pure Ti. Experimental testing and FE analyses incorporating the GTN based ductile fracture model were used in order to evaluate the significance of each parameter and to examine the degree of its effect on formability and fracture occurrence. In addition, the sensitivity of material type to forming parameters is discussed in this work. The optimal parameters from the parametric study of ISF process were employed to investigate the feasibility of manufacturing titanium cranial plate using ISF approach.

A comparison between the FE analysis using the stress triaxiality modified GTN model and experimental testing data highlighted the accuracy of the GTN model in terms of stress triaxiality to evaluate the formability and predict the fracture during ISF process to form truncated hyperbolic cone and pyramidal shapes. It was found that the step size, feed rate and tool size have different degrees of effect on the formability and fracture occurrence of the ISF process. The grade 2 pure Ti is more sensitive to forming parameters than grade 1 pure Ti. The maximum wall angle of the grade 1 pure Ti hyperbolic truncated cone increases by 0.85^{o}, 2.73^{o} and 5.68^{o} when the step size is changed from 0.6 mm to 0.2 mm; the feed rate changes from 3000 mm/min to 1000 mm/min and the tool diameter changes from 15 mm to 8 mm, respectively, whereas the increase in the maximum wall angle of grade 2 pure Ti is 5^{o}, 6.1^{o} and 7.65^{o} with the same changes in the ISF parameters.

According to the parametric study of the ISF process of a hyperbolic truncated cone, the best formability was achieved with a step size equal to 0.2 mm and a tool diameter of 8 mm. Moreover, the tool was non-rotating with a feed rate of 1000 mm/min. Therefore, these parameters were used to generate the cranial plate. The results showed that ISF can satisfactorily form a customized titanium cranial plate with thickness reduction about 20% and very low percentage of void volume fraction (0.0286). Moreover, all the major-minor strain of the cranial plate is distributed in the safe zone of the FLD.

CHAPTER 7

DEFORMATION AND FRACTURE OF ALUMINIUM MATRIX COMPOSITE AND ITS APPLICABILITY FOR ISF

7.1 Introduction

In metal matrix composite (MMC) materials, the reaction between the metal matrix and reinforcement particles could change the composition of the matrix and the interface and lead to interfacial compounds. These intermetallic compounds may have either a deleterious effect on the mechanical properties or beneficial effect in enhancing the fracture toughness and ductility of the composite. An aluminium 6092 alloy with 17.5% volume fraction silicon carbide (SiC) particles sheet (6092Al/SiCp), heat treated to T6 condition, is used in this chapter to obtain a fundamental understanding of the heat treatment effect on the fracture mechanism, the microstructural changes and the interface between the Al-matrix and SiC particles. Also the investigation of the applicability of using incremental sheet forming process to form the 6092Al/SiCp aluminium matrix composite (AMC) under different heat treatment conditions is undertaken. Changes in the microstructure of the Al/SiCp and the topography of the fracture are investigated using scanning electron microscopy (SEM) coupled with energy dispersive X-ray spectroscopy (EDS) and transmission electron microscopy (TEM) to characterise the precipitate and intermetallic compounds formed at the Al/SiC interface. X-ray diffraction (XRD) is utilized to characterise the phase formation and to give confidence in the results of TEM and EDS. Tensile tests with different strain rates ($8x10^{-5}$, $8x10^{-4}$, $8x10^{-3}$, $8x10^{-2}$ and $0.16\ s^{-1}$) were carried out to study the fracture mechanism and to find a correlation between the deformation behaviour and heat treatment.

The MMC material is composed of a ductile metal matrix (e.g. aluminium or titanium) reinforced with a ceramic such as silicon carbide or graphite [160]. The MMC has excellent mechanical properties, compared to monolithic alloys including much improved strength to weight ratio and stiffness, which makes it attractive for

automobile and aerospace applications [161, 162]. ISF is a suitable process for manufacturing small batch or customised AMC sheet components. However, it can be technically challenging to form a complex shape of AMC sheets due to their low ductility as an inherited trade-off for the enhanced strength. The discontinuous reinforced MMCs have a number of properties, which are more beneficial than those of continuous fibre-reinforced composites, e.g. ease of fabrication and isotropy [163]. The silicon carbide, as a fibre or particle reinforced Al matrix composite (Al/SiC), can be considered the most favourable type of AMC [164]. The SiC reinforcement can enhance the Young's modulus and yield stress, but the ductility of the composite is significantly lower than those of wrought alloys [161, 165]. The hexagonal platelet shape of Al_4C_3 and elemental Si are formed at the carbide/matrix interface as a result of direct reaction between the SiC and Al [166, 167]. The presence of Al_4C_3 has an undesirable effect on the mechanical properties of the composite due to the fact that it is brittle and unstable in corrosive environments such as hydrochloric acid, methanol and water, under which fatigue crack growth can accelerate.[168, 169]. Therefore, there are two methods to suppress or minimize the formation of Al_4C_3: the first method is to add a large amount of Si to the Al matrix, normally 10-12% [168]. The second is to produce a SiO_2 layer on the surface of the SiC by artificial oxidation [170]. The percentage of Cu has a significant effect on the ageing behaviour and hardness of Al-Si-Mg cast alloy and AA6082 Al-Mg-Si alloy; e.g. the age hardening rate decreases and the hardness increases as the weight percentage of Cu rises [171, 172]. The physical and mechanical properties of Al-SiC composites are altered by changing the particle size of Al and SiC and the SiC volume fraction. The physical properties deteriorate when the Al and SiC particle size decreases and the SiC volume fraction increases. On the other hand, the hardness is enhanced by increasing the SiC volume fraction and decreasing the particle size of Al and SiC [173].

Primary and secondary voids exist on the fracture surface of 6061/SiCp; the primary voids are identified with the brittle fracture of composites and are nucleated either at the decohering interface or from broken particles and their shape and size correlate with the SiC particles. The secondary voids govern the ductile fracture of composites and are created in the maximum ligaments between particles [174]. The quasi-static and dynamic fracture toughness test of 6061Al composite, reinforced with 15% and 20% volume of SiC particles shows that the addition of SiC particles decreases the

fracture toughness of 6061Al alloy [175]. The mechanical properties of 6061Al- and 7108Al-SiCp composites are affected by rolling and heat treatment; hot rolling increases the Young's modulus and ultimate tensile stress of 6061Al- and 7108Al-15%SiC_p as compared to as-cast composite. In addition, elongation to fracture increases by 3-4 times in 6061/SiCp when annealed at 413 °C as compared to rolled composite [176]. The strain rate has a significant effect in increasing the strain hardening coefficient and maximum strength of Al-Li (8090)/SiCp composite; increasing the strain rate from 10^{-3} s^{-1} to 6500 s^{-1}, doubles the strain hardening coefficient [163]. The strength of 6061/SiCp is significantly affected by heat treatment; the strength increases by modification of the standard T6 heat treatment for 6061Al alloys.

Preliminary investigation to evaluate the applicability of ISF to composite/laminate materials was attempted by Fiorotto et al. [177]. The initial results showed ISF is suited to make parts from composite/metal hybrid materials. Various designs of sandwich panel were used to evaluate the feasibility of ISF to form the sandwich panel. It was found the ductile and large incompressible core sandwich panel can be produced using ISF [178].

The reinforcement of SiC particles is used to enhance the strength and stiffness of Al-alloys, and T6 treatment is utilized to increase the strength of Al-alloy via the formation of precipitations in the Al-matrix. Therefore, the Al/SiCp composites with T6 treatment have high strength and low ductility. Consequently, the Al/SiCp composite after T6 treatment may not be suitable for direct application in large deformation processes e.g. SPIF. The purpose of this chapter is threefold; the first is to characterize the phases and intermetallic compounds formed due to interaction between the Al-matrix and SiC particles or from the hardening precipitation treatment, when O-condition annealing is used to reduce the detrimental effect of these compounds by dissolving or refining them so as to improve its ductility. Secondly, there is little research published in the literature on the effect of strain rate on the tensile properties and fracture behaviour of MMC materials. Tensile tests with different strain rates are conducted to study the influence of the strain rate on the mechanical properties and fracture behaviour and to find a correlation between the fracture mechanism under tensile loading and the type of heat treatment as well as to illustrate the effect of the precipitations on the fracture toughness. Finally, experimental testing

is carried out to investigate the applicability of using the ISF process to form the AMC under different heat treatment conditions for the first time.

7.2 Experimental procedures

7.2.1 Material

The experimental work was carried out using a 6092 aluminium matrix composite sheet reinforced with a 17.5% volume fraction of silicon carbide particles. The composite sheet was treated by T6. Table 7-1 shows the chemical composition of the 6092 Al matrix alloy. The Al6092/17.5% SiCp–T6 has low ductility and high strength. Therefore, to improve the ductility of Al6092/SiCp and to alleviate the deleterious effect of the intermetallic compounds on the mechanical properties, heat treatment may be used to improve the formability of this composite material under large deformation conditions.

Table 7-1 Chemical composition of 6092 Al alloy.

Alloy	Cu	Mg	Si	Fe	Zn	Ti	O	others	Al
6092	0.7-1.0	0.8-1.2	0.4-0.8	0.3	0.25	0.15	0.05-0.5	0.15	bal.

7.2.2 Heat treatment

O-condition annealing was employed in this work due to the fact that this can improve the ductility of 6xxx aluminium alloys, according to the recommendations of ASM [179]. Figure 7.1 illustrates how the annealing cycle was applied to the 6092/SiCp composite. The O-condition process consisted of three steps. The first step was to heat the 6092/SiCp composite sheet to 415 $^{\circ}$C with a rapid heating rate to avoid grain growth. The second step involved holding the AMC sheet at this temperature for 2.5 hours (the soaking stage). The final step was to cool the sheet at 30 $^{\circ}$C increments to reach 260 $^{\circ}$C in 5.2 hours. Note that the subsequent cooling does not require a strict cooling rate.

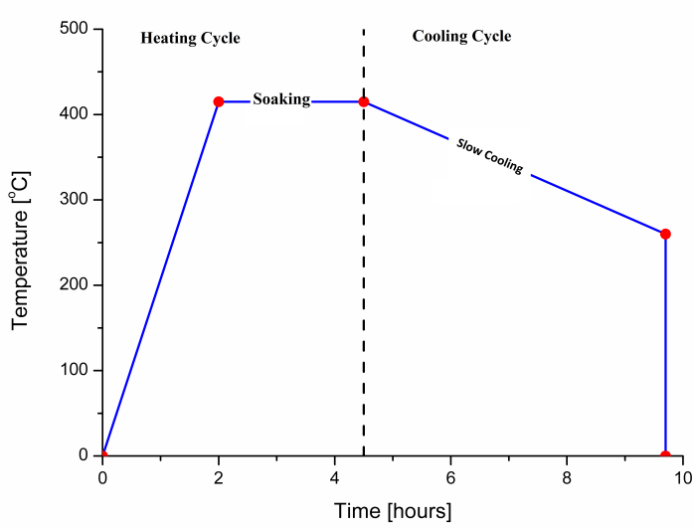


Figure 7.1 O-condition annealing for 6092Al composite based on ASM recommendations [179].

7.2.3 Tensile test

Tensile tests were carried out to study the effect of O-condition annealing on the mechanical properties and fracture toughness of the 6092/SiCp composite with T6 heat treatment. A quasi-static tensile test was performed at five strain rates ($8x10^{-5}$, $8x10^{-4}$, $8x10^{-3}$, $8x10^{-2}$ and 0.16 s^{-1}) to evaluate the effect of the strain rate on the Al/SiCp formability. These tensile tests were conducted using an INSTRON testing machine and the dimensions of the specimen were designed based on ASTM-E8[180]. Tensile specimens were obtained by using an EDM cutting from a 1.04 mm thick 6092/SiC/17.5P sheet.

7.2.4 Focused Ion Beam (FIB)

Several methods are employed for preparing electron-transparent foils for TEM, e.g. electro-polishing (twin jet) and the precise ion polishing system (PIPS), but the disadvantage of these techniques is that it is difficult to prepare a sample on a nano-scale. In this work a focused ion beam (FEI Quanta200 3D FIB-SEM) was used to prepare nano-scale transparent foils for TEM. The FIB system is equipped with a liquid metal ion source (LMIS); this ion is Gallium (Ga^{+}) which can be used for site-specific milling or for depositing materials onto a defined area. In this study, platinum (Pt) was deposited on the surface of the Al/SiC sample to protect the sample surface during the milling process for cross section analysis. The milling process was used to remove a required amount of material to obtain an accurate milled pattern shape. The milling

process was monitored continuously using SEM. TEM was used to characterize the precipitate and intermetallic compounds formed in the interface region. Therefore, the Pt was deposited on the SiC particle (Figure 7.2(a)); then, the material was removed from both sides (Figure 7.2(b)) to obtain a transparent foil at the interface region between the Al-matrix and SiC particle (Figure 7.2 (c)); finally, EDS was used to ensure that both the Al-matrix and SiC particles were in the sample (Figure 7.2 (d)).

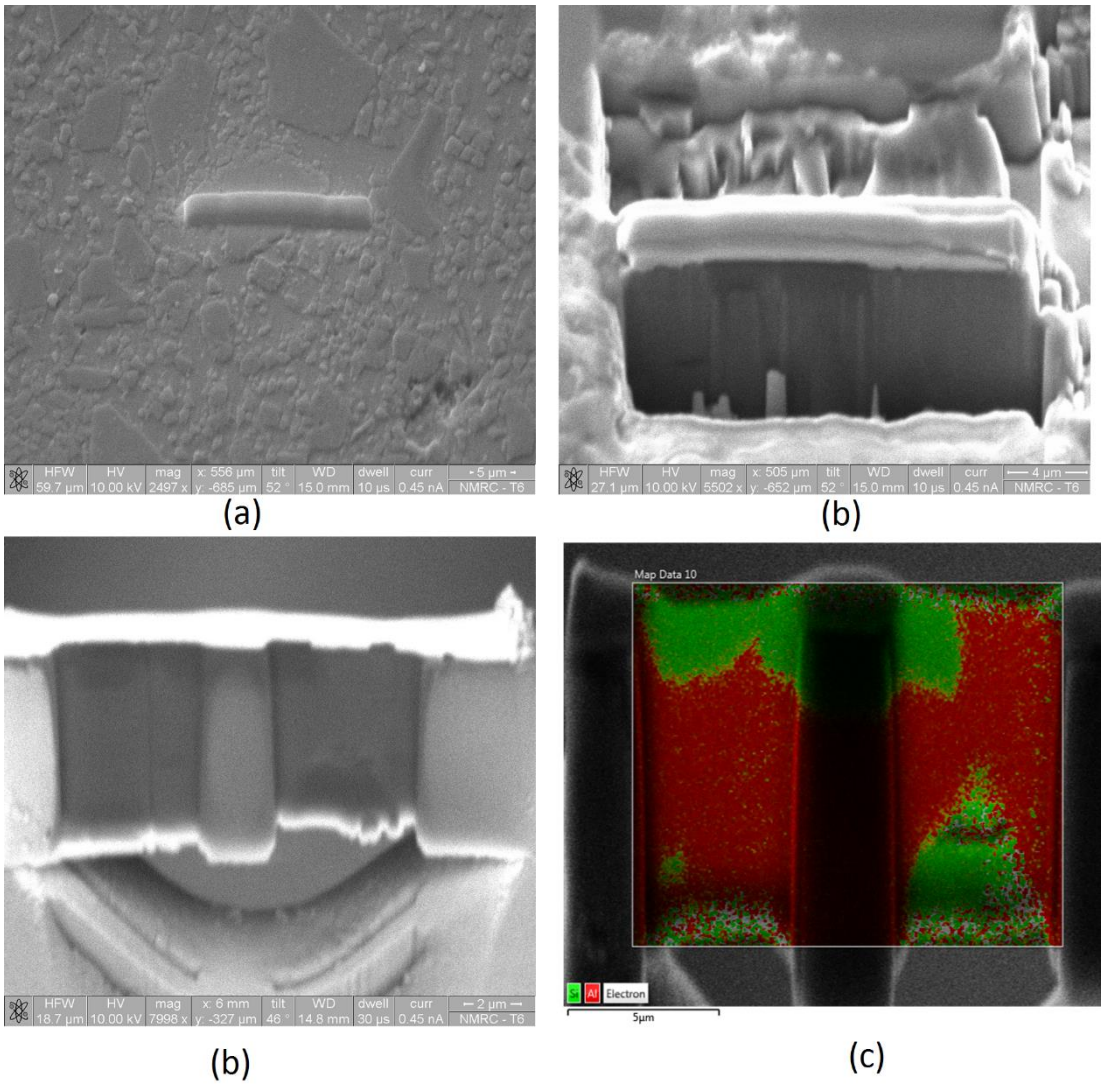


Figure 7.2 SEM micrographs showing the stages of preparing samples of Al/SiC_p using a FIB machine: (a) platinum coating, (b) milling, (c) transparent foil of MMC and (d) EDS of MMC.

7.3 Results and discussion

7.3.1 Microstructural analysis

In order to analyse and evaluate the microstructure of the composite material, a series of preparations were carried out, including cutting, mounting, grinding and polishing of the AMC sheet. The microstructure of the 6092/SiCp composite was investigated in as-received (T6 heat treatment) and O-condition annealing using XL30 SEM with a linked EDS, TEM and XRD. The SEM image for a typical microstructure of 6092/SiCp composite with T6 heat treatment is shown in Figure 7.3; from this figure, it can be seen that there are three distinct regions clearly marked on the backscattered electron (BSE) image, which are Al matrix, the SiC particles and inclusion. In addition, it can be observed from the figure that both the size and the distributions of SiC particles are not uniform; the composite contains a cluster of SiC particles in some regions of the Al matrix. Moreover, porosity can also be observed around the SiC particles. Generally, porosity is associated with SiC particles, due to differences in the thermal conductivity of the SiC particles and Al matrix and this leads to weak bonding between the SiCp and Al matrix.

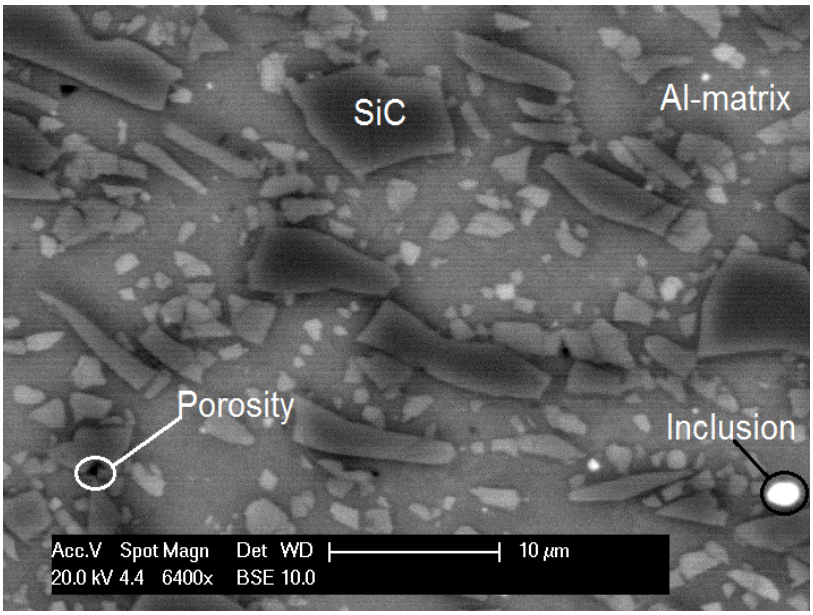


Figure 7.3 Microstructure of MMC-T6 Al6092/17.5% SiCp showing the distribution of reinforcement as well as phases and porosity.

To analyse the effect of heat treatment on the chemical composition of the Al/SiCp composite, SEM-EDS spot analysis was conducted in three different regions along the

composite metal, e.g. the Al-matrix, SiC particle and interface between the Al and SiCp. The SEM-EDS spot analysis was repeated six times in different places in each distinct region and the average value was taken, as shown in Figure 7.4.

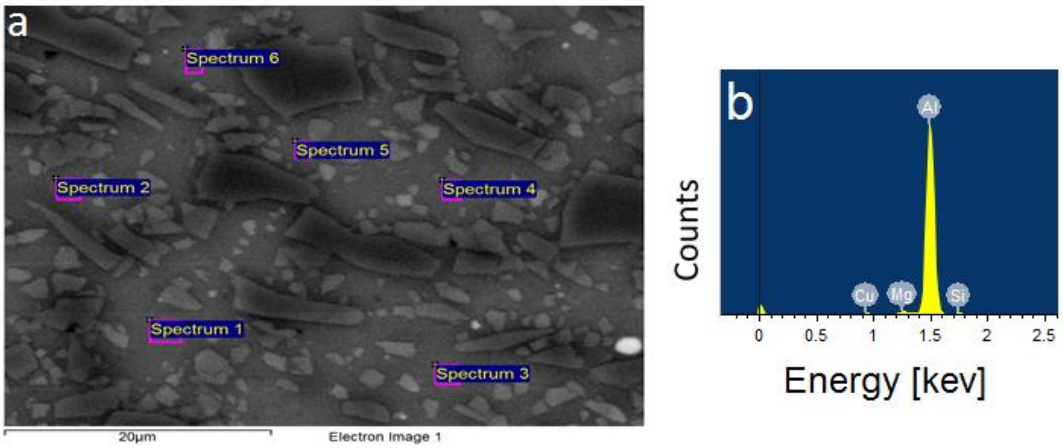


Figure 7.4 : (a) BSE image showing the spectrum distribution in 6092Al matrix. (b) EDX spectrum from the matrix.

The chemical compositions of each region are summarized in Table 7-2. It is clear from the table there were minor changes in the chemical compositions of both the Al-matrix and SiC particles after the O-condition heat treatment. On the other hand, significant changes were observed after annealing in the chemical compositions of the interface region of Al/SiC, especially in the concentrations of Al and Si.

Table 7-2 Elemental distribution of Al- matrix, SiC particle and interface region with T6 and O-condition annealing.

Element	Al-matrix (wt %)		SiC particle (wt %)		Interface (wt %)	
	T6	O-cond.	T6	O-cond.	T6	O-cond.
Mg	0.72	0.49	0.036	0.040	0.63	0.30
Al	95.03	90.07	4.322	3.44	69.76	88.24
Si	3.37	8.76	58.938	59.60	29.11	10.86
Cu	0.88	0.68	-	-	0.5	0.60
C	-	-	36.704	36.92	-	-
total	100	100	100	100	100	100

It is noted from the data that the concentration of Si in the interface region between the Al-matrix and SiC particle in the T6-condition was higher compared to that in the O-condition annealing. The results also show that after O-condition treatment, the concentration of Si decreased in the interface region and increased in the Al matrix, which means there was an exchange of Si between the interface and Al matrix during

the heat treatment. It can be concluded that, in the T6-condition, the Si is absorbed into the interface between the Al-matrix and SiC particles by the SiC particles and this makes the composite material brittle due to the lack of Si in the Al matrix, which in turn leads to reduced ductility and elongation. In contrast, the O-condition treatment works to diffuse Si from the interface region to the matrix, leading to a more uniform distribution of Si.

Under both heat treatment conditions (T6 and O-condition), TEM was used to characterize the phases and intermetallic compounds formed at the interface between the Al-matrix and SiC particle as a result of the interaction between them or due to the precipitation hardening treatment. Figure 7.5 (a) shows the matrix - interface region of the Al/SiCp composite after T6 treatment. The large interfacial compound in the interface line was clearly identified as Al_2Cu by a selected area electron diffraction pattern (SADP) (Figure 7.5 (b)) and EDS (Figure 7.5 (c)). Al_2Cu has an orthorhombic crystal structure with a lattice parameter of a=0.496nm, b=0.866 and c=0.833nm. It is well known that the T6 heat treatment consists of two steps: solution heat treatment and artificial ageing precipitation hardening. Precipitation hardening is used to strengthen aluminium alloys via the formation of precipitations. These precipitations grow within grains and at grain boundaries. The intermetallic compound phase (Al_2Cu) was observed at the interface between the Al-matrix and SiC particle and the main influence of this intermetallic is to increase the hardness of the AMC and reduce its ductility. Al_2Cu usually is formed in the Al-Cu alloy (2xxx and 2xx.x) after ageing [181] when the percentage of Cu in Al alloy is from 0.2% to 5.6% [182]. Therefore, due to the high percentage of Cu (1%) in the 6092Al alloy (Table 7-1), this phase can be generated after the ageing treatment of 6092Al/SiCp composite.

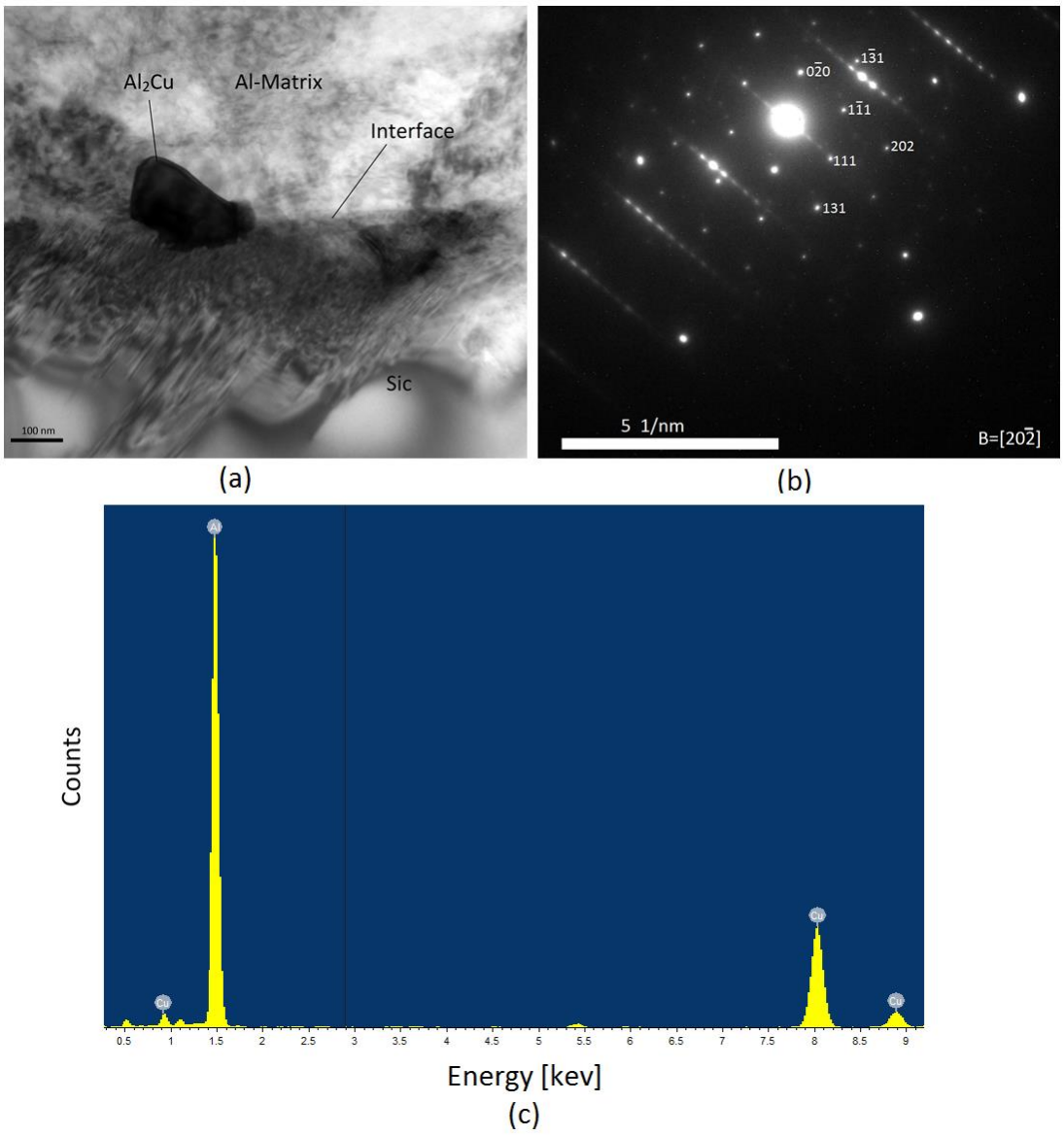


Figure 7.5 TEM micrographs and corresponding SADP of the interface of the 6092Al/SiC composites after T6 treatment: (a) TEM image of Al/SiC interface showing the intermetallic compound (Al_2Cu) formed around the SiC particle, (b) SAD pattern of Al_2Cu and (c) EDS analysis of Al_2Cu.

After O-condition annealing, TEM observation showed that the Al_2Cu completely dissolved into the matrix, whilst another phase was observed as shown in Figure 7.6 (a). Based on the SADP (Figure 7.6 (b)) and the EDS (Figure 7.6 (c)) analysis, this phase was $Al_4Cu_2Mg_8Si_7$. The $Al_4Cu_2Mg_8Si_7$ has a hexagonal crystal structure with the lattice parameters of a=1.039nm and c=0.4017nm. This phase could increase the strength of composite materials.

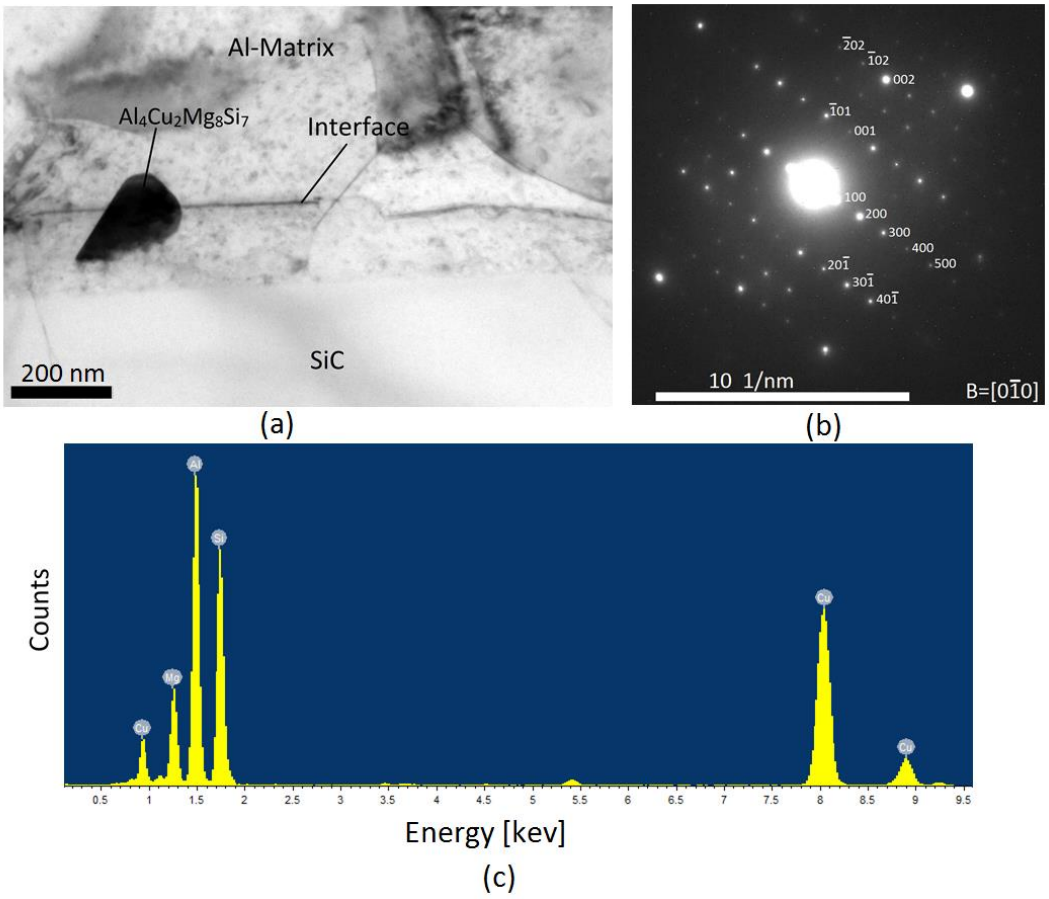


Figure 7.6 TEM micrographs and corresponding SADP of the interface of 6092Al/SiC composites after O-condition annealing: (a) TEM image of the Al/SiC interface showing the phase of $Al_4Cu_2Mg_8Si_7$ formed around the SiC particle, (b) SAD pattern of $Al_4Cu_2Mg_8Si_7$ and (c) EDS analysis of $Al_4Cu_2Mg_8Si_7$.

It is difficult to produce a detailed identification of the interfacial reaction compounds using one method. Therefore, X-ray diffraction (XRD) was utilized to characterise and observe the effect of heat treatment on the phase formation and to give confidence in the results of TEM and EDS. The results of the XRD pattern are given in Figure 7.7 (a and b) for T6 treatment and O-condition annealing, respectively. The observed peaks confirmed the results of the TEM diffraction pattern and EDS. Figure 7.7 (a) shows the formation of Al_2Cu, $Al_4Cu_2Mg_8Si_7$ and $MgAl_2$ precipitations after T6 heat treatment, while Figure 7.7 (b) demonstrates that $Al_4Cu_2Mg_8Si_7$ and $MgAl_2$ precipitations were formed after O-condition annealing.

The XRD results show that the Al_2Cu and $Al_4Cu_2Mg_8Si_7$ are formed with Al6092/SiCp after T6 treatment due to the high percentage of Cu (1wt. %), and the main role of these precipitations is to increase the hardness of the Al/SICp. The O-condition

annealing works to enhance the ductility and fracture toughness by reducing the Al_2Cu phase as shown in Figure 7.8.

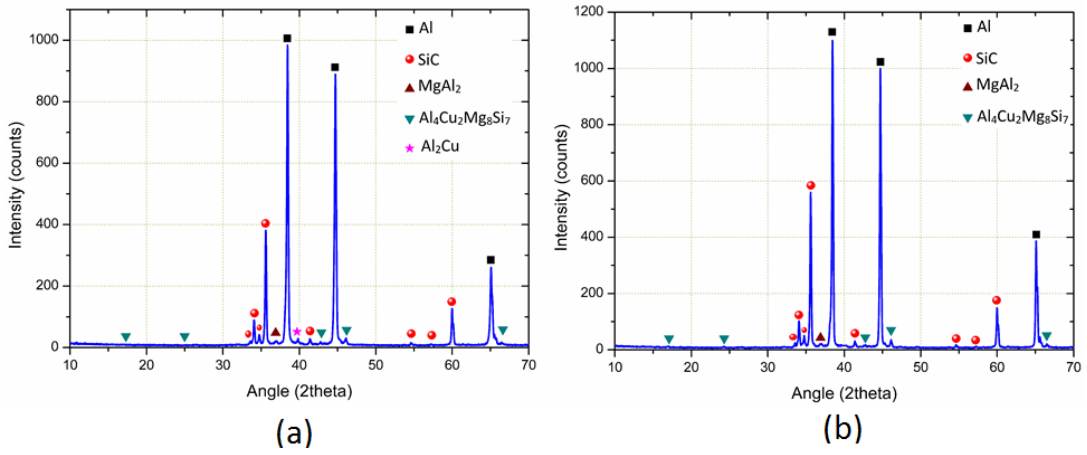


Figure 7.7 XRD pattern of 6092Al/SiCp: (a) T6 treatment composite and (b) O-condition annealing composite.

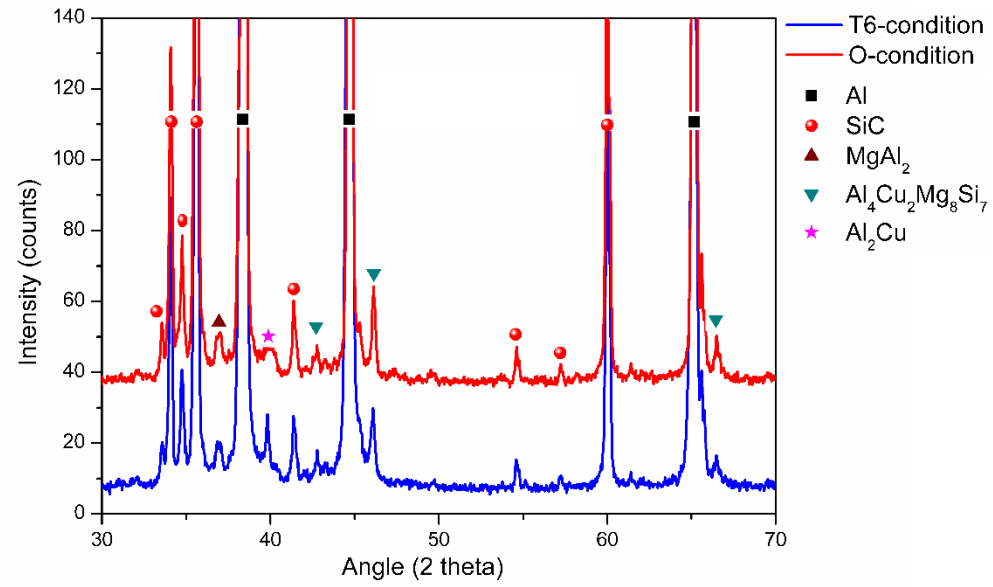


Figure 7.8 X-ray diffraction patterns measured on the specimen of 6092Al/SiCp under different heating conditions.

7.3.2 Hardness

To evaluate the effect of heat treatment on the hardness of 6092Al/SiC_p composite, the Vickers hardness test was utilized with diamond indenter. The load was set to 5kg for 15 seconds. The area of indentation was measured using microscope with magnification power 5X, the hardness is obtained by dividing the load (kgf) by area of indentation (mm^2). The test was repeated six times in different positions to get the average value of hardness. The results show that the distribution of the hardness was

almost uniform after both heat treatments (T6 and O-condition), as shown in Figure 7.9. The hardness was reduced by 58% after O-condition annealing indicating that the O-condition can improve the ductility of the AMC by decreasing the hardening precipitation (Al_2Cu) formed in the interface region and redistributing the Si in the AMC.

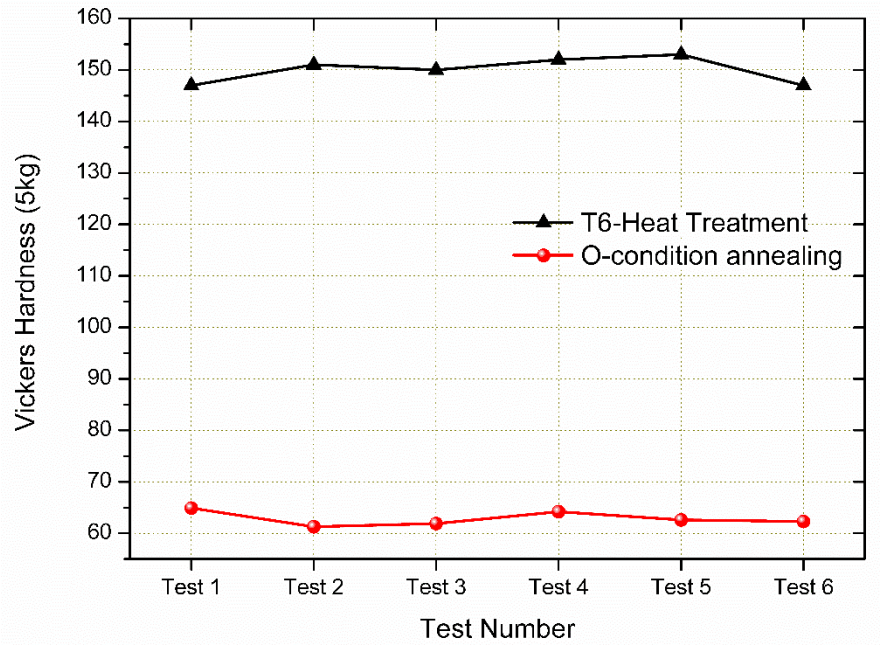


Figure 7.9 Hardness of 6092Al/SiC_p after different heat treatments.

7.3.3 Tensile test

Figure 7.10 illustrates the true stress-strain curves of 6092/17.5% SiC_p composite for two different heat treatment conditions (T6 and O-condition) at five different strain rates. It is observed from the figure that O-condition annealing significantly enhanced the ductility of the Al/SiCp material as compared to the T6-condition at all strain rates with lower ultimate tensile strengths (UTS) obtained. Moreover, the strain rate had a significant effect on the fracture elongation of the Al/SiC_p composite. Compared to the T6-condition, the fracture elongation of Al/SiC_p at O-condition was more sensitive to the strain rate. As shown in Figure 7.11 (a), the elongation to fracture of Al/SiC_p at O-condition increased from 0.055 to 0.193 when the strain rate decreased from 0.16 s^{-1} to $8x10^{-5}$ s^{-1}, whilst at the T6-condition, it increased from 0.013 to 0.08. The strain rate had a slight effect on the UTS, (Figure 7.11(b)), where the values of UTS decreased by decreasing the strain rate. The UTS of the Al/SiC_p-T6 composite decreased by 13.9% with decreased strain rate and the UTS reduction in the material

subjected O-condition annealing was 9.8%. Based on the aforementioned results, the fracture is accelerated by increasing the strain rate at both heat treatment conditions. An explanation for this is that, with high strain rates, dislocations in the matrix are generated more rapidly due to fact that the plastic flow is constrained by the SiC particles. Therefore, increasing strain rate can help these dislocations escape to the free surface (the debonded surface between SiCp and the Al-matrix and crack interface) and this accelerates the fracture in AMC materials. On the other hand, the low strain rate has a significant effect on postponing the fracture occurrence in Al/SiCp composite material with both heat treatment conditions (T6 and O-condition) but its effect is greater with O-condition. Indeed, it seems that stabilising effects are present with low strain rates which delay the damage evolution as compared to the test conditions of high strain rates.

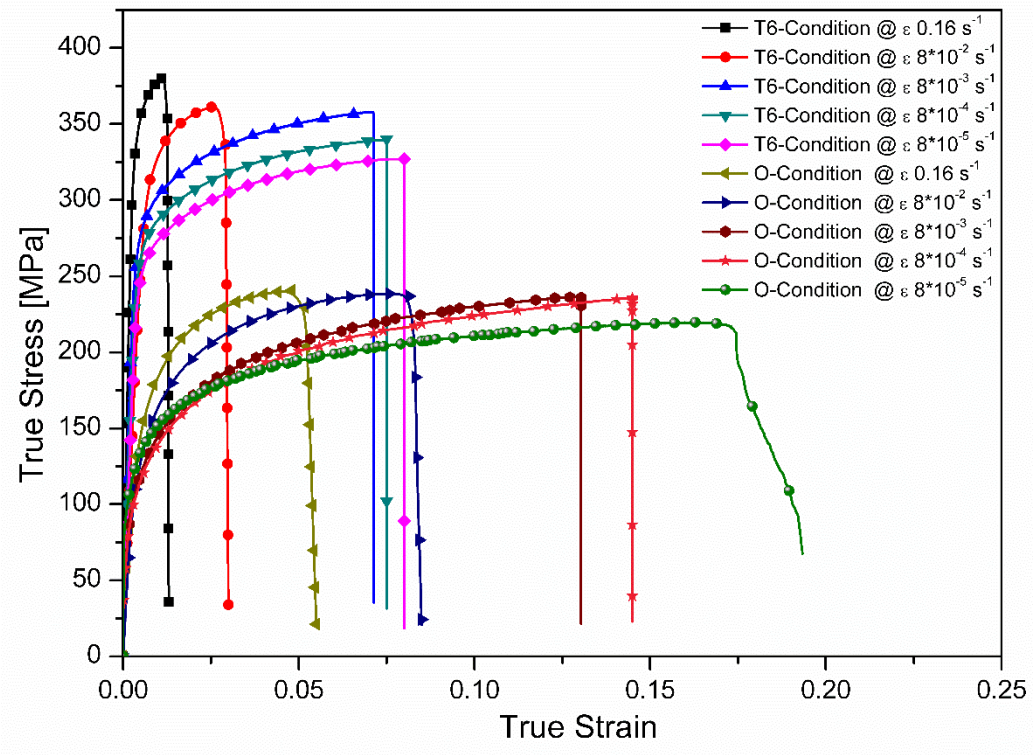


Figure 7.10 True stress-true strain curves of Al6092/SiC/17.5p.

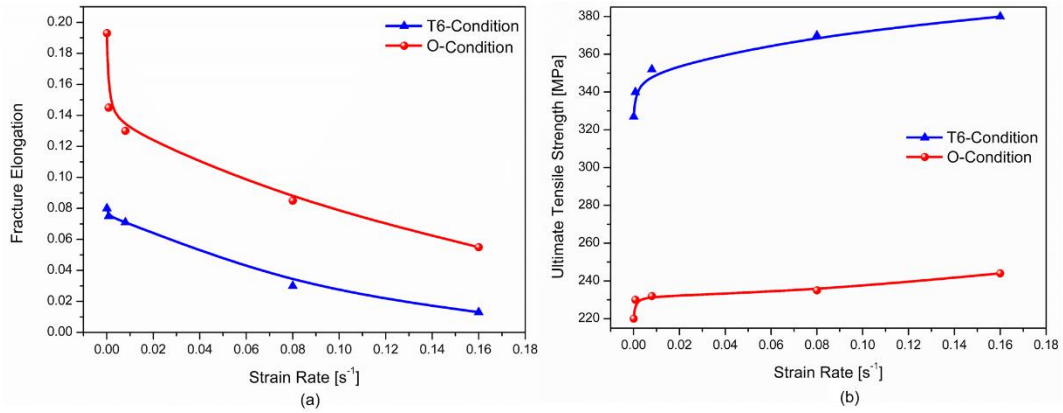


Figure 7.11 Effect of strain rate on fracture elongation and ultimate tensile strength: (a) relation between fracture elongation and strain rate and (b) relation between tensile strength and strain rate.

7.3.4 Fracture mechanism in tensile test

Figure 7.12 shows the morphologies of the tensile fracture surface of the Al/SiCp composite subjected to two different heat treatment conditions and tensile test with a strain rate of $8x10^{-5}$ s^{-1}. As shown in Figure 7.12 (a), the fracture surface of the sample at T6-condition contains some shallow dimples with many broken SiC particles and debonding along the interface between the SiCp and Al matrix. The broken particles and debonding are responsible for the brittle fracture and low ductility of the Al/SiCp of the T6-condition. Figure 7.12 (b) depicts the fracture surface for O-condition annealing. It is observed that a high percentage of deep dimples appear on the fracture surface as compared to the T6-condition sample with a limited number of SiC particles covered by the matrix; this is due to the fact that, after O-condition annealing, the ductility of Al/SiCp interface is improved and the Al matrix has high elongation before fracture. Consequently, it is difficult to observe the SiC particles on the fracture surface with O-condition annealing at a low strain rate due to the deep dimples in the Al matrix. The debonding phenomenon along the interface between the SiC particles and Al matrix can be observed clearly in Figure 7.13 at a high strain rate, as at a low strain rate the SiC particles are almost covered by the metallic matrix. The debonding occurs during deformation, when the shear stress at the interface exceeds the strength of bond [183]. Based on the observations of the fracture surface with both heat treatment conditions, the fracture mechanism of the Al/SiCp composite indicates that there is a correlation between the fracture mechanism mode under tensile loading and the type of heat treatment. Therefore, two types of fracture can be noticed in this study: the first

type is for material in T6-condtion, which is a combination of brittle and ductile fracture. The second type is the ductile fracture for material subjected to O-condition annealing.

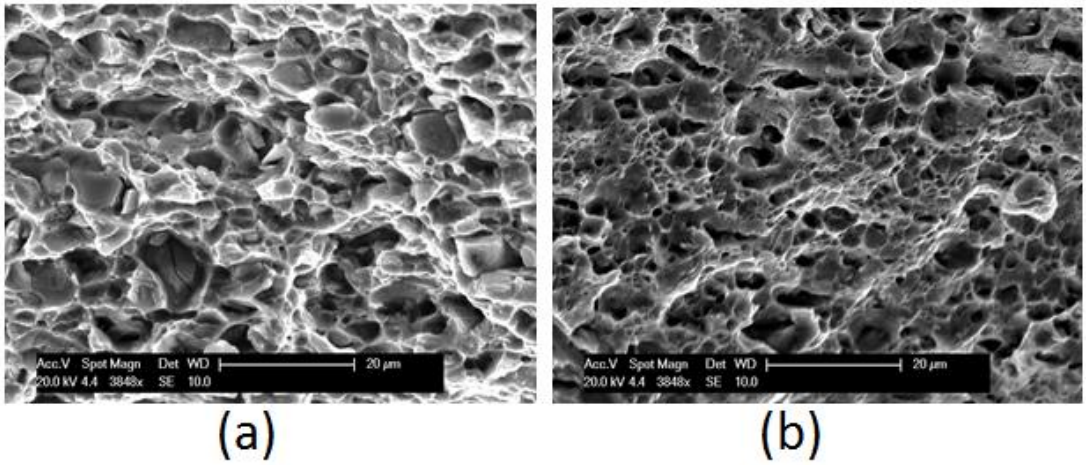


Figure 7.12 Effect of heat treatment on fracture surface at strain rate 8x10-5 s^{-1}: (a) T6- treatment and (b) O-condition annealing.

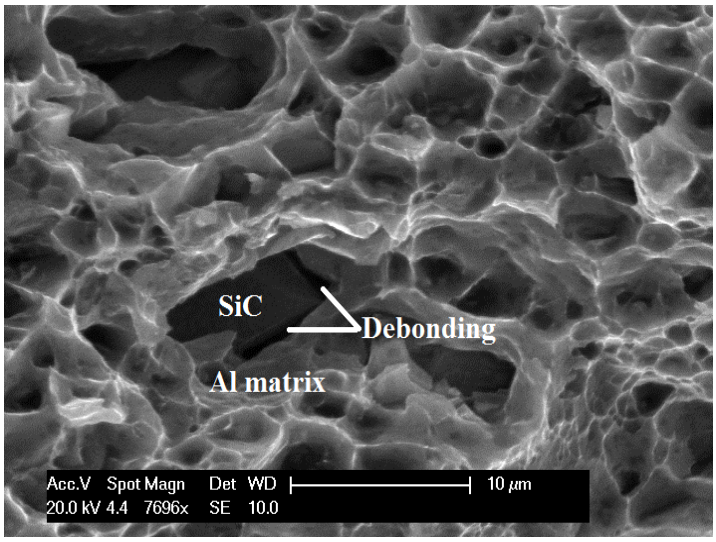


Figure 7.13 Debonding phenomenon with T6-treatment.

The effect of strain rate on the morphologies of the fracture surface is investigated with tensile samples subjected to T6 treatment and O-condition annealing. As shown in Figure 7.14, when the strain rate varies from 0.16 s^{-1} to 8x10^{-5} s^{-1}, there is no significant fracture morphology difference with T6 treatment tensile samples; the fracture is still brittle with shallow dimples and cracked SiC particles, however, with a high strain rate, interfacial cracks appear on the fracture surface (Figure 7.14 (a)) which are not present with a low strain rate Figure 7.14 (b).

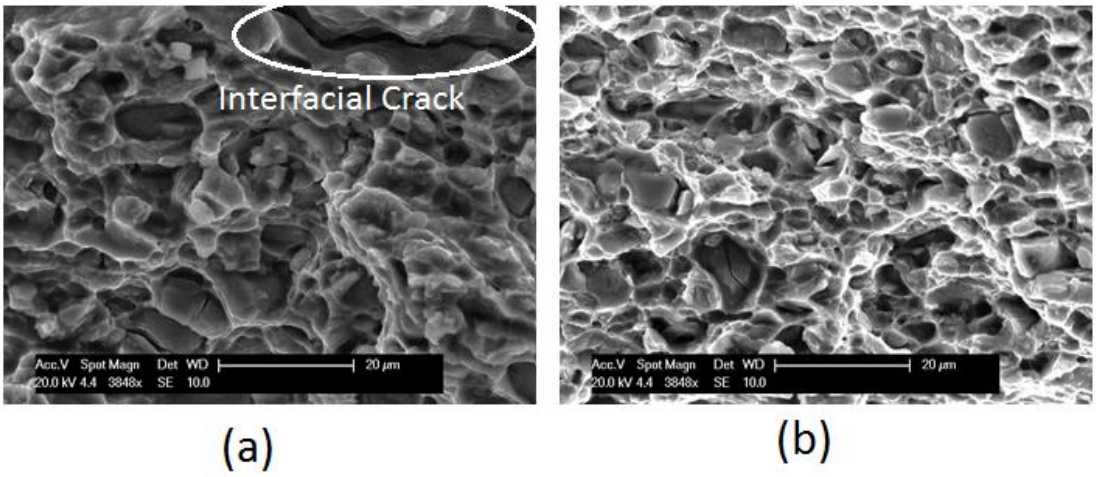


Figure 7.14 Effect of strain rate on fractograph of 6092Al/SiCp with T6-treament: (a) strain rate 0.16 s^{-1} (b) strain rate $8x10^{-5}$ s^{-1}.

Typical SEM fractographs of the fracture surface of the O-condition samples with different strain rates are shown in Figure 7.15. It is observed from the figure that, at high strain rate (0.16 s^{-1} and $8x10^{-2}$ s^{-1}), there is an interfacial crack on the fracture surface. The depth of the dimples increases with decreased strain rates. Moreover, the SiCp particles disappear from the fracture surface at a low strain rate due to the high deformation in the Al matrix before fracture resulting in many voids, which almost cover the SiC particles. It can be concluded that the fracture mechanisms in the Al/SiCp material change with the strain rate. As a result, more ductile void coalescence is observed on the fracture surface at the slowest strain rate, while shallow dimples with SiC particles are noted on the fracture surface at the fastest strain rate. Based on the mechanical properties and the SEM fracture surface fractography, the tensile samples at O-condition appear more sensitive to the strain rate than those at T6 condition. Also the results show that there is interfacial crack in fracture surface when high values of strain rate are used with both type of heat treatment (T6 and O-condition), which can be related to higher level of stress causing decohesion.

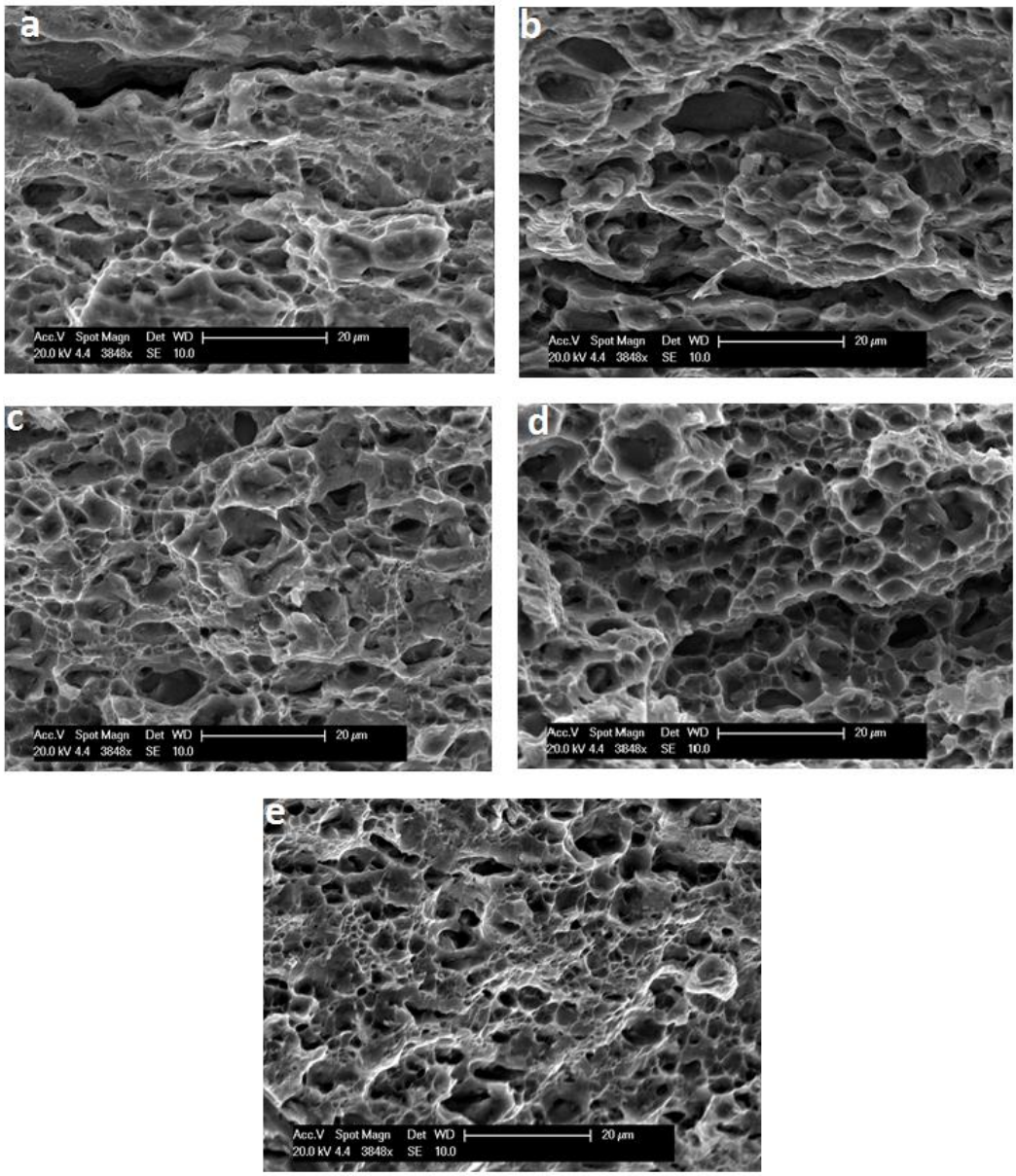


Figure 7.15 Effect of strain rate on fractograph of 6092Al/SiCp with O-condition annealing: (a) strain rate 0.16 s^{-1}, (b) strain rate $8x10^{-2}$ s^{-1}, (c) strain rate $8x10^{-3}$ s^{-1}, (d) strain rate $8x10^{-4}$ s^{-1} and (e) strain rate $8x10^{-5}$ $s^{-1.}$

Under different strain rate, the results showed that there is a correlation between the fracture elongation and ultimate tensile strength (UTS) of the material with the depth and density of dimples formed for both heat treatment conditions as shown in Figures 7.14 and 7.15 and Table 7-3. Under T6-condition with high strain rate (0.16 s^{-1}) low fracture elongation (0.013) and high UTS (380 MPa) are obtained from the tensile test and that leads to fracture surface with shallow and low density dimples, whereas when the strain rate is decreased to $8x10^{-5}$ s^{-1} the fracture elongation was still low (0.08) with value of UTS 327 MPa, therefore, there is no significant change on the fracture surface

morphology. On the other hand, with O-condition annealing there is a significant change in the fracture elongation with a little change in the UTS value, i.e. when the fracture elongation is increased from 0.055 to 0.193 and the UTS is decreased from 244 MPa to 220 MPa when the strain rate decreased from 0.16 s^{-1} to $8x10^{-5}$ s^{-1}, respectively, and that obtains a fracture surface with a dense and deep dimples.

Based on the aforementioned results, the strain rate has a significant effect on the depth and density of the dimples of 6092/17.5%SiCp composite. Compared to the T6-condition, the fracture surface of 6092/17.5%SiCp with O-condition is more sensitive to the strain rate. It can be concluded that the shape and ductility of the dimples density formed in the fracture surface of Al/SiCp composite correlate closely with strain rate conditions of the tested specimens.

Table 7-3 Effect of strain rate on the fracture elongation and UTS of 6092Al/SiCp.

Strain Rate [S^{-1}]	Fracture Elongation		Ultimate tensile strength [MPa]	
	T6-treatment	O-condition	T6-treatment	O-condition
0.16	0.013	0.055	380	244
$8*10^{-2}$	0.03	0.085	370	235
$8*10^{-3}$	0.071	0.13	352	232
$8*10^{-4}$	0.075	0.145	340	230
$8*10^{-5}$	0.08	0.193	327	220

7.3.5 Fracture mechanism in the SPIF

The SPIF test of a truncated hyperbolic shape with varying wall angles from 22° to 80° (Figure 6.8 (b)) was carried out for the 6092Al/SiCp sheets under T6 and O-condition treatments. Digital height gage was used to measure the fracture depth and this depth was utilized to determine the wall angle of SPIF parts at fracture. As shown in Figure 7.16, the fracture occurs early at a wall angle equal to 31.2° with a high degree of springback and the fracture cut across the tool path for the specimen at T6 condition. After O-condition annealing, the fracture of the hyperbolic shape was propagated along the tool path at 25.5 mm depth with a wall angle 63.15°.

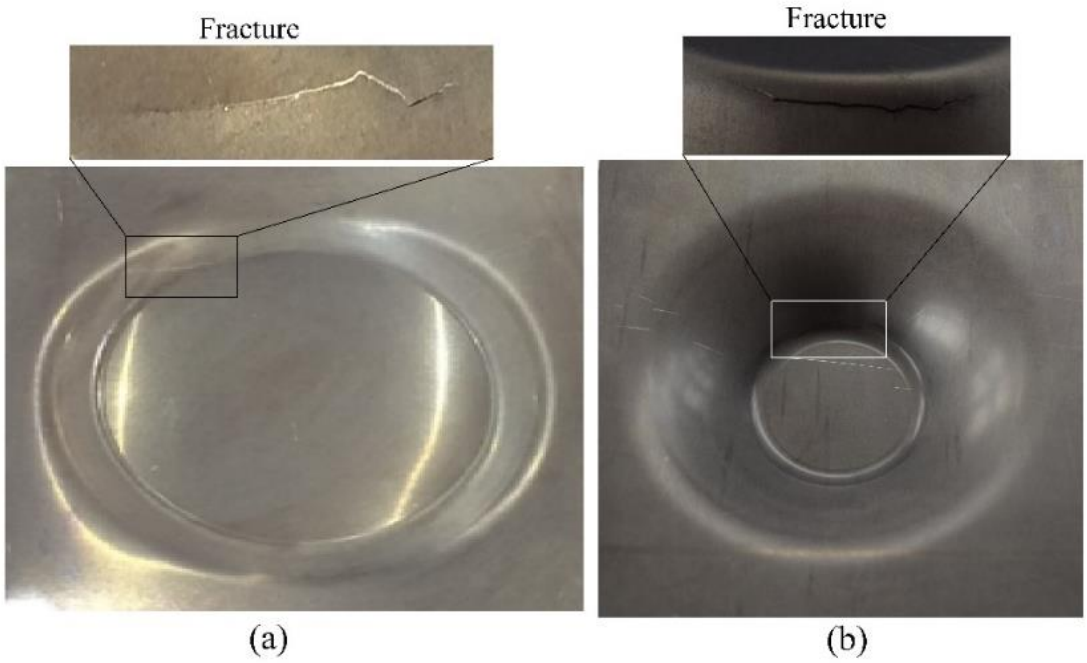


Figure 7.16 Effect of heat treatment on the fracture of hyperbolic truncated shape: (a) after T6 treatment; (b) after O-condition annealing.

To study the effect of feed rate on the fracture behaviour of ISF parts, four feed rates, i.e. 500, 1000, 2000, 3000 mm/min were used in forming the 6092Al/SiCp sheets at O-condition with a non-rotating tool. The maximum wall angles with feed rates of 500, 1000, 2000 and 3000 mm/min are 63.15^{o}, 62^{o}, 61^{o} and 59.63^{o}, respectively (see Figure 7.17). This is equivalent to a wall angle increase by 5.9% when the feed rate is decreased from 3000 mm/min to 500 mm/min. The clamping equipment of SPIF was mounted on a three-component dynamometer (Kistler 5073A3 Amp) in order to record the vertical forming load during the SPIF process. As shown in Figure 7.18, the forming load increases with increased feed rate and the fracture occurs earlier with a higher feed rate value, a clear indication of increasing strain rate hardening of the 6092Al/SiCp sheets at O-condition.

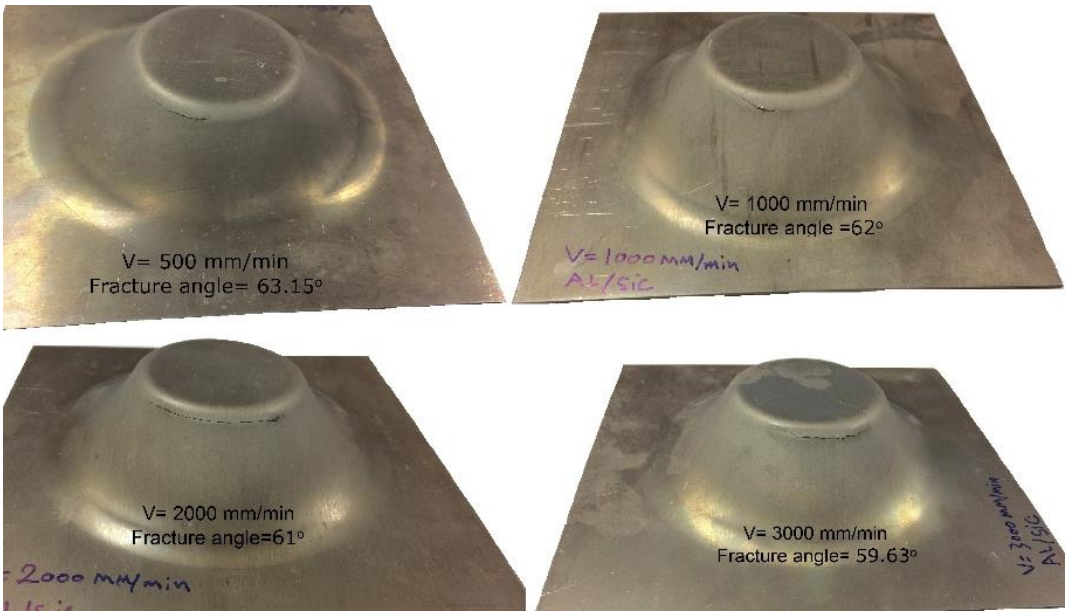


Figure 7.17 Effect of feed rate on fracture angle.

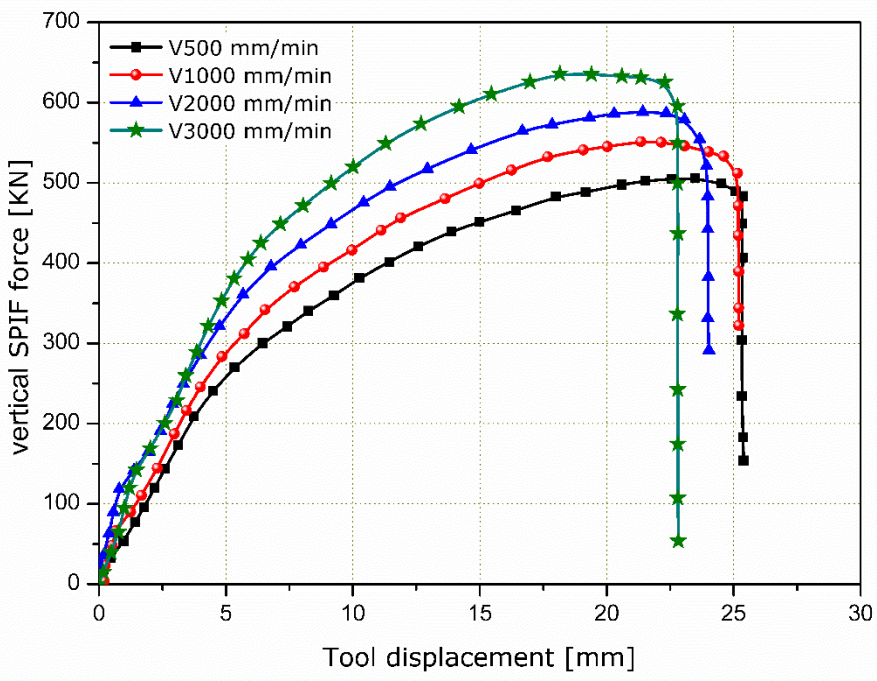
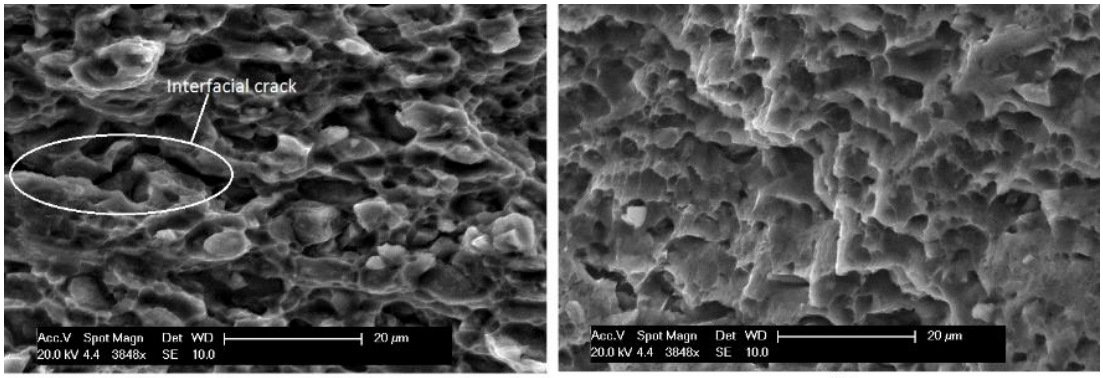


Figure 7.18 Comparison of forming load at different feed rates.

The morphologies of fracture surfaces of the SPIF formed 6092Al/SiCp sheets were evaluated using SEM, as shown in Figure 7.19. Brittle fracture was observed under T6 treatment with shallow dimples, broken SiC particles and debonding occurring at the interface of the Al matrix/SiCp. In addition, there was an interfacial crack in the Al matrix, while a ductile fracture with a high percentage of deep dimples was observed in the fracture surface of the SPIF part after O-condition annealing with a limited number of SiC particles. The results show a good correlation between the dimple

density on the fracture surface and heat treatment type. Brittle/ductile fracture occurs with a low density of dimples under T6-treatment, while ductile fracture with a high density of dimples can be seen under O-condition annealing.



(a) (b)

Figure 7.19 Effect of heat treatment on fracture surface of SPIF part: (a) T6-treatment and (b) O-condition annealing.

7.4 Conclusions

By evaluating the deformation and fracture mechanisms of the AMC sheet (6092Al/SiCp) using SEM, EDS, TEM and XRD, this work investigates the applicability of using incremental sheet forming process to form the 6092Al/SiCp sheet. O-condition annealing was applied to reduce the detrimental effect of these precipitations and to improve the ductility and fracture toughness. In addition, tensile tests with a range of strain rates ($8x10^{-5}$, $8x10^{-4}$, $8x10^{-3}$, $8x10^{-2}$ and 0.16 s^{-1}) were used to investigate the effect of strain rate on the mechanical properties and fracture behaviour of AMC materials.

The results showed that, under T6 condition the mechanical behaviour of this AMC is brittle due to the formation of precipitations as a result of either the interaction between the Al and SiCp or from hardening precipitation treatment resulting in creation of Al_2Cu, $Al_4Cu_2Mg_8Si_7$ and $MgAl_2$ components. O-condition annealing can improve the fracture toughness and ductility of the material by decreasing the amount intermetallic compound (Al_2Cu) in the interface region.

With a low strain rate ($8x10^{-5}s^{-1}$), the ductility of 6092Al/SiCp composite can be improved significantly especially with O-condition annealing due to two types of fracture which can be observed. The first type shows a combination of brittle and

ductile fracture and it contains shallow dimples with many broken SiC particles at T6 treatment. The second type is the ductile fracture at O-condition annealing, with a high percentage of deep dimples. However, the Al/SiC sheet treated with O-condition annealing is more sensitive to the strain rate than the one treated with T6.

By investigating the feasibility of using SPIF to form 6092Al/SiCp AMC sheets for the first time, the results show that the 6092Al/SiCp sheets can be satisfactorily formed after O-condition annealing. At T6 condition, ISF testing showed unsatisfactory results for the 6092Al/SiCp with a low wall angle (31.2^{o}) to fracture and a significant amount of springback. After annealing to O-condition, a much increased wall angle was achieved with reduced springback due to the enhanced ductility of the 6092Al/SiCp material. Microstructural and topographic evaluation of the 6092Al/SiCp parts formed by ISF allowed a detailed characterisation of brittle and ductile fractures for different heat treatments. The results also show a degree of strain rate hardening effect in incremental sheet forming of the 6092Al/SiCp AMC material. Low feed rate improves the formability through increasing depth and higher wall angle in the SPIF process.

CHAPTER 8

CONCLUSIONS AND FUTURE WORK

8.1 Introduction

The key conclusions on the deformation and fracture mechanics of the ISF process, and its application to manufacturing a customised medical product from pure titanium metal sheets, are summarised in this chapter. In addition, the potential of using the ISF process to form 6092Al/SiCp composite sheet under different heat treatment conditions is examined. Recommendations for future work with ISF are also outlined in this chapter.

8.2 Conclusions

In this study, extensive experimentation and finite element-based simulation have been carried out to develop a necessary understanding of the formability and failure mechanics of sheet metals during the SPIF process using rigid tools. The key findings for each of the five main chapters of this work may be summarized as follows:

8.2.1 Finite element simulation

The main aim of this chapter was to develop a three-dimensional model using commercial finite element software Abaqus/Explicit to simulate the deformation of a pure titanium sheet metal blank during SPIF with a particular attention given to the effect of simulation parameters on simulation results including element size, mass scaling factor and friction coefficient. From the finite element simulation, it can be concluded that:

- The element size affects the finite element results, especially in terms of equivalent plastic strain, so a suitable element size should be selected carefully to get accurate results. The best element size for simulating the ISF process is 0.5 mm.
- Using the mass scaling factor may lead to errors or failure of the explicit SPIF simulation due to the fact that kinetic energy can be increased if a high value of mass scaling is chosen. On the other hand, long computing time may be expected if too small a value of mass scaling is used. From this study, it is

found that a $2x10^{-6}$s stable time increment would be suitable for achieving an acceptable level of kinetic and internal energy ratio of less than 4%-10%.

- The FE model of SPIF is robust to the friction as the change in friction coefficient can alter the predictions; in addition, the SPIF model shows good prediction of sheet thickness when the results are compared with the experimental work.

8.2.2 Modelling of ductile fracture in ISF

A modified GTN damage model with shear was employed to comprehensively study fracture in SPIF with a specific attention to the effect of shear for the first time by using a combined approach of experimental testing for GTN parameters and SPIF processing for FE results validation. The following conclusions may be drawn from this study:

- DIC system was used to analyse and evaluate the necking and instability along the tensile specimen, and the SEM was utilised to scan the affected zone of the tensile specimen to determine the parameters of the modified GTN model experimentally. Based on the results obtained, the DIC and SEM are considered an effective means to derive the modified GTN model parameters.
- Single element hydrostatic tension and simple shear tests were run to validate the modified GTN model with Abaqus and analytical shear model. the obtained results showing an excellent convergence achieved in both test cases.
- Fracture prediction using GTN model is significantly influenced by mesh density, i.e., sufficiently small element size is required to capture the correct deformation pattern and real shape of fracture.
- To determine the ability of the modified GTN model to predict the damage under shear loading, two experimental tests (tensile and shear test) were conducted with DIC. The results showed that the modified GTN model with shear improved the modelling accuracy of fracture over the original GTN model under shear loading conditions.
- The experimental results from SPIF testing for a truncated hyperbolic cone and a truncated pyramid showed a good agreement of the occurrence of fracture for both shapes using the modified GTN model with shear. This clearly shows that

the shear plays a role together with the meridional tensile stress to accelerate damage in SPIF process.

8.2.3 Formability in ISF

The aim of this study was twofold: first, to evaluate the capability of the original and shear modified GTN models to predict fracture with moderate stress triaxiality ratios. Secondly, to evaluate the formability in the ISF process and to examine the applicability of the Nakajima test to describe the fracture in the ISF process. The results of this work can be summarized as follows:

- The shear modified GTN model can predict fracture accurately in a uniaxial strain state and the original GTN model can work in the range of the equi-biaxial strain state, while the stress triaxiality modified GTN model should be used for cases under moderate stress triaxiality in the range from plain strain to equi-biaxial region.
- The ratios of strain at fracture in SPIF were determined quantitatively to evaluate under which strain states the conical and pyramidal truncated specimens failed. With the hyperbolic truncated cone and hyperbolic truncated pyramid shapes, two points can be recorded in the FLD: the first are in the plain strain region with a strain ratio equal to 0.05, and another are in the equi-biaxial region with a strain ratio equal to 0.87.
- The stress triaxiality modified GTN model showed a good agreement with the experimental test of SPIF in predicting the fracture for both shapes (hyperbolic cone and hyperbolic pyramid).
- The Nakajima test can be applied to establish the FLCF, which can be utilized to describe the formability of conical and pyramidal truncated specimens produced by SPIF.

8.2.4 Parametric study and cranial plate concluding remarks

A parametric investigation was undertaken in order to provide a better understanding of the relationship between three key ISF parameters, namely the step size, feed rate and tool size, and the formability and fracture occurrence of grade 1 and 2 pure Ti using experimental testing and FE analysis incorporating the stress triaxiality modified GTN damage model. Optimal parameters were used to investigate the suitability of using the SPIF process to form a customized titanium cranial plate. In addition, the

different in sensitivity of two pure Ti materials to three ISF parameters was explained. The following conclusions may be drawn from this investigation:

- The comparison between the experimental data and FE analysis using the stress triaxiality modified GTN damage model highlighted its accuracy in predicting fracture occurrence accurately in the ISF of truncated hyperbolic cone and pyramidal shapes with different forming parameters.
- The step size, feed rate and tool size have different degrees of effect on the formability and fracture in the ISF process. The grade 2 pure Ti is more sensitive to forming parameters than grade 1 pure Ti. The maximum wall angle of the grade 1 pure Ti hyperbolic truncated cone increases by 0.85^{o}, 2.73^{o} and 5.68^{o} when the step size is changed from 0.6 mm to 0.2 mm; the feed rate changes from 3000 mm/min to 1000 mm/min and the tool diameter changes from 15 mm to 8 mm, respectively. On the other hand, the increase in the maximum wall angle of grade 2 pure Ti is 5^{o}, 6.1^{o} and 7.65^{o} with the same level of changes seen in the ISF parameters.
- With the increased step size, feed rate and tool size, the vertical forming force will increase accordingly for both types of pure Ti. The increase in the forming force with increased step size and tool size can be attributed to the increase of material to deform and to the increased contact area between the tool and the sheet, respectively. The increases in feed rate result in a degree of strain rate hardening effect in ISF.
- The level of major strain at fracture decreases by increasing the three forming parameters, i.e. step size, feed rate and tool size for both types of pure Ti.
- The increases in the step size, feed rate and tool size can help to nucleate new voids in a pure Ti matrix and accelerate the growth of initial voids, leading to an increase in the value of the void volume fraction in the transition region between the contact and non-contact zones. In addition, fracture occurs when the void volume fraction reaches a certain value (0.305 in pure Ti Grade 1 and 0.116 in pure Ti grade 2).
- More sheet thinning can be seen in the wall of the hyperbolic truncated cone in the transition region between the contact and non-contact zone when the step size, feed rate and tool size decrease due to a higher wall angle being achieved when these parameters are decreased.

- In the study of using ISF to form a cranial plate, the thickness distribution of the formed cranial plate is quite uniform with a reduction of about 20%, which is considered satisfactory compared to the thickness reduction at fracture (68%) of a pure titanium sheet with the same ISF parameters.
- The percentage of voids in the pure titanium of the formed cranial plate is very low (0.0286) compared to the percentage of voids at fracture (0.3025). The major-minor strain of the cranial plate is distributed in the safe zone of the forming limit diagram.
- The strain ratio during forming of the cranial plate was determined quantitatively to be 0.0488, indicating that the cranial plate deformed under plane strain conditions.

8.2.5 Deformation and fracture of AMC and its applicability for ISF

By evaluating the deformation and fracture mechanisms of a 6092Al alloy metal matrix composite reinforced with 17.5p vol. % SiC particles (6092Al/SiCp) using SEM, EDS, TEM and XRD, this work investigated the applicability of using incremental sheet forming process to form the 6092Al/SiCp aluminium matrix composite (AMC) under different heat treatment conditions. O-condition annealing was applied to reduce the detrimental effect of the precipitations and to improve the ductility and fracture toughness of the material. In addition, tensile tests with a range of strain rates ($8x10^{-5}$, 8×10^{-4}, 8×10^{-3}, 8×10^{-2} and $0.16\ s^{-1}$) were used to investigate the effect of strain rate on the flow stress and ductility of the AMC material. The results show that the 6092Al/SiCp composite with T6 treatment is not suitable for direct application of high deformation processes, e.g. ISF process, due to the intermetallic compounds. Therefore, heat treatment is required to enhance the ductility of the 6092Al/SiCp composite. The following conclusions may be drawn from this study:

- Al_2Cu, $Al_4Cu_2Mg_8Si_7$ and $MgAl_2$ precipitates are formed in the interface between the Al-matrix and SiC particle after T6-treatement. These precipitations have an important effect on the mechanical properties with an increased hardness and reduced ductility of the 6092Al/SiCp sheets. O-condition annealing can decrease the Al_2Cu intermetallic compound and increase the elongation to fracture.

- The shape and ductility dimples density and forms in the fracture surface of Al/SiCp composite correlate closely with heat treatment and strain rate conditions of the tested specimens.
- The ductility of the 6092Al/SiCp composite can be improved significantly using heat treatment (O-condition annealing) at a low strain rate. The 6092Al/SiCp composite with O-condition annealing is more sensitive to strain rate than the one of T6-treatment.
- With a low strain rate ($8x10^{-5}s^{-1}$), two types of fracture can be observed in 6092Al/SiCp composite; the first type shows a combination of brittle and ductile fracture and it contains shallow dimples with many broken SiC particles for the material subjected to T6 treatment. The second type is the ductile fracture with a high percentage of deep dimples for the material subjected to O-condition annealing.
- Under high strain rate, an interfacial crack in Al matrix was observed in the fracture surface with both heat treatment conditions (T6 and O-condition). This crack is generated due to high stress level caused by high strain rate.
- By investigating the feasibility of using SPIF to form 6092Al/SiCp AMC sheets for the first time, the results show that the 6092Al/SiCp sheets can be satisfactorily formed under O-condition annealing.
- The results also show a degree of strain rate sensitivity in incremental sheet forming of the 6092Al/SiCp AMC material. Low feed rate improves the formability and enables higher wall angle to be achieved in the SPIF process.

8.3 Future work

The aims of this thesis were to investigate the deformation and fracture mechanisms in ISF processes and to examine the suitability of ISF to manufacture customised Ti cranial plates and the applicability of ISF to form new materials, e.g. Al/SiCp composite materials with new modelling methods developed and valuable results and insights achieved in a number of focused areas. However further work is still needed for improvement of FE modelling and experimental testing in the following areas:

- In this study, the GTN damage model was employed to predict fracture in the ISF process based on the assumption that the material behaviour of the sheet was isotropic. The GTN model can be extended to include and study the effects of kinematic hardening and anisotropy on the location and depth of fracture in ISF.
- The GTN damage model with stress triaxiality can be used to construct the forming limit stress diagram (FLSD) to validate its usability in ISF.
- The formability and fracture mechanisms of the ISF process have been studied individually by many researchers, who attributed the deformation and fracture to different mechanisms, such as meridional tensile stresses, through-thickness shear and bending under tension. Up to now, there are still contradicting views and theories in terms of the formability and fracture in ISF. There is a need for more detailed study into the effect of meridional stress, shear and bending using a wide range of process variables to analyse the deformation and formability ISF and to predict fracture more accurately in ISF.
- In Chapter 6, 7 experimental test cases were performed to study the effect of process parameters on formability and fracture of ISF. This work can be extended by performing the design of experiment from a statistical point of view, e.g. Taguchi design.
- The feasibility of reconstructing a reliable cranial plate from 0.7mm grade 1 pure titanium using the ISF process was examined in this work with regard to formability. Further investigation should be carried out to develop new tool path strategies which take into consideration the effect of materials' properties and forming parameters in order to produce a cranial plate with a lesser degree of springback and to improve the surface finish and dimensional accuracy.

- O-condition annealing was used to improve the ductility of 6092Al/SiCp composite sheet to be able to deform it using the ISF process. There is a scope for looking into using different heat treatments to reduce the detrimental effects of intermetallic compounds on the AMC sheet e.g. $Al_4Cu_2Mg_8Si_7$ and to enhance further its formability.
- After investigating the feasibility of using ISF to form 6092Al/SiCp AMC sheets for the first time, the results show that the 6092Al/SiCp sheets can be satisfactorily formed after O-condition annealing; this work can be extended to study the formability and fracture mechanisms of AMC sheet using a wide range of process variables, such as step size, tool rotation and tool size, as well constructing the forming limit curve at necking (FLCN) and fracture (FLCF) for AMC materials.
- It is believed that it would be beneficial to use FE simulation to analyse the deformation of the 6092Al/SiCp composite sheet during the ISF process and to develop predictive models for fracture as this could help to extend the capability of ISF to manufacture the composite materials for lightweight applications.

REFERENCES

1. Hirt, G. and M. Bambach, *Incremental Sheet Forming*, in *sheet metal forming: processes and applications*, T. Altan and A.E. Tekkaya, Editors. 2012, ASM International: Materials Park, Ohio.
2. Shim, M.-S. and J.-J. Park, *The formability of aluminum sheet in incremental forming.* Journal of Materials Processing Technology, 2001. **113**(1): p. 654-658.
3. Tisza, M., *General overview of sheet incremental forming.* Journal of Achievements in Materials and Manufacturing Engineering, 2012. **55**: p. 113-120.
4. Leszak, E., *Apparatus and process for incremental dieless forming* 1967, United States patent office.
5. Mason, B., *Sheet metal forming for small batches.* Bachelor thesis, Univ. of Nottingham, 1978.
6. Appleton, E. and B. Mason, *Sheetmetal forming for small batches using sacrificial tooling.* Production Engineer, 1984. **63**(9): p. 58-61.
7. Iseki, H. and H. Kumon, *Forming limit of incremental sheet metal stretch forming using spherical rollers.* Journal-Japan Society for Technology of Plasticity 1994. **35**: p. 1336-1336.
8. Iseki, H., *An approximate deformation analysis and FEM analysis for the incremental bulging of sheet metal using a spherical roller.* Journal of Materials Processing Technology, 2001. **111**(1): p. 150-154.
9. Filice, L., L. Fratini, and F. Micari, *Analysis of material formability in incremental forming.* CIRP Annals - Manufacturing Technology, 2002. **51**(1): p. 199-202.
10. Ceretti, E., C. Giardini, and A. Attanasio, *Experimental and simulative results in sheet incremental forming on CNC machines.* Journal of Materials Processing Technology, 2004. **152**(2): p. 176-184.
11. Lora, F.A., U. Boff, C.C. Yurgel, L.F. Folle, and L. Schaeffer, *Validation of the computer simulation process applied to the incremental forming process for the evaluation of strain paths.* Key Engineering Materials, 2013. **554**: p. 2453-2461.
12. Micari, F., G. Ambrogio, and L. Filice, *Shape and dimensional accuracy in single point incremental forming: state of the art and future trends.* Journal of Materials Processing Technology, 2007. **191**(1): p. 390-395.
13. Luigino, F., A. Giusy, and G. Manlio, *Optimised tool-path design to reduce thinning in incremental sheet forming process.* International Journal of Material Forming, 2013. **6**: p. 173–178.
14. Schaeffer, L., J. Castelan, V. Gruber, A. Daleffe, and R. Marcelino. *Development of customized products through the use of incremental sheet forming for medical orthopadic application*. in *3rd International Conference on Integrity, Reliability and Failure, Porto/Portugal*. 2009.
15. Attanasio, A., E. Ceretti, C. Giardini, and L. Mazzoni, *Asymmetric two points incremental forming: improving surface quality and geometric accuracy by tool path optimization.* Journal of Materials Processing Technology, 2008. **197**(1): p. 59-67.
16. Jeswiet, J. and D. Young, *Forming limit diagrams for single-point incremental forming of aluminium sheet.* Proceedings of the Institution of Mechanical

Engineers, Part B: Journal of Engineering Manufacture, 2005. **219**(4): p. 359-364.

17. Verbert, J., B. Belkassem, C. Henrard, A. Habraken, J. Gu, H. Sol, B. Lauwers, and J. Duflou, *Multi-step toolpath approach to overcome forming limitations in single point incremental forming.* International Journal of Material Forming, 2008. **1**(1): p. 1203-1206.
18. Duflou, J., B. Lauwers, J. Verbert, F. Gelaude, and Y. Tunckol, *Medical application of single point incremental forming: Cranial plate manufaturing*, in *Proc. 2nd Internat. Conf. on Advanced Research in Virtual and Rapid Prototyping, VRAP, Leiria*. 2005. p. 161-166.
19. Duflou, J.R., A.K. Behera, H. Vanhove, and L.S. Bertol, *Manufacture of accurate titanium cranio-facial implants with high forming angle using single point incremental forming.* Key Engineering Materials, 2013. **549**: p. 223-230.
20. Silva, M.B., M. Skjoedt, P.A.F. Martins, and N. Bay, *Revisiting the fundamentals of single point incremental forming by means of membrane analysis.* International Journal of Machine Tools & Manufacture, 2008. **48**: p. 73–83.
21. Malhotra, R., L. Xue, T. Belytschko, and J. Cao, *Mechanics of fracture in single point incremental forming.* Journal of Materials Processing Technology, 2012. **212**(7): p. 1573-1590.
22. Jackson, K. and J. Allwood, *The mechanics of incremental sheet forming.* Journal of Materials Processing Technology, 2009. **209**(3): p. 1158-1174.
23. Isik, K., M.B. Silva, A.E. Tekkaya, and P.A.F. Martins, *Formability limits by fracture in sheet metal forming.* Journal of Materials Processing Technology, 2014. **214**(8): p. 1557-1565.
24. Centeno, G., I. Bagudanch, A.J. Martínez-Donaire, M.L. García-Romeu, and C. Vallellano, *Critical analysis of necking and fracture limit strains and forming forces in single-point incremental forming.* Materials and Design, 2014. **63**: p. 20-29.
25. Parsa, M., M. Ettehad, and P. Matin, *Forming limit diagram determination of Al 3105 sheets and Al 3105/polypropylene/Al 3105 sandwich sheets using numerical calculations and experimental investigations.* Journal of Engineering Materials and Technology, 2013. **135**(3): p. 031003.
26. Kami, A., B.M. Dariani, A.S. Vanini, D.S. Comsa, and D. Banabic, *Numerical determination of the forming limit curves of anisotropic sheet metals using GTN damage model.* Journal of Materials Processing Technology, 2015. **216**: p. 472-483.
27. Duflou, J., Y. Tunçkol, A. Szekeres, and P. Vanherck, *Experimental study on force measurements for single point incremental forming.* Journal of Materials Processing Technology, 2007. **189**(1): p. 65-72.
28. Ham, M. and J. Jeswiet, *Single point incremental forming and the forming criteria for AA3003.* CIRP Annals - Manufacturing Technology, 2006. **55**(1): p. 241-244.
29. Bhattacharya, A., K. Maneesh, N. Venkata Reddy, and J. Cao, *Formability and surface finish studies in single point incremental forming.* Journal of Manufacturing Science and Engineering, 2011. **133**(6): p. 061020.
30. Buffa, G., D. Campanella, and L. Fratini, *On the improvement of material formability in SPIF operation through tool stirring action.* The International Journal of Advanced Manufacturing Technology, 2013: p. 1-9.

31. Decultot, N., L. Robert, V. Velay, and G. Bernhart, *Single point incremental sheet forming investigated by in-process 3D digital image correlation.* EPJ Web of Conferences, 2010. **6**: p. 11001.
32. Fritzen, D., A. Daleffe, J. Castelan, and L. Schaeffer, *Brass 70/30 and incremental sheet forming process.* Key Engineering Materials, 2013. **554**: p. 1419-1431.
33. Kim, Y.S., H.J. Lee, J.G. Park, and D.T. Nguyen, *Finite element method study of incremental sheet forming for complex shape and its improvement.* Proceedings of the Institution of Mechanical Engineers, Part B: Journal of Engineering Manufacture, 2010. **224**(6): p. 913-924.
34. Hussain, G., L. Gao, and Z.Y. Zhang, *Formability evaluation of a pure titanium sheet in the cold incremental forming process*. International Journal of Advanced Manufacturing Technology, 2008. **37**: p. 920–926.
35. Kim, Y. and J. Park, *Effect of process parameters on formability in incremental forming of sheet metal.* Journal of Materials Processing Technology, 2002. **130**: p. 42-46.
36. Martins, P.A.F., N. Bay, A.G. Atkins, M. Skjoedt, and M.B. Silva, *Single-point incremental forming and formability–failure diagrams.* The Journal of Strain Analysis for Engineering Design, 2008. **43**(1): p. 15-35.
37. Allwood, J., D. Shouler, and A.E. Tekkaya. *The increased forming limits of incremental sheet forming processes*. in *Key Engineering Materials*. 2007. Trans Tech Publ.
38. Saad, A., *Single point incremental forming*, in *Department of Industrial Engineering And Production*. 2012, Kth Royal Institute of Technology: Stockholm, Sweden.
39. Kim, T.J. and D.Y. Yang, *Improvement of formability for the incremental sheet metal forming process.* International Journal of Mechanical Sciences, 2000. **42**: p. 1271-1286.
40. Han, F. and J.-h. Mo, *Numerical simulation and experimental investigation of incremental sheet forming process.* Journal of Central South University of Technology, 2008. **15**(5): p. 581-587.
41. Jun-chao, L., L. Chong, and T.-g. Zhou, *Thickness distribution and mechanical property of sheet metal incremental forming based on numerical simulation.* Transactions of Nonferrous Metals Society of China, 2012. **22**: p. s54-s60.
42. Junchao, L., H. Jianbiao, P. Junjie, and G. Pei, *Thickness distribution and design of a multi-stage process for sheet metal incremental forming.* International Journal of Advanced Manufacturing Technology, 2012. **62**: p. 981–988.
43. Junchao, L., P. Geng, and J. Shen, *Numerical simulation and experimental investigation of multistage incremental sheet forming.* International Journal of Advanced Manufacturing Technology, 2013. **68**(9-12): p. 2637-2644.
44. Silva, P.J., L.M. Leodido, and C.R.M. Silva, *Analysis of incremental sheet forming parameters and tools aimed at rapid prototyping.* Key Engineering Materials, 2013. **554**: p. 2285-2292.
45. Duflou, J.R., B. Callebaut, J. Verbert, and H. De Baerdemaeker, *Laser assisted incremental forming: formability and accuracy improvement.* CIRP Annals - Manufacturing Technology, 2007. **56**(1): p. 273-276.
46. Ji, Y.H. and J.J. Park, *Formability of magnesium AZ31 sheet in the incremental forming at warm temperature.* Journal of Materials Processing Technology, 2008. **201**(1): p. 354-358.

47. Fan, G., L. Gao, G. Hussain, and Z. Wu, *Electric hot incremental forming: a novel technique.* International Journal of Machine Tools and Manufacture, 2008. **48**(15): p. 1688-1692.
48. Liu, R., B. Lu, D. Xu, J. Chen, F. Chen, H. Ou, and H. Long, *Development of novel tools for electricity-assisted incremental sheet forming of titanium alloy.* International Journal of Advanced Manufacturing Technology, 2016. **85**(5): p. 1-8.
49. Göttmann, A., J. Diettrich, G. Bergweiler, M. Bambach, G. Hirt, P. Loosen, and R. Poprawe, *Laser-assisted asymmetric incremental sheet forming of titanium sheet metal parts.* Production Engineering, 2011. **5**(3): p. 263-271.
50. Mosecker, L., A. Göttmann, A. Saeed-Akbari, W. Bleck, M. Bambach, and G. Hirt, *Deformation mechanisms of Ti6Al4V sheet material during the incremental sheet forming with laser heating.* Key Engineering Materials, 2013. **549**: p. 372-380.
51. Adams, D. and J. Jeswiet, *Single-point incremental forming of 6061-T6 using electrically assisted forming methods.* Journal of Engineering Manufacture, 2014. **228**(7): p. 757–764.
52. Minutolo, F.C., M. Durante, A. Formisano, and A. Langella, *Evaluation of the maximum slope angle of simple geometries carried out by incremental forming process.* Journal of Materials Processing Technology, 2007. **194**(1): p. 145-150.
53. Radu, C., *Determination of the maximum forming angle of some carbon steel metal sheet.* Journal of Engineering Studies and Research, 2011. **17**: p. 71-74.
54. Ambrogio, G., L. Filice, L. Fratini, and F. Micari. *Process mechanics analysis in single point incremental forming*. in *AIP Conference Proceedings*. 2004. AIP
55. Rattanachan, K. and C. Chungchoo, *Formability in single point incremental forming of dome geometry.* Asian International Journal of Science And Technology in Production and Manufacturing Engineering., 2009. **2(4)**: p. 57-63.
56. Ham, M. and J. Jeswiet, *Forming limit curves in single point incremental forming.* CIRP Annals - Manufacturing Technology, 2007. **56**(1): p. 277-280.
57. Lu, B., Y. Fang, D. Xu, J. Chen, H. Ou, N. Moser, and J. Cao, *Mechanism investigation of friction-related effects in single point incremental forming using a developed oblique roller-ball tool.* International Journal of Machine Tools and Manufacture, 2014. **85**: p. 14-29.
58. Yamashita, M., M. Gotoh, and S.-Y. Atsumi, *Numerical simulation of incremental forming of sheet metal.* Journal of Materials Processing Technology, 2008. **199**(1): p. 163-172.
59. Zhou, L.R., *Study on mechanism of NC sheet metal incremental forming.* Advanced Materials Research, 2011. **239**: p. 940-943.
60. Azaouzi, M. and N. Lebaal, *Tool path optimization for single point incremental sheet forming using response surface method.* Simulation Modelling Practice and Theory, 2012. **24**: p. 49-58.
61. Liu, Z., Y. Li, and P.A. Meehan, *Experimental investigation of mechanical properties, formability and force measurement for AA7075-O aluminum alloy sheets formed by incremental forming.* International Journal of Precision Engineering and Manufacturing, 2013. **14**(11): p. 1891-1899.

62. Sy, L.V., *Modeling of single point incremental forming process for metal and polymeric sheet* in *Department of Innovation in Mechanics and Management*. 2009, University of Padua: Italy.
63. Martins, P.A.F., N. Bay, M. Skjoedt, and M.B. Silva, *Theory of single point incremental forming.* CIRP Annals - Manufacturing Technology, 2008. **57**(1): p. 247-252.
64. SIMULIA, *ABAQUS 6.16, Alalysis User's Manual*. 2016.
65. Malhotra, R., L. Xue, J. Cao, and T. Belytschko, *Identification of deformation mechanisms responsible for failure in incremental forming using a damage based fracture model.* AIP Conference Proceedings, 2011. **1383**(1): p. 469-476.
66. Guzmán, C.F. and A.M. Habraken, *Towards fracture prediction in single point incremental forming.* Key Engineering Materials, 2013. **554**: p. 2355-2362.
67. Xu, D., R. Malhotra, J. Chen, B. Lu, and J. Cao, *Numerical and experimental studies for the effects of through-the-thickness shear on formability in single point incremental forming.* AIP Conference Proceedings, 2013. **1532**(1): p. 969-976.
68. Fang, Y., B. Lu, J. Chen, D.K. Xu, and H. Ou, *Analytical and experimental investigations on deformation mechanism and fracture behavior in single point incremental forming.* Journal of Materials Processing Technology, 2014. **214**(8): p. 1503-1515.
69. Mirnia, M.J. and M. Shamsari, *Numerical prediction of failure in single point incremental forming using a phenomenological ductile fracture criterion.* Journal of Materials Processing Technology, 2017. **244**: p. 17-43.
70. Li, Y., W.J. Daniel, and P.A. Meehan, *Deformation analysis in single-point incremental forming through finite element simulation.* International Journal of Advanced Manufacturing Technology, 2016. **88**(1): p. 1-13.
71. Ai, S., B. Lu, J. Chen, H. Long, and H. Ou, *Evaluation of deformation stability and fracture mechanism in incremental sheet forming.* International Journal of Mechanical Sciences, 2017. **124**: p. 174-184.
72. Câmara, J., *Single Point Incremental Forming*. 2009, Master Thesis, Instituto Superior Tecnico, Lisbon.
73. Han, H.N. and K.-H. Kim, *A ductile fracture criterion in sheet metal forming process.* Journal of Materials Processing Technology, 2003. **142**(1): p. 231-238.
74. Araújo, R., P. Teixeira, L. Montanari, A. Reis, M.B. Silva, and P.A. Martins, *Single point incremental forming of a facial implant.* Prosthetics and Orthotics International, 2014. **38**(5): p. 369-378.
75. Nguyen, D.-T. and Y.-S. Kim, *A numerical study on establishing the forming limit curve and indicating the formability of complex shape in incremental sheet forming process.* International Journal of Precision Engineering and Manufacturing, 2013. **14**(12): p. 2087-2093.
76. Centeno, G., A.J. Martínez-Donaire, C. Vallellano, L.H. Martínez-Palmeth, D. Morales, C. Suntaxi, and F.J. García-Lomas, *Experimental study on the evaluation of necking and fracture strains in sheet metal forming processes.* Procedia Engineering, 2013. **63**: p. 650-658.
77. Lu, B., Y. Fang, D. Xu, J. Chen, S. Ai, H. Long, H. Ou, and J. Cao, *Investigation of material deformation mechanism in double side incremental sheet forming.* International Journal of Machine Tools and Manufacture, 2015. **93**: p. 37-48.

78. Haque, M.Z. and J.W. Yoon, *Stress based prediction of formability and failure in incremental sheet forming.* International Journal of Material Forming, 2016. **9**(3): p. 413-421.
79. Valentin, S.O., M.P. Adrian, V.D. Cristian, F. Radu , and R. Mihai, *Numerical simulation of the incremental forming process for knee implants.* X International Conference on Computational Plasticity, 2009(Barcelona): p. 1-4.
80. Oleksik, V., A. Pascu, C. Deac, R. Fleaca, M. Roman, and O. Bologa, *The influence of geometrical parameters on the incremental forming process for knee implants analyzed by numerical simulation.* AIP Conference Proceedings, 2010. **1252**(1): p. 1208-1215.
81. Silva, M.B., P.S. Nielsen, N. Bay, and P.A.F. Martins, *Failure mechanisms in single-point incremental forming of metals.* International Journal of Advanced Manufacturing Technology, 2011. **56**(9-12): p. 893-903.
82. Jeswiet, J., F. Micari, G. Hirt, A. Bramley, J. Duflou, and J. Allwood, *Asymmetric single point incremental forming of sheet metal.* CIRP Annals - Manufacturing Technology, 2005. **54**(2): p. 88-114.
83. Ambrogio, G., I. Costantino, L. De Napoli, L. Filice, L. Fratini, and M. Muzzupappa, *Influence of some relevant process parameters on the dimensional accuracy in incremental forming: a numerical and experimental investigation.* Journal of Materials Processing Technology, 2004. **153**: p. 501-507.
84. Dejardin, S., S. Thibaud, J.C. Gelin, and G. Michel, *Experimental investigations and numerical analysis for improving knowledge of incremental sheet forming process for sheet metal parts.* Journal of Materials Processing Technology, 2010. **210**(2): p. 363-369.
85. Han, F., J.-h. Mo, P. Gong, and M. Li, *Method of closed loop springback compensation for incremental sheet forming process.* Journal of Central South University of Technology, 2011. **18**(5): p. 1509-1517.
86. Essa, K. and P. Hartley, *An assessment of various process strategies for improving precision in single point incremental forming.* International Journal of Material Forming, 2011. **4**(4): p. 401–412.
87. Fu, Z., J. Mo, F. Han, and P. Gong, *Tool path correction algorithm for single-point incremental forming of sheet metal.* International Journal of Advanced Manufacturing Technology, 2013. **64**: p. 1239–1248.
88. Lu, B., J. Chen, H. Ou, and J. Cao, *Feature-based tool path generation approach for incremental sheet forming process.* Journal of Materials Processing Technology, 2013. **213**(7): p. 1221-1233.
89. Vahdati, M., M. Sedighi, and H. Khoshkish, *An analytical model to reduce spring-back in incremental sheet metal forming (ISMF) process.* Advanced Materials Research, 2010. **83**: p. 1113-1120.
90. Pohlak, M., R. Küttner, J. Majak, K. Karjust, and A. Sutt. *Experimental study of incremental forming of sheet metal products*. in *Proc of the fourth International DAAAM Conference, Tallinn, Estonia*. 2004.
91. Zhang, Z., H. Zhang, Y. Shi, N. Moser, H. Ren, K.F. Ehmann, and J. Cao, *Springback reduction by annealing for incremental sheet forming.* Procedia Manufacturing, 2016. **5**: p. 696-706.
92. Cerro, I., E. Maidagan, J. Arana, A. Rivero, and P.P. Rodríguez, *Theoretical and experimental analysis of the dieless incremental sheet forming process.* Journal of Materials Processing Technology, 2006. **177**(1): p. 404-408.

93. Durante, M., A. Formisano, A. Langella, and F.M. Capece Minutolo, *The influence of tool rotation on an incremental forming process.* Journal of Materials Processing Technology, 2009. **209**(9): p. 4621-4626.
94. Hamilton, K. and J. Jeswiet, *Single point incremental forming at high feed rates and rotational speeds: surface and structural consequences.* CIRP Annals - Manufacturing Technology, 2010. **59**: p. 311–314.
95. Ham, M., B.M. Powers, and J. Loiselle, *Surface topography from single point incremental forming using an acetal tool.* Key Engineering Materials, 2013. **549**: p. 84-91.
96. Oleksik, V., A. Pascu, C. Deac, R. Fleacă, O. Bologa, and G. Racz, *Experimental study on the surface quality of the medical implants obtained by single point incremental forming.* International Journal of Material Forming, 2010. **3**: p. 935-938.
97. Skjoedt, M., M.H. Hancock, and N. Bay, *Creating helical tool paths for single point incremental forming.* Key Engineering Materials, 2007. **344**: p. 583-590.
98. Hagan, E. and J. Jeswiet, *Analysis of surface roughness for parts formed by computer numerical controlled incremental forming.* Journal Engineering Manufacture, 2004. **218 Part B**: p. 1307-1312.
99. Ambrogio, G., L. Filice, and F. Gagliardi, *Formability of lightweight alloys by hot incremental sheet forming.* Materials & Design, 2012. **34**: p. 501-508.
100. Daleffe, A., L. Schaeffer, D. Fritzen, and J. Castelan, *Analysis of the incremental forming of titanium F67 grade 2 sheet.* Key Engineering Materials, 2013. **554**: p. 195-203.
101. Shakir, M.G., *The effect of anisotropy on deep drawing operation*, in *Anisotropy on Deep Drawing Operation*. 2011, LAP LAMBERT Academic GmbH & Co. KG: Saarbrucken, German.
102. Magnus, S., *Finite eelement simulation of punching*, in *Department of Applied Physics and Mechanical Engineering*. 2006, Lulea University of Technology.
103. Djavanroodi, F. and A. Derogar, *Experimental and numerical evaluation of forming limit diagram for Ti6Al4V titanium and Al6061-T6 aluminum alloys sheets.* Materials & Design, 2010. **31**(10): p. 4866-4875.
104. Dunne, F. and N. Petrinic, *Introduction to computational plasticity*. 2005: Oxford University Press on Demand.
105. Mielnik, E.M., *Metalworking science and engineering.* McGraw-Hill, Inc.(USA), 1991: p. 976.
106. Voyiadjis, G.Z. and P. Woelke, *Elasto-plastic and damage analysis of plates and shells*. 2008: Springer Science & Business Media.
107. Hooputra, H., H. Gese, H. Dell, and H. Werner, *A comprehensive failure model for crashworthiness simulation of aluminium extrusions.* International Journal of Crashworthiness, 2004. **9**(5): p. 449-464.
108. Johnson, G.R. and W.H. Cook, *Fracture characteristics of three metals subjected to various strains, strain rates, temperatures and pressures.* Engineering Fracture Mechanics, 1985. **21**(1): p. 31-48.
109. Wierzbicki, T., Y. Bao, Y.-W. Lee, and Y. Bai, *Calibration and evaluation of seven fracture models.* International Journal of Mechanical Sciences, 2005. **47**(4): p. 719-743.
110. Tvergaard, V. and A. Needleman, *Analysis of the cup-cone fracture in a round tensile bar.* Acta Metallurgica, 1984. **32**(1): p. 157-169.

111. Hans, m.H. and J.R.H. THomas, *Collocation, Dissipation and overshoot for time Integration schemes in structuralo dynamics.* Earthquake Engineering and Structural Dynamics, 1978. **6**: p. 99-117.
112. Sun, J.S., K.H. Lee, and H.P. Lee, *Comparison of implicit and explicit finite element methods for dynamic problems.* Journal of Materials Processing Technology, 2000. **105**: p. 110 -118.
113. Chung, W.J., J.W. Cho, and T. Belytschko, *On the dynamic effects of explicit FEM in sheet metal forming analysis.* Engineering Computations, 1998. **15**: p. 750-776.
114. Bambach, M. and G. Hirt, *Error Analysis In Explicit Finite Element Analysis Of Incremental Sheet Forming.* AIP Conference Proceedings, 2007. **908**(1): p. 859-864.
115. Lin, W., *Analysis of Material Deformation and Wrinkling Failure in Conventional Metal Spinning Process*, in *School of Engineering and Computing Sciences*. 2012, Durham University.
116. Manco, L., L. Filice, and G. Ambrogio, *Analysis of the thickness distribution varying tool trajectory in single-point incremental forming.* Proceedings of the Institution of Mechanical Engineers, Part B: Journal of Engineering Manufacture, 2011. **225**(3): p. 348-356.
117. Cao, T.S., P. Montmitonnet, and P.O. Bouchard, *A detailed description of the Gurson–Tvergaard–Needleman model within a mixed velocity–pressure finite element formulation.* International Journal for Numerical Methods in Engineering, 2013. **96**(9): p. 561-583.
118. Isik, K., G. Gerstein, T. Clausmeyer, F. Nürnberger, A.E. Tekkaya, and H.J. Maier, *Evaluation of Void Nucleation and Development during Plastic Deformation of Dual-Phase Steel DP600.* Steel Research International, 2016. **87**: p. 1-9.
119. Chen, Z. and X. Dong, *The GTN damage model based on Hill'48 anisotropic yield criterion and its application in sheet metal forming.* Computational Materials Science, 2009. **44**(3): p. 1013-1021.
120. Kami, A., B. Mollaei Dariani, A. Sadough Vanini, D.-S. Comsa, and D. Banabic, *Application of a GTN damage model to predict the fracture of metallic sheets subjected to deep-drawing.* Proceedings of the Romanian Academy, Series A, 2014. **15**: p. 300-309.
121. Vrh, M., M. Halilovic, and B. Stok, *Impact of Young's modulus degradation on springback calculation in steel sheet drawing.* Strojniški Vestnik, 2008. **54**(4): p. 288-296.
122. Lievers, W.B., A.K. Pilkey, and D.J. Lloyd, *Using incremental forming to calibrate a void nucleation model for automotive aluminum sheet alloys.* Acta Materialia, 2004. **52**(10): p. 3001-3007.
123. Smith, J., R. Malhotra, W. Liu, and J. Cao, *Application of a shear-modified GTN model to incremental sheet forming.* AIP Conference Proceedings, 2013. **1567**(1): p. 824-827.
124. El-Magd, E., H. Gese, R. Tham, H. Hooputra, and H. Werner, *Fracture criteria for automobile crashworthiness simulation of wrought aluminium alloy components.* Materialwissenschaft und Werkstofftechnik, 2001. **32**(9): p. 712-724.
125. Emmens, W.C. and A.H. van den Boogaard, *An overview of stabilizing deformation mechanisms in incremental sheet forming.* Journal of Materials Processing Technology, 2009. **209**(8): p. 3688-3695.

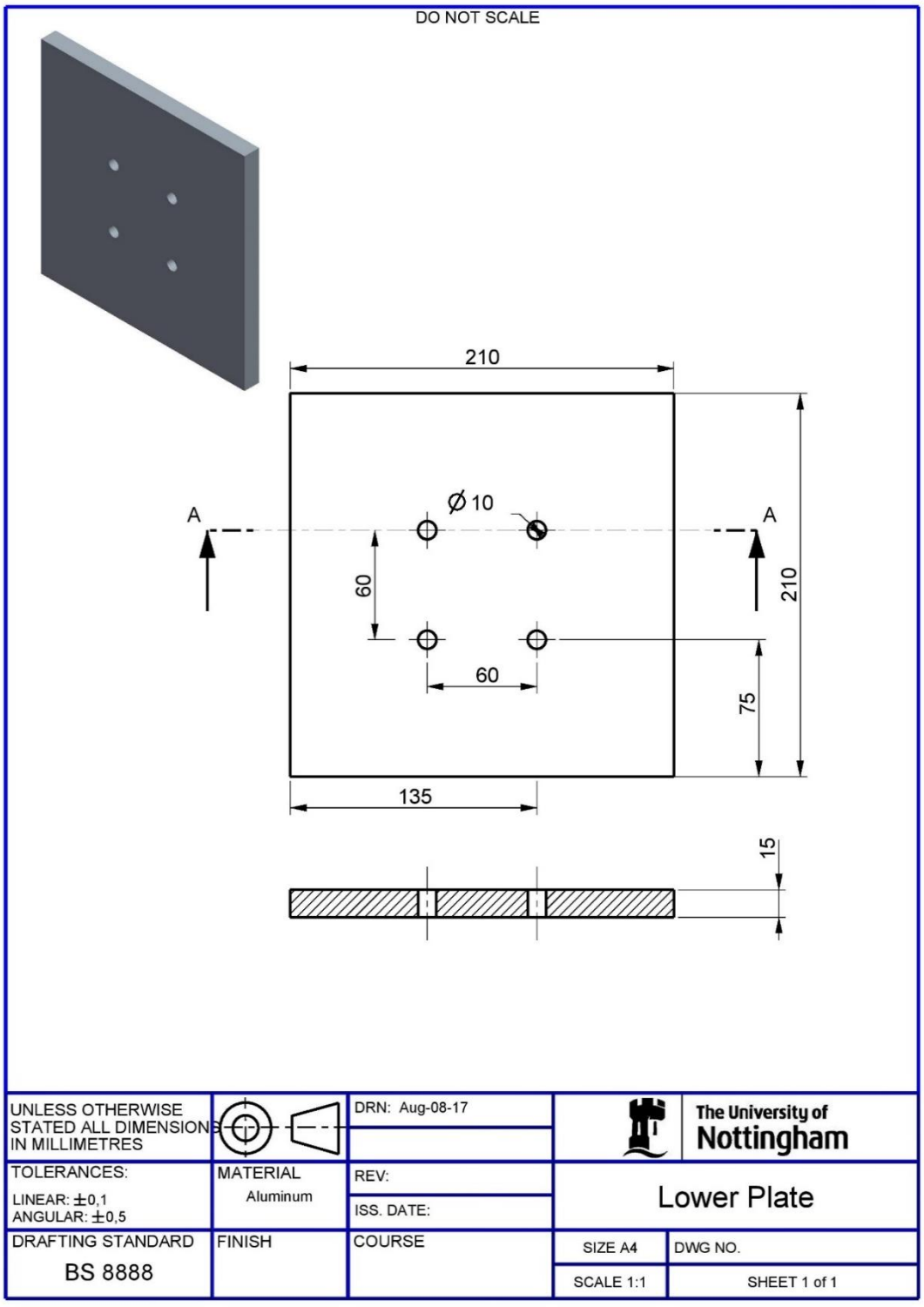
126. Emmens, W. and A. Van den Boogaard, *Incremental forming by continuous bending under tension—an experimental investigation.* Journal of Materials Processing Technology, 2009. **209**(14): p. 5456-5463.
127. Kachanov, L., *On rupture time under condition of creep.* Izvestia Akademi Nauk USSR, Otd. Techn. Nauk, Moskwa, 1958. **8**: p. 26-31.
128. Lemaitre, J., *Local approach of fracture.* Engineering Fracture Mechanics, 1986. **25**(5-6): p. 523-537.
129. Lemaitre, J. and R. Desmorat, *Engineering damage mechanics: ductile, creep, fatigue and brittle failures*. 2005: Springer Science & Business Media.
130. Gurson, A.L., *Continuum theory of ductile rupture by void nucleation and growth: Part I—Yield criteria and flow rules for porous ductile media.* Journal of Engineering Materials and Technology, 1977. **99**(1): p. 2-15.
131. Batista, R.G., I. Iturrioz, and A.P. Cisilino, *Computational modelling of the micromechanics of void growth and coalescence in ductile failure via the Discrete Element Method.* Solid Mechanics in Brazil 2007: p. 97.
132. Kossakowski, P.G. and W. Trampczynski, *Microvoids evolution in S235JR steel subjected to multi-axial stress state.* Engineering Transactions, 2012. **60**(4): p. 287–314.
133. McClintock, F.A., *A criterion for ductile fracture by the growth of holes.* Journal of Applied Mechanics, 1968. **35**(2): p. 363-371.
134. Rice, J.R. and D.M. Tracey, *On the ductile enlargement of voids in triaxial stress fields.* Journal of the Mechanics and Physics of Solids, 1969. **17**(3): p. 201-217.
135. Anderson, T., *Fundamentals and applications (fracture mechanics)*. 1995, CRC Press.
136. Xue, L., *Constitutive modeling of void shearing effect in ductile fracture of porous materials.* Engineering Fracture Mechanics, 2008. **75**(11): p. 3343-3366.
137. Aravas, N., *On the numerical integration of a class of pressure-dependent plasticity models.* International Journal for Numerical Methods in Engineering, 1987. **24**(7): p. 1395-1416.
138. Tvergaard, V., *Influence of void nucleation on ductile shear fracture at a free surface.* Journal of the Mechanics and Physics of Solids, 1982. **30**(6): p. 399-425.
139. Zhang, Z., *A sensitivity analysis of material parameters for the Gurson constitutive model.* Fatigue and Fracture of Engineering Materials and Structures, 1996. **19**(5): p. 561-570.
140. Benseddiq, N. and A. Imad, *A ductile fracture analysis using a local damage model.* International Journal of Pressure Vessels and Piping, 2008. **85**(4): p. 219-227.
141. Corigliano, A., S. Mariani, and B. Orsatti, *Identification of Gurson–Tvergaard material model parameters via Kalman filtering technique. I. Theory.* International Journal of Fracture, 2000. **104**(4): p. 349-373.
142. Nahshon, K. and J. Hutchinson, *Modification of the Gurson model for shear failure.* European Journal of Mechanics-A/Solids, 2008. **27**(1): p. 1-17.
143. Zhou, J., X. Gao, J.C. Sobotka, B.A. Webler, and B.V. Cockeram, *On the extension of the Gurson-type porous plasticity models for prediction of ductile fracture under shear-dominated conditions.* International Journal of Solids and Structures, 2014. **51**(18): p. 3273-3291.

144. McClintock, F.A., *Plasticity aspects of fracture.* Fracture: an advanced treatise, 1971. **3**: p. 47-225.
145. Ortiz, M. and J. Simo, *An analysis of a new class of integration algorithms for elastoplastic constitutive relations.* International Journal for Numerical Methods in Engineering, 1986. **23**(3): p. 353-366.
146. Engelmann, B.E. and R.G. Whirley, *Recent developments in NIKE2D for metalforming analysis and low rate impact.* Nuclear Engineering and Design, 1992. **138**(1): p. 23-35.
147. Nahshon, K. and Z. Xue, *A modified Gurson model and its application to punch-out experiments.* Engineering Fracture Mechanics, 2009. **76**(8): p. 997-1009.
148. Becker, R. and A. Needleman, *Effect of yield surface curvature on necking and failure in porous plastic solids.* Journal of Applied Mechanics, 1986. **53**(3): p. 491-499.
149. Soyarslan, C., M.M. Gharbi, and A. Tekkaya, *A combined experimental–numerical investigation of ductile fracture in bending of a class of ferritic–martensitic steel.* International Journal of Solids and Structures, 2012. **49**(13): p. 1608-1626.
150. Miyauchi, K., *A proposal for a planar simple shear test in sheet metals.* Scientific Papers of the Institute of Physical and Chemical Research, 1984. **78**(3): p. 27-40.
151. Brosius, A., Q. Yin, A. Güner, and A. Tekkaya, *A new shear test for sheet metal characterization.* Steel Research International, 2011. **82**(4): p. 323-328.
152. Bao, Y. and T. Wierzbicki, *On fracture locus in the equivalent strain and stress triaxiality space.* International Journal of Mechanical Sciences, 2004. **46**(1): p. 81-98.
153. Jain, M., J. Allin, and D. Lloyd, *Fracture limit prediction using ductile fracture criteria for forming of an automotive aluminum sheet.* International Journal of Mechanical Sciences, 1999. **41**(10): p. 1273-1288.
154. Vladimirov, I.N., M.P. Pietryga, Y. Kiliclar, V. Tini, and S. Reese, *Failure modelling in metal forming by means of an anisotropic hyperelastic-plasticity model with damage.* International Journal of Damage Mechanics, 2014. **23**(8): p. 1096-1132.
155. Ozturk, F. and D. Lee, *Analysis of forming limits using ductile fracture criteria.* Journal of Materials Processing Technology, 2004. **147**(3): p. 397-404.
156. Uthaisangsuk, V., U. Prahl, S. Münstermann, and W. Bleck, *Experimental and numerical failure criterion for formability prediction in sheet metal forming.* Computational Materials Science, 2008. **43**(1): p. 43-50.
157. Min, H., L. Fuguo, and W. Zhigang, *Forming limit stress diagram prediction of aluminum alloy 5052 based on GTN model parameters determined by in situ tensile test.* Chinese Journal of Aeronautics, 2011. **24**(3): p. 378-386.
158. Skjødt, M., M. Silva, P. Martins, and N. Bay, *Strategies and limits in multi-stage single-point incremental forming.* The Journal of Strain Analysis for Engineering Design, 2010. **45**(1): p. 33-44.
159. Nielsen, K.L. and V. Tvergaard, *Ductile shear failure or plug failure of spot welds modelled by modified Gurson model.* Engineering Fracture Mechanics, 2010. **77**(7): p. 1031-1047.
160. Fang, C.-K., R. Fang, W. Weng, and T. Chuang, *Applicability of ultrasonic testing for the determination of volume fraction of particulates in alumina-*

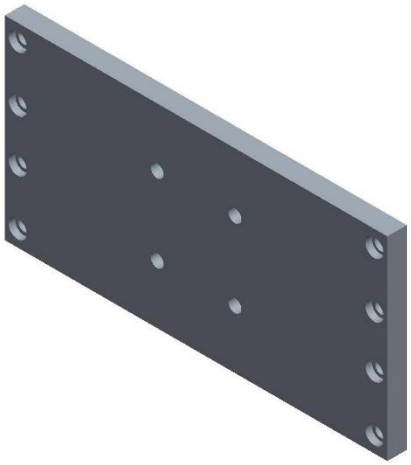
reinforced aluminum matrix composites. Materials Characterization, 1999. **43**(4): p. 217-226.
161. Yuan, W.-h. and B.-l. AN, *Effect of heat treatment on microstructure and mechanical property of extruded 7090/SiC p composite.* Transactions of Nonferrous Metals Society of China, 2012. **22**(9): p. 2080-2086.
162. Sozhamannan, G., S.B. Prabu, and R. Paskaramoorthy, *Failures analysis of particle reinforced metal matrix composites by microstructure based models.* Materials & Design, 2010. **31**(8): p. 3785-3790.
163. Vaidya, R. and A. Zurek, *Dynamic mechanical response of an SiCp/Al-Li (8090) composite.* Journal of Materials Science, 1995. **30**(10): p. 2541-2548.
164. Mandal, D. and S. Viswanathan, *Effect of heat treatment on microstructure and interface of SiC particle reinforced 2124 Al matrix composite.* Materials Characterization, 2013. **85**: p. 73-81.
165. Aidun , D., P. Martin, and J. Sun, *Effects of Heat Treatment on the Mechanical Properties of SiCp/6061 AI Composite.* Journal of Materials Engineering and Performance, 1992. **1**(5): p. 615-624.
166. Lee, J.-C., J.-Y. Byun, C.-S. Oh, H.-K. Seok, and H.-I. Lee, *Effect of various processing methods on the interfacial reactions in SiC p/2024 Al composites.* Acta Materialia, 1997. **45**(12): p. 5303-5315.
167. Zerilli, F. and R. Armstrong, *The effect of dislocation drag on the stress-strain behavior of fcc metals.* Acta Metallurgica et Materialia, 1992. **40**(8): p. 1803-1808.
168. Lee, J.-C., J.-P. Ahn, J.-H. Shim, Z. Shi, and H.-I. Lee, *Control of the interface in SiC/Al composites.* Scripta Materialia, 1999. **41**(8): p. 895-900.
169. Lee, J.-C., H.-K. Seok, and H.-I. Lee, *Alloy design of thixoformable wrought SiC/Al alloy composites.* Materials Research Bulletin, 1999. **34**(1): p. 35-42.
170. Ribes, H., M. Suery, G. L'esperance, and J. Legoux, *Microscopic examination of the interface region in 6061-Al/SiC composites reinforced with as-received and oxidized SiC particles.* Metallurgical Transactions A, 1990. **21**(9): p. 2489-2496.
171. Jin, M., J. Li, and G.J. Shao, *Study of Cu addition on precipitation behaviors and mechanical properties in AA6082 Al-Mg-Si alloy.* Materials Science Forum, 2007. **546**: p. 825-828.
172. Wang, G., Q. Sun, L. Feng, L. Hui, and C. Jing, *Influence of Cu content on ageing behavior of AlSiMgCu cast alloys.* Materials & Design, 2007. **28**(3): p. 1001-1005.
173. Salem, M., I. El-Batanony, M. Ghanem, and M.I.A. ElAal, *Effect of the Matrix and Reinforcement Sizes on the Microstructure, the Physical and Mechanical Properties of Al-SiC Composites.* Journal of Engineering Materials and Technology, 2017. **139**(1): p. 011007.
174. Ge, X. and S. Schmauder, *Micromechanism of fracture in Al/SiC composites.* Journal of Materials Science, 1995. **30**(1): p. 173-178.
175. Qian, L., T. Kobayashi, H. Toda, and Z.-g. Wang, *Dynamic fracture toughness of 6061Al composites reinforced with SiC particulates.* Materials Science and Engineering: A, 2001. **318**(1): p. 189-196.
176. El-Sabbagh, A.M., M. Soliman, M.A. Taha, and H. Palkowski, *Effect of rolling and heat treatment on tensile behaviour of wrought Al-SiCp composites prepared by stir-casting.* Journal of Materials Processing Technology, 2013. **213**(10): p. 1669-1681.

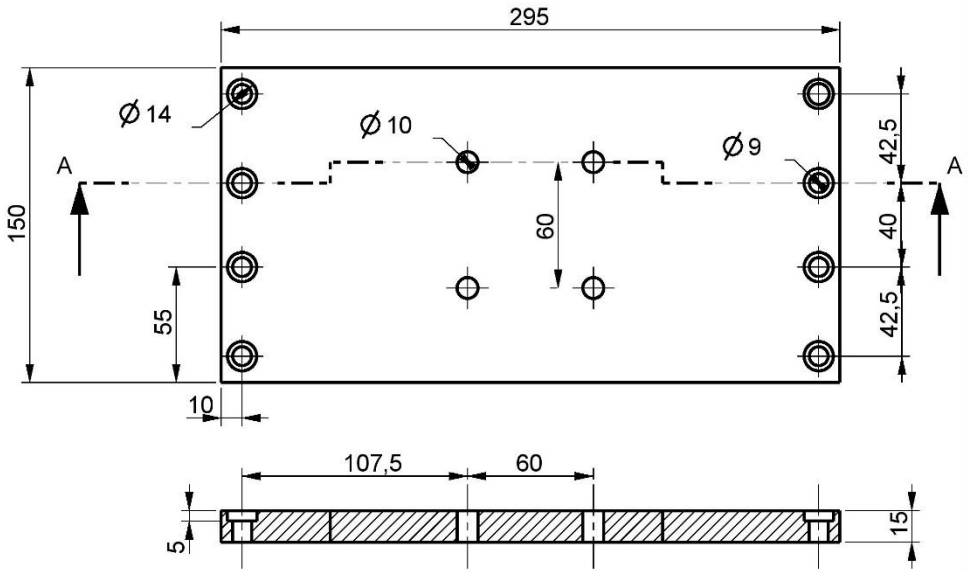
177. Fiorotto, M., M. Sorgente, and G. Lucchetta, *Preliminary studies on single point incremental forming for composite materials.* International Journal of Material Forming, 2010. **3**(1): p. 951-954.
178. Jackson, K., J. Allwood, and M. Landert, *Incremental forming of sandwich panels.* Journal of Materials Processing Technology, 2008. **204**(1): p. 290-303.
179. Davis, J.R. and J.R. Davis, *Aluminum and aluminum alloys*. 1993: ASM International.
180. Standard, A., *E8-04.* Standard Test Methods for Tension Testing of Metallic Materials," Annual Book of ASTM Standards, 2004. **3**.
181. Moniz, B., *Metallurgy*. 1994: American Technical Publishers.
182. Treating, H. and A. Handbook, *Vol 4.* ASM Handbook, ASM International, 1991.
183. Yuan, W., J. Zhang, C. Zhang, and Z. Chen, *Processing of ultra-high strength SiC p/Al–Zn–Mg–Cu composites.* Journal of Materials Processing Technology, 2009. **209**(7): p. 3251-3255.

APPENDIX A: Mechanical drawings used for manufacture of SPIF fixture



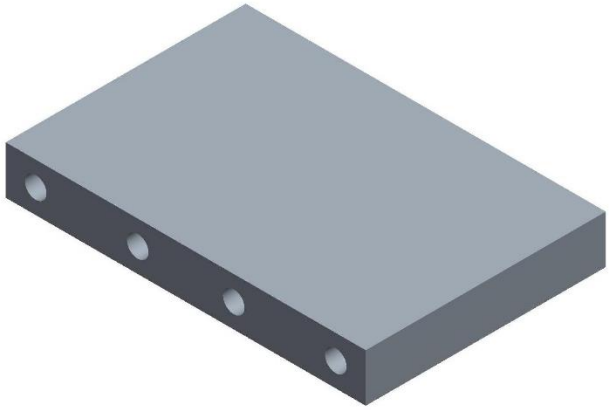
DO NOT SCALE

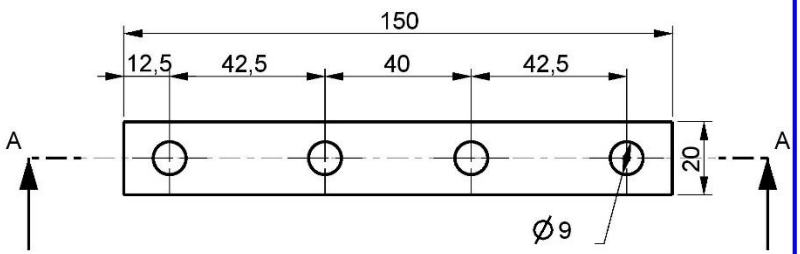


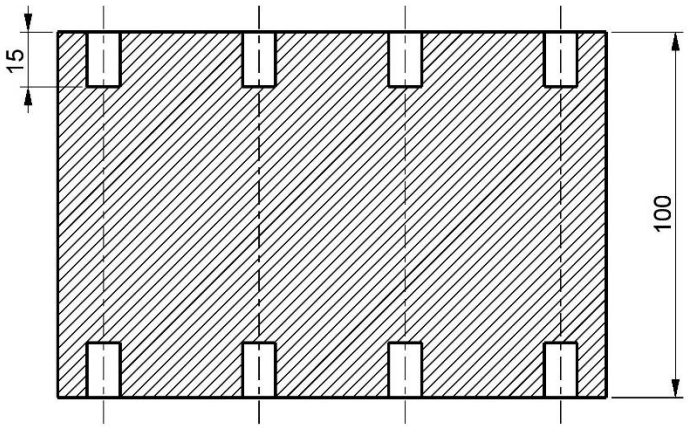


UNLESS OTHERWISE STATED ALL DIMENSIONS IN MILLIMETRES		DRN: Aug-08-17	The University of Nottingham	
TOLERANCES: LINEAR: ±0,1 ANGULAR: ±0,5	MATERIAL Aluminum	REV: ISS. DATE:	Base Plate	
DRAFTING STANDARD BS 8888	FINISH	COURSE	SIZE A4 SCALE 1:1	DWG NO. SHEET 1 of 1

DO NOT SCALE



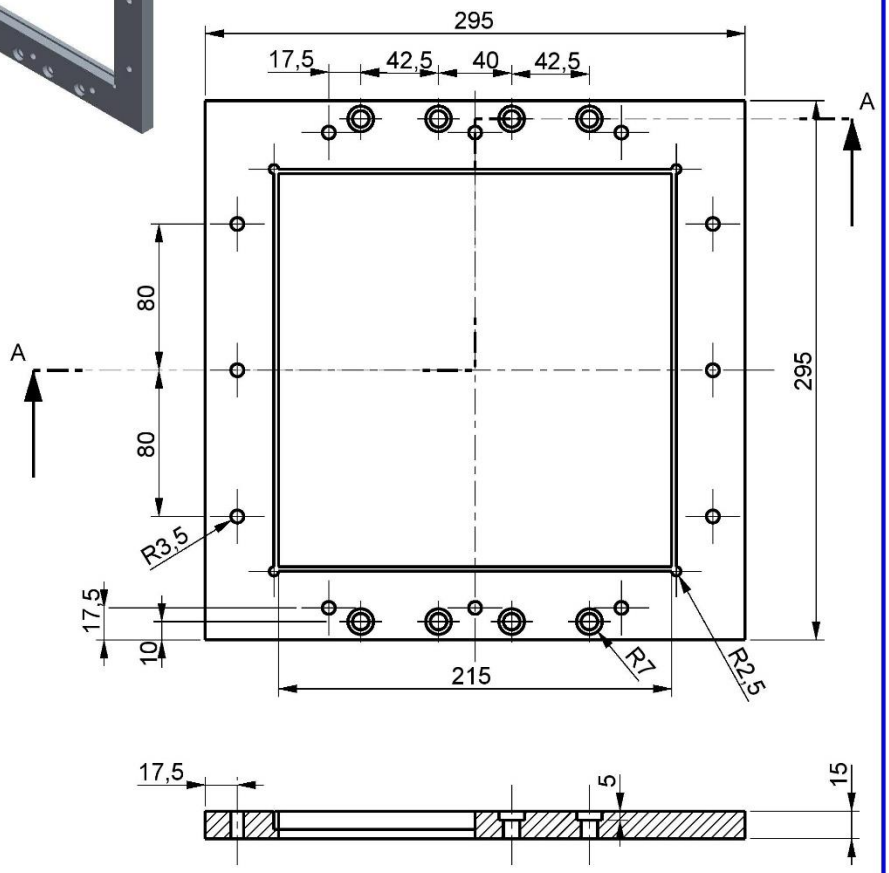




UNLESS OTHERWISE STATED ALL DIMENSIONS IN MILLIMETRES		DRN: Aug-08-17	The University of Nottingham	
TOLERANCES: LINEAR: ±0,1 ANGULAR: ±0,5	MATERIAL Aluminum	REV: ISS. DATE:	Column	
DRAFTING STANDARD BS 8888	FINISH	COURSE	SIZE A4	DWG NO.
			SCALE 1:1	SHEET 1 of 1

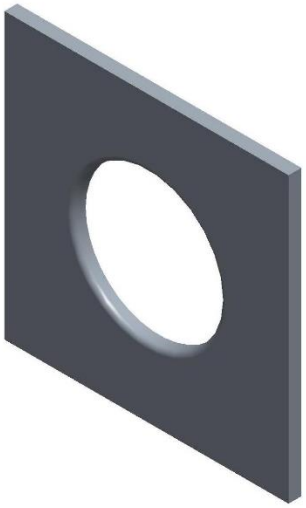
DO NOT SCALE

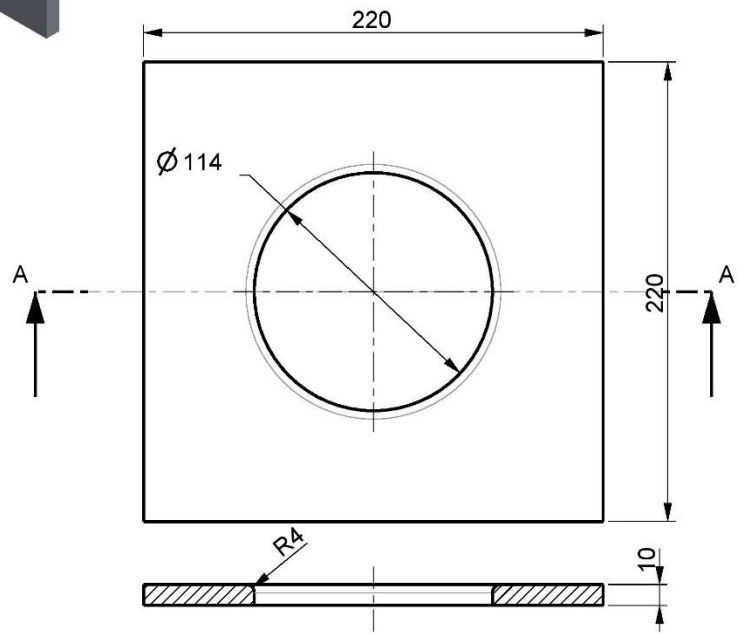




UNLESS OTHERWISE STATED ALL DIMENSIONS IN MILLIMETRES		DRN: Aug-08-17	The University of Nottingham	
TOLERANCES: LINEAR: ±0,1 ANGULAR: ±0,5	MATERIAL Aluminum	REV: ISS. DATE:	Upper Plate	
DRAFTING STANDARD BS 8888	FINISH	COURSE	SIZE A4	DWG NO.
			SCALE 1:1	SHEET 1 of 1

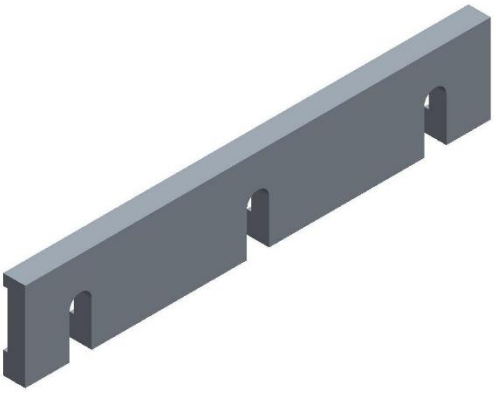
DO NOT SCALE

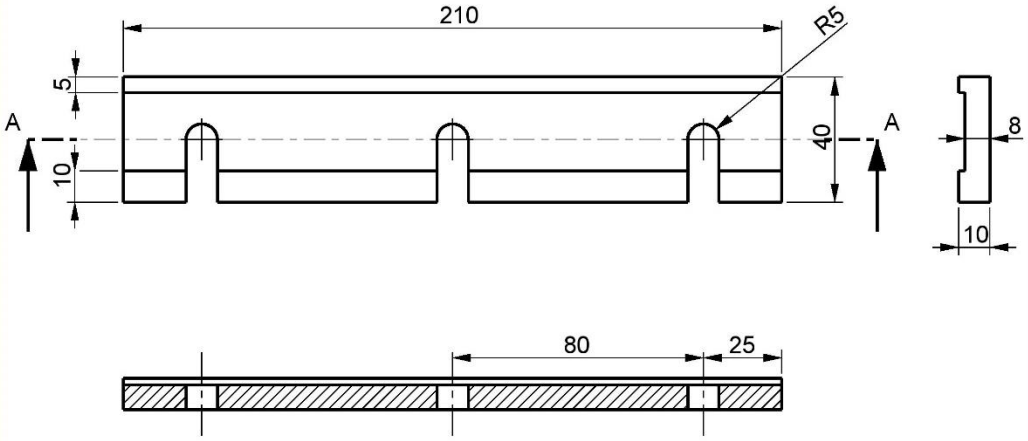




UNLESS OTHERWISE STATED ALL DIMENSIONS IN MILLIMETRES		DRN: Aug-08-17	The University of Nottingham
TOLERANCES: LINEAR: ±0,1 ANGULAR: ±0,5	MATERIAL Mild Steel	REV: ISS. DATE:	Backing Plate
DRAFTING STANDARD BS 8888	FINISH	COURSE	SIZE A4 / DWG NO. SCALE 1:1 / SHEET 1 of 1

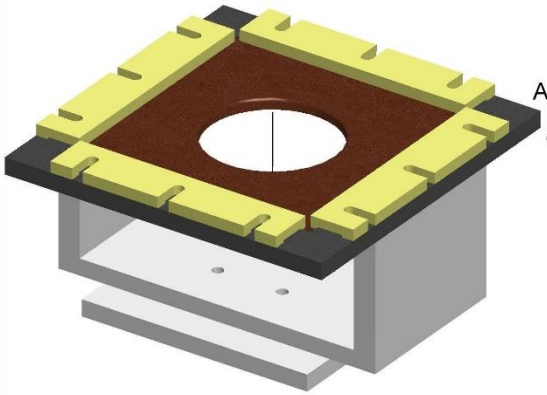
DO NOT SCALE

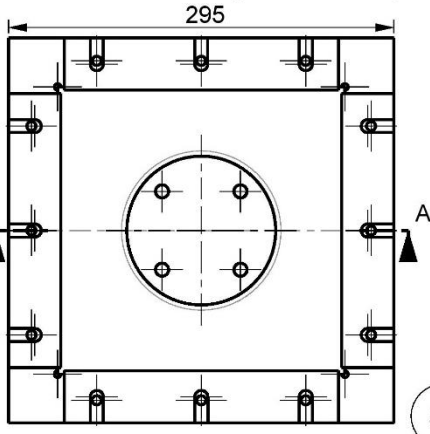


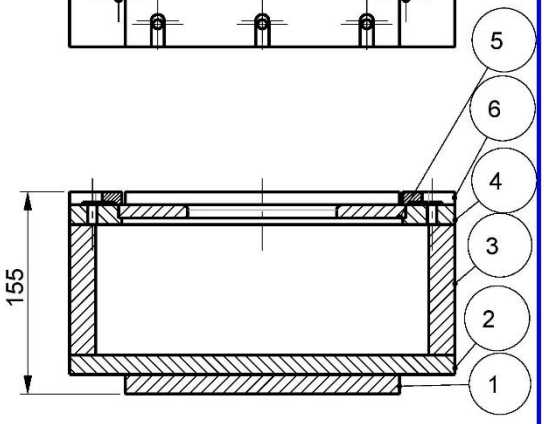


UNLESS OTHERWISE STATED ALL DIMENSIONS IN MILLIMETRES		DRN: Aug-08-17	The University of Nottingham	
TOLERANCES: LINEAR: ±0,1 ANGULAR: ±0,5	MATERIAL Aluminum	REV: ISS. DATE:	Holder	
DRAFTING STANDARD BS 8888	FINISH	COURSE	SIZE A4 SCALE 1:1	DWG NO. SHEET 1 of 1

ITEM	DWG or PART NO.	DESCRIPTION	MATERIAL	QTY
1		Lower Plate	Aluminum	1
2		Base Plate	Aluminum	1
3		Column	Aluminum	2
4		Upper Plate	Aluminum	1
5		Backing Plate	Mild Steel	1
6		Holder	Aluminum	4





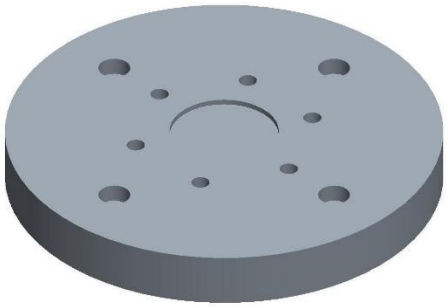


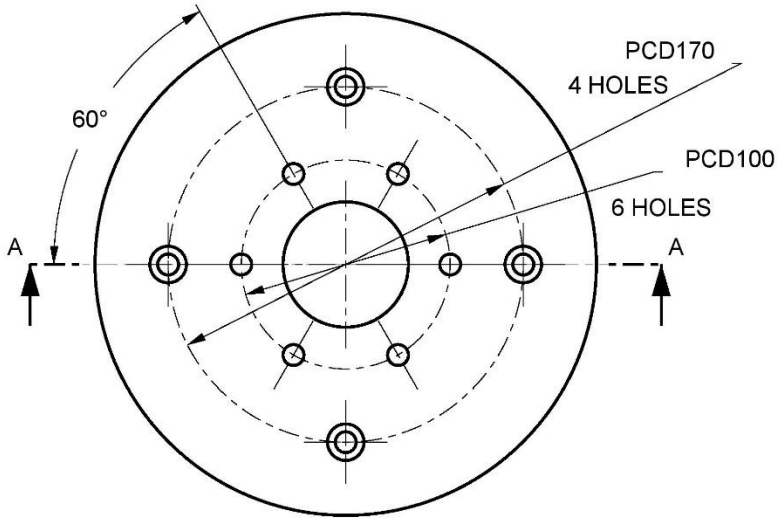
DO NOT SCALE

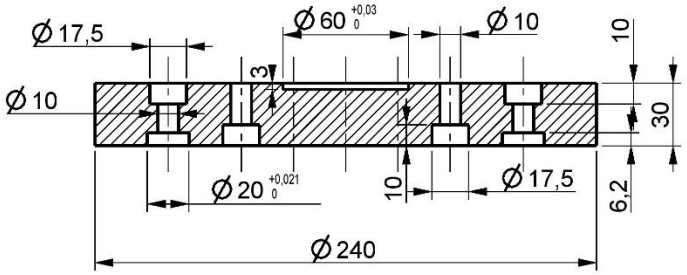
UNLESS OTHERWISE STATED ALL DIMENSIONS IN MILLIMETRES		DRN: Aug-08-17	The University of Nottingham	
TOLERANCES: LINEAR: ±0,1 ANGULAR: ±0,5	MATERIAL	REV: ISS. DATE:	SPIF Fixture	
DRAFTING STANDARD BS 8888	FINISH	COURSE	SIZE A4	DWG NO.
			SCALE 1:1	SHEET 1 of 1

APPENDIX B: Mechanical drawings used for manufacture of Nakajima die

DO NOT SCALE



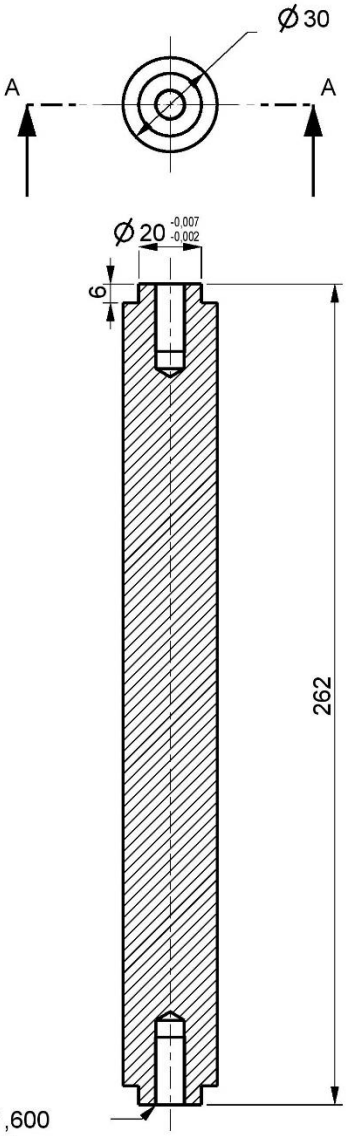




UNLESS OTHERWISE STATED ALL DIMENSIONS IN MILLIMETRES		DRN: Aug-14-14	The University of Nottingham	
TOLERANCES: LINEAR: ±0,1 ANGULAR: ±0,5	MATERIAL Mild steel	ISS. DATE: 14/08/2014	Upper Plate	
DRAFTING STANDARD BS 8888	FINISH	COURSE	SIZE A4	DWG NO.
			SCALE 1:1	SHEET 1 of 1

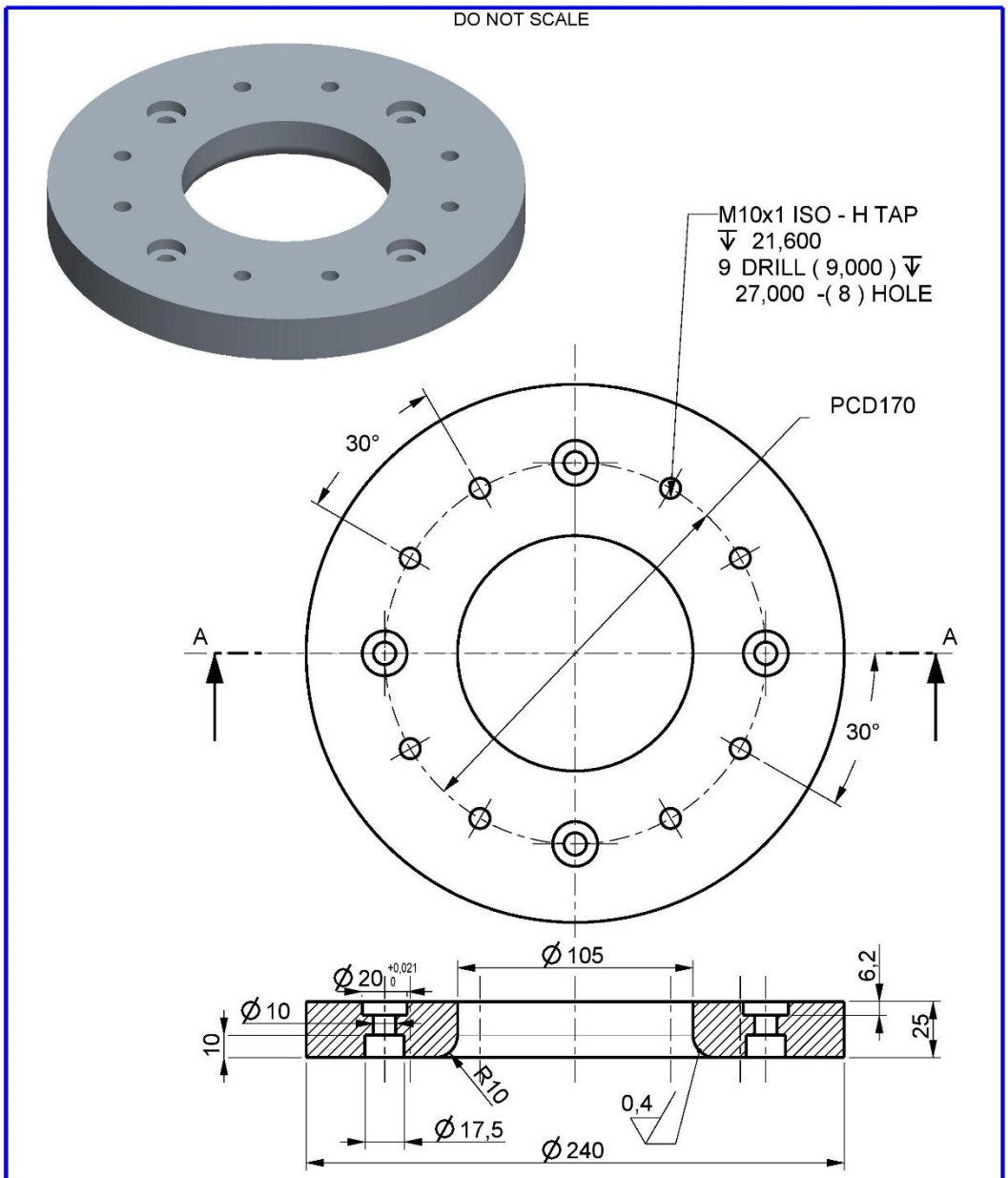
DO NOT SCALE



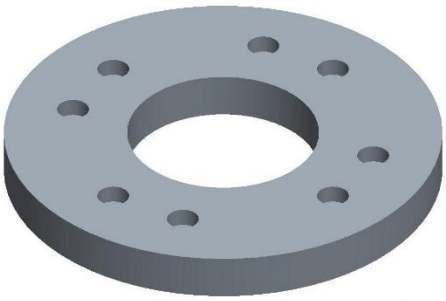


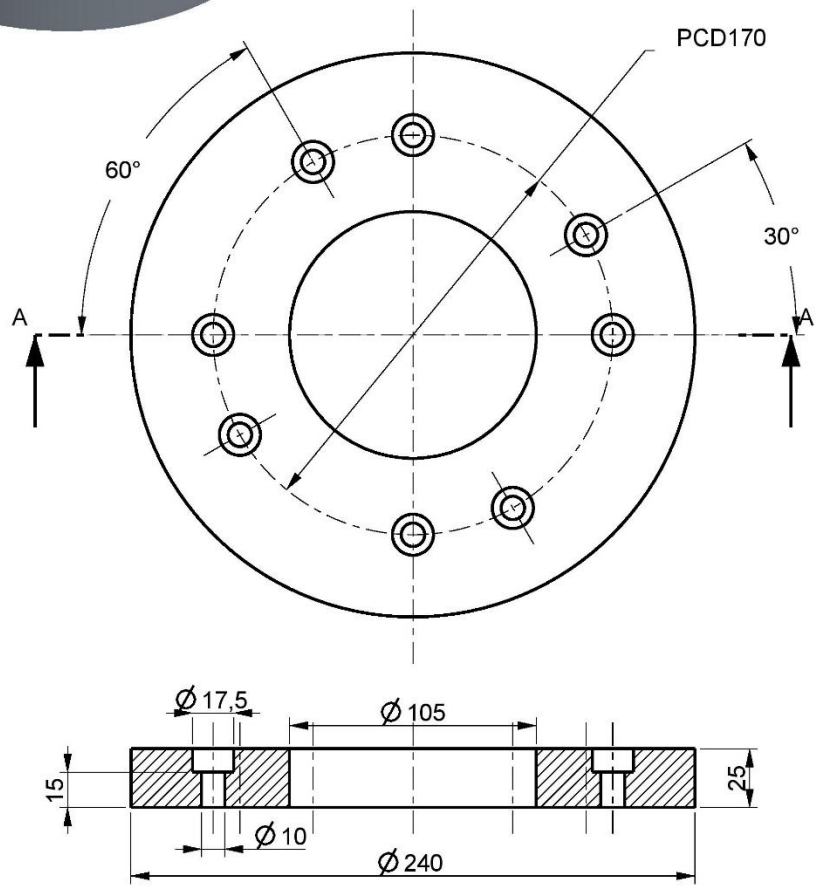
M10x1 ISO - H TAP ↧ 21,600
9 DRILL (9,000) ↧ 27,000 -(1) HOLE

UNLESS OTHERWISE STATED ALL DIMENSIONS IN MILLIMETRES		DRN: Jul-31-17	The University of Nottingham	
TOLERANCES: LINEAR: ±0,1 ANGULAR: ±0,5	MATERIAL Mild steel	REV: ISS. DATE:	Column	
DRAFTING STANDARD BS 8888	FINISH	COURSE	SIZE A4	DWG NO.
			SCALE 1:1	SHEET 1 of 1

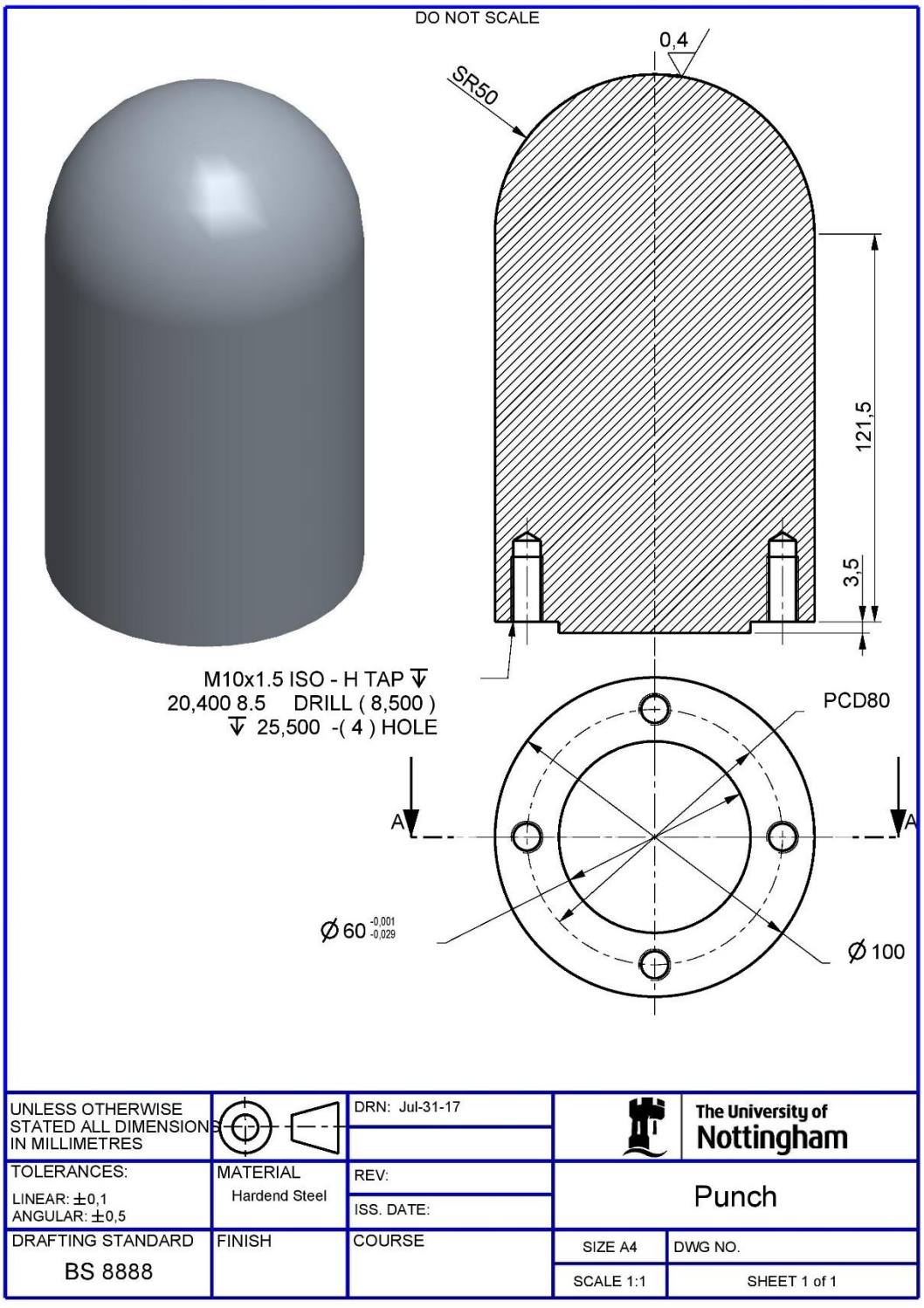

DO NOT SCALE
M10x1 ISO - H TAP
↧ 21,600
9 DRILL (9,000) ↧
27,000 -(8) HOLE
PCD170
30°
30°
A
A
Ø 105
Ø 20 +0,021 0
Ø 10
6,2
25
10
R10
0,4
Ø 17,5
Ø 240
UNLESS OTHERWISE STATED ALL DIMENSIONS IN MILLIMETRES
DRN: Jul-31-17
The University of Nottingham
TOLERANCES:
LINEAR: ±0,1
ANGULAR: ±0,5
MATERIAL
Hardened steel
REV:
ISS. DATE:
Die
DRAFTING STANDARD
BS 8888
FINISH
COURSE
SIZE A4
DWG NO. Die
SCALE 1:4
SHEET 1 of 1

DO NOT SCALE

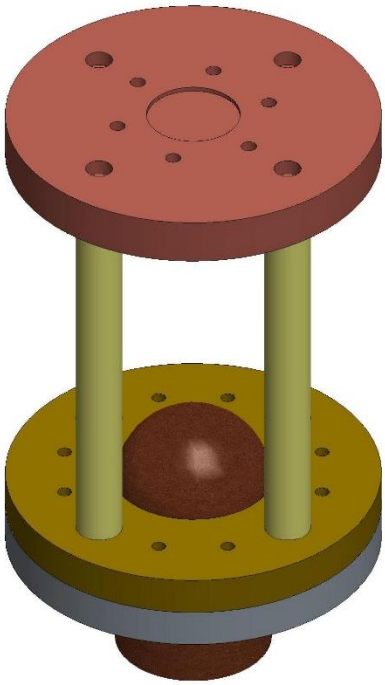


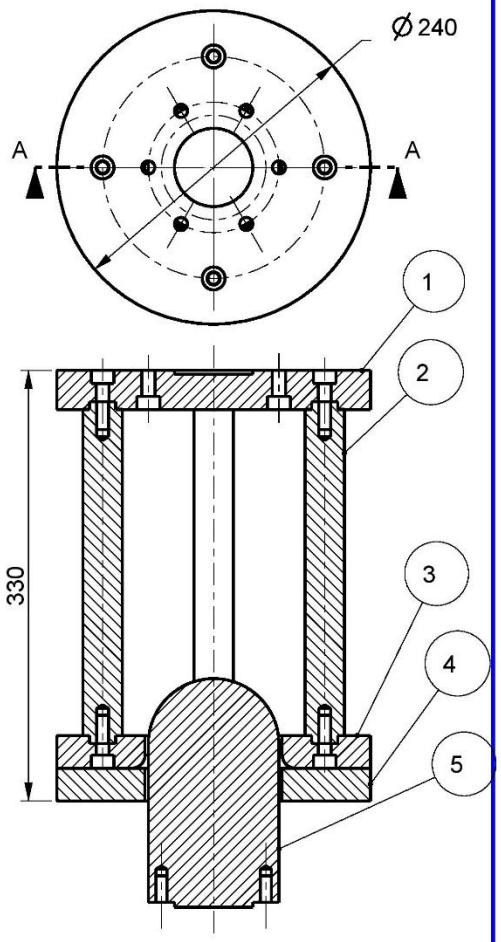


UNLESS OTHERWISE STATED ALL DIMENSIONS IN MILLIMETRES		DRN: Jul-31-17	The University of Nottingham
TOLERANCES: LINEAR: ±0,1 ANGULAR: ±0,5	MATERIAL mild steel	REV: ISS. DATE:	Holder
DRAFTING STANDARD BS 8888	FINISH	COURSE	SIZE A4 / DWG NO. SCALE 1:1 / SHEET 1 of 1


DO NOT SCALE
0,4
SR50
121,5
3,5
M10x1.5 ISO - H TAP ↧
20,400 8.5 DRILL (8,500)
↧ 25,500 -(4) HOLE
PCD80
A
A
Ø 60 -0,001 -0,029
Ø 100
UNLESS OTHERWISE STATED ALL DIMENSIONS IN MILLIMETRES
DRN: Jul-31-17
The University of Nottingham
TOLERANCES:
LINEAR: ±0,1
ANGULAR: ±0,5
MATERIAL
Hardend Steel
REV:
ISS. DATE:
Punch
DRAFTING STANDARD
BS 8888
FINISH
COURSE
SIZE A4
DWG NO.
SCALE 1:1
SHEET 1 of 1

ITEM	PART NAME	DESCRIPTION	MATERIAL	QTY
1	Upper plate		Mild steel	1
2	Column		Mild steel	4
3	Die		Hardened steel	1
4	Holder		Mild steel	1
5	Punch		Hardened steel	1





DO NOT SCALE

UNLESS OTHERWISE STATED ALL DIMENSIONS IN MILLIMETRES		DRN: Aug-18-14	The University of Nottingham	
TOLERANCES: LINEAR: ±0,1 ANGULAR: ±0,5	MATERIAL	REV: ISS. DATE: 18/08/2014	Nakajima test setup	
DRAFTING STANDARD BS 8888	FINISH	COURSE	SIZE A4	DWG NO.
			SCALE 1:1	SHEET 1 of 1